AN EXPERIMENTAL STUDY ON THE BEHAVIOR OF SEGMENTAL PILE WITH VARIABLE FLEXURAL RIGIDITY

by

Yasser Ibrahim Osman Yahia

B.S., Civil Engineering, Sinnar University, 1999

M.S., Civil Engineering, Geotechnical Department, Khartoum University, 2004

Submitted to the Institute for Graduate Studies in
Science and Engineering in partial fulfillment of
the requirements for the degree of
Doctor of Philosophy

Graduate Program in Civil Engineering
Boğaziçi University
2014

ACKNOWLEDGEMENTS

The author is greatly indebted to Prof. G. Baykal for his supervision throughout the years of my graduate study at BU. The orginal idea of variable rigidity piles is first suggested by Prof. Baykal. I am extremely grateful for his assistance, guidance and many valuable suggestions throughout the entire study. I would also like to thank Assoc. Prof. Ö. Çinicioğlu, Assoc. Prof. A. Edinçliler, Assoc. Prof. K. Orakcal and Prof. K. Özaydın for serving in my committee and for providing me assistance and guidance whenever I needed it in my research.

The beam tests are conducted at the BU material laboratory with the help of research assistant A. Akça. The author would like to thank Mr. A. Akça for his kind friendship and support.

The financial support provided by Bogaziçi University Scientific Research Fund (Project No: BAP D6389) is acknowledged. Finally, I would like to express my sincere gratitude to my parents and my best friend and wife for their continuous and unselfish support which contributed immensely to the completion of this work. I thank my brothers and sisters for their encouragement and spiritual support. I wold like to express my thanks to department secretary A. Aydın for her kind support.

ABSTRACT

AN EXPERIMENTAL STUDY ON THE BEHAVIOR OF SEGMENTAL PILE WITH VARIABLE FLEXURAL RIGIDITY

Alternating mortar blocks and rubber pads are connected to each other by a cable passing through the center of each block to form a fixed beam/pile model with variable flexural rigidity. The fixed beam/pile model is supported on manufactured springs with 1K, 2K and 3K (K=4 N/mm) spring constants to partially represent sandy soil at different relative densities. Varying tension loads are applied to the cable to achieve desired flexural rigidity for the fixed beam/pile model. Three point beam tests are conducted and the load-deflection behavior is recorded, from which representative flexural rigidity values are obtained. All other fixed beam/pile model tests are conducted on spring supports by applying load from the end (top) and middle section of the beam and measuring load and deflection at the load application point. Static and cyclic loads are applied to reach a maximum displacement of 4 mm. In addition prescale films are placed at five locations at the rubber mortar interfaces. These films are scanned, calibrated and with the help of a software the contact stress maps are obtained. From the measured deflections, corresponding spring forces are determined. From the spring reaction forces, the boundary conditions are obtained and integrated to obtain the shear forces. With the second integration moment values are determined. The stress maps obtained from prescale films are used to backcalculate the moment distribution along the fixed beam. The comparision of the moment distribution showed a similar trend with the experimental findings. The magnitude of the moment obtained from the backcalculation of prescale stress maps are upto two times of that obtained from the load-deflection measurements which is due to small number of deflection measurements which underestimated the beam curvature.

ÖZET

DEĞİŞKEN EĞİLME RİJİTLİĞİNE SAHİP EKLEMLİ KAZIK DAVRANIŞI ÜZERİNE BİR ÇALIŞMA

Eğilme rijitliği değişebilen ankastre eklemli kiriş/kazık modeli oluşturmak amacıyla çimento harç blokları ve kauçuk levhalar ardısıra yerleştirilmiş ve blok merkezinden geçen bir kablo vasıtasıyla bu bloklar birbirlerine birleştirilmiştir. Oluşturulan ankastre kiriş/kazık modeli 1K, 2K ve 3K (K=4 N/mm) yay sabitleri ile imal ettirilen lineer yaylar üzerine yerleştirilerek, farklı rölatif sıkılıktaki kumlu zemin davranışı kısmen modellenmeye çalışılmıştır. Kabloya farklı germe kuvvetleri uygulanarak kiriş/kazık modeli için değişken eğilme rijitliği elde edilmiştir. Üç nokta eğilme deneyleri yapılarak model kiriş/kazık için yük-deplasman eğrileri saptanmıştır. Bu veriler kullanılarak eklemli kiriş/kazık modeli için eğilme rijitliği değerleri hesaplanmıştır. Diğer tüm deneyler yaylar üzerine yerleştirilen ankastre eklemli kiriş/kazık modeli üzerinde modelin uç noktasına ve merkez noktasına yük uygulanarak ve bu noktalarda yük-deplasman değerleri ölçülerek gerçekleştirilmiştir. Numune üzerine maksimum 4 mm deplasman yapacak büyüklükte statik ve çevrimsel yük uygulanmıştır. Harç blok-kauçuk levha arayüzlerine beş ayrı noktada Prescale film yerleştirilmiştir. Deney sonrasında bu filmlerde oluşan renk değişimleri taranmış, kalibre edilmiş ve yazılım kullanılarak kontakt gerilme haritaları çıkarılmıştır. Deneylerde ölçülen deplasmanlardan, yay reaksiyon kuvvetleri elde edilmiştir. Sınır şartları saptandıktan sonra entegrasyon yoluyla kesme kuvvetleri bulunmuştur. İkinci entegrasyon ise moment eğrisini vermektedir. Kontakt gerilme haritasından geri hesaplanarak elde edilen moment büyüklüğü yük-deplasman eğrilerinden elde edinen moment büyük-lüğünün iki misli kadar bulunmuştur. Bunun sebebi de deney sırasında üç noktada deplasman ölçümü yapılmasının model kiriş/kazığın eğimini yeteri kadar verememiş olmasındandır.

TABLE OF CONTENTS

LIST OF FIGURES

LIST OF TABLES

LIST OF SYMBOLS

$1K$	Spring Stiffness to represent loose sand
$2K$	Spring Stiffness to represent medium dense sand
$3K$	Spring Stiffness to represent dense sand
A	Acceleration
A_y, B_y	Non-dimensional parameter (deflection)
A_s, B_s	Non-dimensional parameter (slope)
A_m, B_m	Non-dimensional parameter (moment)
A_v, B_v	Non-dimensional parameter (shear)
B	Pile diameter
b	Width of concrete block
C	Cohesion of soil
C_1	Constant of integration
C_2	Constant of integration
C_3	Constant of integration
C_4	Constant of integration
C_u	Undrained strength of the soil
D	Deflection
d	Depth of concrete block
E	Elastic modulus
e	Eccentricity
E_f	Flexural modulus of elasticity
E_{jg}	Soil modulus of jet grouting
F	Force
F_s	Factor of safety
I	Moment of Inertia
K	Spring Stiffness
K_o	Earth Pressure at rest
K_p	Coefficient of passive earth pressure
L	Length

M	Bending moment
P_t	Applied lateral load at pile head [KN]
S	Slope
T_f	Frictional resistance to shear
V	Shear force
X	Horizontal distance
α	Interface dilation a noel
δ	Settlement in soil layer
γ	Unit weight of soil
ϕ	The angle of internal friction
Φ	Effective angle of shearing resistance
θ	Slope angle
$\in_f$	Flexural strain
δ_1	Interface friction angle between soil and concrete
σ_1	Vertical effective stress
σ_3	Horizontal effective stress
σ_f	Flexural stress
σ_n	Normal stress
σ'_v	Effective overburden stress
σ_x	Stress in the x-direction

LIST OF ACRONYMS/ABBREVIATIONS

AF	A Film
ASTM	American society for testing and materials
CF	C Film
CL	Cyclic load
CRR	Cyclic resistance ratio
CSR	Cyclic stress ratio
DFS	Deformable foundation systems
DSD	Three dimensional stress distribution
FEA	Finite element analysis
FHWA	Federal highway administratio
FS	Factor of safety
GCCs	Geotextile confined columns
GPAs	Granular pile anchors
HDPE	High density polyethylene
HMFS	High modulus foundation system
LC	Load cell
LLW	Super low pressure
LTP	Load transfer platform
LVDT	Linear variable differential transformer
MTS	Control test equipment
NDM	Non-dimensional method
RFS	Rigid foundation system
PSC	Particle size control
RIs	Rigid inclusions
SCs	Stone columns
SL	Static load
SPVFR	Segmental pile with variable flexural rigidity
ST	Stone column

1. INTRODUCTION

1.1. General

Ground improvement is achieved by constructing a regular grid of vertical elements, or inclusions (either stone columns or rigid inclusions), across soil layers with low bearing capacity and/or high compressibility, extending down to a more resistant layer. Because these vertical elements are stiffer than the surrounding soil, they "attract" a portion of the loads applied at the ground surface. Columns make a unique contribution to ground improvement in that the soil bears a portion of the structural loads in relative proportion to its own strength, while the bulk of the loads are transmitted by various mechanisms to the columns. This process applies to earthworks as well as civil structures and buildings (Gniel and Bouazz, 2010).

A new construction technique for rigid inclusion is proposed: segmental concrete blocks, pretensioned with anchor cable. A fundamental study is needed to understand the behavior of segmental pile with variable flexural rigidity SPVFR. In this investigation, the performance of the pile model under static and cyclic lateral loads are studied; therefore, Winkler's beam method resting on elastic spring is used.

1.2. Problem Definition

It has been observed that stone columns are too weak to resist lateral forces; and they experience excessive vertical settlement and lateral deformation under sustained loads. Another consideration is the spreading and loss of stone column material to the surrounding soil. A new technique is introduced to install rigid inclusion with some lateral load capacity.

1.3. Objective of the Research

The main objective of this research is to develop a segmental pile with variable flexural rigidity system SPVFR whose flexural rigidity can be controlled, and to investigate the behavior of the pile model under lateral load. The advantages of controlling the flexural rigidity of the pile model can be summarized as the prevention of the total collapse by enabling the system to bend without breaking under horizontal forces.

1.4. Organization of the Dissertation

To achieve the previous objectives an experimental research program has been carried out where the influence of each variable on the behavior of a segmental structural member has been investigated.

The following is a brief outline of the remaining chapters of the thesis. Chapter 2. The literature review, presents geosynthetic encasement of stone column, utilization of high modulus columns in foundation engineering, relationship between rigid inclusions and stone columns, rigid inclusions, the theory of non-dimensional analysis method, post-tension techniques of materials, hysteretic behavior, ground acceleration and building damage, Winklers' beam on elastic soil, evaluation of elastic modulus, compressive strength test, rubber properties and a summary. Chapter 3 methodology deals with test equipment and measuring tools, material properties and testing. Specimen preparation and three point bending tests of segmental pile with variable flexural rigidity SPVFR are presented.

Chapter 4 deals with segmental pile with variable flexural rigidity SPVFR on Winkler foundation test results under static load. The pile model on Winkler foundation test results under cyclic load. P-y curve of the pile model on Winkler foundation is listed numerically. Moment, shear and deflection values for different soil stiffnesses are also evaluated.

Chapter 5 focuses on evaluation of test results, flexural rigidity of the SPVFR, and the effect of post-tension forces on the pile model. P-y curves, comparison of experimental results to L-pile and non-dimensional method are presented. Evaluation of stress distribution of the plie model is presented. Chapter 6 includes conclusions and recommendations.

2. LITERATURE REVIEW

2.1. Introduction

Some structural foundations and compression members like stone columns have less resistance against lateral load which result in failure due to lateral loading application. Therefore, some researchers published papers regarding improvement of the behavior of foundation members against lateral loading. The problem of the laterally loaded pile is originally of particular interest in the offshore industry. Lateral loads from wind and waves are frequently the most critical factor in the design of such structures. Solution to the general problem can also apply to a variety of onshore cases including pile-supported earthquake resistance structures, power poles, and pile supported structures which may be subjected to lateral blast forces or wind forces.

The purpose of this chapter is: (i) to discuss the factors that affect the lateral capacity of rigid inclusions, stone columns and pile, (ii) to provide a brief introduction of non-dimensional analysis method and post tension forces, (iii) to describe available criteria of beam on Winkler foundation and constructing p-y curves for sands cohesionless soil.

2.2. Soil Improvement Techniques

2.2.1. Utilization of High Modulus Columns in Foundation Engineering

2.2.1.1. General. In the selection of various foundation systems, loading conditions together with hazard identification are considered. In seismically active areas such as Turkey, often the design of the foundation is controlled by the parameters of the selected design earthquakes. Liquefaction of subsoil, under earthquakes is one of the primary hazards that have to be considered during the design and construction. The factor of safety against liquefaction could easily be determined based on the detailed soil modeling at a given site for a design earthquake. There are various mitigation procedures against liquefaction based on the following principles (Gniel and Bouazza, 2010).

- Utilization of prefabricated special high permeability drains or stone columns to facilitate the immediate drainage of excess pore water pressure developed during shaking.
- Utilization of subsoil compaction by means of vibroflotation, vibroreplacement, compaction piles, and dynamic compaction to increase cyclic resistance ratio CRR.
- Utilization of high modulus columns by means of deep mixing and/or jet grouting within the subsoil to decrease cyclic stress ratio CSR taken by the subsoil.

The construction and design parameters of such columns will be defined. A simplified design algorithm for the utilization of these columns against liquefaction and their effects towards the factor of safety will be provided. The result of three case studies related to positive performance of such improved foundations during 17 August 1999 Kocaeli/Turkey Earthquake is also provided (Gniel *et al.*, 2009).

<u>2.2.1.2. Definition of High Modulus Columns.</u> Structural members-columns having different stiffnesses are designed and constructed for various purposes within the soil as part of the foundation systems in different civil engineering structures. These columns having higher modulus than the original foundation subsoil could be classified in three groups as follows:

<u>2.2.1.3. Rigid Foundation Systems - RFS.</u> The reinforced concrete piles constructed using various techniques could be included in this group. Driven piles, driven cast-in-situ piles, cast-in-situ piles and micropiles are some examples of rigid foundation systems. In this system, the rigidity of the structural member, i.e. the pile is much larger than the surrounding soil, and therefore, the vertical loads from the upperstructure is carried mainly by these members by means of skin friction and/or tip-resistance.

For the lateral loads, pile caps supported by the foundation subsoil or structural slab-on-grade slab and special steel reinforcement close to the top of the pile are often utilized. For such rigid structural reinforced concrete column, the deformation modulus could be taken as E_{cl}= 25,000 MPa and the modulus ratio (modulus of column/modulus of subsoil) E_{cl}/Es ranging between 1000- 6000 depending on the nature and stiffness of the subsoil.

2.2.1.4. High Modulus Foundation System - HMFS. These systems, also named high (controlled) modulus columns, are constructed within the soil by mixing with cement slurry with the in-situ subsoil. In the deep-mix procedure, the soil is mixed with the cement slurry using mechanical equipment. High modulus columns can also be constructed by means of jet grouting technique. In both cases, the in-situ soil is mixed with controlled cement slurry resulting in a partially controlled material called soilcrete. The mechanical properties of soilcrete column are determined and controlled by means of various factors, such as construction procedure, quality of cement slurry and the nature of in-situ soil. For various soils, the modulus of these columns constructed using both techniques could vary in the range of E_{jg}= 500-1200 MPa, Therefore, this will yield to modulus ration of E_{jg}/E_s=10-150 (Durgunoğlu, 2004).

2.2.1.5. Deformable Foundation Systems - DFS. In these systems, the rigidity of the structural column within the soil is the least among the three different categories. Therefore, these systems are named deformable foundation systems which are utilized using crushed stones. Dry and wet systems together with top and bottom feeding mechanisms using vibroreplacement technique have been adopted in various stonecolumn construction procedures. In Turkey, stone columns are usually constructed by closed end steel pipes driven into the soil; and later crushed stone is placed within the casing while vibrating and extracting the casing (Durgunoğlu *et al.*, 1995). The modulus of stone column could be taken as Esc= 40-80 MPa, yielding modulus ratio of Esc/Es ranging between 5-30. The foundations supplied by stone column may experience excessive vertical displacement, especially when utilized in soft clays due to the limited confinement of the subsoil.

<u>2.2.1.6. Jet Grout System Construction Parameters.</u> In the jet grouting system, controlled quantities of cement is injected through small diameter nozzles into the subsoil to create certain diameter soilcrete columns. The construction parameters of the system could be stated as follows:

- Fluid system (namely, single Jet-1, double Jet-2 and triple Jet-3 fluid systems, using grout alone, grout + air, grout + water + air),
- The injection pressure (Bar),
- Number and diameter of nozzles (mm),
- The rotation speed of the monitor (rpm),
- The retrieval speed of the monitor (cm/min),
- Water/cement ratio,
- The pump capacity (lt/min).

The typical parameters and their range of values are summarized in Table 1, (Lunardi, 1997).

Table 2.1. Jet Grout Parameters, (Lunardi, 1977).

System	Fluid Type	Pressure [Bar]	No. of Nozzles and Dia[no.mm]	Lifting Speed [cm/min]	Rotation Speed[rpm]	W/C Ratio	Pump Capacity [Lt/min]
Jet 1	Cement	400-550	1-2x2-5	15-100	5-15	1.0-1.5	70-600
Jet 2	Cement	400-550	1-2x2-5	10-30	4-8	1.0-1.5	70-600
	Air	10,12	-	10-30	-	-	4000-10000
Jet 3	Cement	50-100	1-2x4-5	6-15	4-8	1.2-1.5	80-200
	Air	10-12	-	6-15	-	-	4000-10000
	Water			6-15	-	-	40-100

<u>2.2.1.7. The Utilization of High Modulus Columns in the Foundation Engineering.</u> The high modulus columns constructed by means of jet grouting have been utilized in various foundation engineering applications for various purposes in the past (Durgunoğlu, 2004). These could be summarized as:

- Utilization as compression members, under foundations to increase bearing capacity and to reduce settlement,
- Utilization as compression members below slabs on grade under high surcharge

loads to increase bearing capacity and to reduce settlement,

- Utilization as compression members under fills and embankments to increase bearing capacity and to reduce settlement,
- Utilization as compression members below approach embankments in bridges to prevent negative skin friction on abutment piles, and to decrease lateral loads due to embankment on abutment piles.
- Utilization as tension member against uplift complementing with reinforcement in water reservoirs and structures located below ground water table.
- Utilization in series of rows as gravity type retaining structures in excavations.
- Utilization as vertical bending member complemented with steel reinforcement within a retaining structure in excavation.
- Utilization as special anchor complemented with steel reinforcement in tieback excavation.
- Utilization as a member of diaphragm wall between structural piles, instead of intersecting piles.
- Utilization as bottom strut in a deep excavation in soft clays constructed from the top prior to excavation.
- Utilization as cut-off member at the base of the excavation against seepage towards the cut.
- Utilization as soil improvement system above the tunnels prior to excavation and mucking of the tunnel.
- Utilization as structural umbrella in front and above the tunnel face excavation in soft ground tunneling.

In addition to these applications, high modulus columns could also be utilized against seismic loads due to the earthquakes in seismically active areas. Such practice in the past could be litsed as:

- To reduce the vertical and horizontal displacements of foundations under seismic loadings utilize it restraining structure around and below the foundation.
- To reduce the lateral loads to be transferred to pile foundations, under seismic loading, by utilizing together with piles under the foundation mats and finally,

- To utilize with certain spacing and diameter below the foundations, and to mitigate the liquefaction hazard under earthquake loading.

2.2.2. Stone Columns

2.2.2.1. Installation Effects. The installation of stone columns alters the soil around the column, that may have positive, negative or negligible effects. Installation effects are one of the major concerns in all stone column applications, and require better understanding. (Magnan *et al.*, 2005) presents empirical evidence suggesting that the column diameter depends on several factors, such as the strength of the soil, the type of construction (e.g., dry vs. wet methods), the energy transmitted to the soil by the vibrator and construction sequence, among others. Similarly, the quality of workmanship has a significant influence on the quality of the column, and in particular, on ensuring that the required column diameter is achieved (Slocombe *et al.*, 2000). (Alonso and Jimenez, 2012) report an 8 - 10% variation in the diameters of more than 9000 stone columns built by a specialised contractor in a well-controlled environment.

The functions of such a column are to improve ground characteristics (i.e. increase bearing capacity and reduce settlement), and facilitate drainage by changing the preferred drainage path from vertical to horizontal. During installation, as the soil is displaced laterally:

- excess pore pressure is generated, and subsequently assumed to dissipate towards the permeable columns;
- horizontal stresses increase, leading to a post-construction coefficient of earth pressure $\bar{K}$ that exceeds the original at rest coefficient $\bar{K}0$; and - the surrounding soil is in part remoulded by the vibrator penetration. Smear and plastic annuli that appear during installation can have a negative influence on both of the above mentioned functions of columns.

Lateral earth pressure clearly influences the improvement factor achieved with a stone column improvement, because it provides lateral support for the column and influences its yielding. The $\bar{K}$ value is, therefore, an important parameter for stone column design, and is generally assumed to be equal to 1 (Priebe, 1995). (Castro *et al.*, 2012) also draw attention to the reduction of the undrained shear strength caused by the installation of vibro-displacement columns in sensitive soft soils, (Slocombe *et al.*, 1991).

2.2.2.2. Failure Modes. Two failure mechanisms of stone columns are acknowledged under vertical loading shown in the Figure 2.1. The failure results either from relatively low lateral support in the upper third of the column "bulging failure", or because the column toe is punched into the underlying soil, such as in "floating foundations" (Sondermann and Wehr, 2004). However, the failure is always preceded by such high rates of deformation that the column's serviceability is generally no longer provided. Sondermann and Wehr observe that the equations used to calculate the deformations, or "serviceability state", of the foundations in question are much more relevant than the outcome of the limit load assessment of stone columns. Columns belonging to a small group under a rigid footing, or columns placed close to the edges of a loaded area (embankment slopes), may fail by a combination of bulging and bending.

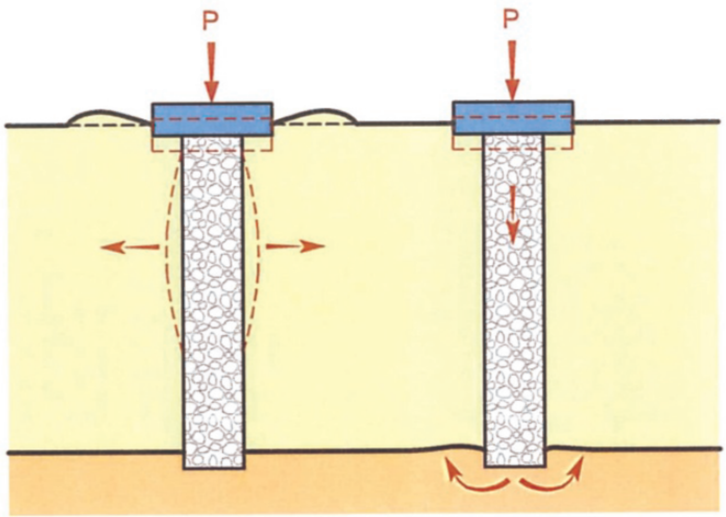

Figure 2.1. Failure Mechanism in Vibro-Replacement Stone Columns Under Vertical Loading (Sondermann and Wehr, 2004).

2.2.2.3. Design. Placed on the considerations described above, the design of stone column ground improvements may, therefore, consider either the prevailing conditions when load is applied, which are governed by the initial undrained strength s_u (possibly modified by column installation), or those attained later, when part or all of the excess pore pressure due to installation and loading has dissipated. If the load share taken by the soil is ignored, the column behaviour is treated as though it were that of an isolated foundation element in a soil retaining its initial undrained shear strength, which is rather a pessimistic assumption. However, this is implicitly assumed when a minimum undrained shear strength value, often su = 15 kPa, is given for SC ground improvement. (Sonderman and Wehr, 2004) show that this limit value is not adapted to the design of stone columns under spread loads with, the example of columns routinely installed in soils with shear strengths as low as 6 kPa in Malaysia to bear spread loads from embankments. The load share taken by the soil must be considered to produce an optimal design for SC grid patterns.

In Europe, (Priebe's, 1995) design method for vibro replacement stone columns has gained acceptance as a valid method. This method defines the improvement factor (n) as a function of the coverage area ratio and the angle of internal friction of the column material. Corrections are applied to cover the influence of column compressibility and overburden. The improvement factor n falls within the range of 2 to 6, with values of 3 to 4 being more common (Mitchell *et al.*, 1991). Because n should represent the ratio of the column and soil's constrained modul in an equivalent linear elastic model of a unit cell, one assumes that plastic deformation of the columns is implicitly included in that experimental figure. A much higher stiffness ratio would be expected between gravel in a dense state and soil if the gravel behaved within the elastic range.

An interesting question is whether the improvement factor also depends on load intensity (Özkeskin *et al.*, 2012) give an interesting example of full-scale group load tests where the improvement factor is found to increase with load intensity.

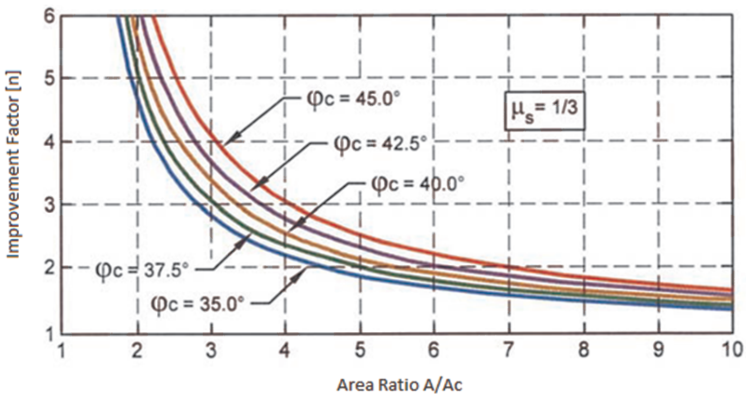

Figure 2.2. Design Diagram for Improving the Ground Conditions Using Vibro Replacement Stone Columns (Priebe, 1995).

As already mentioned, a small group of columns does not match the assumptions of an infinite grid, and its design calls for more specific approaches. Priebe gives practical design charts that allow the settlement of a rigid foundation on a limited number of columns to be estimated as a proportion of the settlement of an infinite raft supported by an infinite grid of columns as given in the Figure 2.2 (Priebe, 1995). These charts are to be taken as approximations; (Sondermann and Wehr, 2004) recommend that it is best to install test columns with the achievable column diameters and load them to obtain results with an effective outcome before making final design decisions. Numerical modelling can overcome some of the difficulties met when designing groups of columns and help determine their stress-deformation behaviour in the service load range, (Schweiger, 2008) gives an overview of analytical and numerical methods for stone column design. Unless certain homogenization methods are used, such models remain computationally demanding, particularly when they are 3D. The incorporation of installation effects in these models are still researched.

Stone column design is concerned with the assessment of settlement (amount and rate) and safety against failure (bulging failure, punching failure or combined bending and bulging). The verification of serviceability limit states is accomplished by calculating displacement with an adapted numerical model and characteristic values for the soil parameters.

The verification of ultimate limit states requires that an appropriate set of partial safety factors be set up so that safety against any failure mode can be calculated with appropriate design values for the soil parameters. Consensus on the most appropriate calculation models, together with the calibration of associated partial safety factor values, remains to be reached in many countries that lack national design guidelines in line with structural standards for SC ground improvement design.

Geotextile confined columns GCCs are made by driving or vibrating a 80-cm-diameter steel casing into the bearing soil followed by the placement of a seamless cylindrical closed bottom geotextile “sock” with a tensile strength ranging from 200 to 400 kN/m (Chu *et al.*, 2009). The sock is then filled with sand to form a sand column. The main advantage of this method over the SC technique is assumed to lie in its reduced installation effects (i.e., less alteration of the soil structure). GCCs were used for the construction of a dyke over a very soft surface mud layer of 3- to 12-m thickness in Hamburg. Accounting for the benefits of the geotextile confinement necessitated the use of refined numerical procedures (Raithel *et al.*, 2005).

Granular pile anchors GPAs are another interesting development devised for mitigating the problems posed by swelling clay beds. In a granular pile anchor, the footing is anchored to an anchor plate at the bottom of the granular pile. This makes the granular pile tension-resistant and enables it to absorb the tensile force imposed on the foundation by the swelling clay (Rao, *et al.*, 2007), (Aljorany, 2012) presents a numerical study of this technique in this session.

2.2.3. Rigid Inclusions

<u>2.2.3.1. Description.</u> This technique, which is increasingly used in many countries, has many different names: piledembankment, column-supported embankment, geosynthetic reinforced pile supported GRPS embankment, pile-supported earth platform or soil column reinforcement. Rigid inclusions are also called columns, pile-like inclusions or non-contact settlement-reducing piles in a generic sense; deep mixed columns, lime columns, or jet grouting columns in reference to some of the installation techniques

commonly used; and Controlled Modulus Columns CMCs or Vibro Concrete Columns VCCs in reference to proprietary names.

The general concept of the technique is the combination of an array of vertical rigid columns and a granular mattress (load transfer layer) so that loading from an embankment or slab is transferred to a deep bearing stratum shown in the Figure 2.3. The columns may have enlarged heads or caps. The presence of a transition layer with a load transfer function on top of the column heads is a primary attribute of RI ground improvement techniques. The fact that there is no connection between piles and the superstructure clearly distinguishes RI ground improvements from piled raft foundations.

The load transfer platform LTP should ideally be made of high grade granular material, most often a gravel layer. The designer should carefully consider shear resistance and compactness in the design. Under an embankment, this layer may simply comprise the bottom fill layer if it is of good enough quality. The load transfer layer may be reinforced by one or more high-strength geotextile or geogrid reinforcements or even welded wire mesh. Hydraulically stabilized soils are sometimes used to build the transition layer when mineral resources are scarce or costly. Soil treatment with hydraulic binders leads to an enhanced tensile strength and improved shear resistance over the untreated soil, but care should be taken to ensure that treated soil retains its ductile behavior. Brittle behavior would put the shear mechanisms that operate the load transfer at risk. The presence of a concrete slab or raft on top of the LTP causes other differences (Rathmeyer, 1975):

- Without a slab (piled embankments), the load transfer above the column head is operated only through a shear mechanism in the LTP and any fill layer on top of it. The applicable stress boundary conditions are found in a calculable surcharge on top of the model. With a slab or a raft, the structural element also contributes to the transfer of the load onto columns. Specific boundary conditions are obtained by assuming that the settlement is uniform under the structural element base. This is justified by the fact that its own deformations are negligible when compared to the soil deformations. This assumption leads to a non-uniform vertical stress distribution on top of the LTP (Rathmeyer, 1975).

2.2.3.2. Development. The first applications of RIs date from the late 1970s, mainly in road embankments in Scandinavian countries (Rathmeyer, 1975). A renewed interest in this technique stemmed from a study about negative side friction by Combarieu during that time period (1974, 1988). The technique has since been extended to a range of other construction types with wide spread loading, such as storage tanks, water treatment basins and slabs-on-grade for industrial or commercial facilities, as shown in Figure 2.3 (Simon and Schlosser, 2006).

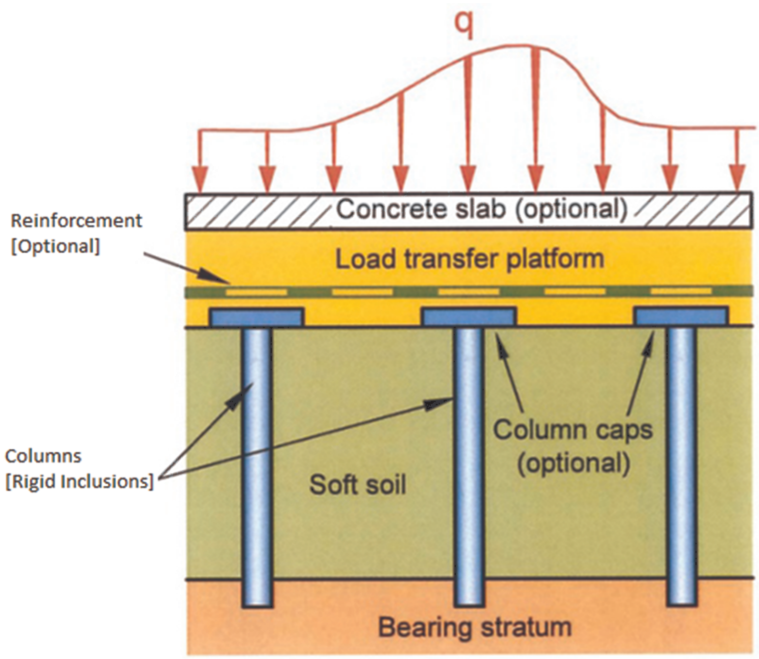

Figure 2.3. Constituents of the Rigid Inclusion Ground Improvement Concept (Simon and Schlosser, 2006).

Siman and Schlosser, (2006) in the latter case, concentrated loads from columns or bearing walls are often also supported by a compound foundation comprised of a concrete spread footing, a granular cover, and a limited number of inclusions below. RI ground improvement is now a very cost-effective foundation solution for common construction projects. Several landmark applications punctuate its development and illustrate that this basic concept can be applied equally effectively to complex construction projects.

As occurs in many fields, construction practice has developed ahead of the design methods adapted for this new foundation concept. Partial reference to pile foundation standards could be made during the design process, although designers recognize that these are not quite adapted to the columns most often used as settlement reducing elements instead of load-bearing elements. Current practice varies between countries in which the applications of rigid inclusions pertain to piled embankments and those in which their use has been extended to occur under structural elements such as rafts, slabs or even spread footings (Briançon, 2002). Identified some of these differences: higher values for the coverage area ratio (10 to 35%) and a thicker transition layer (minimum thickness being taken as Hmin = 0.8(s - a), the clear span between inclusion heads along the mesh diagonal) are generally used in piled-embankment design, and geogrid reinforcement of the LTP is often the norm. Lower area ratio values (2 to 10%) apply under concrete slabs or rafts, while the thickness of the load transfer layer is commonly reduced to between 0.4 m and 0.8 m. The LTP is seldom reinforced under concrete slabs. The soil reaction between inclusion heads may be neglected (BS 8006, 2010) assuming that all loads are transferred to the inclusions by shear (arching) and membrane effects. The soil reaction may also be accounted for simply through the use of a subgrade reaction coefficient (EBGEO, 2010, CUR 226, 2010). The interaction between the soil and column is often treated as a secondary factor in load transfer design models, which focus on what happens above the inclusion heads.

2.2.3.3. Advantages and Drawbacks. The following advantages explain why RI ground improvement has drawn so much interest:

- Loading can be partly carried by the soil.
- A wide range of techniques may be used to install inclusions.
- There is no spoil to dispose of if a pile displacement technique is used, and the technique can be applied in brownfields or old landfills.
- More columns of smaller diameter and lesser embedment in the bearing stratum

are generally faster and cheaper to build than an equivalent pile foundation for the same total load; this is a result of the steady capacity development of installation equipment by specialised contractors.

- There is no connection between columns and the structure above them, which generally simplifies structural design.
- The construction time period is significantly shorter than for other solutions, such as preloading with vertical drains.
- The technique provides good seismic performance when properly designed, as illustrated by the Rion- Antirion project (Pecker, 2004).

The following drawbacks, however, should not be ignored:

- The qualifications required to perform RI designs include knowledge of composite foundation systems, necessitating a comprehensive approach encompassing the design and execution phases.
- Execution constraints are more severe (e.g., interfacing between distinct contractors installing the inclusions, the load transfer platform and any slab on it).
- Newly completed inclusions are sensitive to asymmetric loadings that may have negative and potentially destructive effects.
- Horizontal forces and wide load differentials generate bending moments and shear forces in the inclusions that must remain within the capacity of the material's structural resistance.

2.2.4. Relationship Between Rigid Inclusions and Stone Columns

2.2.4.1. General. Both rigid inclusions RIs and stone columns SCs are classified by the TC17 State of the Art Report about Construction Processes (Chu *et al.*, 2009) as ground improvement methods with admixtures or inclusions in the same category as dynamic replacement, sand compaction piles and geotextile confined columns. Rigid inclusions and stone columns can be installed using many different techniques, which the same report describes in detail along with the latest developments in these techniques. Stone columns and rigid inclusions can also be described as two different methods for improving soil behaviour through the use of columns that are often cylindrical in shape, mechanically continuous and typically vertical.

Both of these methods are very cost-effective ways to obtain an adequate foundation conditions for a wide range of engineering works, and their use grows around the world. The scarcity of land for new projects in urban areas and the increased attention given to project cost optimization explain the growing interest in these techniques.

The use of stone columns is older than that of rigid inclusions. Stone columns are the product of a technique called vibro compaction that dates back to the late 1930s (Sondermann and Wehr, 2004). The use of rigid inclusions for ground improvement is documented only since the early 1980s mostly for road embankment construction in northern Europe (Briancon, 2002). However, the emergence of this technique could be viewed as the rebirth of an antique construction technique whereby a group of closely spaced timber piles topped with a stone cover served as the foundation for bridge piers. have described a pre-Columbian example in an aqueduct in the Mexico City area, (Auvinet and Rodriguez, 2006).

2.2.4.2. Differences Between SCs and RIs. Ground improvement elements deserve the adjective "rigid" whenever the component material displays a strong permanent cohesion, thereby generating a level of stiffness significantly greater than that of the surrounding soil. Nonetheless, this stiffness may vary widely depending on the type of inclusion developed, which can range from a lime column to a metal section, but also includes the vibro concrete column, mortar column and concrete column (both with and without reinforcement). The rigid inclusion concept assumes that column stability is achieved without any lateral confinement of the surrounding soil (Asırı, 2012). From that standpoint, RI ground improvement can also be viewed as a soil reinforcement technique using resistant elements inserted in the soil in a similar manner to soil nailing, where the soil is reinforced by installing an array of tensile resistant steel elements. Unlike rigid inclusions, stone columns require lateral confinement from the surrounding soil.

Stone columns must undergo lateral deformations in order to mobilize the lateral support and generate an interaction between the soil and the columns. The plasticity of the columns strongly controls their behavior, which is also quite different from that of rigid inclusions that exhibit small and nearly elastic deformations. Stone column behavior depends on the angle of shear resistance of the granular material as well as on its angle of dilatancy. Both techniques depend on the granular material's in situ density that can be achieved by the vibration and construction process. Because the stone column behavior is controlled by confinement of the soil, it will depend on two main factors: first, the modifications to soil properties caused by the installation process (including the consequences of the lateral displacement imposed by inserting and moving the vibrator and densifying the granular material, the increase in horizontal stress in the ground and the remoulding) and second, the time factor reflecting progressive dissipation of excess pore pressures created by the installation process, and by the loads imposed on the ground surface (Magnan *et al.*, 2005).

The RI diameter can be of any value permitted by the installation technique (whether it is one specific RI technique or any other among the common piling techniques) with a generally accepted minimum value close to 25 cm. Yet, this parameter does not make a key difference, because the replacement ratio (or coverage area ratio), which is the ratio of the cross-sectional area at the column head over the treatment mesh area, is more relevant. Both techniques employ a wide range of replacement ratio values: 7-15% for stone columns, but only 2 to 10% for rigid inclusions. It should be noted that RI ground improvement can achieve a better settlement reduction factor than SC ground improvement. The choice of grid layout and mesh size (which determines the replacement ratio) is a major step in designing column reinforcement. This step influences how loads will be shared between columns, and the ground consequently, the overall efficiency of the ground improvement is also affected (Magnan *et al.*, 2005).

Another difference between these techniques is that rigid inclusions are always associated with a load transfer layer (generally a granular layer, known as the load transfer platform or LTP, unless the base of the embankment fill itself acts as this transition layer). Shear mechanisms that develop within the transfer layer and around the inclusion shafts are essential for this technique; and are activated by differential settlements that arise between the “rigid” inclusion with low compressibility and the surrounding soil (Figure 2.4). Differential settlements, and therefore the shear, extend to the layers above the inclusion heads between the column centrelines and the mesh centreline, which means that some load transfer already takes place at a distance above the inclusion heads. If one considers the average soil settlement over one mesh and the settlement at the column centreline at any given elevation, it appears that these values are equal only in some horizontal planes: the upper plane located in the LTP or the fill (and all planes above), the plane located along the column length and the plane located at a certain depth below the column top and all planes below (Slocombe *et al.*, 2000).

The existence of these “equal settlement planes” is characteristic of RI ground improvements. This scenario differentiates RI ground improvement from SC ground improvement. A stone column design generally assumes that settlements are uniform in any horizontal plane such that all planes are “equal settlement planes”.

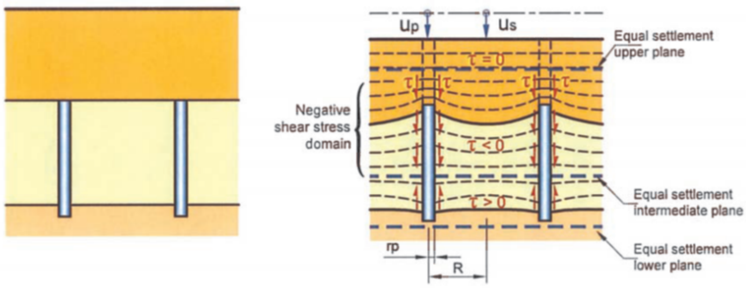

Figure 2.4. Equal Settlement Planes that Develop in a Ground Improvement Solution Using Rigid Inclusions Under an Embankment (Slocombe*et al.*, 2000).

2.2.5. Geosynthetic Encasement of Stone Column

Various deep soil stabilization methods commonly employed in the field are; stone columns (Greenwood, *et al.*, 1970). Among all these methods, the stone column technique is preferred because it gives the advantage of reduced settlements and accelerated consolidation settlements due to reduction in flow path lengths. Another major advantage with this technique is the simplicity of its construction method (Murugesan and Rajagopal, 2006). The stone column derives its axial capacity from the passive earth pressure developed due to the bulging effect of the column and increased resistance to lateral deformation under superimposed surcharge load.

When the stone columns are installed in very soft clays, they may not derive significant load capacity owing to low lateral confinement. (McKenna *et al.*, 1975) reported cases where the stone column was not restrained by the surrounding soft clay, which led to excessive bulging, and also the soft clay squeezed into the voids of the aggregate. The squeezing of clay into the stone aggregate ultimately reduces the bearing capacity of the stone column. Also the lower undrained cohesion value demand more stone column material. It is very important to have an appropriate prediction of undrained shear strength as it is having more influence on the design of stone column.

All traditional design of the stone column considers the undrained shear strength value Cu $\geq$15 kN/m^2. So, the soil having undrained shear strength value less than 15 kN/m^2, demand the new development technique. This problem can be solved by confining the compacted sand or gravel column in a high-modulus geosynthetic encasement (Alexiew *et al.*, 2005), as shown in Figure 2.5.

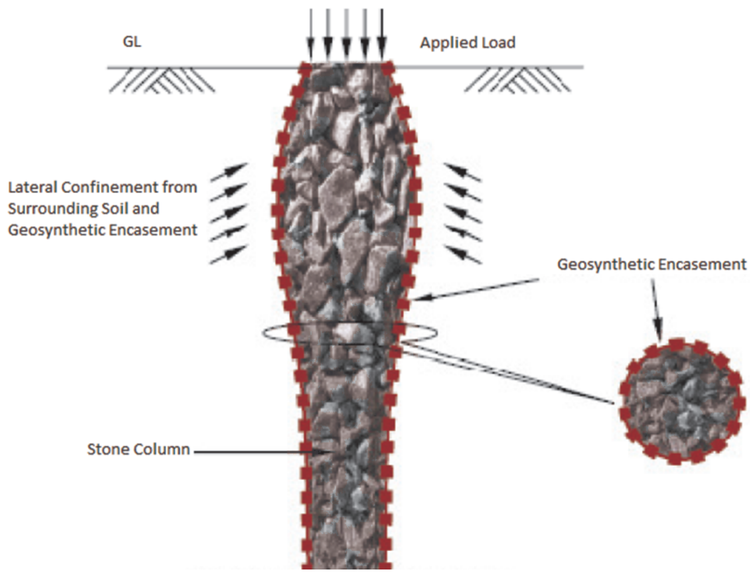

Figure 2.5. Geosynthetic Encasement of Stone Column (Lothspeich, (2005)).

Van Impe and Silence (1986) were probably the first to recognize that columns could be encased by geotextile. They produced an analytical design technique that was used to assess the required geotextile tensile strength. In the 1990s, a seamless geotextile sock was developed for column encasement. Columns were generally installed using a displacement technique. Earlier, details on this technique were provided by (Kempfert *et al.*, 1997). Later, (Raithel *et al.*, 2005) produced an analytical design technique for assessing column settlement placed on geotextile stiffness. An update, including use on recent projects in Europe, was provided by (Alexiew *et al.*, 2005), and in South America by (De Mello *et al.*, 2008). (Wu and Hong, 2009) reported an analytical method that investigated the stress-strain relation of granular columns reinforced with horizontal disks or external encapsulation. (Murugesan and Rajagopal, 2007), performed model tests and numerical analyses to study the behavior of a single geosynthetic encased stone column with a limited zone of soil influence (a tributary area approach to column group behavior). (Khabbazian *et al.*, 2008) carried out 3D finite element analyses to simulate the behavior of a single geosynthetic - encased stone column in a soft clay soil using the computer program ABAQUS. The influence of geosynthetic stiffness, column diameter, and the stiffness and friction angle of the column material were studied in the numerical analyses. (Gniel and Bouazza, 2010), developed a method for the encasement construction. The technique comprises overlapping the geogrid encasement by a nominal amount, and relying on interlock between the stone aggregate and section of overlap to provide a level of fixity similar to welding.

2.3. Analysis Methods

2.3.1. Winklers' Beam on Elastic Foundation

According to (Winkler, 1876) basic assumptions, each soil reacts independently to the forces influencing its layer. A beam or independent system of springs can be used in order to model lateral loading. Although it is assumed that there is no transfer of shear force among soil layers in this assertion, it is known that this method is frequently used for dynamic and static pile analysis. The aforementioned method is used for providing stiffness of the soil-pile system by utilizing spring and damper on surfaces where the soil and the pile touch each other. These springs are modeled as linear elastic or non-linear. P-y curves for soil-pile interactions are derived from experimental data. Meanwhile, these p-y curves take into account the force exerted by the pile on soil in a different way compared to other methods.

McClelland and Focht, (1958) are the pioneers of the analysis of lateral loaded piles with p-y curves. (McClelland and Focht, 1958) propounded the empirical formula establishing correlations between the data that they have gathered from their three-dimensional experiments and the impulses exerted on the pile and the soil from different layers. Meanwhile, the method proposed by (Reese *et al.*, 1974), uses P-y curves belonging to the soil and does the first solution of differential equation. In addition, in this method, the P-y values gathered from these solutions are compared to the inserted p-y values, and iterations are carried out until these two values converge. With this method, it is possible to calculate moment distribution on the pile, shearing stress, and displacements.

Long before the research on laterally loaded piles, engineers had looked into the possibility of representing shallow foundations that are long and flexible enough (e.g., strip footings) as beams resting on foundations. In the context of beam-on foundation approach, the beam represents the foundation (e.g., footings, piles etc.) and the foundation represents the soil mass. As early as 1867, (Winkler, 1867) proposed that the vertical resistance of a ground against external forces can be assumed to be proportional to the ground deflection. Researchers, extending the idea, represented the ground with a series of elastic springs so that the compression (or extension) of the spring (which is the same as the deflection of the ground) is proportional to the applied load. The spring constant represents the stiffness of the ground (foundation) against the applied loads.

This concept is extended by placing an Euler-Bernoulli beam on top of the elastic foundation and applying loads on top of the beam as shown in Figure 2.6. A differential equation governing the beam deflection for such a beam-foundation system is developed (which is a fourth order linear differential equation), and analytical solutions for different types and positions of loads and load distributions are obtained (Biot, 1937), (Hetenyi, 1946). The input parameters required are the elastic modulus and geometry of the beam, the spring constant of the foundation (soil) and the magnitude and distribution of the applied load. As a result of the analysis, the beam deflection, bending moment and shear force along the span of the beam can be determined.

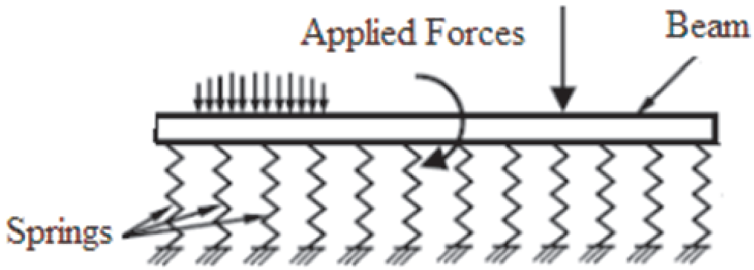

Figure 2.6. A Beam on an Elastic Foundation (Hetenyi, 1946).

It is important to mention here that there is a subtle difference between the foundation springs and the conventional springs. In conventional springs, the spring constant multiplied by the spring deflection gives the spring force. In foundation springs, the spring constant multiplied by the spring deflection (which is the same as the beam deflection) produces the resistive force of the foundation (ground) per unit beam length. Therefore, the unit of spring constant of a foundation spring is in FL^{-2} (F= force, L= length), while the unit of spring constant of a conventional spring is FL^{-1}.

The beam-on-foundation approach can also be called subgrade-reaction approach because the foundation spring constant can be related to the modulus of subgrade reaction of a soil mass (Terzaghi, 1955), (Bowles, 1997) (if the pressure at a point on the contact surface between the foundation and the beam is p and if because of p the deflection of the point is δ, then the modulus of subgrade reaction is given by (p/δ)). In fact, the spring constants are often estimated by determining the soil subgrade reaction modulus (the modulus can be determined experimentally, e.g., by performing a plate load test).

The elastic springs, as hypothesized by (Winkler, 1867), could no longer be used for laterally loaded piles, and are replaced by nonelastic springs (for which the value of the spring constant changes with pile deflection). As a result, the governing fourth order differential equation becomes nonlinear; and the finite difference method is used to iteratively solve the equation (McClelland and Focht, 1958). In order to simplify the problem, some researchers assumed the soil to be linear elastic up to a certain value of pile deflection and perfectly plastic beyond that value (Baykal, 1982), (Hsiung and Chen, 1997), Figure 2.7.

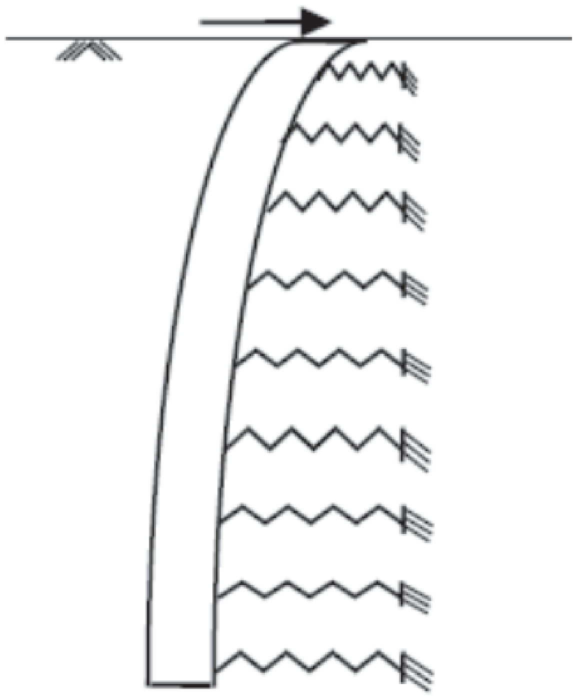

Figure 2.7. A Laterally Loaded Pile in a Bed of Springs (Bowles, 1997).

Further modification of the beam-on-nonlinear-foundation approach led to the p-y method (Matlock *et al.*, 1970). In the p-y method, p stands for the soil pressure (resistance) per unit pile length, and y stands for pile deflection (note that the soil resistance p is the product of pile deflection and the nonlinear spring constant). Instead of giving inputs for the nonlinear spring constant (i.e., the values of the spring constant as a function of pile deflection), p-y curves are given as inputs to the analysis in the p-y method. Different p-y curves have been developed over the years for different soil types, which give the magnitude of soil pressure as a function of the pile deflection (Reese *et al.*, 1975).

2.3.2. Beam Theory on Winkler Foundation

The governing equation for a uniform beam on Winkler foundation can be presented as follows:

$$\mathrm{EI}\frac{\mathrm{dy}^4}{\mathrm{dy}^4}+\mathrm{ky} = \mathrm{p} \tag{2.1}$$

Where EI is the flexural rigidity, E is the elastic modulus, I is the moment of inertia, k is the soil modulus, y is the deflection, p is the soil reaction per unit length. By introducing a parameter β[unit L^{-1}]

$$\beta = [\mathrm{k}/4\mathrm{EI}]^{1/4} \tag{2.2}$$

The solution of the governing equation can be written as follows:

$$\mathrm{w} = \mathrm{e}^{\beta \mathrm{x}}\,(\mathrm{C}_1\sin\beta\mathrm{x} + \mathrm{C}_2\cos\beta\mathrm{x}) + \mathrm{e}^{-\beta \mathrm{x}}\,(\mathrm{C}_3\sin\beta\mathrm{x} + \mathrm{C}_4\cos\beta\mathrm{x}) + \mathrm{y}\,(\mathrm{p}) \tag{2.3}$$

Particular solution related with p y(p)=0 when p=0 C1, C2, C3, and C4 are integration constants which are determined by boundary condition, For the convenience the following symbols are defined:

$$\mathrm{A}_{\beta\mathrm{x}} = \mathrm{e}{-}^{\beta\mathrm{x}}(\cos\beta\mathrm{x} + \sin\beta\mathrm{x}), \beta\mathrm{x} = \mathrm{e}{-}^{\beta\mathrm{x}}\sin\beta\mathrm{x} \tag{2.4}$$

$$\mathrm{C}_{\beta\mathrm{x}} = \mathrm{e}{-}^{\beta\mathrm{x}}(\cos\beta\mathrm{x} - \sin\beta\mathrm{x}), \mathrm{D}_{\beta\mathrm{x}} = \mathrm{e}{-}^{\beta\mathrm{x}}\cos\beta\mathrm{x} \tag{2.5}$$

These quantities are related by certain derivatives, and the values of the above quantities are listed in the Table 2.2.

Table 2.2. Selected Values of Terms Defined by Equation 2.7.

βx	$A_{\beta x}$	$B_{\beta x}$	$C_{\beta x}$	$D_{\beta x}$
0	1	0	1	1
0.02	0.9996	0.0196	0.9604	0.9800
0.04	0.9984	0.0384	0.9216	0.9600
0.10	0.9907	0.0903	0.8100	0.9003
0.20	0.9651	0.1627	0.6398	0.8024
0.30	0.9267	0.2189	0.4888	0.7077
0.40	0.8784	0.2610	0.3564	0.6174
0.50	0.8231	0.2908	0.2415	0.5323
0.60	0.7628	0.3099	0.1431	0.4530
0.70	0.6997	0.3199	0.0599	0.3798
$\pi/4$	0.6448	0.3224	0.0	0.3224
0.80	0.6354	0.3223	-0.0093	0.3131
0.90	0.5712	0.3185	-0.0657	0.2527
1.00	0.5083	0.3096	-0.1108	0.1988
1.10	0.4476	0.2967	-0.1457	0.1510
1.20	0.3899	0.2807	-0.1716	0.1091
1.30	0.3355	0.2626	-0.1897	0.0729
1.40	0.2849	0.2430	-0.2011	0.0419
1.50	0.2384	0.2226	-0.2068	0.0158
$\pi/2$	0.2079	0.2079	-0.2079	0
1.60	0.1959	0.2018	-0.2077	-0.0059
1.70	0.1576	0.1812	-0.2047	-0.0235
1.80	0.1234	0.1610	-0.1985	-0.0376
1.90	0.0932	0.1415	-0.1899	-0.0484
2.00	0.0667	0.1231	-0.1794	-0.0563
2.20	0.0244	0.0896	-0.1548	-0.0652
$3\pi/4$	0	0.0670	-0.1340	-0.0670
2.40	-0.0056	0.0613	-0.1282	-0.0669
2.60	-0.0254	0.0383	-0.1019	-0.0636
2.80	-0.0369	0.0204	-0.0777	-0.0573
3.00	-0.0423	0.0070	-0.0563	-0.0493
π	-0.0432	0	-0.0432	-0.0432
3.20	-0.0431	-0.0024	-0.0383	-0.0407
3.40	-0.0408	-0.0085	-0.0237	-0.0323
3.60	-0.0366	-0.0121	-0.0124	-0.0245
3.80	-0.0314	-0.0137	-0.0040	-0.0177
$5\pi/4$	-0.0279	-0.0139	0	-0.0139
4.00	-0.0258	-0.0139	0.0019	-0.0120
$3\pi/2$	-0.0090	-0.0090	0.0090	0
2π	0.0019	0	0.0019	0.0019

2.3.3. Infinite Beams with Concentrated Load

The equation of concentrated force can be generated by using the solution for semi-infinite beam under concentrated load: At

$$x = 0, \theta = -2\beta^2[P_o/2]/k + 4\beta^2 M_o/k = 0 \rightarrow M_o = P_o/4\beta \tag{2.6}$$

due to symmetry , at x = 0 , V=0 ; substituting Po/2 and Mo=Po/4β in previous solution [semi-infinite beam under concentrated load],the solution for infinite beam can yield :

$$W = [\beta Po/2k]A_{\beta x}; \theta = dw/dx = -\beta^2 P_o B_{\beta x}/k; \tag{2.7}$$

$$M = [P_o/4\beta]C_{\beta x}; V = -[P_o/2]D_{\beta x} \tag{2.8}$$

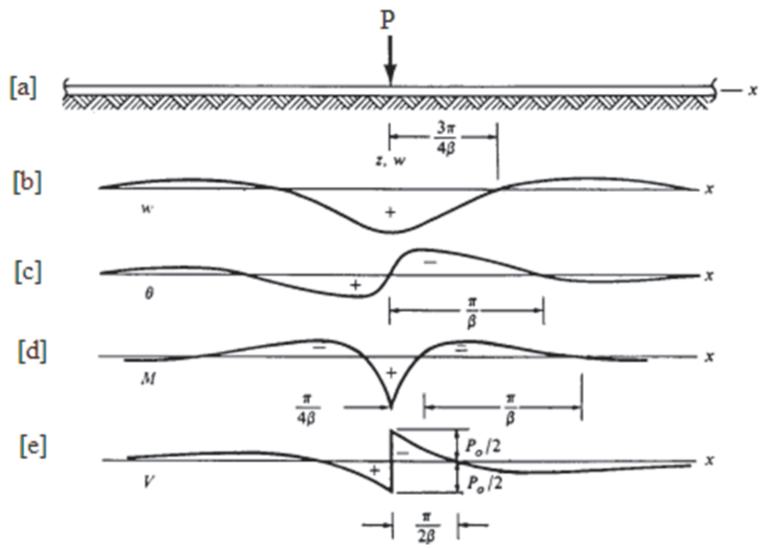

Figure 2.8. Concentrated Load (a) Concentrated Load Po at x = 0 on a Uniform Infinite Beam that Rests on a Winkler Foundation. (b-e) Curves for Deflections, Rotation, Bending Moment and Transverse Shear Force in the Beam. These Curves are Proportional to $A_{\beta x}$, $B_{\beta x}$, $C_{\beta x}$, $D_{\beta x}$, Respectively.

2.3.4. Application of P-y Curves to Cohesionless Soil

Lateral capacity of piles calculated by the subgrade reaction approach can be extended beyond the elastic range where soil yields plastically. This can be done by employing p-y curves (Matlock *et al.*, 1970). In the following paragraphs, first the theoretical basis for the use of p-y curves are explained, then the procedure of establishing p-y curves is be described. A step-by-step iterative design procedure for a pile under lateral load is then developed. The differential equation for the laterally loaded piles, assuming that the pile is a linearly elastic beam, is as follows:

$$EI\frac{dy^4}{dx^4} + P\frac{dy^2}{dx^2} - p = 0 \tag{2.9}$$

Where El is flexural rigidity of the pile, y is the lateral deflection of the pile at point x along the pile length, P is axial load on pile, and p is soil reaction per unit length. p is expressed by equation:

$$\mathrm{P} = \mathrm{ky} \tag{2.10}$$

Where, k is the soil modulus The solution for Equation 2.10 can be obtained if the soil modulus k can be expressed as a function of x and y. The numerical description of the soil modulus is best accomplished by a family of curves that show the soil reaction p as a function of deflection y (Reese and Welch, 1975). In general, these curves are nonlinear and depend on several parameters, including depth, soil shear strength, and number of load cycles (Reese, 1977). A concept of p-y curves is presented in Figure 2.9. These curves are assumed to have the following characteristics:

- A set of p-y curves represent the lateral deformation of soil under a horizontally applied pressure on a discrete vertical section of pile at any depth.
- The curve is independent of the shape and stiffness of the pile and is not affected by loading above and below the discrete vertical area of soil at that depth. This assumption, of course, is not strictly true. However, experience indicates that pile deflection at a depth can, for practical purposes, be assumed to be essentially

dependent only on soil reaction at that depth. Thus, the soil can be replaced by a mechanism represented by a set of discrete p-y characteristics as shown in Figure 2.1.

Thus, as shown in Figure 2.9 (Shape of Curves at Various Depths (x) below Soil Surface), a series of p-y curves would represent the deformation of soil with depth for a range of lateral pressures varying from zero to the yield strength of soil. This figure also presents deflected pile shape Figure 2.10 and p-y curves when plotted on a common axis Figure 2.9 (Curves Plotted on Common Axes). At present, the application of p-y curves is widely used to design laterally loaded piles and has been adopted in (API Recommended Practice, 2008).

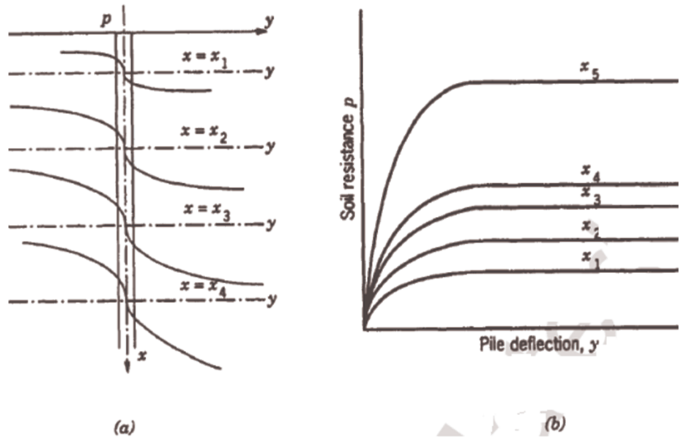

Figure 2.9. Set of p-y Curves and Representation of Deflected Pile: (a) Shape of Curves at Various Depths [x] Below Soil Surface, (b) Curves Plotted on Common Axes.

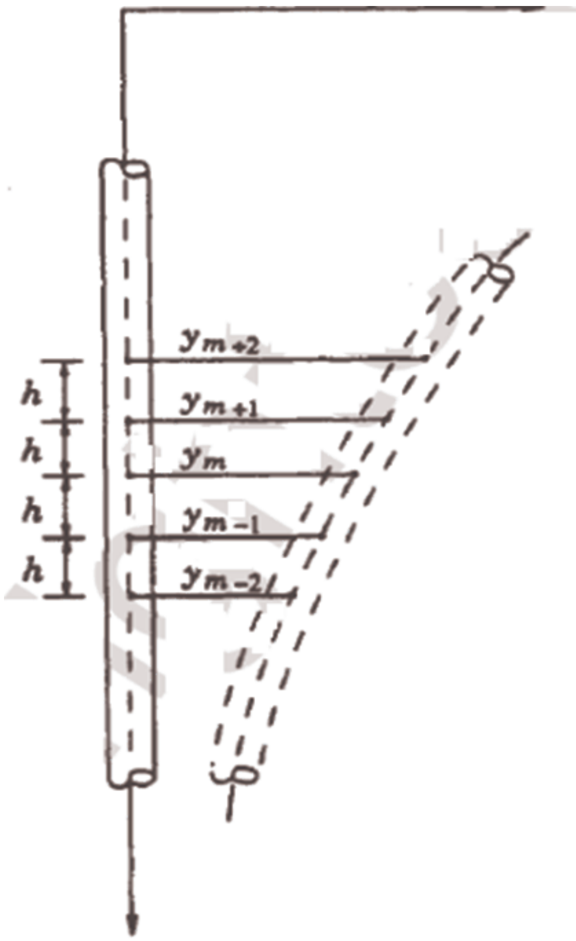

Figure 2.10. Representation of Deflected Pile (Reese, 1970).

Once a set of p-y curves has been established for a soil-pile system, the problem of laterally loaded piles can be solved by an iterative procedure consisting of the following steps:

- As described earlier, calculate T or R, as the case may be, for the soil-pile system with an estimated or given value of n_h or k. T will apply for cohesionless soils and normally consolidated clays, and R will apply to over-consolidated clays.
- With the calculated T or R and the imposed lateral force Q, and moment M, determine deflection y along the pile length by (Reese and Matlock, 1956) or (Davisson and Gill, 1963) procedures, as applicable. These procedures have been described in Section 6.1.3 and 6.6.1, respectively.

- For these calculated deflections (step (2) above), determine the lateral pressure p with depth from the earlier established p-y curves. The soil modulus and relative stiffness (R or T) will then be determined as:

$$\mathrm{k} = \mathrm{p/y} \tag{2.11}$$

$$n_h = \frac{k}{x}\mathrm{T} = \sqrt[5]{\frac{EI}{n_h}} \tag{2.12}$$

For modulus increasing with depth

$$k_1 = kR = \sqrt[4]{\frac{EI}{k}} \tag{2.13}$$

For modulus constant with depth

Compare the (R or T) value with those calculated in step (1). If these values do not match carry out a second trial as outlined in the following steps.

- Assume k or n_h value closer to the one in step (3). Then repeat steps (2) and (3) and obtain new R or T. Continue the process until calculated and assumed values agree. Then, deflections and moments along the pile section can be established for the final R or T value.

Reese, (1977) provides a computer program documentation that solves for deflection and bending moment for a pile under lateral loading. A step-by-step procedure has been provided here to establish p-y curves for cohesionless soils. A numerical example has also been given to explain the procedure to establish p-y curves.

2.3.4.1. Procedure for Establishing p-y Curves for Laterally Loaded Piles in Sand. For the solution of the problem of a laterally loaded pile, it is necessary to predict a set of p-y curves. If such a set of curves can be predicted, Equation 2.10 can readily be solved to yield pile deflection, pile rotation, bending moment, and shear and soil reaction for any load capable of being sustained by the pile.

The set of curves shown in Figure 2.9 would seem to imply that the behavior of the soil at a particular depth is independent of the soil behavior at all other depths. This is not strictly true. However, (Matlock, 1970) showed that for the patterns of pile deflections that can occur in practice, the soil reaction at a point is essentially dependent on the pile deflection at that point only. Thus, for purposes of analysis, the soil can be removed and replaced by a set of discrete closely spaced independent and elastic springs with load-deflection characteristics.

Cox *et al.*, (1971), performed lateral loads tests in the field on full-sized piles, which were instrumented for the measurement of bending moment along the length of the piles. In addition to the measurement of the load at the ground line, measurements were made of pile-head deflection and pile-head rotation. Loadings were static and cyclic. For each type of loading, a series of lateral loads were applied, beginning with a load of small magnitude, and a bending moment curve was obtained for each load.

The sand at the test site varied from clean fine sand to silty fine sand, both having high relative densities. The sand particles were subangular with a large percentage of flaky grains. The angle of internal friction ϕ was 39^o and γ was 66 lb/ft^3 10.57 KN/m^3.

From the sets of experimental bending moment curves, values of p and y at points along the pile can be obtained by integrating and differentiating the bending moment curves twice to obtain deflections and soil reactions, respectively. Appropriate boundary conditions were used and the equations were solved numerically.

The p-y curves so obtained were critically studied and form the basis for the following procedure for developing p-y curves in cohesionless soils (Reese *et al.*, 1977).

- Step 1 Carry out field or laboratory tests to estimate the angle of internal friction (Φ)and unit weight (γ) for the soil at the site
- Step 2 Calculate the following factors:

$$\alpha = \Phi/2 \tag{2.14}$$

$$\beta = 45 + \alpha \tag{2.15}$$

$$\mathrm{Ko} = 0.4 \tag{2.16}$$

$$\mathrm{K_A} = \tan^2(45 - \Phi/2) \tag{2.17}$$

P_{cr} is applicable for depths from ground surface to a critical depth x, and P_{cd} is applicable below the critical depth. The value of critical depth is obtained by plotting P_{cr} and P_{cd} with depth (x) on a common scale. The point of intersection of these two curves will give x, as shown on Figure 2.11. P_{cr} and P_{cd} equations are derived for failure surface in front of a pile shown in Figure 2.12 for shallow depth and Figure 2.12 for depths below the critical depth (x,).

- Step 3 First select a particular depth at which a p-y curve will be drawn. Compare this depth (x) with the critical depth (x,) obtained in step (2) above and then find if the value of P_{cr} or P_{cd} is applicable. Then carry out calculations for a p-y curve discussed as follows. Refer to Figure 2.11 when following these steps.
- Step 4 Select appropriate n_k from Table 2.3 for the soil. Calculate the following items:

$$\mathrm{P_m} = \mathrm{B.P_c} \tag{2.18}$$

Where B, is taken from Table 2.3 and Pc is from $\mathrm{P_{cr}}$ for depths above critical point and from $\mathrm{P_{cd}}$ for depths below the critical point.

$$\mathrm{y_m} = \mathrm{B/60} \tag{2.19}$$

Where, B is the pile width

$$\mathrm{P_y} = \mathrm{A_1 P_c} \tag{2.20}$$

and where $\mathrm{A_1}$ is taken from Table 2.3

$$y_u = \frac{3B}{80} \tag{2.21}$$

$$\mathrm{m} = \frac{P_u - P_m}{y_u - y_m} \tag{2.22}$$

$$n = \frac{P_m}{m.y_m} \tag{2.23}$$

$$C = \frac{P_m}{(y_m)^{\frac{1}{n}}} \tag{2.24}$$

$$y_k = (\frac{C}{(n_h).x})n/n - 1 \tag{2.25}$$

$$P = C.y^{1/n} \tag{2.26}$$

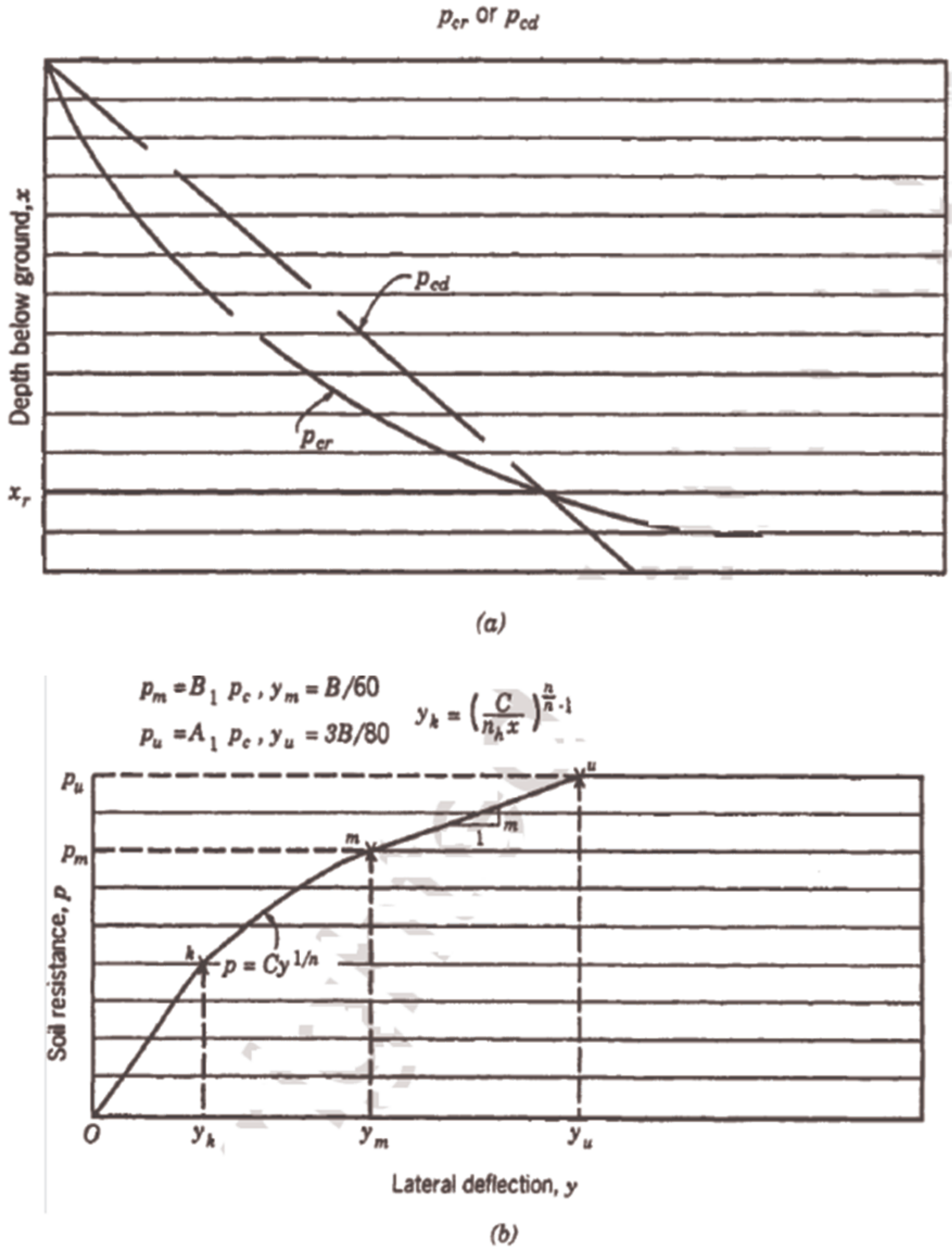

Figure 2.11. Obtaining the Value of X_r and Establishing p-y Curve (Reese and Mablock, 1970).

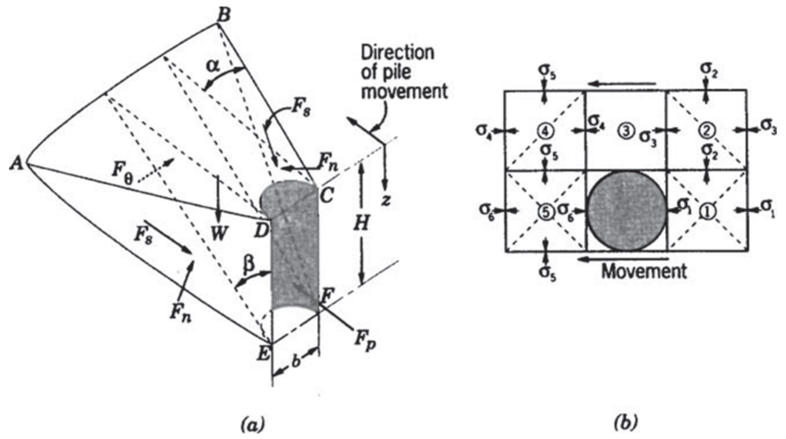

Figure 2.12. Assumed Failure Surfaces Around a Pile Under Lateral Load: (a) Assumed Passive Wedge Type at Shallow Depth, (b) Assumed Mode of Soil Failure by Lateral Flow Around the Pile at Larger Depth (After Reese *et al.*, 1974).

- Step 5 (i) Locate y_k on the y axis in Figure 2.11. Substitute this value of y, as y in Equation 2.26 to determine the corresponding p value. This p value will define the k point and Joint point k with origin 0; thus establishing line OK as shown in Figure 2.11. (ii) Locate the point m for the values of y, and pm from Equation 2.18 and Equation 2.19 respectively. (iii) Then plot the parabola between the point k and m by using equation of Pcr. (iv) Locate point u from the values of y, and Pu from Equation 2.20 and Equation 2.21, respectively (v) Join points m and u with a straight line.
- Step 6 Repeat the above procedure for various depths to obtain p-y curves at each depth below ground.

Table 2.3. Values for Coefficients A_1 and B_1.

	A1		B1	
$\frac{x}{B}$	Static	Cyclic	Static	Cyclic
1	2	3	4	5
0	2.85	0.77	2.18	0.50
0.2	2.72	0.85	2.02	0.60
0.4	2.60	0.93	1.90	0.70
0.6	2.42	0.93	1.90	0.70
0.8	2.20	1.02	1.70	0.80
1.0	2.10	1.08	1.56	0.84
1.2	1.96	1.10	1.46	0.86
1.4	1.85	1.11	1.38	0.86
1.6	1.74	1.08	1.24	0.86
1.8	1.62	1.06	1.15	0.84
2.0	1.50	1.05	1.04	0.83
2.2	1.40	1.02	0.96	0.82
2.4	1.32	1.00	0.88	0.81
2.6	1.22	0.97	0.85	0.80
2.8	1.15	0.96	0.80	0.78
3.0	1.05	0.95	0.75	0.72
3.2	1.00	0.93	0.68	0.68
3.4	0.95	0.92	0.64	0.64
3.6	0.94	0.91	0.61	0.62
3.8	0.91	0.90	0.56	0.60
4.0	0.90	0.90	0.53	0.58
4.2	0.89	0.89	0.52	0.57
4.4 to 4.8	0.89	0.89	0.51	0.56

2.3.5. Non-Dimensional Method (NDM)

This model, developed by (Matlock and Reese, 1956), is based on p-y curves and numerical solutions that were obtained by hand-operated calculators. This model offered at the time a desirable solution to fully design piles in both the ultimate limit state and serviceability limit state while including nonlinear soil behavior (Reese and Van, 2001).

2.3.5.1. Possibilities and Limitations of the (NDM). With the NDM, it is possible to check on real p-y analyses and good insight into the problem can be obtained. Another major possibility is that the decision on which p-y curve to use is completely open. The disadvantages of the model are that the soil has to be homogeneous. The pile has to have a constant bending stiffness over the length of the pile. And most importantly, the calculation procedure is time consuming. In this research, full p-y analyses have been executed with the program M-Pile. This program uses p-y curves recommended by the American Petrol Institute, (API). Therefore, the analyses with the NDM use other p-y curves, namely those developed by Reese and Matlock.

2.3.5.2. Analysis with Non-Dimensional Chart - 1962. This model, developed by (Matlock *et al.*, 2006), is placed on p-y curves and numerical solutions were obtained by hand-operated calculators. Examination of the analytical parameters in the numerical solutions led to the proposal of a formal analytical procedure for $\mathrm{E}_{py} = \mathrm{k}_{py}$ x, (Reese and Matlock, 1956) and later to the use of non-dimensional methods to develop a wide range of solutions for a pattern of variations of E_{py} with depth (Matlock and Reese, 1962). Engineers understood many years ago that the physical nature of soils led to the argument that E_{py} should be zero at the mud-line and increase linearly with depth.

$$E_{py} = k_{py}x \tag{2.27}$$

The following equations can be derived by numerical analysis for the case where stiffness of the soil increases linearly with depth. A lateral load may be imposed at the pile head, and the length of the pile may be considered.

$$y = A_y \frac{P_t T^3}{E_p I_p} + B_y \frac{M_t T^2}{E_p I_p} \tag{2.28}$$

$$S = A_s \frac{P_t T^2}{E_p I_p} + B_s \frac{M_t T}{E_p I_p} \tag{2.29}$$

$$M = A_m P_t T + M_t B_m \tag{2.30}$$

$$V = A_V P_t + \frac{M_t}{T} B_v \tag{2.31}$$

$$T = \sqrt[5]{\frac{I_p E_p}{K_{py}}} \tag{2.32}$$

$$Z_{max=}\frac{L}{T} \tag{2.33}$$

where y is the deflection (mm), S is the Slope (degree), M is the Moment (KN.m), V is the Shear (KN), T is the Relative Stiffness Factor (m), P_t is the Applied lateral-load at pile head (KN), M_t is the Applied moment at pile head (KN.m), Z_{max} is the depth coefficient.

A_y,B_y,A_s,B_s,A_m,B_m, A_v, B_v= non-dimensional parameter for respectively the deflection by lateral load, deflection by moment, slope by lateral load, slope by moment, moment by lateral load, moment by moment, shear by lateral load, shear by moment.

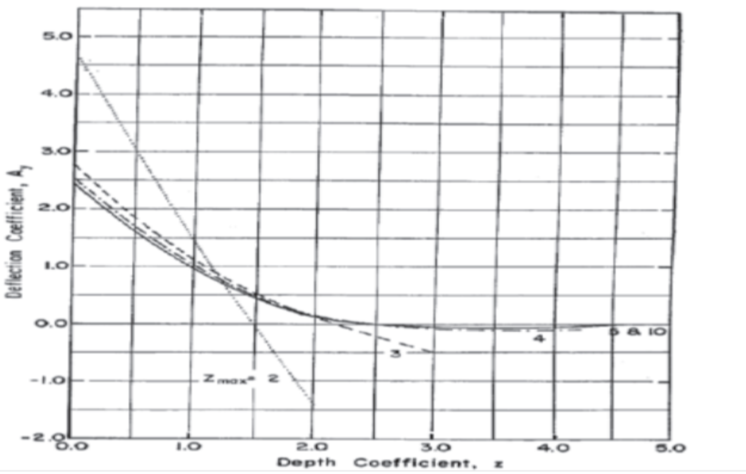

Figure 2.13. Pile Deflection Produced by a Lateral Load at the Mud-Line.

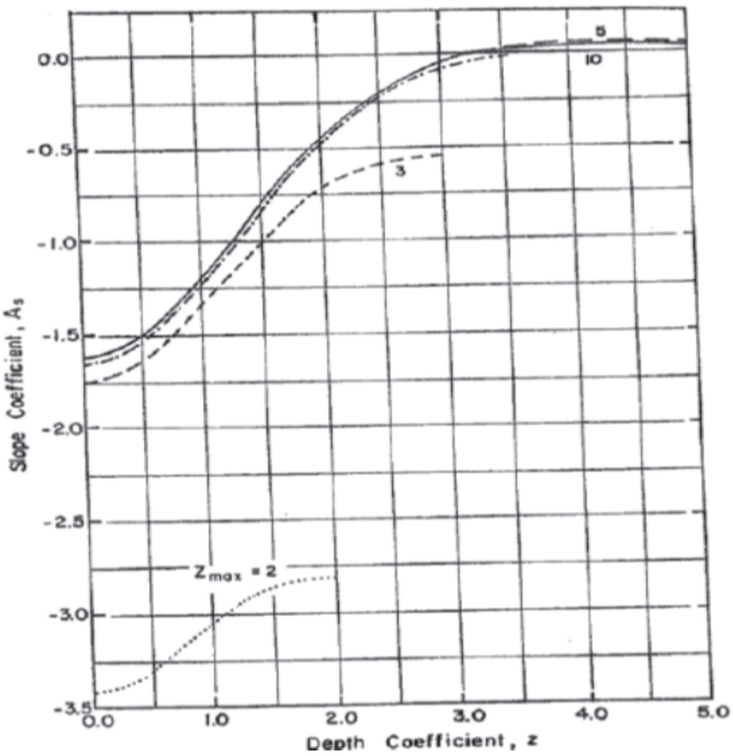

Figure 2.14. Slope of a Pile Caused by a Load at the Mud-Line.

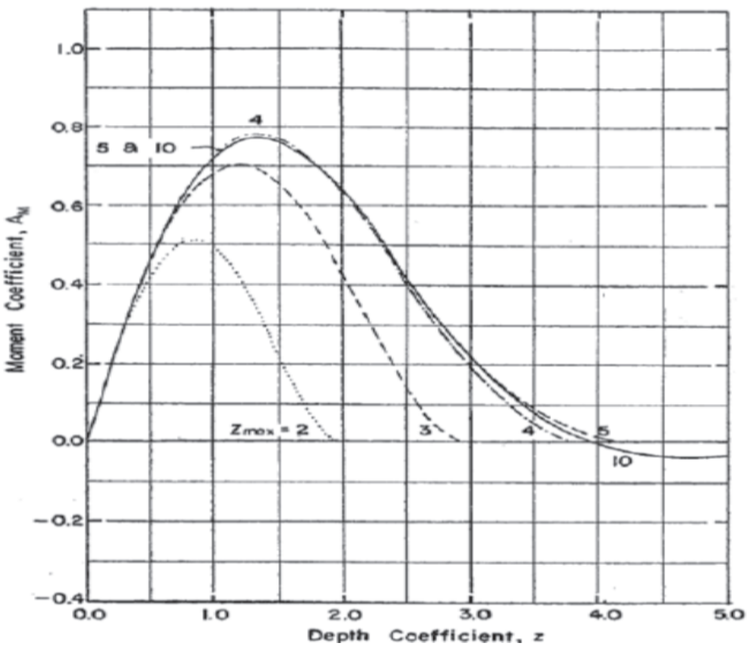

Figure 2.15. Bending Moment Caused by a Lateral Load at the Mud-Line.

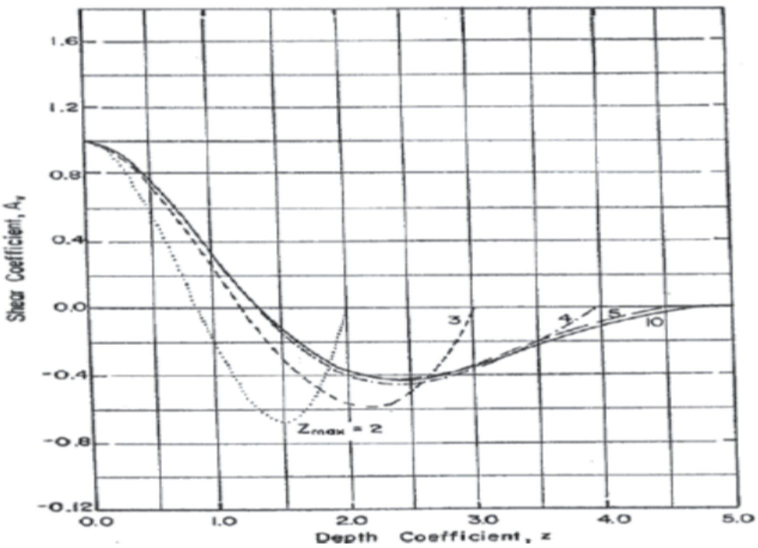

Figure 2.16. Slope of a Pile Caused by a Moment at the Mud-Line.

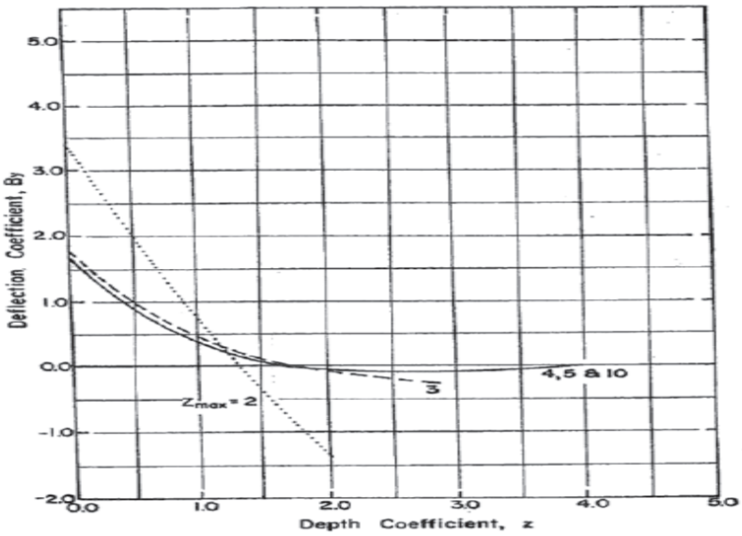

Figure 2.17. Deflections Caused by a Moment at the Mud-Line.

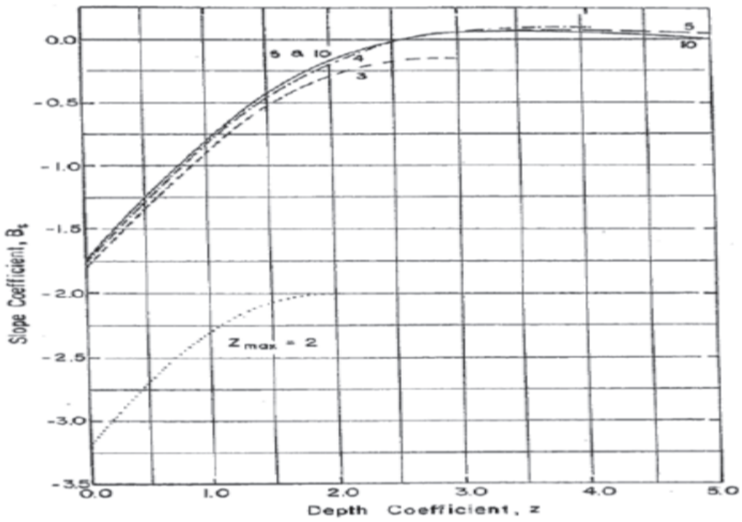

Figure 2.18. Slope of a Pile Caused by a Moment at the Mud-Line.

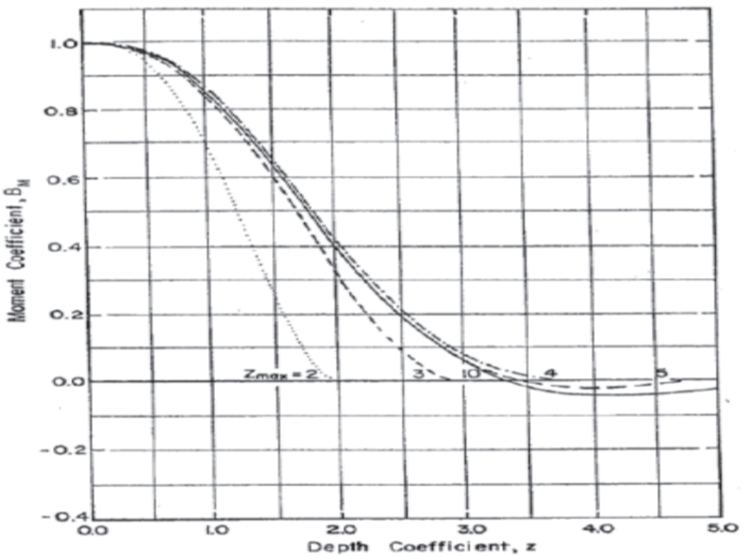

Figure 2.19. Bending Moment Produced by a Moment at the Mud-Line.

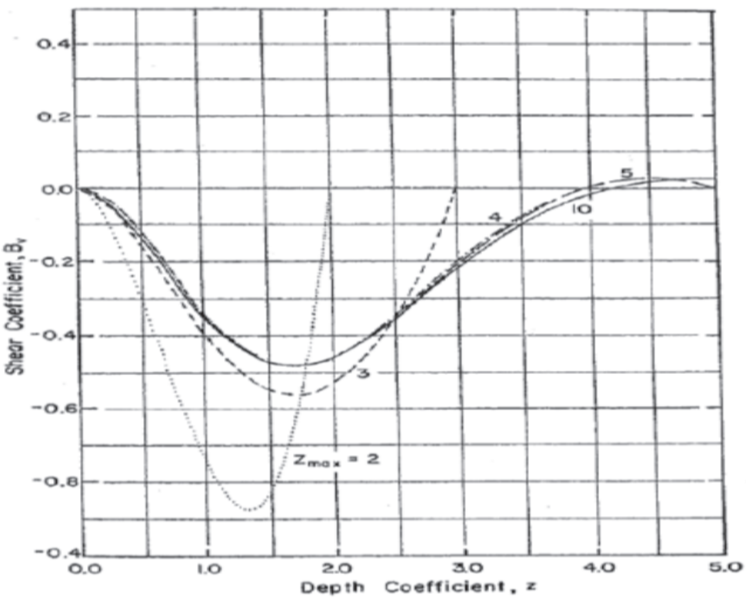

Figure 2.20. Shear Produced by a Moment at the Mud-Line.

2.3.5.3. Calculation of Lateral Pile Response Using (NDM). Compared with the computer calculations, the non-dimensional method is time consuming and tedious. The, nonlinearity of the problem requires, because the values must be estimated from curves. The method is valuable, because computer calculations can be checked and the solution gives good insight into the problem.

To start the calculation, a family of p-y curves has to be developed. Next, assume a value of T, T_{tried}. Then calculate Z_{max} to select the curve to use in the non-dimensional plots. (See plots on the bottom of this summary). Now, compute a trial deflection of the pile using equation for y. Now, with the p-y curves determine the corresponding p. By dividing p with y, E_{py} is obtained for every depth a p-y curve is generated. Now all the values E_{py} are plotted versus the depth. E_{py}=k_{py} x, the line through the values should be linear and pass through the origin. The slope of the graph is K_{py}. With this value and the formula for T, a new value for T, $T_{obtained}$, can be calculated. If, $T_{obtained} \neq T_{tried}$, the procedure must be repeated with another value of T_{tried}. This is the iteration needed because of the nonlinearity of the soil. The iteration procedure can be sped up by finding the intersection between the line connecting two iterations and the line, $T_{tried} = T_{obtained}$, Figure 2.21. With T known, the correct curves for the non-dimensional parameters can be selected; and y and M can be calculated.

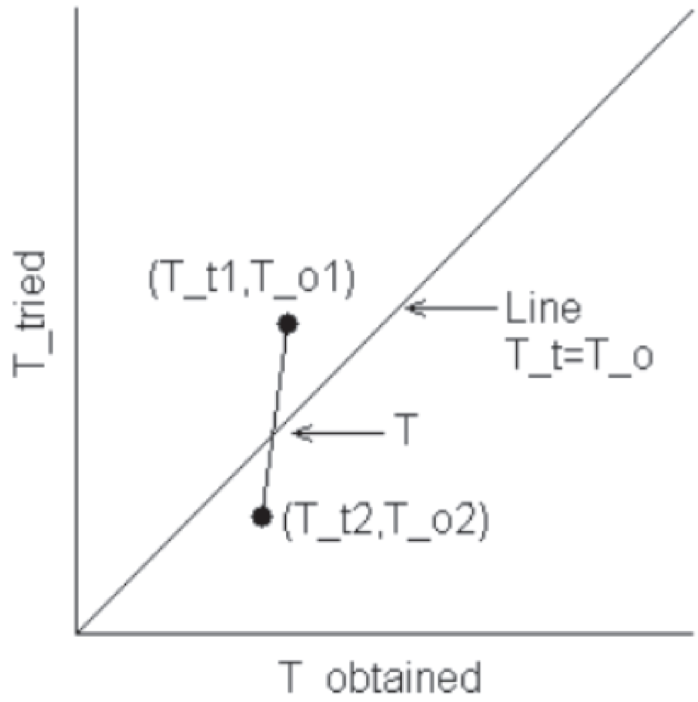

Figure 2.21. Method of Iteration for the Non-Dimensional Method.

<u>2.3.5.4. Calculation with P-Y Curves.</u> Calculations with the p-y curve method are bounded to be executed on a computer. The iterative procedure and complexity make manual calculation very hard and time-consuming. Calculation with the non-dimensional method is an option, but not for complex situations with layered soil and axial loads. Fortunately, several software packages are developed that make it possible to calculate the pile-soil behavior within seconds. Examples of such programs are L-Pile (LPILE Plus 5.0 for windows) and M-Pile (M-Pile, version 4.1, 3D modeling of single piles and pile groups). The mathematical heart of the Cap model in M-Pile (Bijnagte and Luger, M-Pile Version 4.1, 3D Analysis of single piles and pile groups, 2006) program will be used to describe the calculation procedure of the p-y method.

The lateral soil resistance in M-Pile is modeled as a number of parallel springs, which define p-y curves. To calculate the stiffness of the springs, the recommendations by the API are used. With the rules of the API, M-Pile separates p-y recommendations into five different cases: clay under a static lateral load, clay under a cyclic lateral load, sand under a static lateral load, sand under a cyclic lateral load and undrained sand under lateral load. In M-Pile, it is also possible to apply user defined p-y curves to manually model the soil stiffness. It should therefore also be possible to apply the curves proposed by Reese into the program.

The calculation process is designed in such a way that, after several numerical iterations, equilibrium is reached between the mobilized soil resistance, caused by the deformation of the pile and the load applied on the pile. To speed up the calculation, M-Pile simplifies the p-y curves as they are recommended by the API. Instead of a curve, M-Pile generates five linear portions to approach the p-y curve before p_u is reached.

2.3.6. Pile Foundation Under Lateral Load

Lateral loads and moments may act on piles in addition to the axial loads. The two pile head fixity conditions-free-head and fixed headed-may occur in practice. The allowable lateral loads on piles is determined from the following two criteria:

(i) Allowable lateral load is obtained by dividing the ultimate (failure) load by an adequate factor of safety.
(ii) Allowable lateral load is corresponding to an acceptable lateral deflection. The smaller of the two above values is the one actually adopted as the design lateral load.

2.3.6.1. Methods of Calculating Lateral Resistance of Vertical Piles. Brinch Hansen's Method (1961), this method is based on earth pressure theory and has the advantage that it is:

- Applicable for (c - Φ) soils
- Applicable for layered system. However, this method suffers from disadvantages

that it is:

- Applicable only for short piles
- Requires trial-and-error solution to locate point of rotation

(i) Broms' Method (1964): This also is based on earth pressure theory, but simplifying assumptions are made for distribution of ultimate soil resistance along the pile length. This method has the advantage that it is:

- Applicable for short and long piles
- Considers both purely cohesive and cohensioless soils
- Considers both free-head and fixed-head piles that can be analyzed. However, this method suffers from disadvantages that:
- It is not applicable to layered system
- It does not consider (c - Φ) soils

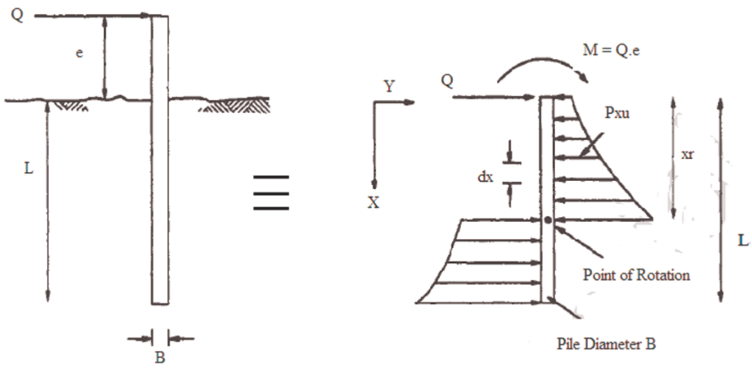

Figure 2.22. Mobilization of Lateral Resistance for a Free-Head Laterally Loaded Rigid Pile (Hansen Method).

Ultimate Lateral Resistance Figure 2.22 shows the mechanism in which the ultimate soil resistance is mobilized to resist a combination of lateral force Q and moment M applied at the top of a free-head pile. The ultimate lateral resistance Q, and the corresponding moment Mu can then be related with the ultimate soil resistance pu by considering the equilibrium conditions as follows: sum of Forces in horizontal direction= ΣFy = 0

$$Q_u - \int_{x=0}^{x=x_r} p_{xu} B dx + \int_{x=x_r}^{x=L} p_{xu} B dx = 0 \tag{2.34}$$

$\sum moments = 0$

$$Q_u e + \int_{x=0}^{x=x_r} P_{xu} B x dx - \int_{x=x_r}^{x=L} P_{xu} B x dx = 0 \tag{2.35}$$

where is the B width of pile, is the X_r depth of point of rotation.

2.3.6.2. Brinch Hansen's Method. For short rigid piles, (Brinch, 1961) recommended a method for any general distribution of soil resistance. The method is based on earth pressure theory for c-ϕ soils. It consists of determining the center of rotation by taking moment of all forces about the point of load application and equating it to zero. The ultimate resistance can then be calculated by using equation similar to Equation 2.34 such that the sum of horizontal forces is zero. Accordingly, the ultimate soil resistance at any depth is given by following equation.

$$\mathrm{P_{xu}} = \sigma_{\mathrm{vx}} \mathrm{K_q} + \mathrm{cK_c} \tag{2.36}$$

where is the σ_{vx} vertical effective overburden pressure, is the c cohesion of soil, is the K$_c$ and K$_p$ factors that are function of Φ and x/B as shown in Figure 2.23.

The method is applicable to both uniform and layered soils. For short-term loading conditions such as wave forces, undrained strength cu and $\Phi = 0$ can be used. For long-term sustained loading conditions, the drained effective strength values (c$^-$, Φ) can be used in this analysis.

2.3.6.3. Vertical Pile Under Lateral Load in Cohesionless Soil. This section presents the application of general approaches to the analysis of vertical piles subjected to lateral loads.

- Ultimate lateral load resistance of a single pile in cohesionless soil the two methods that can be used to determine the ultimate lateral load resistance of a single pile are by (Brinch, 1961) and by (Broms, 1964). Basic theory and assumptions behind these methods have already been discussed. This section stresses the application aspect of the concept discussed earlier.

- Brinch Hansen's Method For cohesionless soils where c = 0, the ultimate soil reaction at any depth is given by Equation 2.35, which then becomes:

$$\sigma_{\mathrm{xu}} = \sigma_{\mathrm{vx}}.\mathrm{K_q} \tag{2.37}$$

where σ_{vx} is the effective vertical overburden pressure at depth x and coefficient K_p is determined from Figure 2.23.

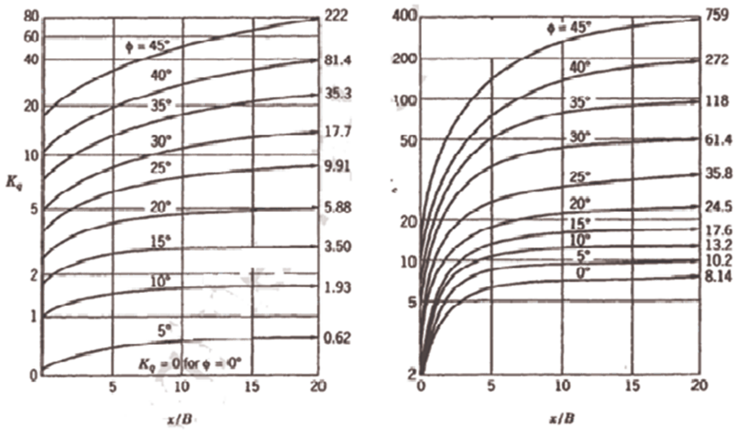

Figure 2.23. Coefficients K_q and K_c (Brinch, 1961).

The procedure for calculating ultimate lateral resistance consists of the following steps:

(i) Divide the soil profile into a number of layers.

(ii) Determine σ_{vx} and k_p for each layer and then calculate p_{xu} for each layer and plot it with depth.

(iii) Assume a point of rotation at a depth x_r below ground and take the moment about the point of application of lateral load Q_u.

(iv) If this moment is small or near zero, then x_r is the right value. If not, repeat step (1) through (3) until the moment is near zero,

(v) Once x_r (the depth of the point of rotation) is known, take moment about the point of rotation and calculate Q_u.

2.4. Building Behavior under Lateral Loading

2.4.1. Ground Acceleration and Building Damage

The absolute movement of the ground and buildings during an earthquake is not actually all that large, even during a major earthquake. That is, they do not usually undergo displacements that are large relative to the building's own dimensions. So, it is not the distance that a building moves which alone causes damage. It is because a building is suddenly forced to move very quickly that it suffers damage during an earthquake. The damage that a building suffers primarily depends not upon its displacement, but upon acceleration. Whereas displacement is the actual distance the ground and the building may move during an earthquake, acceleration is a measure of how quickly they change speed as they move. During an earthquake, the speed at which both the ground and building are moving will reach some maximum. The more quickly they reach this maximum, the greater their acceleration.

2.4.2. Newton's Law

Acceleration has an important influence on damage, because, as an object in movement, the building obeys Newton' famous Second Law of Dynamics. The simplest form of the equation which expresses the Second Law of Motion is:

$$\mathrm{F} = \mathrm{MA} \tag{2.38}$$

This states the Force acting on the building is equal to the Mass of the building times the Acceleration. So, as the acceleration of the ground, and in turn, of the building, increases, so does the force which affects the building, since the mass of the building doesn't change. The greater the force affecting a building, the more damage it will suffer; decreasing F is an important goal of earthquake resistant design. When designing a new building, for example, it is desirable to make it as light as possible, which means, of course, that M, and in turn, F will be lessened (Mahin and Bertero, 1976).

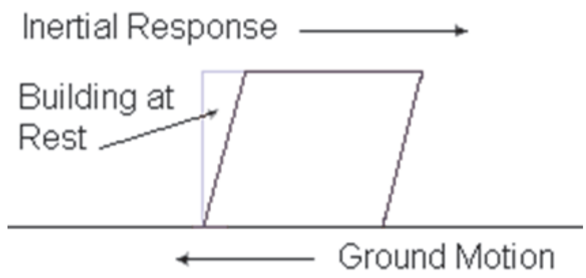

Figure 2.24. Acceleration of Inertial Forces (Mahin and Bertero, 1976).

2.4.3. Inertial Forces

It is important to note that F is actually known as an inertial force, that is, the force created by the building's tendency to remain at rest, and in its original position, even though the ground beneath it is moving. This inertial force F imposes strains upon the building's structural elements. These structural elements primarily include the building's beams, columns, load-bearing walls, floors, as well as the connecting elements that tie these various structural elements together. If these strains are large enough, the building's structural elements suffer damage of various kinds (Mahin and Bertero, 1976).

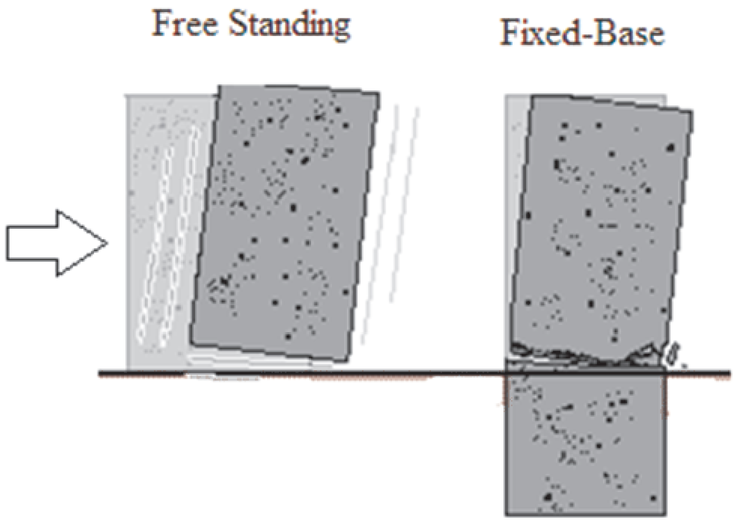

Figure 2.25. Simple Rigid Block (Mahin and Bertero, 1976).

To illustrate the process of inertia-generated strains within a structure, we can consider the simplest kind of structure imaginable–a simple, perfectly rigid block of stone. (See Figure 2.25) During an earthquake, if this block is simply sitting on the ground without any attachment to it, the block will move freely in a direction opposite that of the ground motion, and with a force proportional to the mass and acceleration of the block.

If the same block, however, is solidly founded in the ground, and is no longer able to move freely, it must in some way absorb the inertial force internally. In Figure 2.25, this internal uptake of force is shown to result in cracking near the base of the block.

Real buildings do not respond as simply as described above. There are a number of important characteristics common to all buildings which further affect and complicate a building's response in terms of the accelerations it undergoes, and the deformations and damages it suffers (Chung and Loh, 2002).

2.4.4. Building Stiffness

The taller a building, the longer its natural period tends to be. But the height of a building is also related to another important structural characteristic, the building flexibility. Taller buildings tend to be more flexible than short buildings (Chung and Loh, 2002).

Stiffness greatly affects the building's uptake of earthquake generated force. Reconsider our first example above, of the rigid stone block deeply founded in the soil. The rigid block of stone is very stiff; as a result, it responds in a simple, dramatic manner. Real buildings, of course, are more inherently flexible, being composed of many different parts.

Furthermore, not only is the block stiff, it is brittle; and because of this, it cracks during the earthquake. This leads us to the next important structural characteristic affecting a building's earthquake response and performance ductility.

2.4.5. Ductility

Ductility is the ability to undergo distortion or deformation - bending, without resulting in complete breakage or failure. To take once again the example of the rigid block in Figure 2.25, the block is an example of a structure with extremely low ductility. To see how ductility can improve a building's performance during an earthquake, consider Figure 2.26.

For the block, we have substituted a combination of a metal rod and a weight. In response to the ground motion, the rod bends, but does not break. Of course, metals in general are more ductile than materials such as stone, brick and concrete. Obviously, it is far more desirable for a building to sustain a limited amount of deformation than for it to suffer a complete breakage failure.

The ductility of a structure is in fact one of the most important factors affecting its earthquake performance. One of the primary tasks of an engineer designing a building to be earthquake resistant is to ensure that the building will possess enough ductility to withstand the size and types of earthquakes it is likely to experience during its lifetime.

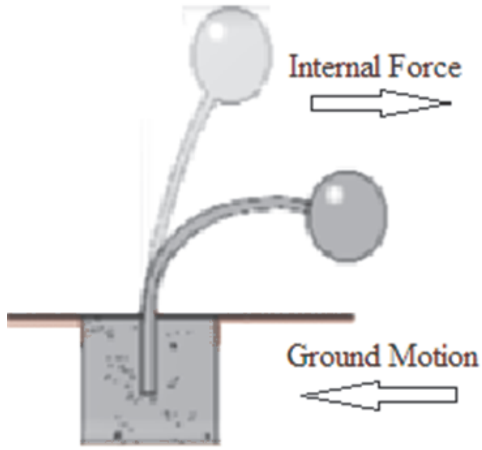

Figure 2.26. Metal Rode Ductility (Stephen and Nelson, (2000).

2.4.6. Hysteretic Behavior

This section provides background information about the model of component hysteretic behavior. It summarizes how various types of hysteretic behavior have been investigated in past studies; and explains how these behaviors have been observed to affect seismic response.

2.4.6.1. Effects of Hysteretic Behavior on Seismic Response. Many hysteretic models have been proposed over the years with the purpose of characterizing the mechanical nonlinear behavior of structural components (e.g., members and connections) and estimating the seismic response of structural systems (e.g., moment frames, braced frames, shear walls). Available hysteretic models range from simple elasto-plastic models to complex strength and stiffness degrading curvilinear, (Krawinkler, Miranda, 2004).

2.4.6.2. Elasto-Plastic Behavior. In the literature, most studies that have considered nonlinear behavior have used non-degrading hysteretic models, or models in which the lateral stiffness and the lateral yield strength remain constant throughout the duration of loading. These models do not incorporate stiffness or strength degradation when subjected to repeated cyclic load reversals. The simplest and most commonly used non-deteriorating model is an elasto-plastic model in which system behavior is linear-elastic until the yield strength is reached (Figure 2.27). At yield, the stiffness switches from elastic stiffness to zero stiffness. During unloading cycles, the stiffness is equal to the loading (elastic) stiffness. Early examples of the use of elasto-plastic models include studies by (Bernal *et al.*, 1960). The latter study is the first one to note that peak lateral displacements of moderate and long-period single-degree-of-freedom SDOF systems with elasto-plastic behavior are, on average, about the same as that of linear elastic systems with the same period of vibration and the same damping ratio. Their observations formed the basis of what is now known as the "equal displacement approximation". This widely-used approximation implies that the peak displacement of moderate and long period non-degrading systems is proportional to the ground motion intensity, meaning that if the ground motion intensity is doubled, the peak displacement will be on average approximately twice as large (Brown *et al.*, 1998).

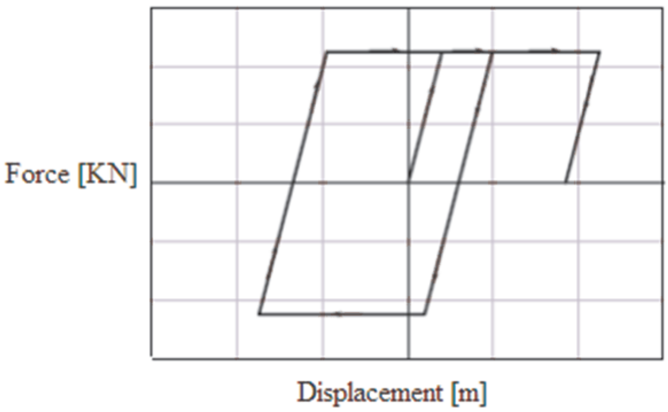

Figure 2.27. Elasto-Plastic Non-Degrading Linear Hysteretic Model (Bernal *et al.*, 1960).

Veletsos and Newmark, (1960), also observed that peak lateral displacement of short period SDOF systems with elasto-plastic behavior are, on average, larger than those of linear elastic systems, and increases in peak lateral displacements are larger than the increment in ground motion intensity. Thus, the equal displacement approximation is observed to be less applicable to short-period structures.

Using many more ground motions, recent studies have corroborated some of the early observations by Veletsos, identified some of the limitations in the equal displacement approximation, and provided information on record-to record variability. These studies have shown that, in the short-period range, peak inelastic system displacements increase with respect to elastic system displacements as the period of vibration decreases and as the lateral strength decreases. These observations formed the basis of the improved displacement modification coefficient C1, which accounts for the effects of inelastic behavior in the coefficient method of estimating peak displacements, as documented in FEMA 440 Improvement of Nonlinear Static Seismic Analysis Procedures.

2.5. Construction Techniques

2.5.1. Post-Tension Techniques of Materials

Post-tensioning is a method of reinforcing (strengthening) concrete or other materials with high-strength steel strands or bars, typically referred to as tendons. Post tensioning applications include office and apartment buildings, parking structures, slabs-on-ground, bridges, sports stadiums, rock and soil anchors, and water-tanks VSL International.

Although post-tensioning systems require specialized knowledge and expertise to fabricate assembly and installation, the concept is easy to explain. Imagine a series of wooden blocks with holes drilled through them, into which a rubber band is threaded. If one holds the ends of the rubber band, the blocks will sag. Post-tensioning can be demonstrated by placing wing nuts on either end of the rubber band and winding the rubber band so that the blocks are pushed tightly together. If one holds the wing nuts after winding, the blocks will remain straight. The tightened rubber band is comparable to a post-tensioning tendon that has been stretched by hydraulic jacks and is held in place by wedge-type anchoring devices (Collins and Mitchell 1991).

2.5.2. Benefits

To fully appreciate the benefits of post-tensioning, it is helpful to know a little bit about concrete. Concrete is very strong in compression but weak in tension, i.e. it will crack when forces act to pull it apart. In conventional concrete construction, if a load such as the cars in a parking garage is applied to a slab or beam, the beam will tend to deflect or sag. This deflection will cause the bottom of the beam to elongate slightly. Even a slight elongation is usually enough to cause cracking. Steel Reinforcing bars "rebar" are typically embedded in the concrete as tensile reinforcement to limit the crack widths (Collins and Mitchell, 1991).

Rebar, which is called "passive" reinforcement, however does not carry any force until the concrete has already deflected enough to crack. Post-tensioning tendons are considered "active" reinforcing. Because it is prestressed, the steel is effective as reinforcement even though the concrete may not be cracked. Post-tensioned structures can be designed to have minimal deflection and cracking even under full load. The resulting reinforced concrete member may crack, but it can effectively carry the design loads as shown in Figure 2.28 (Collins and Mitchell, 1991).

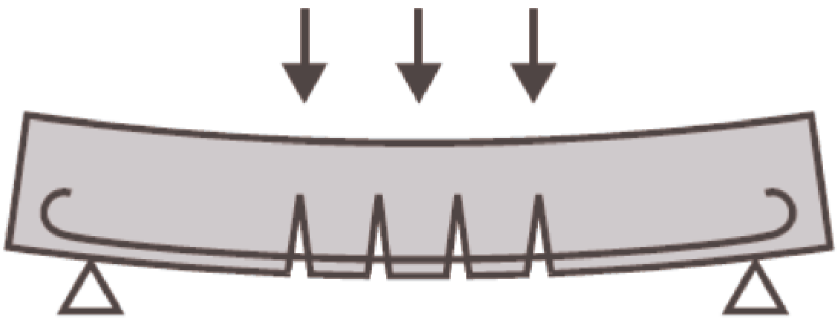

Figure 2.28. Reinforced Concrete Beam Under Load.

2.5.3. Post-Tension Applications

There are many post-tensioning applications in almost all facets of construction. In building construction, post-tensioning allows longer clear spans, thinner slabs, fewer beams and more slender, dramatic elements. Thinner slabs mean less concrete is required. In addition, it means a lower overall building height for the same floor-to-floor height. Post-tensioning can thus allow a significant reduction in building weight versus a conventional concrete building with the same number of floors. This reduces the foundation load, and can be a major advantage in seismic areas. A lower building height can also translate to considerable savings in mechanical systems and costs. Another advantage of post-tensioning is that beams and slabs can be continuous, i.e. a single beam can run continuously from one end of the building to the other. Structurally, this is much more efficient than having a beam that just goes from one column to the next. Post-tensioning is the system of choice for parking structures since it allows a high degree of flexibility in the column layout, span lengths and ramp configurations. Post-tensioned parking garages can be either stand-alone structures, or one or more floors in an office or residential building. In areas where there are expansive clays or soils with low bearing capacity, post-tensioned slabs-on-ground and mat foundations reduce problems with cracking and differential settlement (Collins and Mitchell, 1991).

Lin and Burns, (1983) stated that post-tensioning allows bridges to be built to very demanding geometry requirements, including complex curves, variable super elevation and significant grade changes. Post-tensioning also allows extremely long span bridges to be constructed without the use of temporary intermediate supports. This minimizes the impact on the environment and avoids disruption to water or road traffic below. In stadiums, post-tensioning allows long clear spans and very creative architecture. Post-tensioned rock and soil anchors are used in tunneling and slope stabilization and as tie-backs for excavations. Post-tensioning can also be used to produce virtually crack-free concrete for water-tanks.

2.5.4. Terminology

A post-tensioning "tendon" is defined as a complete assembly consisting of the anchorages, the prestressing strand or bar, the sheathing or duct, and any grout or corrosion-inhibiting coating (grease) surrounding the prestressing steel. There are two main types of post tensioning: un-bonded and bonded grouted.

An unbonded tendon is one in which the prestressing steel is not actually bonded to the concrete that surrounds it except at the anchorages. The most common unbounded systems are mono-strand (single strand) tendons, which are used in slabs and beams for buildings, parking structures and slabs-on-ground. A mono-strand tendon consists of a seven-wire strand that is coated with corrosion-inhibiting grease and encased in an extruded plastic protective sheathing. The anchorage consists of an iron casting and a conical, two-piece wedge which grips the strand (Nilson, 1978).

In bonded systems, two or more strands are inserted into a metal or plastic duct that is embedded in the concrete. The strands are stressed with a large, multi-strand jack and anchored in a common anchorage device. The duct is then filled with a cementitious grout that provides corrosion protection to the strand and bonds the tendon to the concrete surrounding the duct. Bonded systems are more commonly used in bridges, both in the superstructure (the roadway) and in cable-stayed bridges. In buildings, they are typically only used in heavily loaded beams such as transfer girders and landscaped plaza decks where the large number of strands required makes them more economical (Warner and Faulkes, 1997).

Rock and soil anchors are also bonded systems but the construction sequence is somewhat different. Typically, a cased hole is drilled into the side of the excavation, the hillside or the tunnel wall. A tendon is inserted into the casing; and then the casing is grouted. In slope and tunnel wall stabilization, the anchors hold loose soil and rock together; in excavations they hold the wood lagging and steel piles in place (Collins and Mitchell, 1991).

2.5.5. Principle of Prestressing

The function of prestressing is to place the concrete structure under compression in those regions where load causes tensile stress. Tension caused by the load will first have to cancel the compression induced by the prestressing before it can crack the concrete. Figure 2.29 shows a plainly reinforced concrete simple-span beam and fixed cantilever beam cracked under applied load. Figure 2.29 shows the same unloaded beams with prestressing forces applied by stressing high strength tendons. By placing the prestressing low in the simple-span beam and high in the cantilever beam, compression is induced in the tension zones: creating upward camber.

Figure 2.29 shows the two pre-stressed beams after loads have been applied. The loads cause both the simple-span beam and cantilever beam to deflect down, creating tensile stresses in the bottom of the simple-span beam and top of the cantilever beam. The Bridge Designer balances the effects of load and prestressing in such a way that tension from the loading is compensated by compression induced by the prestressing. Tension is eliminated under the combination of the two and tension cracks are prevented. Also, construction materials (concrete and steel) are used more efficiently; optimizing materials, construction effort and cost.

Prestressing can be applied to concrete members in two ways, by pre-tensioning or post tensioning. In pre-tensioned members, the prestressing strands are tensioned against restraining bulkheads before the concrete is cast. After the concrete has been placed, and allowed to harden and then attain sufficient strength, the strands are released and their force is transferred to the concrete member. Prestressing by post-tensioning involves installing and stressing prestressing strand or bar tendons only after the concrete has been placed, hardened, and it attained a minimum compressive strength for that transfer (Cook and Mitchell, 1988).

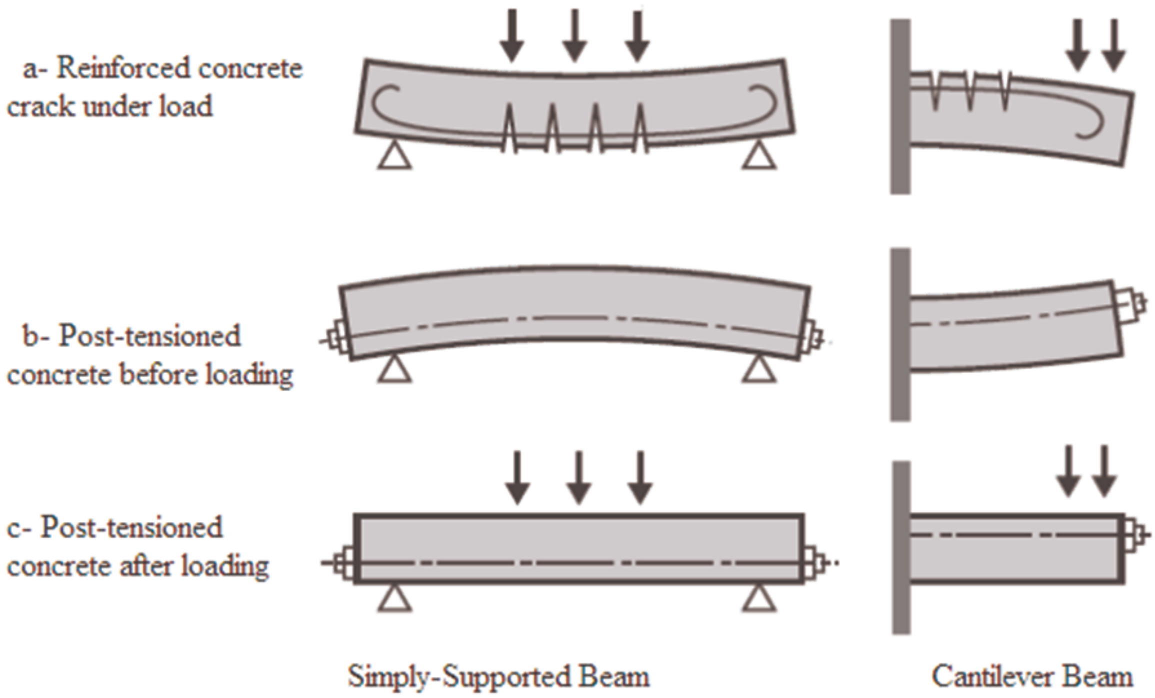

Figure 2.29. Comparison of Reinforced and Pre-stressed Concrete Beams.

2.5.6. Post-Tensioning Operation

Compressive forces are induced in a concrete structure by tensioning steel tendons of strands or bars placed in ducts embedded in the concrete. The tendons are installed after the concrete has been placed and sufficiently cured to a prescribed initial compressive strength. A hydraulic jack is attached to one or both ends of the tendon and pressurized to a predetermined value while bearing against the end of the concrete beam. This induces a predetermined force in the tendon and the tendon elongates elastically under this force. After jacking to the full, required force, the force in the tendon is transferred from the jack to the end anchorage.

Tendons made up of strands are secured by steel wedges that grip each strand and seat firmly in a wedge plate. The wedge plate itself carries all the strands and bears on a steel anchorage. The anchorage may be a simple steel bearing plate or may be a special casting with two or three concentric bearing surfaces that transfer the tendon force to the concrete. Bar tendons are usually threaded and anchored by means of spherical nuts that bear against a square or rectangular bearing plate cast into the concrete, (Ciolko and Tabatabai, 1999).

After stressing, protruding strands or bars of permanent tendons are cut off using an abrasive disc saw. Flame cutting should not be used as it negatively affects the characteristics of the prestressing steel. Approximately 20mm ($\frac{3}{4}$ in) of strand is left to protrude from wedges or a certain minimum bar length is left beyond the nut of a bar anchor. Tendons are then grouted using a cementations based grout. This grout is pumped through a grout inlet into the duct by means of a grout pump. Grouting is done carefully under controlled conditions using grout outlets to ensure that the duct anchorage and grout caps are completely filled. For final protection, after grouting, an anchorage may be covered by a cap of high quality grout contained in a permanent non-metallic and/or concrete pour-back with a durable seal-coat. (Corven, 2001).

2.5.7. Post-Tensioning Systems

Several suppliers produce systems for tendons made of wires, strands or bars. The most common systems found in bridge construction are multiple strand systems for permanent post-tensioning tendons and bar systems for both temporary and permanent situations. Refer to manufacturers' and suppliers' literature for details of available systems. Key features of three common systems (multiple strand and bar tendons) are illustrated in Figure 2.30, Figure 2.31 and Figure 2.32.

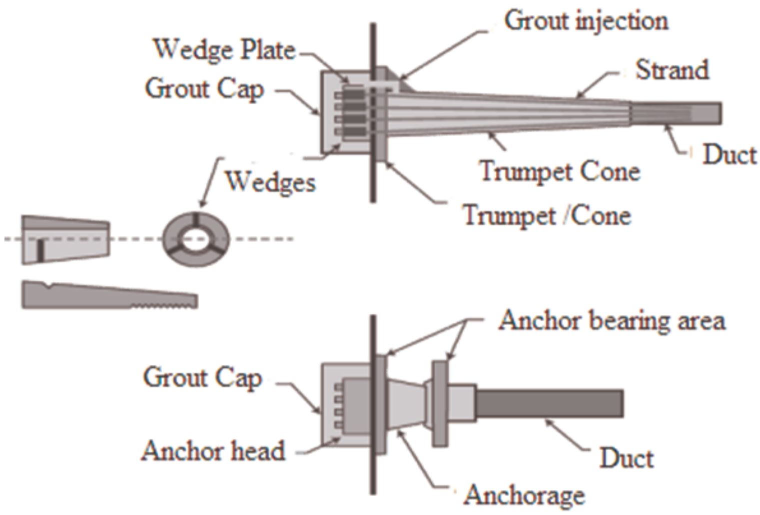

Figure 2.30. Typical Post-Tensioning Anchorage Hardware for Strand Tendons.

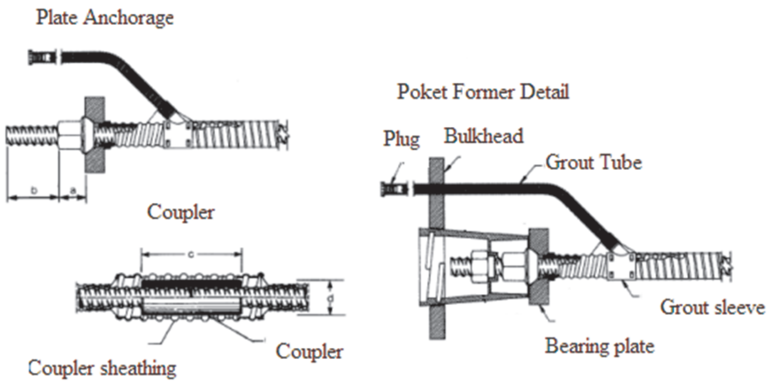

Figure 2.31. Typical Post-Tensioning Bar System Hardware. (Courtesy of Dywidag Systems International).

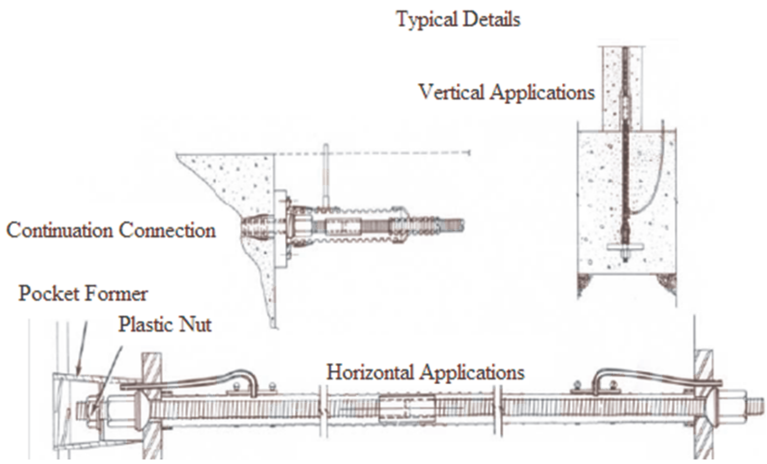

Figure 2.32. Typical Post-Tensioning Bar System Hardware (Courtesy of Williams Form Engineering Corporation).

2.5.8. Critical Elements

There are several critical elements in a post-tensioning system. In un-bonded construction, the plastic sheathing acts as a bond breaker between the concrete and the prestressing strands. It also provides protection against damage by mechanical handling and serves as a barrier that prevents moisture and chemicals from reaching the strand. The strand coating material reduces friction between the strand and the sheathing and provides additional corrosion protection.

Anchorages are another critical element, particularly in un-bonded systems. After the concrete has cured and obtained the necessary strength, the wedges are inserted inside the anchor casting and the strand is stressed. When the jack releases the strand, the strand retracts slightly, and pulls the wedges into the anchor. This creates a tight lock on the strand. The wedges thus maintain the applied force in the tendon and transfer it to the surrounding concrete. In corrosive environments, the anchorages and exposed strand tails are usually covered with a housing and cap for added protection (Corven and Moreton, 2004).

2.6. Summary

This chapter contained a review of a general introduction of post tension forces and hysteretic behavior of compressive member under lateral load. In addition, estimation of elastic modulus is presented experimentally. A brief introduction of springs and rubber properties are given.

Stone columns are suitable for improving soft silts, clays and loose silty sands. Stone columns offer a valuable technique under specific conditions for (i) increasing bearing capacity and slope stability, (ii) reducing settlement and increasing the time-rate of consolidation and (iii) reducing liquefaction potential. Applications of stone columns include the support of embankments, bridge abutment, sewer facility, tanks and to stabilize the existing slopes. Using of stone columns in sensitive soils should be given special care. However, the use of stone columns in highly compressible peat and organic soils is not recommended. The design and analysis of stone columns include the ultimate capacity and settlement. Stone columns design and analysis is given by different methods ranging from experience based empirical expressions and advanced finite element analyses. The principal and analysis of non-dimensional method is used to calculate the response of the SPVFR in terms of bending moment, shear force, slope and deflection.

3. METHODOLOGY

3.1. Introduction of the Pile Model SPVFR

In this study, a new proposed segmental pile is analyzed in laboratory environment to improve the properties of weak soil under lateral load. The Segmental Pile with Variable Flexural Rigidity SPVFR is composed of concrete blocks and rubber connected with pre-stressed wire anchor system. The engineering properties of materials which are used for developing the pile model are determined. Three different post-tension forces are applied to the pile system (750 N, 1500 N, and 2250 N) and tested to measure the flexural rigidity of the pile model. The pile model is placed on elastic springs, which represent the range of the soil stiffness (loose-dense).

By applying static/cyclic loading at the mid and top point of the SPVFR specimen, the deflection and lateral load are measured. A post-tension force of 2250 N is selected and the performance of the SPVFR under static and cyclic loading are investigated for maximum deflection of 4 mm at the mid/top point of the SPVFR, which is equivalent of 8% of the pile diameter. In addition the p-y curves are constructed corresponding to the static and cyclic loading. The methodology of this investigation is presented in four main components such as follow:

- Material properties
- Specimen Preparation
- Test Equipment and Measuring Tools
- SPVFR on Winkler Foundation

3.2. Material Properties

3.2.1. Concrete Mortar Blocks

In this investigation, mortar concrete blocks are used to develop the model of segmental post-tension beam SPVFR. Portland cement is used to produce mortar blocks. According to ASTM C270 standard specification for mortar and unit masonry, the mix proportions are 1:0.5:3 (cement: water: sand).

3.2.1.1. Manufacture of Mortar blocks. Concrete mortar cubes with dimension (50 mm x 50 mm x 20 mm) are molded, including a plastic pipe with external diameter 10 mm and internal diameter 7 mm in the center of 50 mm x 50 mm cross section. A steel mold is made to cast the mortar blocks with specifically given dimension and details. Figure 3.1 illustrates the steel mold details; and Figure 3.2 shows mortar blocks.

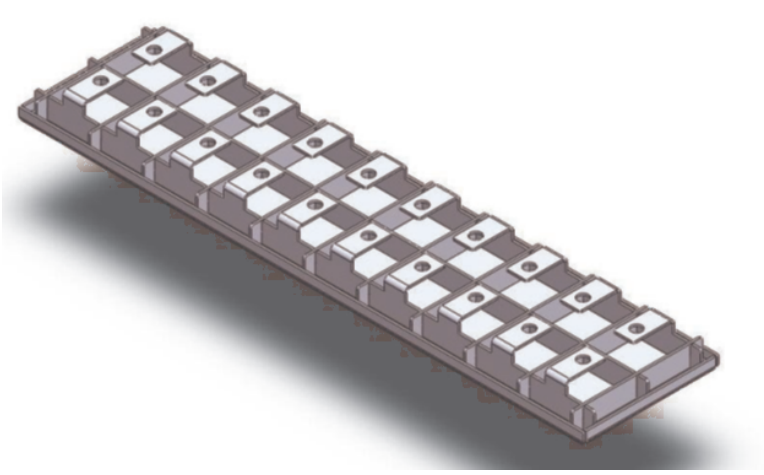

Figure 3.1. Steel Mold Details.

3.2.1.2. Compressive Strength of Mortar Blocks. Compressive strength test is conducted for six mortar blocks with 50 mm x 50 mm x 50 mm dimension, Figure 3.3 shows the standard mold to construct the mortar blocks. The average compressive strength of the blocks is close to 20 MPa. The exact values of the load and stress are given in Table 3.1.

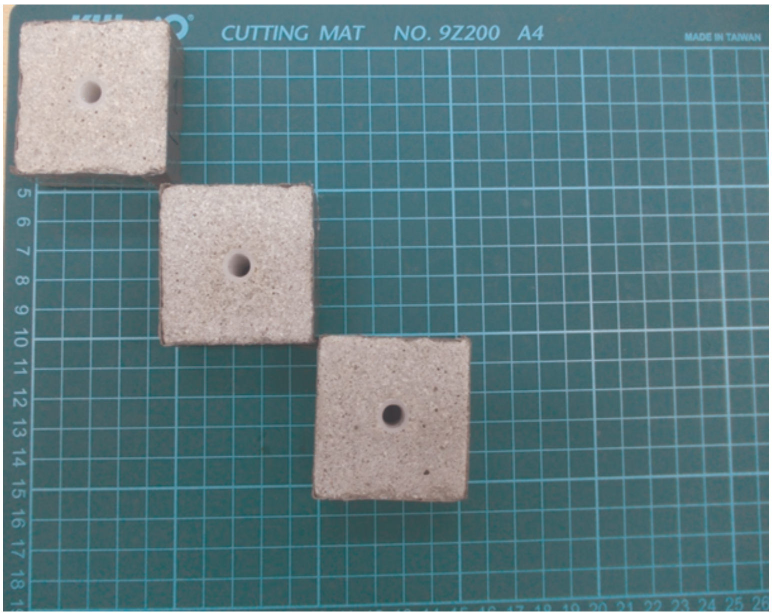

Figure 3.2. Mortar Block Units.

The mortar block dimension and weight are presented in Table 3.2, the width of block range between (50.23-50.72) and the length range between (50.24 - 50.74). The with of the blocks range between (95.01 gr - 100.81 gr).

Figure 3.3. Standard Mold (50 mmx50 mmx50 mm) for Mortar Block.

3.2.1.3. Rubber Shore 60. Rubber shore 60 can be considered a general purpose industrial rubber used in any application needing a common elastic rubber material. In this study, rubber shore 60 is used and placed between each mortar blocks on SPVFR Table 3.3 and Figure 3.4.

Table 3.1. Compressive Strength Test Results.

Sample No.	1	2	3	4	5	6	Average values
Load (KN)	52.1	51.1	48.5	47.5	49.3	48.6	49.5
Stress(MPa)	20.8	20.4	19.4	19	19.7	19.4	19.8

Table 3.2. Mortar Blocks Properties.

Block Number	Block Cross Section (mm)AxB	Block Thickness [mm][t]	Unite Weight (Gr)	Block Number	Block Cross Section AxB	Unit weight [Gr]	Block Thickness [mm] [t]
1	50.62x50.33	20.08	97.72	23	50.61x50.60	100.55	19.99
2	50.30x50.24	19.97	100.40	24	50.72x50.41	99.32	20.17
3	50.28x50.55	20.13	98.12	25	50.30x50.24	98.12	20.13
4	50.72x50.41	20.11	99.81	26	50.28x50.55	99.81	19.99
5	50.23x50.49	19.99	99.32	27	50.72x50.41	99.32	20.17
6	50.48x50.40	20.01	98.91	28	50.23x50.49	98.91	20.13
7	50.42x50.40	19.99	95.01	29	50.48x50.40	95.01	19.95
8	50.48x50.60	20.17	100.81	30	50.42x50.40	100.81	19.99
9	50.65x50.69	20.13	100.55	31	50.65x50.69	100.55	20.23
10	50.61x50.60	19.95	98.92	32	50.61x50.60	98.92	19.56
11	50.33x50.51	19.99	100.13	33	50.33x50.51	100.13	19.97
12	50.46x50.67	20.23	97.60	34	50.46x50.67	97.60	19.56
13	50.53x50.66	19.56	98.92	35	50.53x50.66	98.92	19.99
14	50.60x50.74	20.10	100.97	36	50.53x50.66	100.40	20.17
15	50.59x50.70	19.99	97.98	37	50.60x50.74	99.81	20.13
16	50.28x50.55	20.17	100.40	38	50.59x50.70	99.32	19.95
17	50.72x50.41	20.13	98.12	40	50.28x50.55	98.91	19.99
18	50.23x50.49	19.95	99.81	41	50.72x50.41	95.01	20.23
19	50.48x50.40	19.99	99.32	42	50.23x50.49	100.81	19.56
20	50.42x50.40	20.23	98.91	43	50.48x50.60	100.55	19.97
21	50.48x50.60	19.56	95.01	44	50.65x50.69	100.13	20.18
22	50.65x50.69	19.97	100.81	45	50.72x50.41	95.01	20.22

3.2.1.4. Rubber Shore 60 Properties. In this experimental study, black color (60 shores) rubber is used; the following table illustrates rubber properties.

Table 3.3. Rubber Properties Details.

Rubber Type	Neoprene Rubber.1
General Description	Soft rubber
Style	7797
Color	Black
Tensile Strength (KN/m^2)	$10x10^3$
Elongation at Failure (%)	125
Elastic Modulus (MPa)	3
Thickness (t) (mm)	3-20
Rubber Shore(A)	60

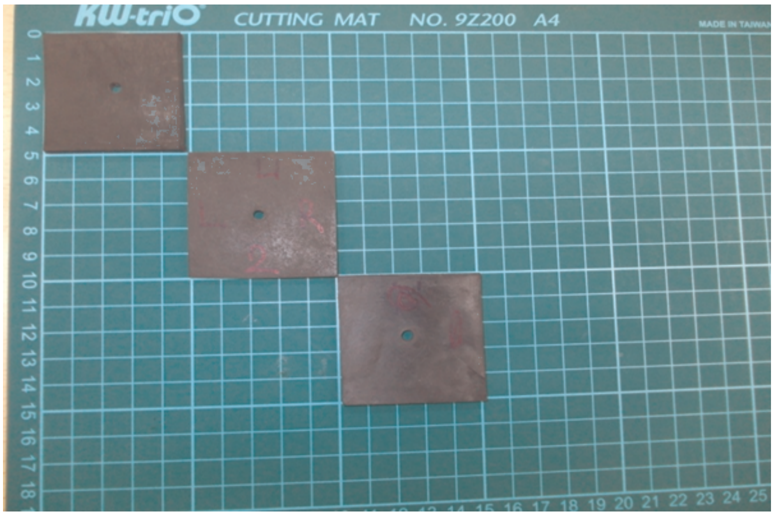

Figure 3.4. Rubber Units (Shore60).

3.2.2. Compression Springs

Compression springs are open-coil helical springs constructed to oppose compression along the axis of wind. Helical Compression Springs are the most common metal spring configuration. Generally, these coil springs are either placed over a rod or fitted inside a hole. When a load is placed on a compression coil spring, making it shorter, it pushes back against the load, and tries to get back to its original length. Compression springs offer resistance to linear compressing forces. Figure 3.5 shows details of compression spring.

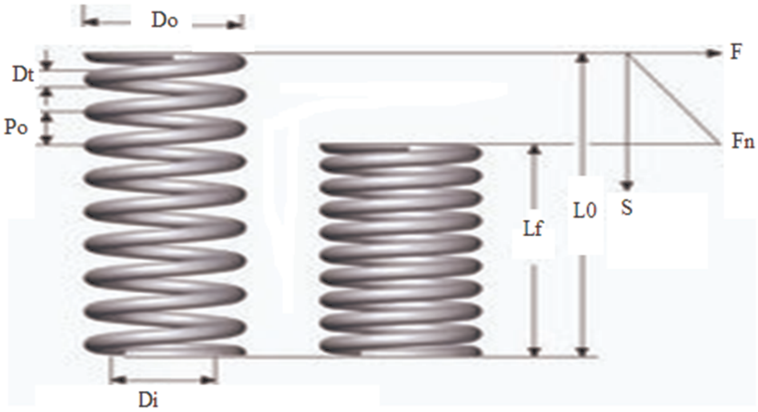

Figure 3.5. Details of Compression Springs.

3.2.2.1. Application. Compression Metal Springs are found in a wide variety of applications ranging from automotive engines and large stamping presses to major appliances and lawn mowers to medical devices, cell phones, electronics and sensitive instrumentation devices. Cone shape metal springs are generally used in applications requiring low solid height and increased resistance to surging.

3.2.2.2. Key Parameters. Dimensions: D_o: Outer Diameter,D_i: Inner Diameter, Wire Diameter: Dt , L_o:Free Length, and L_f: Solid Height.

3.2.2.3. Configurations. The most common compression spring, the straight metal coil spring, has the same diameter for the entire length. Other configuration options for compression coil springs include hourglass (concave), conical and barrel (convex) types. The straight coil spring configuration is the standard coil type for stock compression springs. In this study, compression springs with stiffness 4 N/mm are used to represent the soil stiffness (loose/medium and dense sand). The springs are specially manufactured for this study.

3.2.2.4. Spring Stiffness. In this section, the stiffness of four springs are determined using zwick machine. A member of wood with total length of 50 mm, external diameter

20 mm and internal diameter 10 mm is carefully prepared. The spring is placed inside the hole as shown in Figure 3.6.

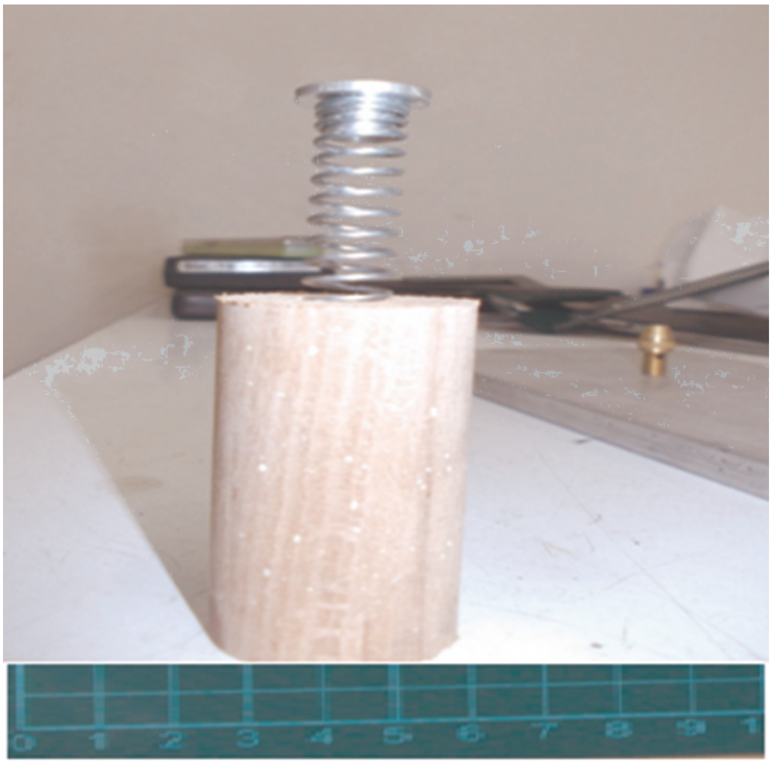

Figure 3.6. Spring Specimen and Wood Member before Test Application.

3.2.2.5. Spring Test Results. Four springs are selected randomly and their stiffness is determined using zwick equipment. The stiffness of each spring is 4N/mm.

3.2.3. High-Density Polyethylene

High-Density Polyethylene HDPE is an extremely versatile product with outstanding properties and good chemical resistance for a wide variety of applications at a very competitive cost. HDPE has a low coefficient of friction, and can be easily cut, machined, welded, and thermoformed for easy fabrication. This material will not splinter, rot or retain harmful bacteria, and is extremely resistant to cleaning agents. In this study, HDPE is used as a base of Compression springs. Figure 3.7 shows profile of HDPE.

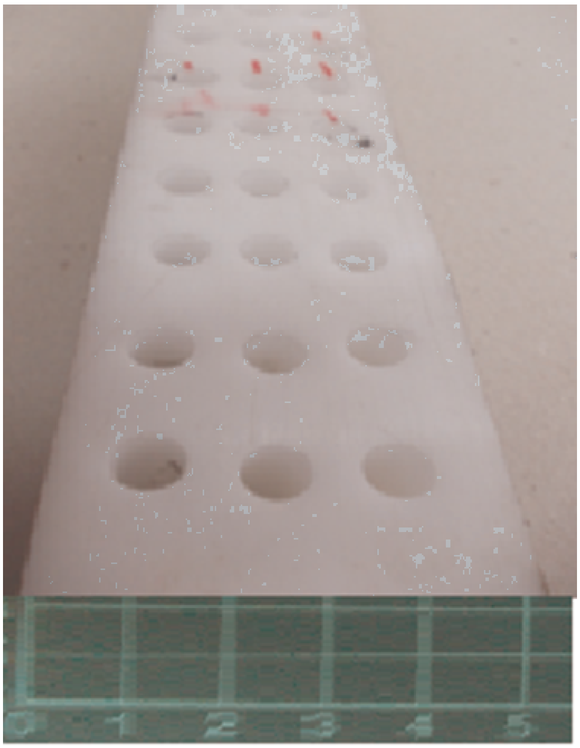

Figure 3.7. HDPE Profile for Experiment Use.

3.2.3.1. HDPE Properties.

- moisture/chemical resistant
- impact resistant
- superior tensile strength
- FDA approved/meets NSF standards 2 and 51

3.2.3.2. HDPE Typical Applications.

- machined parts
- industrial cutting boards
- wear strips
- tank linings
- solar collectors, valve bodies
- vacuum formed parts

- livestock containment
- material handling systems

3.2.4. Aluminum Profile Frame

Aluminum extrusions have nearly the same tensile strength as mild steel with a much higher strength to weight ratio. Aluminum extrusion assembly can easily be done right at the project site with no special safety equipment required. Construction or design changes or adjustments can be easily and immediately implemented. In this investigation, a U-shape of Aluminum profile is formed to function as the main base of the SPVFR.

3.3. Test Equipment and Measuring Tools

3.3.1. Test Equipment (MTS)

Three-point bending tests and Winkler beam tests are conducted using MTS equipment. Typical specimen is a flat, rectangular beam with defined geometries. Examples include metals, composites, rock, concrete and plastics. The specimen is supported on each end while a load is applied at the middle. These tests produce important data about flexural strength, performance, durability and service life. Figure 3.8 shows test equipment.

Figure 3.8. Test Equipment.

3.3.2. S-Type Load Cell (Tension + Compression)

In this study, S-type load cell is used to measure post-tension forces on the cable. S-type load cell are bi-directional force transducers, which generally have S or Z shape, and provide installation flexibility and high resolution especially for measuring lower level load.

3.3.3. Prescale film FPD-8010E

Prescale film is a highly sensitive film that reacts to pressure applied to it. The level of pressure is indicated by the density of the color. This system comprises the calibration sheet for automatic calibration and the software and uses the computer as the processing engine.

3.3.3.1. FPD-8010E System Operating Principles. The following operation steps are given.

(i) Prescale film is composed of microcapsules containing color former and color generation agent. The microcapsules in the color generation agent layer are crushed according to the pressure applied; and the color generation agent released from the crushed microcapsules reacts chemically with the color developer and turns red. Because the microcapsules are adjusted to be crushed at various strengths, the intensity of the red obtained depends on the pressure applied.

(ii) The FPD-8010E is the pressure image software used.

(iii) When the pressurized prescale film is placed on the scan section of the FPD-8010E and scanned in, the intensity of the red color on the prescale film is scanned, the pressure image software converts this to pressures, and the results are displayed on the display.

(iv) The scanned data is displayed on the display with the display method corresponding to the selected display format.

(v) The data displayed on the display can be analyzed and printed as necessary.

<u>3.3.3.2. FPD-8010E System Components.</u> The FPD-8010E system components are as shown in Figure 3.9:

(a) (b)

Figure 3.9. Illustrate the Component of FPD-8010 E: (a) FPD-8010E Dedicated Cover, (b) Calibration Sheet.

<u>3.3.3.3. Prescale Film (PF) Setup Steps.</u>

(i) The Scanner main unit cover is opened.

(ii) The prescale film scan surface is faced down, and is set aligned with the light front of the scan section.

In case that prescale film (PF) is too large to scan at one time, it can be scanned. As divided into max, 15 times. In that case, scan in overlapping the edges of the scan screens is put together with a composite screen. For fine adjustment during composing, check the overlap areas in the enlargement window (The enlargement window is displayed by clicking the magnifying glass icon on the tool bar, but only when an inverted image is displayed in the composite window). When the overlapping images match, the overlap image section becomes black, as shown in Figure 3.10 and Figure 3.11.

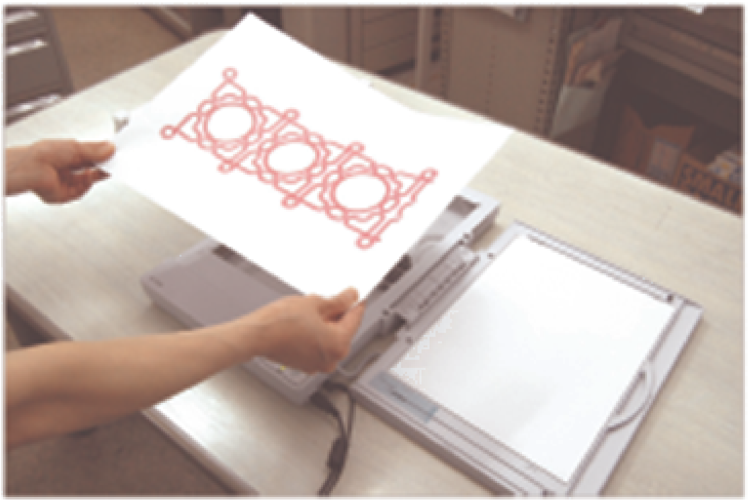

Figure 3.10. Prescale Film Divided in two Parts for Scanning.

Figure 3.11. Set the Dedicated Cover in Place.

3.3.3.4. Two-Sheet Type for Super Low Pressure (LLW). In this study, two-sheet types for super low pressure are used, and the measurement pressure range between (0.5-2.5 MPa).

3.3.3.5. Structure. Two-sheet prescale films are composed of an A-film, which is coated with a micro-encapsulated color-forming material; and a C-film, which is coated with a color-developing material. The A-film and C-film must be positioned with the coated sides facing each other.

3.3.3.6. Method of Used.

(i) Cut the prescale film into the required shape. With the two-sheet film, make sure the coated sides on A-film and C-film face each other.
(ii) Insert cut prescale film into the area to be measured and apply pressure,
(iii) Remove film and observe pressure distribution, and computer format details can be used,

3.3.3.7. Continuous Pressure. With the continuous pressure method, increase the pressure gradually to the given level and check if the pressure can be maintained at that level. (Raise the pressure gradually for two minutes and then maintain it at that level for two additional minutes. The pressure maintained at this level is referred to as continuous pressure).

3.3.3.8. Momentary Pressure. Measure the pressure for a given interval. (Apply pressure for five seconds, and then maintain the pressure at that level for five seconds. The pressure maintained at this time is referred to as momentary pressure).

3.3.3.9. Determining the Pressure Level. When checking the pressure distribution with the prescale film alone:

The red color density of the prescale film will change depending on the amount of applied pressure. Sections where the red color is thick indicate that applied pressure is high: conversely, sections where the red color is pale indicate that the applied pressure is low.

In addition to determining the pressure level by pressure distribution, pressure levels can also be determined to a certain degree by comparing the red color density of the prescale film with the standard color sample chart (Pressure can be determined to a given level from the selected standard pressure chart curve in relation to the temperature and humidity factors along with pressure conditions). The operation of the prescale film is shown Figure 3.12.

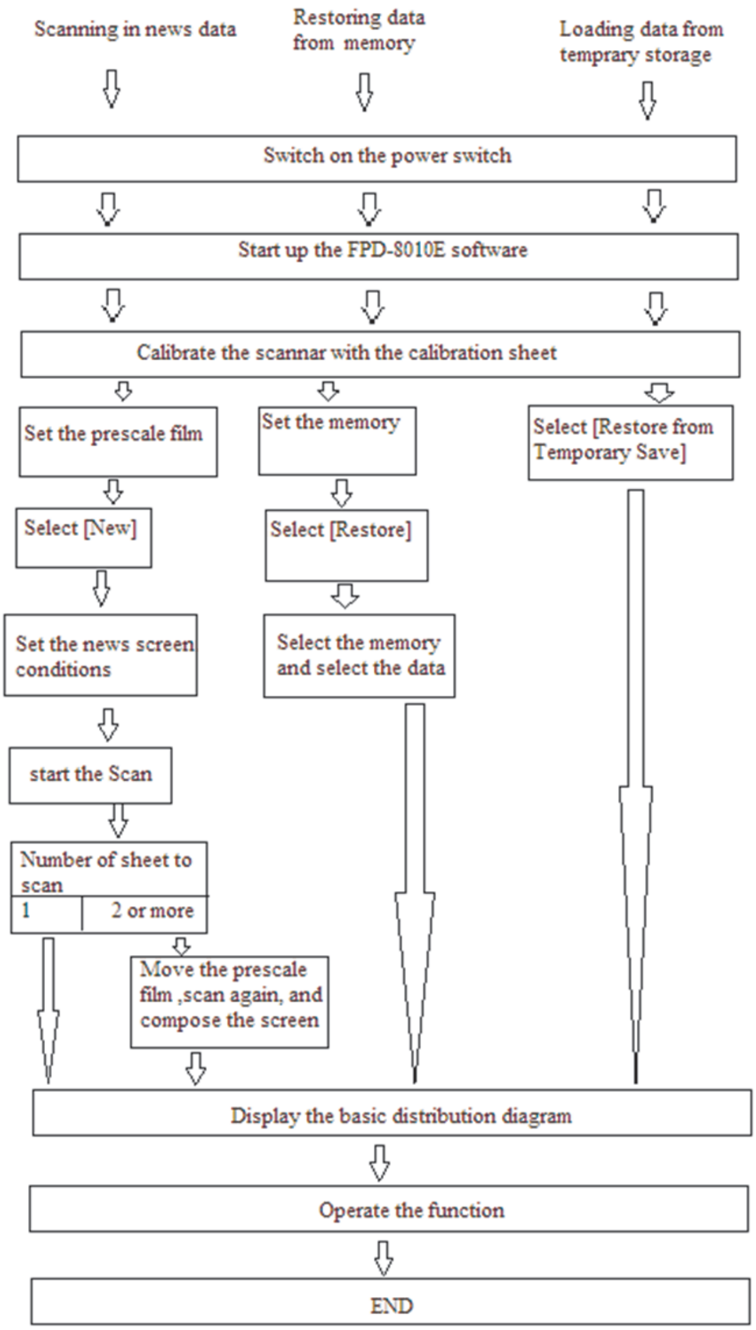

Figure 3.12. Summary of Operation of Prescale Film Software.

3.4. Specimen Preparation

3.4.1. Configuration of the SPVFR

Numbers of six segmental beam models are constructed by using all components of the SPVFR. The details of the pile model components are given later; and each model consists of 15 mortar blocks. The construction process can be given as follows:

- All mortar blocks with specific numbers are placed in horizontal direction,
- Rubber sheet 50 mm x50 mm x 3 mm , with 10 mm hole in centre is placed at each block,
- Two aluminum profile plates with a 50 mm x50 mm 20 mm and 10 mm hole in the center are placed at the two ends of the SPVFR to function as bearing plate,
- High strength wire 5 KN is passed through blocks and rubber to function as one unit by applying post-tension,
- A s-shape load cell is attached to the base of the SPVFR,
- For Winkler SPVFR tests, the load cell is attached at L-shape Aluminum profile, and one end of load cell is attached to the base of the SPVFR,
- High-Density Polyethylene is placed and springs are placed,
- During the setup of the SPVFR, prescale films are placed in five different locations along SPVFR length,
- After applying desired post-tension forces on the SPVFR, the models are placed at springs, as shown in Figure 3.13,
- The SPVFR specimen is ready for testing.

Figure 3.13. SPVFR Prepared for Winkler SPVFR Tests.

3.4.2. Experimental Work for SPVFR

A new technique of the SPVFR is used to improve the properties of weak soil. In the first part, laboratory studies are made to evaluate the stiffness and response of the pile model due to prestress force and flexural stress. To estimate the stress distribution on the concrete units interface prescale film sheets are used in five different positions, along the length of the pile model.

3.4.2.1. Laboratory Tests. The experimental study is carried out with the following objectives:

- To estimate the flexural rigidity of the SPVFR with three different post-tension forces.
- To estimate the stress distribution on concrete block surface of the SPVFR due to applied prestress forces.

(i) Three point bending test: it provides values for the modulus of elasticity in bending E_f, flexural stress σ_f, flexural strain ε_f, and the flexural stress-strain response of the material. The main advantage of a three-point flexural test is the ease of the specimen preparation and testing. However, this method has also some disadvantages: the results of the testing method are sensitive to specimen and loading geometry and strain rate.

(ii) Forces/displacement relationship for rubber shore 60

(iii) Concrete/ rubber interface tests

(iv) Prestress force test: Specimen under study is subject to prestress force to estimate the stress distribution on block concrete surface in different positions.

3.4.2.2. Determination of Flexural Rigidity of the SPVFR Using MTS. The three-points bending test (beam test) provides values for the modulus of elasticity in bending E_f. The main advantages of a three-point bending test are the ease of the specimen preparation for testing. Beam tests are conducted using MTS for different beam materials to determine the flexural rigidity values as shown below:

- Mortar beam [50x50x300mm]
- Segmental post-tensioned beam (50x50x250mm); (750N)

- Segmental post-tensioned beam (50x50x250mm); (1500N)
- Segmental post-tensioned beam (50x50x250mm); 2250N

The load displacement relationship is established for each specimen; and the stiffness of beam materials is obtained.

(i) Arrangement of the SPVFR

- The segmental concrete beam is formed by using high tensile strength wire passing through the middle of each segmental concrete block units which works as post-tension system. The segmental model system functions as one unit by tensioning the wire and the value of applying force and pressure are measured by using load cell which is attached to the model as shown in Figure 3.14. The following forces are applied to the wire as shown below:
- 750 [N]
- 1500 [N]
- 2250 [N]

Figure 3.14. Full Length Specimen Beam Mortar on MTS Equipment.

<u>3.4.2.3. Simple Beam Test Using MTS (Three-Point Bending Test, Static).</u> Simple beam test is conducted to find the flexural rigidity values using beam mortar and segmental beam model with variable post-tension forces. The load-deflection relationship at mid-span for each beam is established. The types of beams are:

- Full length mortar beam
- Segmental mortar beam (post-tension)(750N)
- Segmental mortar beam (post-tension)(1500N)
- Segmental mortar beam (post-tension)2250N

3.4.2.4. Load-Deflection/Interface Relationship for Rubber Shore 60. In this part, the behavior of rubber shore under loading and unloading condition is studied. Two types of tests are conducted i) oedometer test ii) direct shear test.

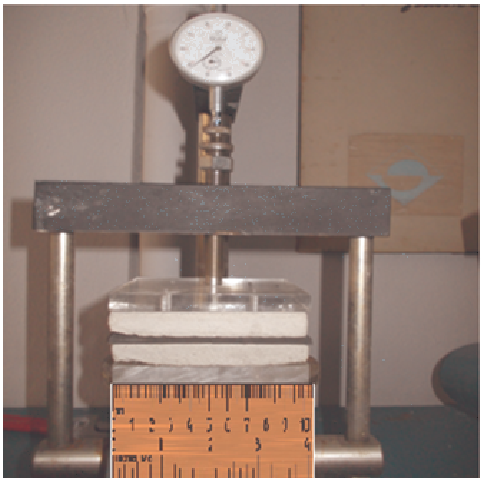

Figure 3.15. Load Deflection Test for Rubber in Oedometer Equipment.

3.4.2.5. Test Procedure. Rubber with shore 60 (100x100x 3 mm) is prepared and sandwiched between two concrete blocks (100x100x20 mm) and (100x100x15 mm). Two units of high stiff plastic pieces (100x100x20 mm) are placed at the top and bottom of the concrete blocks. The model is placed carefully on a consolidation test machine and a displacement gauge is attached at the mid-top of the model system, as shown in Figure 3.15. Loading and unloading procedure is used during test application and the relationship between stress-strain, load-deflection, are recorded and plotted.

3.4.3. The Interface Test for Rubber/Concrete

The direct shear testing of interfaces is approximately similar to the direct shear testing of soils. Normal load is applied to the top of the sample by a loading cap, and then a horizontal load is applied to shear the interface between the soil and the construction material.

The shear strength along the surface of contact of the soil and the foundation for a cohesionless granular material can be given as;

$$\tau_f = \sigma_n tan\,[\delta] \tag{3.1}$$

where is the δ interface friction angle between soil and structure, τ_f is the frictional resistance to shear, σ_n is the normal stress on the soil.

3.4.4. Test Procedure

The test is performed as in the same manner of direct shear test under 100 KPa 200 KPa, 300 KPa and 900 KPa. Differently, the upper half of the direct shear box is replaced with concrete block in order to obtain interface friction angles between concrete and rubber media. The displacement rate is 1 mm/min which resulted in the failure occur approximately in 10 minutes. For each tests horizontal displacements, horizontal forces the vertical displacements, and the constant vertical force are recorded.

3.5. SPVFR on Winkler Foundation

3.5.1. Testing Procedures

In this study, MTS equipment is used to evaluate the stress and displacement of the SPVFR during static and cyclic loading. Displacement controled test procedure is applied.

3.5.2. Type of Loading

Two sets of loading are used in this study:

(i) Static loading

- At the top of the SPVFR
- At the mid-point of the SPVFR

(ii) Cyclic loading

- At the top of the SPVFR, 3 cycles/second
- At the mid-point of the SPVFR, 3 cycles/second

(iii) Construction of p-y curves of the SPVFR

The p-y curves of segmental pile with variable flexural rigidity are determined at three positions of the pile length which are:

- P-y curves at 58 mm from pile tip
- P-y curves at 171 mm from pile tip
- P-y curves at 329 mm from pile tip

The load is increased gradually for each 1 mm deflection, followed with unloading until maximum deflection is reached. To evaluate the lateral capacity of the SPVFR, the maximum value of deflection 4mm is used (8% of pile diameter).

3.5.3. Numerical Analysis Using FED Software (L-Pile)

L-pile software (http:/www.ensoftinc.com) was used to perform the lateral analysis of the deep foundation. L-pile is a commercial program to analyze laterally loaded piles using the p-y method. The capability of defining user-input p-y curves enables the simulation of soil-pile interaction. In this study, the results of experimental study are compared with L-pile and NDM model in terms of bending moment, shear force and deflection. In the Figures 3.16 to Figure 3.21 the test program, the data measured, the analyses conducted, the flow chart for non-dimensional method and the flow chart for L-pile method are presented.

Test No.	Test Type	Purpose of the Tests	Specimen Picture During Test	Test Results	ASTM Specification
1	Compressive strength test	compressive strength of Mortar blocks	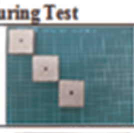	See Chapter [4]	ASTM C39 / C39M - 12a
2	Direct Shear Interface Test	Concrete /Rubber shore 60 Interface shear Properties		See Chapter [4]	ASTM D 3080
3	Load-Deflection Test for Rubber Using Oedometer Equipment	Concrete Block/Rubber shore 60-Load/ Deflection Relationship		See Chapter [4]	-
4	Spring Stiffness Test Using Zwick Equipment	Determination of Spring Stiffness		See Chapter [4]	-
5	Three Point Bending Test	Flexural Rigidity [EI] Prism Mortar		See Chapter [4]	ASTM D 790
		[EI] SPVFR [0.75 KN] [EI] SPVFR 1.5 KN] [EI] SPVFR [2.250 KN]		See Chapter [4]	

Figure 3.16. Test Program.

Test No.	Winkler Springs	Load Type	Load Position	Purpose of The Test	Sample Picture	Test Results
1	[1K]	Static	Top-point	Load/Displacement Curves		See Chapter [4]
2	[1K]	Cyclic	Top-Point			See Chapter [4]
3	[2K]	Static	Mid-point	Load/Displacement Curves		See Chapter [4]
4	[2K]	Cyclic	Mid-Point			See Chapter [4]
5	[3K]	Static	Top-point	Load/Displacement Curves	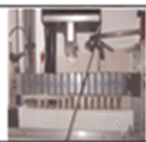	See Chapter [4]
6	[3K]	Cyclic	Top-Point			See Chapter [4]
7	[3K]	Static	Mid-point			See Chapter [4]
8	[3K]	Cyclic	Mid-Point			See Chapter [4]

1K: 4 N/mm, 2K: 8 N/mm, 3K: 12 N/mm

Top Point Loading:  , Mid Point Loading: 

Figure 3.17. Test Program.

Test No.	Winkler Springs	Load Type	Load Position	Deflection Measurement Position	Prescale Film position [m]	Test Results
1	-	-	Post-Tension Force[Cable Force]	-	0,0.09,0.181, 0.271,0.329	See Chapter [4]
2	[1K]	Static	Top-point	LVDT 1-MTS at Load Position LVDT2 at Mid-Point LVDT3 at 0.058 m from the Tip	No	See Chapter [4]
3	[1K]	Cyclic	Top-Point			See Chapter [4]
4	[2K]	Static	Top-point	LVDT 1-MTS at Load Position LVDT2 at Mid-Point LVDT3 at 0.058 m from the Tip	No	See Chapter [4]
5	[2K]	Cyclic	Top-Point			See Chapter [4]
6	[3K]	Static	Top-point	LVDT 1-MTS at Load Position LVDT2 at Mid-Point LVDT3 at 0.058 m from the Tip	0,0.09,0.181, 0.271,0.329	See Chapter [4]
7	[3K]	Cyclic	Top-Point			See Chapter [4]
8	[3K]	Static	Mid-point	LVDT 1-MTS at Load Position LVDT2 at Top-Point LVDT3 at 0.058 m from the Tip	0,0.09,0.181, 0.271.0.329	See Chapter [4]
9	[3K]	Cyclic	Mid-Point			See Chapter [4]

Figure 3.18. Data Measured.

Test No.	Winkler Springs, Test Type	Load Type	Load Position	In-Put	Out Put	Test Results
1	Three Point Bending Test	Static	Mid Point	Load-Deflection Diagram	[EI]0.75, [EI]1.5, [EI]2.25	See Chapter [4]
2	[1K],End Fixed Beam on Elastic Spring	Static	Top-point	Derivative the Displacement Curves along the Pile , → Integration of Spring Reaction Curve along the Pile → Integration of Shear Force →	Slope, Shear Force, Bending Moment	See Chapter [4]
3	[1K], End Fixed Beam on Elastic Spring	Cyclic	Top-Point			See Chapter [4]
4	[2K], End Fixed Beam on Elastic Spring	Static	Top-point	Derivative the Displacement Curves along the Pile , → Integration of Spring Reaction Curve along the Pile → Integration of Shear Force →	Slope, Shear Force, Bending Moment	See Chapter [4]
5	[2K], End Fixed Beam on Elastic Spring	Cyclic	Top-Point			See Chapter [4]
6	[3K], End Fixed Beam on Elastic Spring	Static	Top-point	Derivative the Displacement Curves along the Pile , → Integration of Spring Reaction Curve along the Pile, → Integration of Shear Force , →	Slope, Shear Force, Bending Moment	See Chapter [4]
7	[3K], End Fixed Beam on Elastic Spring	Cyclic	Top-Point			See Chapter [4]
8	[3K], End Fixed Beam on Elastic Spring	Static	Mid-point			See Chapter [4]
9	[3K], End Fixed Beam on Elastic Spring	Cyclic	Mid-Point			See Chapter [4]

Figure 3.19. Analysis Conducted.

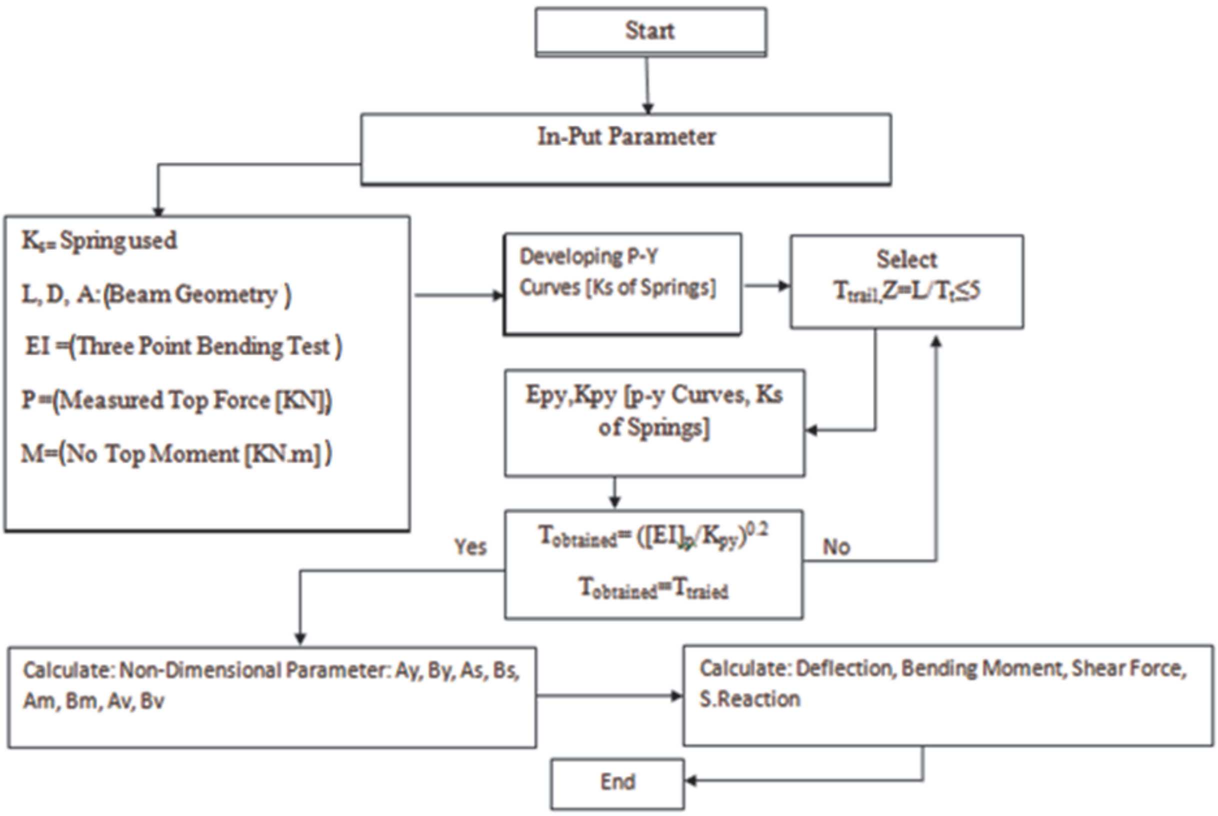

Figure 3.20. Flow Chart of Non-Dimensional Analysis Method.

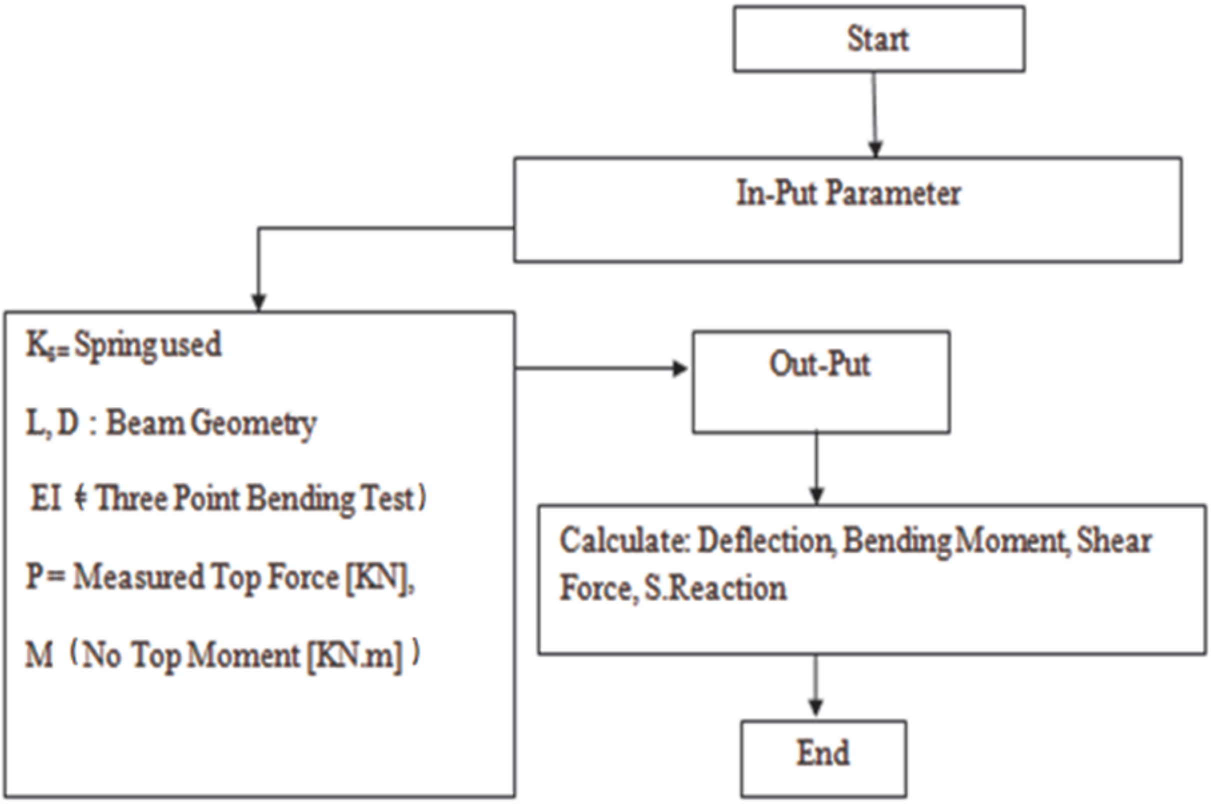

Figure 3.21. Flow Chart of L-Pile Analysis Method.

4. TEST RESULTS AND ANALYSIS FOR SEGMENTAL PILE WITH VARIABLE FLEXURAL RIGIDITY ON ELASTIC SPRINGS

In this chapter, the results of tests on segmental pile with variable Flexural rigidity on Winkler foundation subjected to lateral load are presented. The results of p-y curve for 1K, 2K, 3K springs stiffness for static and cyclic loading are presented. The stress distribution, slope, shear force, deflection and bending moment due to post-tension 2250 N forces and lateral static forces at mid-point of specimen are obtained. The results of stress distribution, shear force, bending moment, slope and deflection due to post-tension forces 2250 N and lateral static/cyclic load at top-point of specimen are given.

4.1. Experimental Test Results of P-Y Curves of the SPVFR on Winkler Foundation

4.1.1. P-Y Curve of the SPVFR on Elastic Foundation-1K

The p-y curves of the SPVFR placed on linear spring 1K subject to lateral static load at top point is presented in Figure 4.1 at 0.058 m give spring reaction of 0.154 N/mm which corresponds to 0.87 mm deflection. The p-y curves of the pile model at 0.171 m from pile tip develop a spring reaction of 0.233 N/mm which corresponds to 1.32 mm deflection. The p-y curves of the pile model at 0.329 m from the tip of the pile produce spring reaction of 0.7075 N/mm, which corresponds to 4 mm deflection.

4.1.2. P-Y Curve of the SPVFR on Elastic Foundation 2K

The p-y curves of the SPVFR placed on linear spring 2K and subjected to lateral static load at top point is presented in Figure 4.2 at 0.297 mm from the pile tip give spring reaction of 1.85 N/mm which corresponds to 0.84 mm. In addition, the p-y curves of the pile model at 0.171 m from the pile tip produce spring reaction of 0.417 N/mm which corresponds to 1.18 mm. According to the p-y curves of the pile model 2K at 0.329 m from the pile tip, the spring reaction increases up to 1.415 N/mm which corresponds to 4 mm deflection at the pile head.

4.1.3. P-Y Curve of the SPVFR on Elastic Foundation-3K

The p-y curves of the SPVFR placed on linear spring 3K and subjected to lateral static load at pile lead is illustrated in Figure 4.3, at 0.058 mm from the pile tip give spring reaction of 0.292 N/mm which corresponds to 0.55 mm. In addition, the p-y curves of the pile model at 0.171 m from the pile tip produce spring reaction of 0.51 N/mm which corresponds to 0.96 mm. According to the p-y curves of the pile model 3K at 0.329 m from the pile tip, the spring reaction increases up to 2.122 N/mm which corresponds to 4 mm deflection at the pile head.

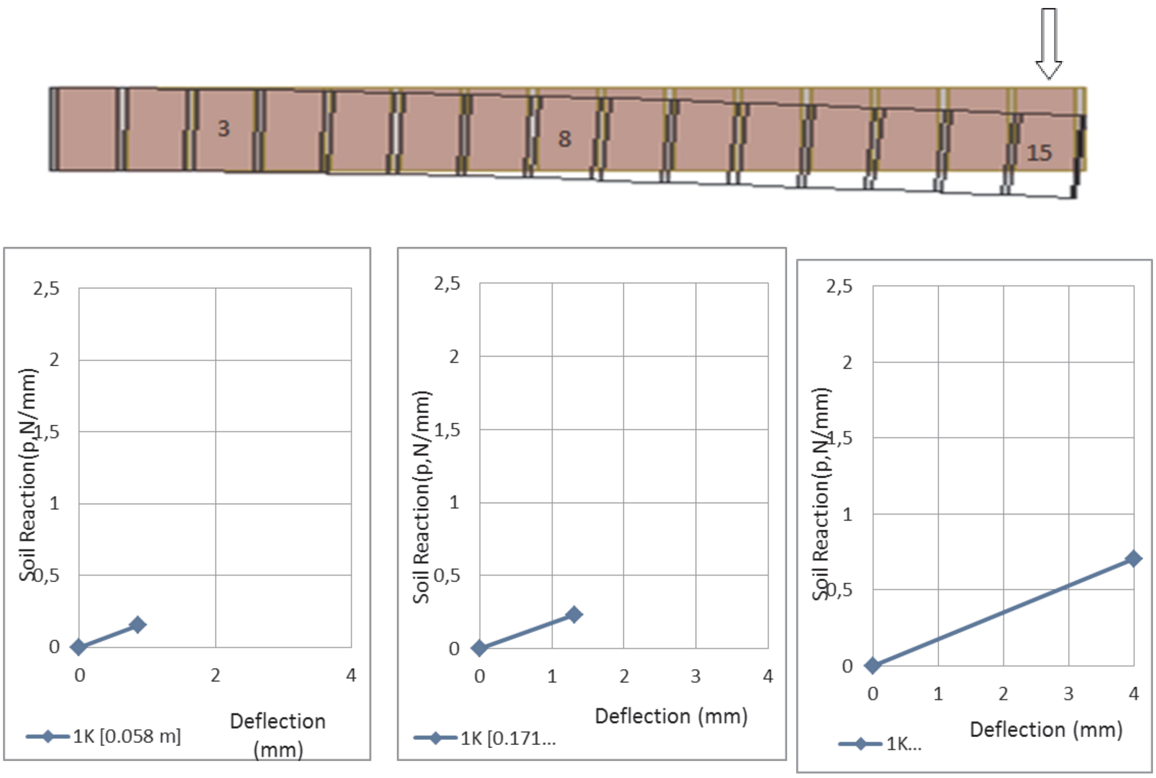

Figure 4.1. P-y Curves of the SPVFR Placed on Elastic Springs 1K/ Static Load.

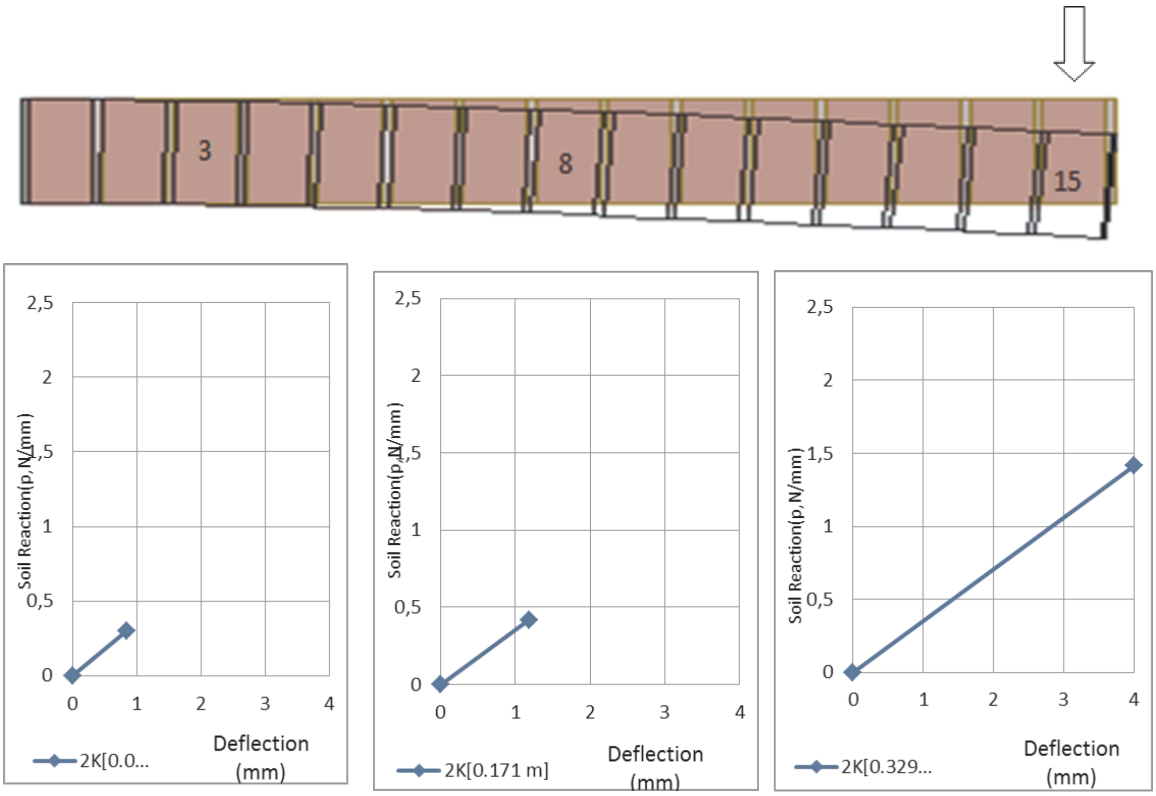

Figure 4.2. P-y Curves of the SPVFR Placed on Elastic Springs 2K/Static Load.

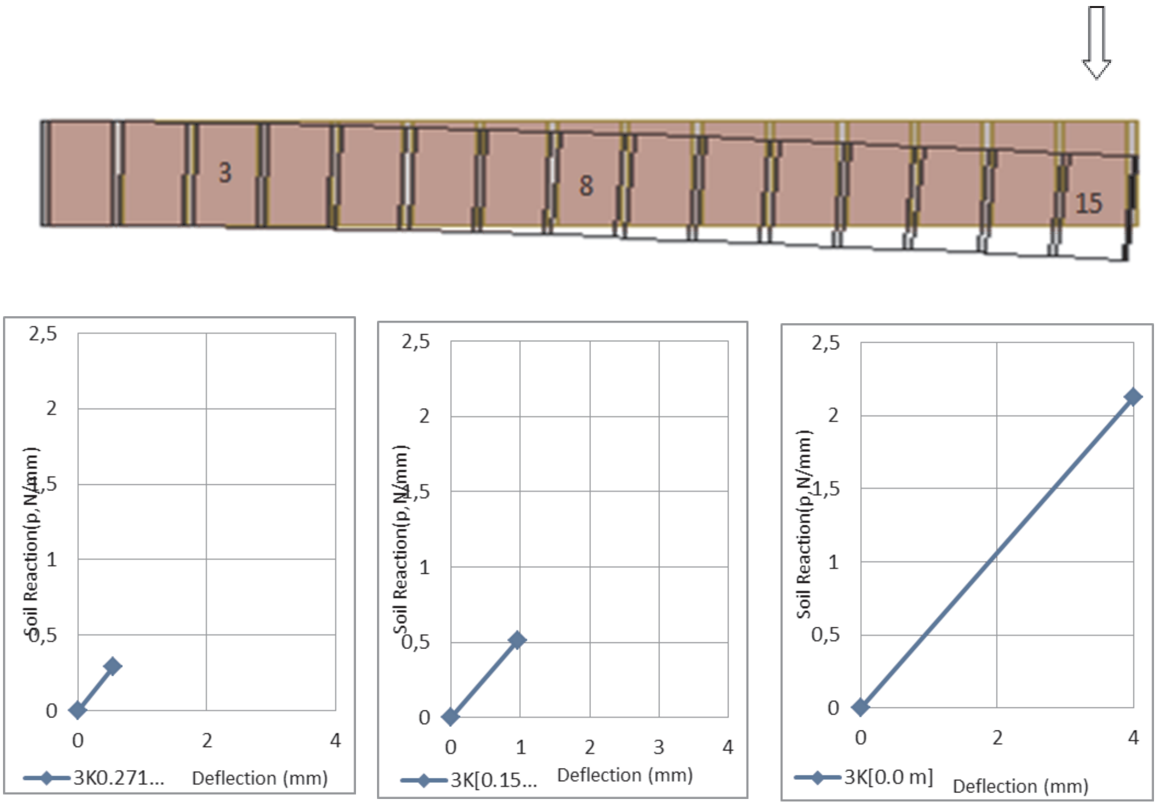

Figure 4.3. P-y Curves of the SPVFR Placed on Elastic Springs 3K/Static Load.

4.2. Analysis of SPVFR Placed Using Experimental Data

In this section, the analysis of the SPVFR is given using the experimental data which are recorded during the tests (deflection and force). The purpose of this section is to find out the following parameters: bending moment, shear force and the spring reaction along the pile model length. Figure 4.4 to Figure 4.9 presented the results of the pile model. These parameters are obtained for different linear springs and loading. In addition, the deflection of the pile model for each 50 seconds are presented, which gives an idea about the pile deflection behavior during the test period.

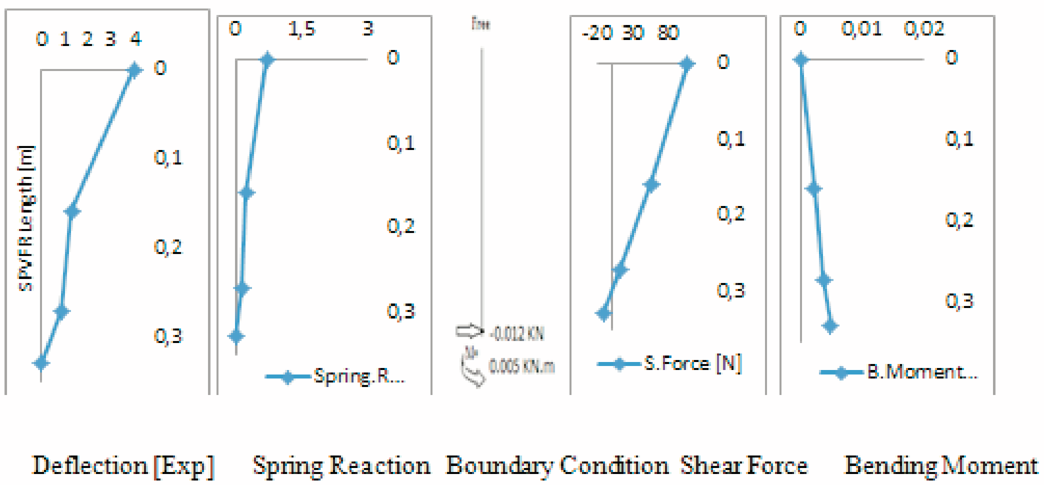

Figure 4.4. Deflection, Spring Reaction, Boundary Condition, Shear Force and Bending Moment Along SPVFR Placed on 1K-Static.

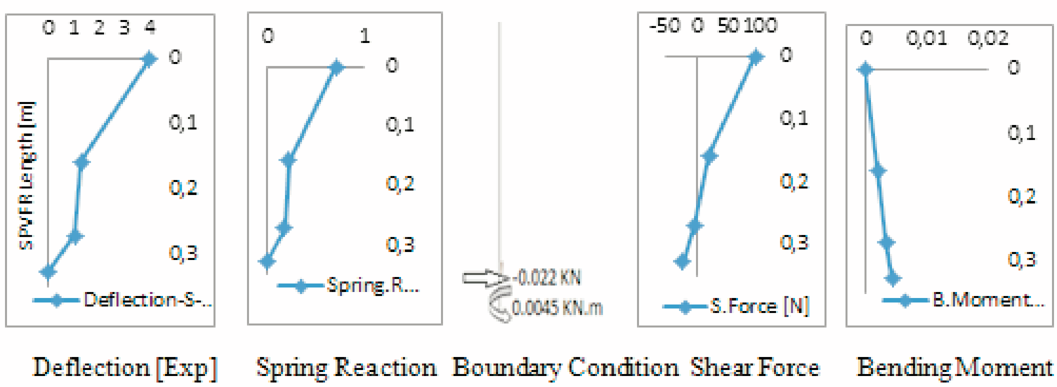

Figure 4.5. Deflection, Spring Reaction, Boundary Condition, Shear Force and Bending Moment Along SPVFR Placed on 1K-Cyclic.

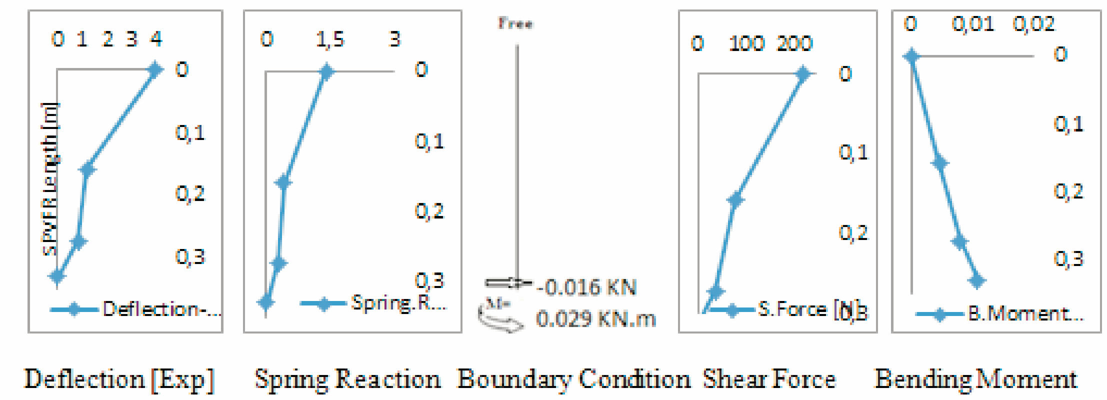

Figure 4.6. Deflection, Spring Reaction, Boundary Condition, Shear Force and Bending Moment Along SPVFR Placed on 2K-Static.

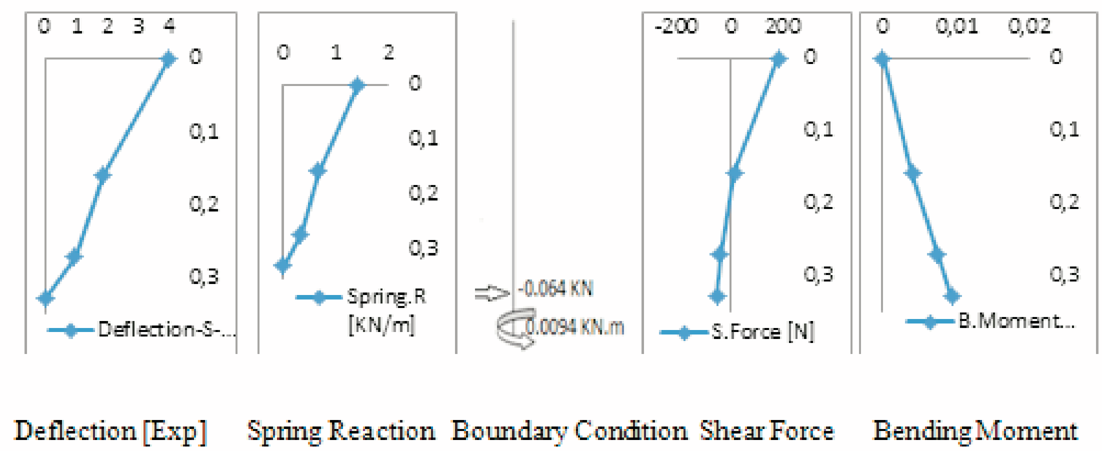

Figure 4.7. Deflection, Spring Reaction, Boundary Condition, Shear Force and Bending Moment Along SPVFR Placed on 2K-Cyclic.

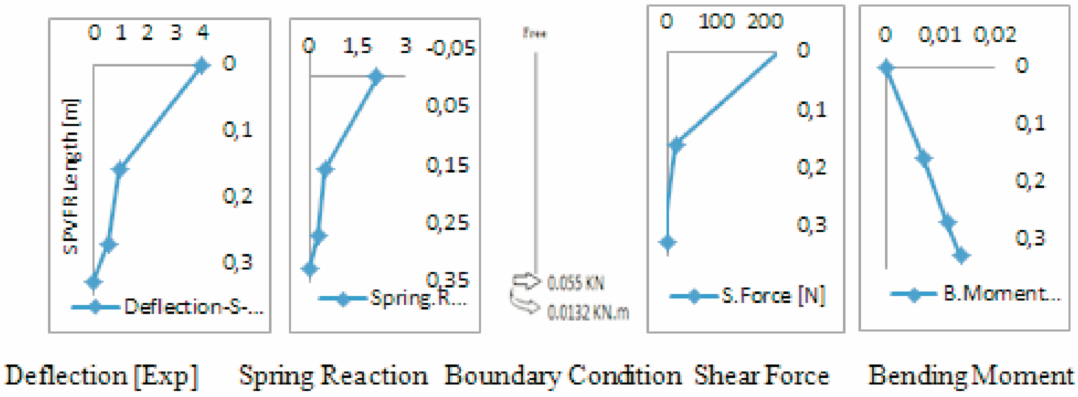

Figure 4.8. Deflection, Spring Reaction, Boundary Condition, Shear Force and Bending Moment Along SPVFR Placed on 3K-Static.

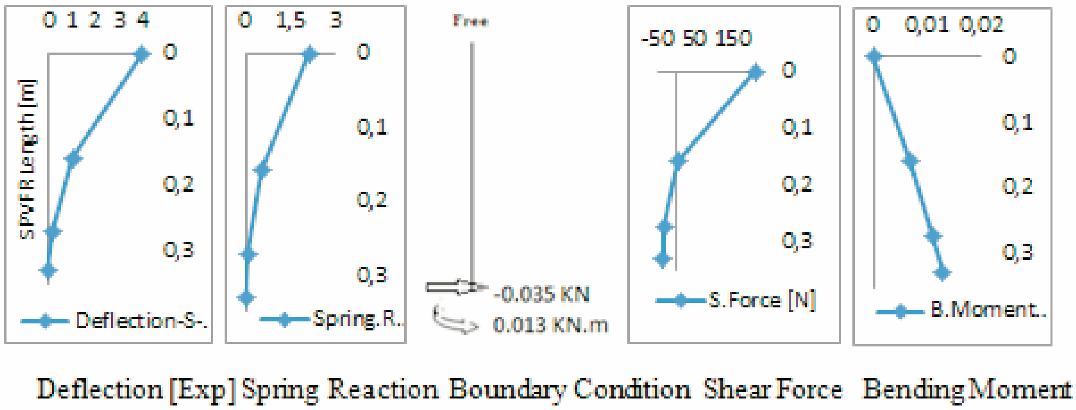

Figure 4.9. Deflection, Spring Reaction, Boundary Condition, Shear Force and Bending Moment Along SPVFR Placed on 3K-Cyclic.

4.2.1. The Deflection of the SPVFR With Time

The deflection-time relationship of the pile model during the test gives an idea about the deflection behavior of the pile until it reached its maximum deflection value 4 mm at the top and mid point of the pile, as shown in Figure 4.10 to Figure 4.12. For the pile model placed on linear spring 1K, the deflection of the pile is given for each 50 second. It's observed that, critical value of deflection is observed in the first 50 second, so additional deflection-time relationship between (0-50) second is plotted. The deflection-time relationship of the pile model subjected to lateral load at mid point is presented. Its observed that between (0-15) second no major changes in LVDT reading.

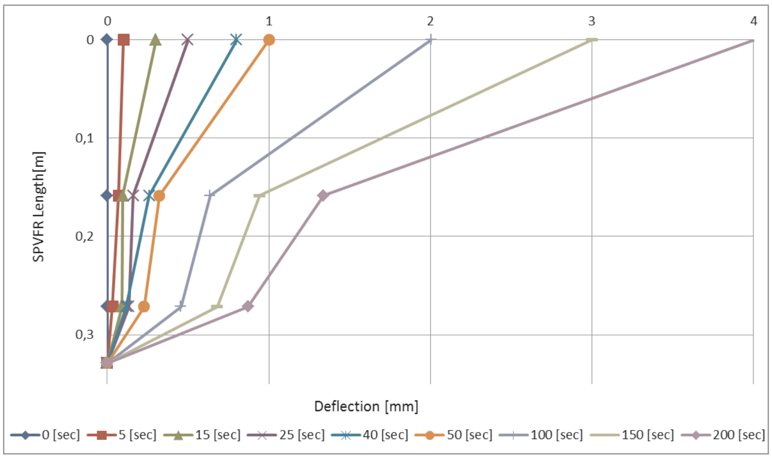

Figure 4.10. Deflection-Time Curves for SPVFR 1K Under Static Load.

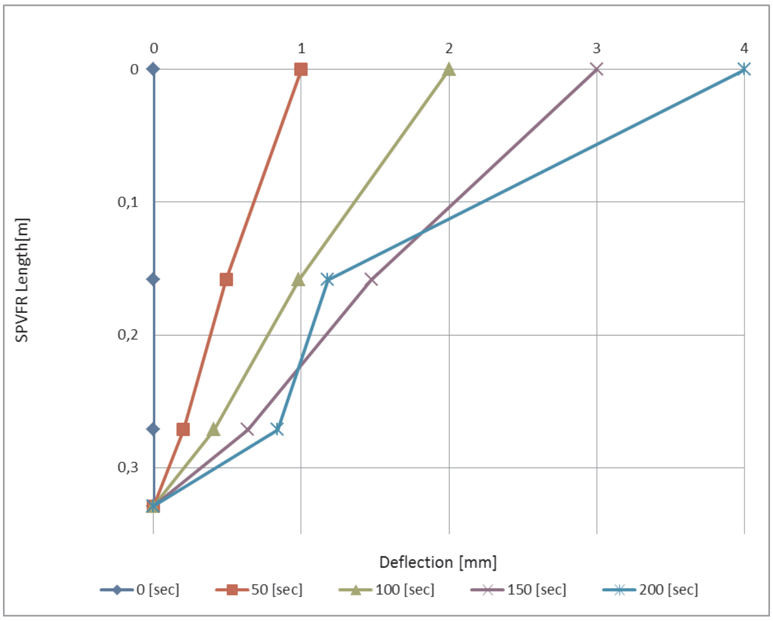

Figure 4.11. Deflection-Time Curves for SPVFR 2K Under Static Load.

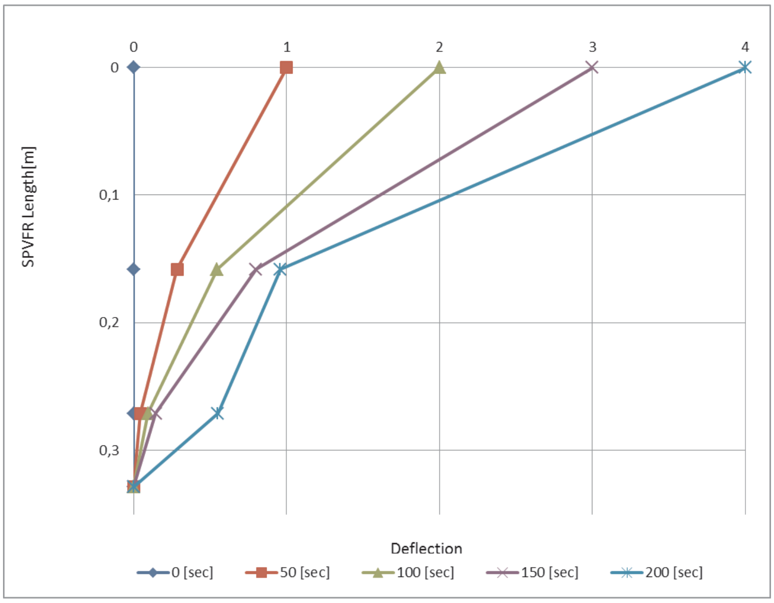

Figure 4.12. Deflection-Time Curves for SPVFR 3K Under Static Load.

4.3. The Slope of the SPVFR Under Static Load at Pile Head using Non-Dimensional Analysis Method

The slope of the SPVFR is calculated using the analysis method with non-dimensional chart as illustrated in the previous chapter. The slope is determined for the pile model placed on elastic springs (1K, 2K and 3K) under static point load at pile head.

4.3.1. The Slope of the SPVFR Subjected to Static Lateral Load at Top-Point (1K, 2K and 3K)

The slope of the SPVFR placed on elastic springs 1K at the top of the pile is $3.95 \text{x} 10^{-3}$ degree and zero value at the pile tip. The slope value along the pile length are shown in Figure 4.13. In addition, the slope of the pile model placed on elastic spring 2K is $9.61 \text{x} 10^{-3}$ degree at the top of the pile and zero value at the pile tip. The slope values along the pile length are shown in Figure 4.14. For the pile model placed on elastic spring 3K, the maximum slope value is 0.0133 degree which is calculated at the top of the pile, whereas the slope at the tip of the pile is zero as shown in Figure

4.15.

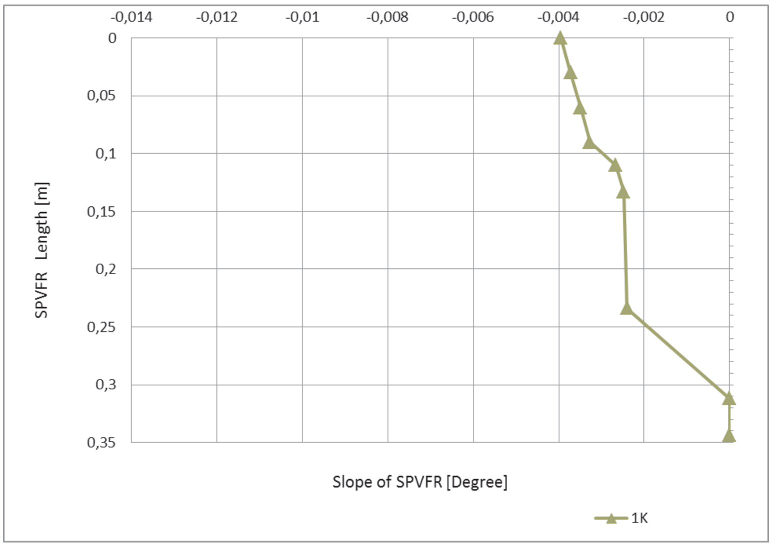

Figure 4.13. Slope of the SPVFR Under Static Load at Pile Head 1K (4N/mm).

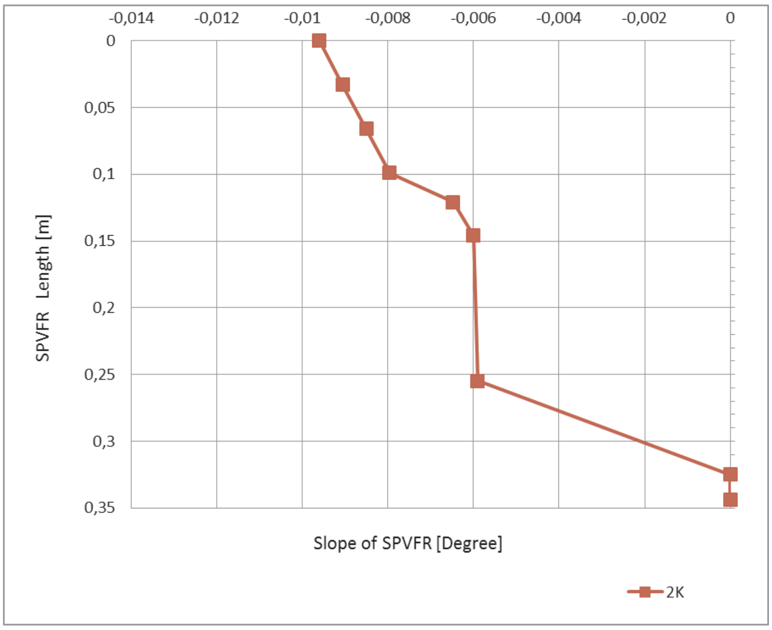

Figure 4.14. Slope of the SPVFR Under Static Load at Pile Head 2K (8N/mm).

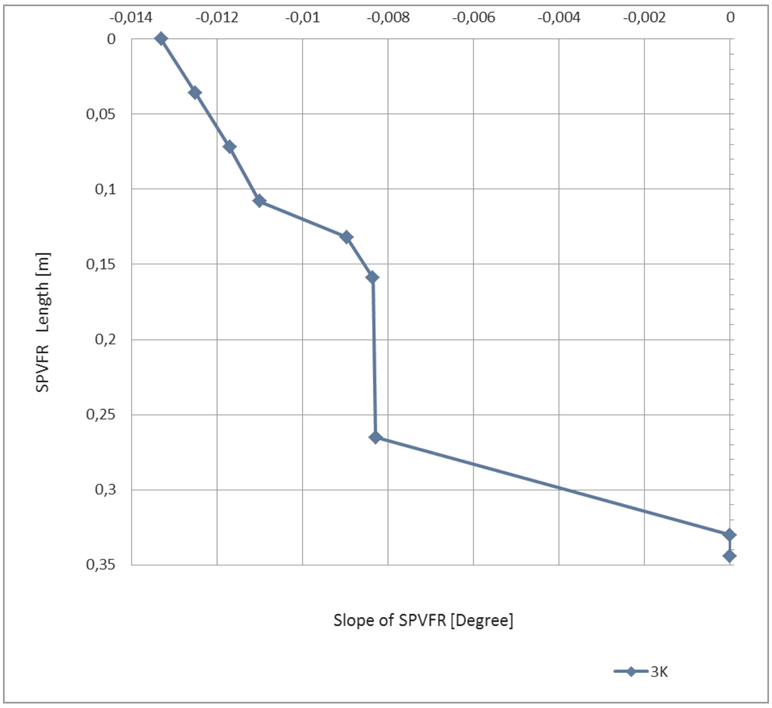

Figure 4.15. Slope of the SPVFR Under Static Load at Pile Head 3K (12N/mm).

4.4. Bending Moment of the SPVFR Under Static Load at Pile Head

Bending moment of the SPVFR is calcuated using analysis with non-dimensional chart as illustrated in the previous chapter. The bending moment is plotted along the pile length for different elastic springs (1K, 2K and 3K).

4.4.1. The Bending Moment of the SPVFR Subjected to Static Lateral Load at Top-Point (1K, 2K and 3K)

The value of bending moment at the top of the SPVFR placed on elastic springs 1K is zero since there is no external moment. The maximum value of bending moment is 6.12x10^{-3} KNm at position 2D from the pile top. At the tip of the pile the bending moment is zero as shown in Figure 4.16. In addition, for the pile model placed on elastic springs 2K, the maximum value of bending moment is 0.014 KNm at 2.5D from the top of the pile. On the other hand, zero values of bending moment are considered at the top and tip of the pile, as shown in Figure 4.17. For the pile model placed on elastic springs 3K, the zero value of bending moment calculated at the top and tip of the pile, whereas the high value is 0.0173 KNm, which located at 2.7D from the pile head, as shown in Figure 4.18.

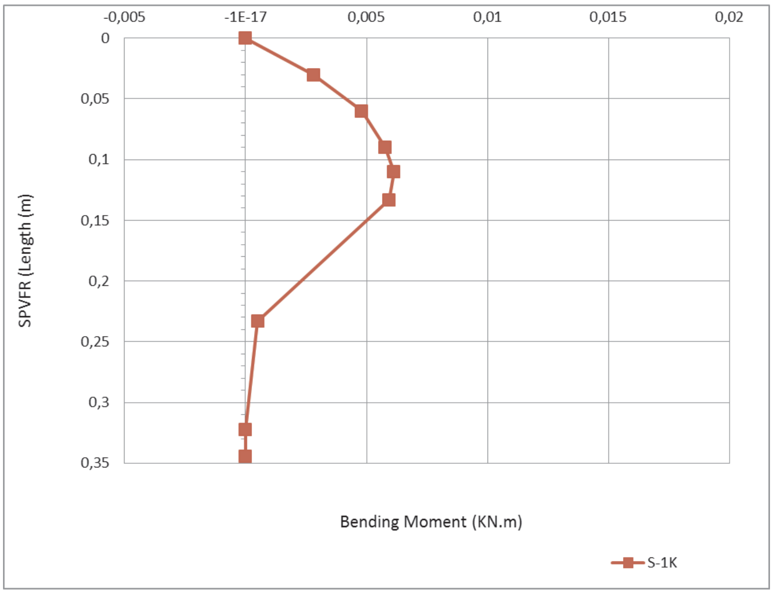

Figure 4.16. The Bending Moment Along SPVFR Under Static Load at Pile Head 1K (4N/mm).

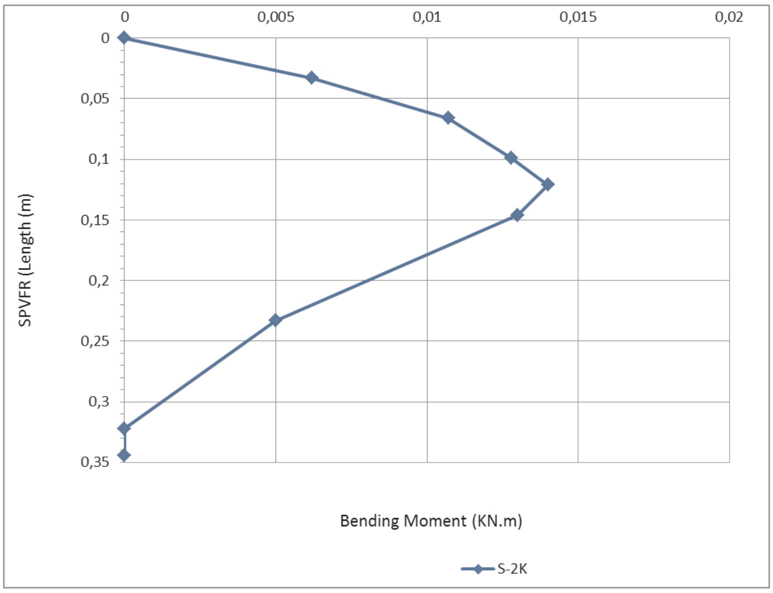

Figure 4.17. The Bending Moment Along SPVFR Under Static Load at Pile Head 2K (8N/mm).

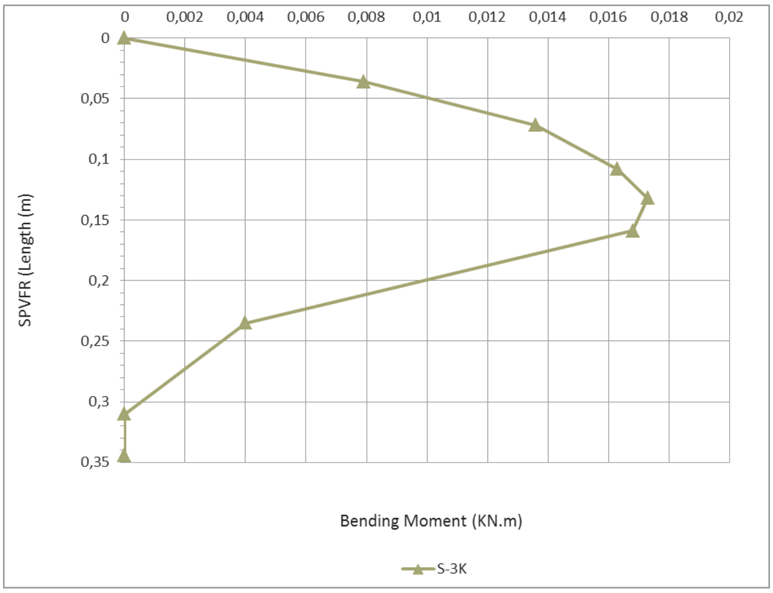

Figure 4.18. The Bending Moment Along SPVFR Under Static Load at Pile Head 3K (12N/mm).

4.5. Shear Force of the SPVFR under Static Load at Pile Head

Shear force of the SPVFR is estimated using analysis with non-dimensional chart as illustrated in the previous chapter. The shear force plotted along the pile length for different elastic springs (1K, 2K and 3K).

4.5.1. The Shear Force of the SPVFR Subjected to Static Lateral Load at Top-Point (1K, 2K and 3K)

According to SPVFR placed on elastic springs 1K, the maximum shear force is 0.088 KN at the top of the pile, and zero shear forces are calculated at the tip of the pile, as shown in Figure 4.19. In addition, for the pile model placed on elastic springs 2K, the highest value of shear force is 0.177 KN at the top of the pile, whereas the minimum value of shear forces are calculated at the tip of the pile. Figure 4.20 gives the shear force distribution along the pile length. For the the pile model placed on elastic springs 3K, the minimum values of shear forces are calculated at the tip of the pile, on the other hand, the maximum value of shear force is calculated at the top of the pile, which is 0.206 KN. Figure 4.21 shows the shear forces diagram along the pile length.

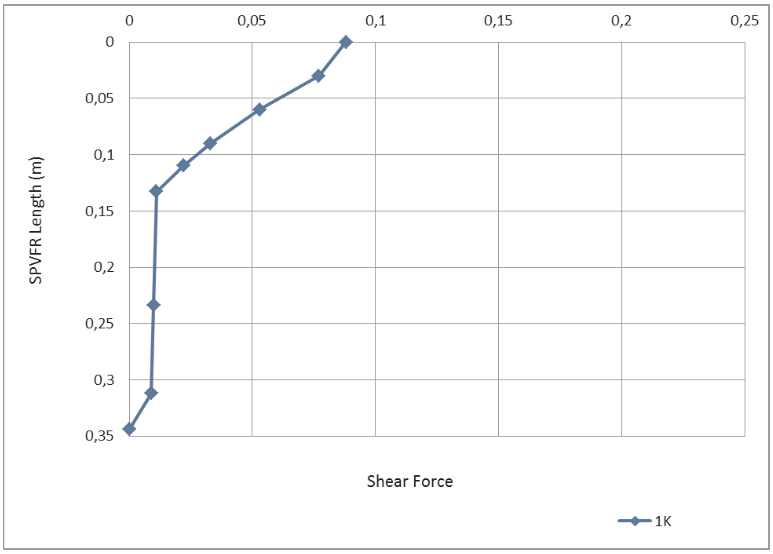

Figure 4.19. The Shear Force Along SPVFR Under Static Load at Pile Head 1K (4N/mm).

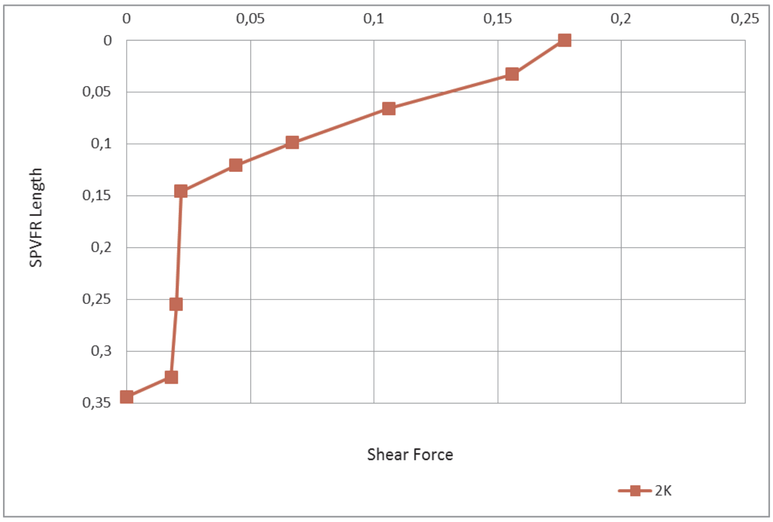

Figure 4.20. The Shear Force Along SPVFR Under Static Load at Pile Head 2K (8N/mm).

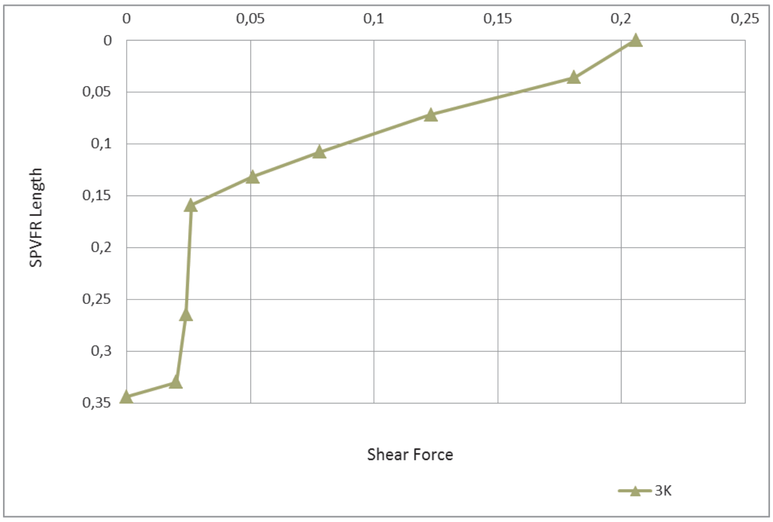

Figure 4.21. The Shear Force Along SPVFR Under Static Load at Pile Head 3K (12N/mm).

4.6. The Deflection of the SPVFR Subjected to Static Lateral Load at Top-Point

Deflection of the SPVFR is evaluated experimentally by using LVDT at three positions, along the pile length, which are 0.329 m from the tip of the pile (segment No.15 /LVDT1), 0.171 m from the tip of the pile (segment No.8 /LVDT2) and at 0.058 m from the tip of the pile (segment No.3 /LVDT3). The deflection is plotted along the pile length for different elastic springs (1K, 2K and 3K).

4.6.1. The Deflection of the SPVFR (1K, 2K and 3K)

The SPVFR is loaded for maximum deflection of 4 mm at the top of the pile (segment number 15) for all elastic springs (1K, 2K and 3K). According to the pile model placed on elastic springs 1K, deflection of 1.32 mm is measured at segment number 8 and 0.87 mm at segment number 3 as shown in Figure 4.22. For the pile model placed on elastic springs 2K, the deflection of 1.18 mm is measured at segment number 8 and 0.84 mm at segment number 3, Figure 4.23. Shows the deflection diagram along the pile model length. According to the pile model placed on elastic springs 3K, the deflection of 0.96 mm is measured at segment number 8, whereas 0.55 mm is memasured at segment number 3. According to Figure 4.24, the deflection diagram along the pile model length is plotted.

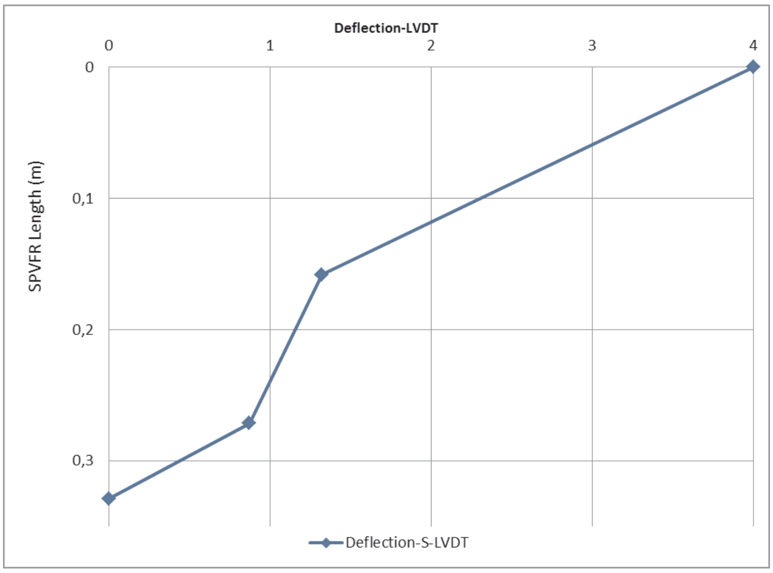

Figure 4.22. Deflection Diagram Along SPVFR 1K (4N/mm).

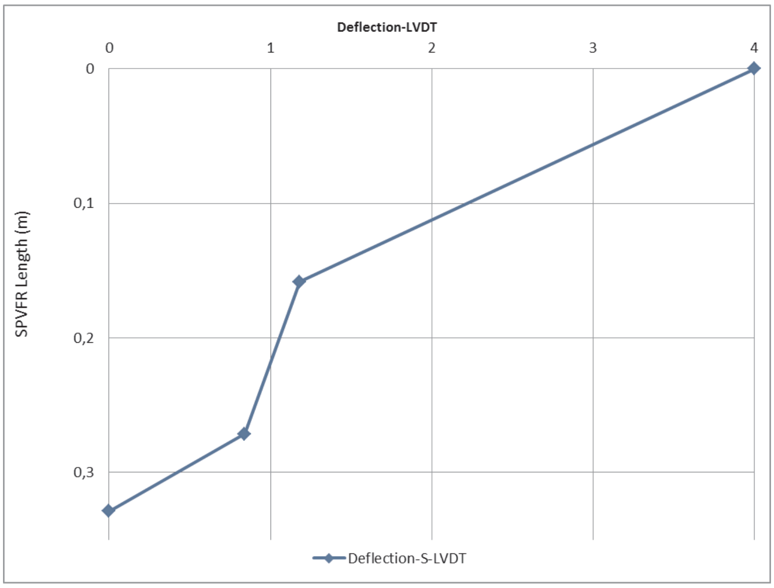

Figure 4.23. Deflection Diagram Along SPVFR 2K (8N/mm).

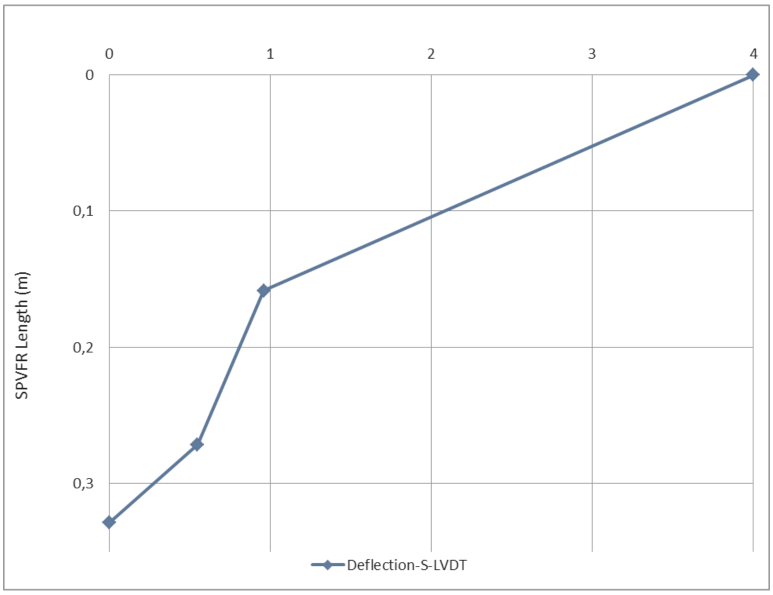

Figure 4.24. Deflection Diagram Along SPVFR 3K (12N/mm).

4.7. The P-Y Curves of the SPVFR 3K Under Static/Cyclic Loading at Mid-Point

4.7.1. P-y Curves of the SPVFR on Elastic Foundation 3K

The p-y curves of the SPVFR at 0.058 mm from the pile tip give spring reaction of 0.99 N/mm which corresponds to 1.86 mm as shown in Figure 4.25. In addition, the p-y curves of the pile model at 0.171 m from the pile tip produce spring reaction of 2.1225 N/mm which corresponds to 4 mm as presented in Figure 4.26. According to the p-y curves of the pile model 3K at 0.329 m from the pile tip, the spring reaction increases up to 1.11 N/mm which corresponds to 2.1 mm deflection. Figure 4.27 shows the p-y curves of the pile model based on linear springs 3K.

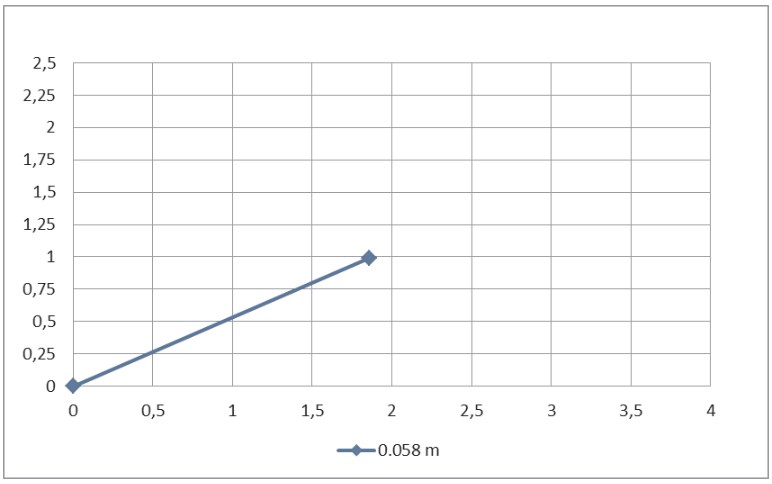

Figure 4.25. P-y Curves for 3K at Segment Number 3 (0.058 m).

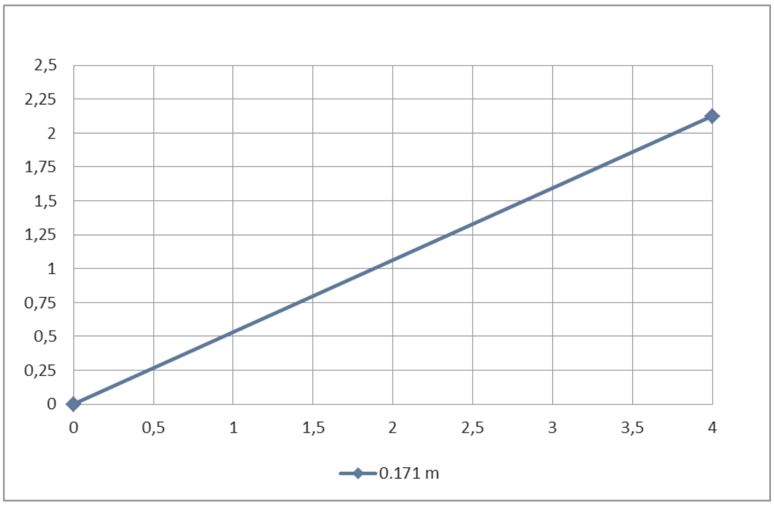

Figure 4.26. P-y Curves for 3K at Segment Number 8 (0.171 m).

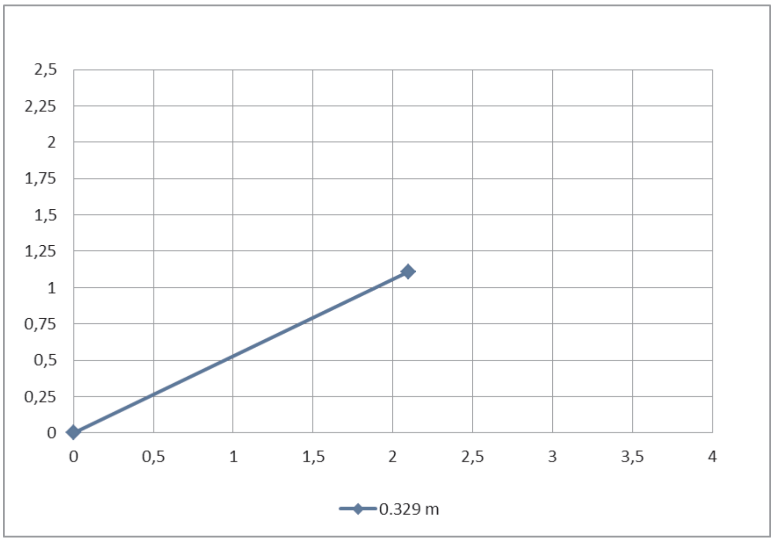

Figure 4.27. P-y Curves for 3K at Segment Number 15 (0.329 m).

4.7.2. The Slope of the SPVFR Under Static-Cyclic Loading Mid-Point 3K

The maximum slope value of the pile model subjected to lateral static load at mid-point of the pile length is 7.42 x 10^{-3} degree at the ends of the pile model, whereas at the mid-point, the slope is zero. Figure 4.28 shows the slope distribution along the pile model. For the same pile model subjected to cyclic loading at mid-point, the maximum slopes are recorded at the pile ends 7.46 x 10^{-3} degree; and zero slope at mid-point of the pile is calculated. Figure 4.29 illustrates the slope variation along the pile model.

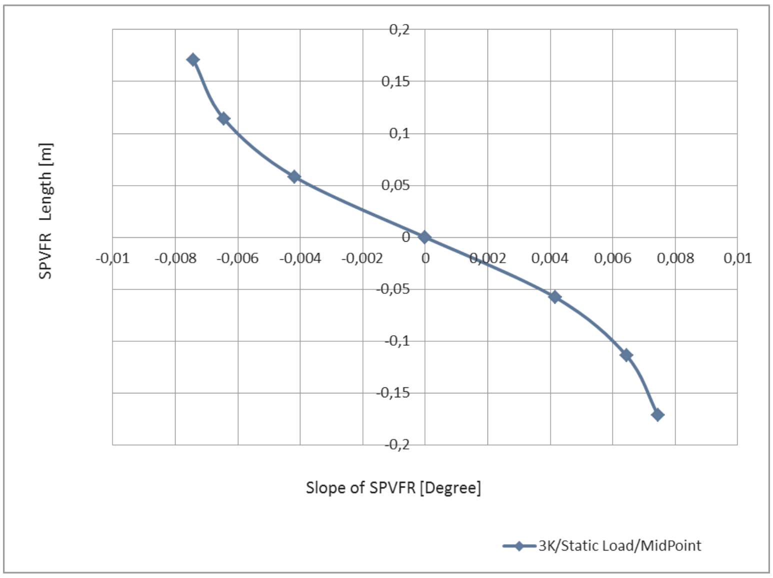

Figure 4.28. The Slope Variation Along the SPVFR Length (Static Loading).

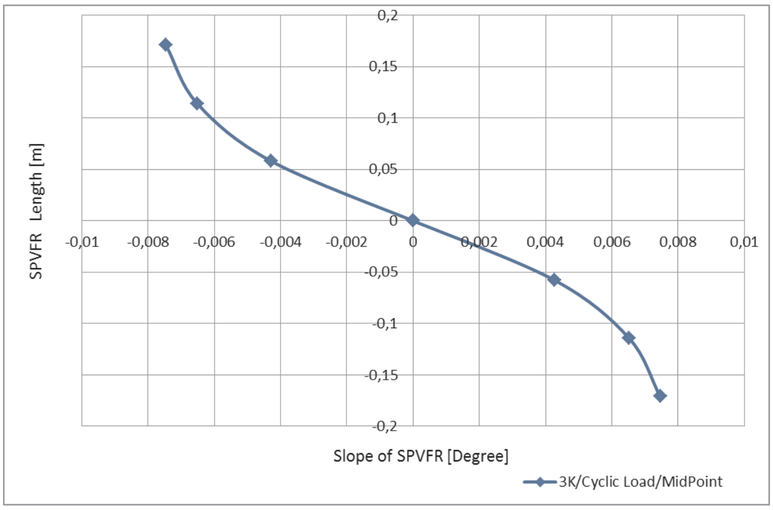

Figure 4.29. The Slope Variation Along the SPVFR Length (Cyclic Loading).

4.7.3. Bending Moment of the SPVFR (Static-Cyclic/Mid-Point/3K)

The peak value of bending moment is 0.0355 KN.m at mid-point of the pile model. The bending moment decreases gradually until it reaches zero at the ends of the pile model. The bending moment distribution of the pile model is shown in Figure 4.30. For the pile model subjected to cyclic loading at mid-point, the maximum bending moment at mid-point is 0.0344 KN m.; and the minimum value is zero at the pile ends. Figure 4.31 shows the bending moment distribution along the pile model.

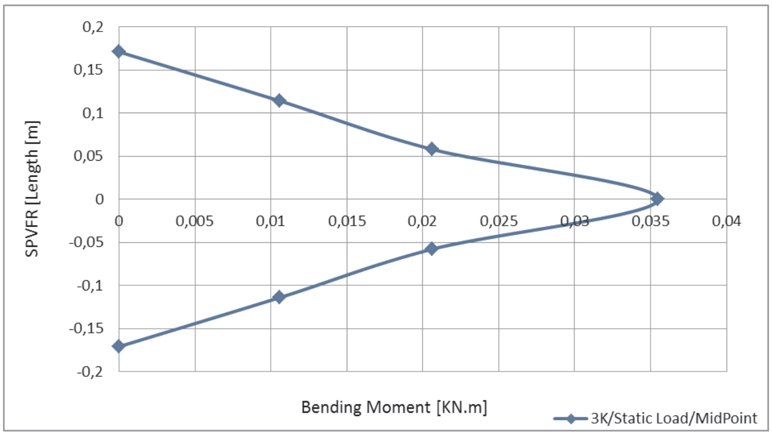

Figure 4.30. The Bending Moment Variation Along the SPVFR Length (Static Loading).

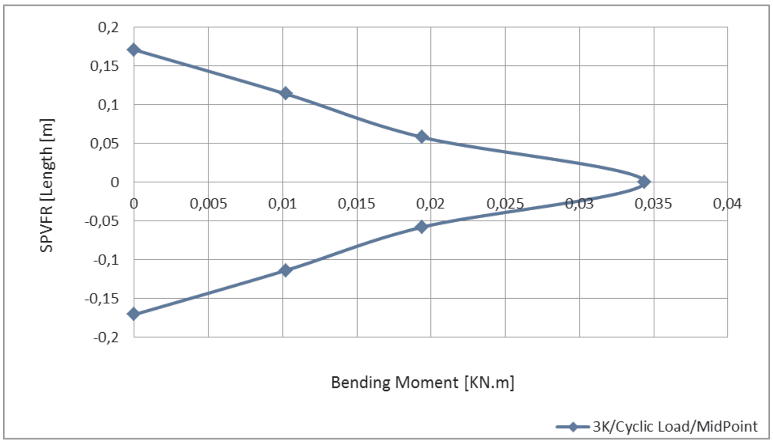

Figure 4.31. The Bending Moment Variation Along the SPVFR Length (Cyclic Loading).

4.7.4. The Shear Force of the SPVFR (Static-Cyclic/Mid-Point/3K)

The peak value of shear force of pile model subjected to static load is 291.5 N at the mid-point of pile length. The value of shear forces decreases gradually until it reaches the minimum value zero at the pile ends. Figure 4.32 gives the shear force distribution along the pile model. For the pile model under cyclic loading, the maximum shear force is 289.5 N at mid-point of pile length, the shear force reaches zero at the pile ends as shown in Figure 4.33.

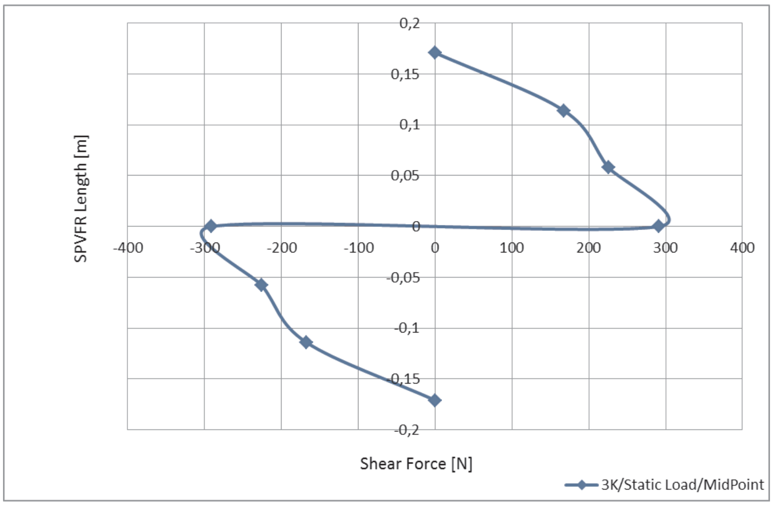

Figure 4.32. The Shear Force Variation Along the SPVFR Length (Static Loading).

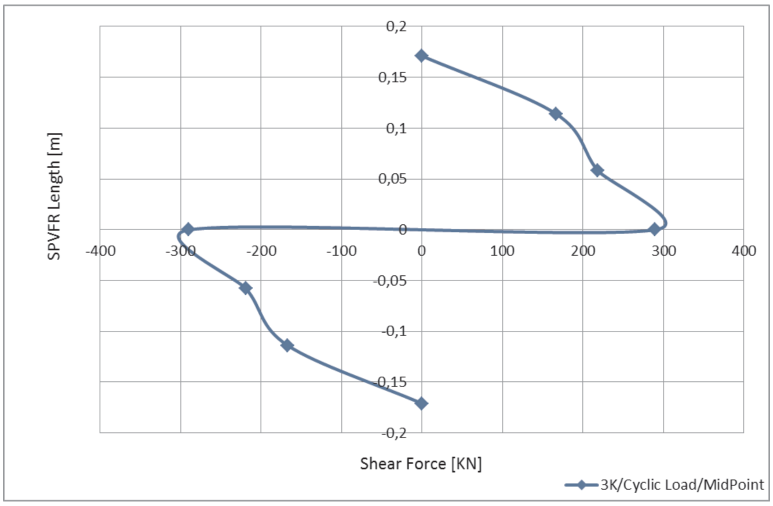

Figure 4.33. The Shear Force Variation Along the SPVFR Length Cyclic Loading).

4.8. Stress Distribution on the Interface Segments of the SPVFR during Static and Cyclic Loading

In the first part, the stress distributions due to prestress forces 2250 N of the pile model are evaluated. In the second part, the stress distribution due to prestress force 2250 N and lateral static load at top-point of the pile model is estimated. Finally, stress distributions due to prestress force 2250 N and cyclic load at top-point of the pile model are evaluated. The prescale films located in five different positions (0, 90.5 mm, 181 mm, 271.5 mm, and 338 mm from the base of the pile model) as shown in Figure 4.34 to measure stress values for different loading condition.

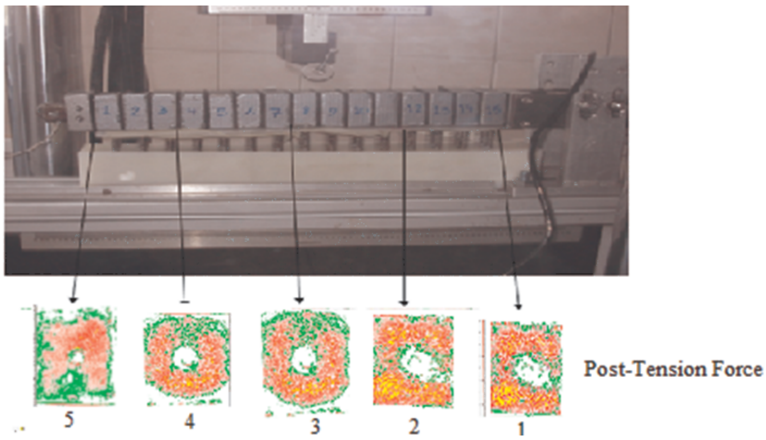

Figure 4.34. The Position of Prescale Film on SPVFR.

4.8.1. Stress Distribution Due to Prestress Force

The average stress distribution of the SPVFR subjected to prestress force 2250 N is 1.041 MPa. In the lower part of prescale film, the average stress is 1.036, whereas in the upper part is 1.046 MPa. Figure 4.35 gives details about stresses of the pile model under prestress forces only.

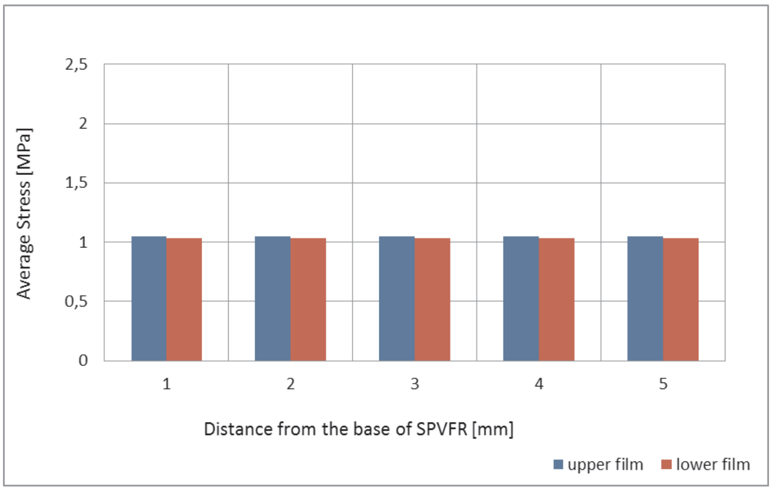

Figure 4.35. Stress Distributions Along SPVFR Due to Post-Tension Forces.

4.8.2. Stress Distribution Due to Static Load at Top-Point of the SPVFR

The results of stress distribution of the SPVFR subjected to lateral static load at top-point are presented. The stress in the lower part of the pile model is 1.58 MPa and in the upper part is 1.34 MPa. Due to the loading condition, the SPVFR develops concave curve. The lateral force of 206 N is recorded corresponding to maximum deflection of 4 mm at top-point of the pile model. The stress values of five prescale films are recorded; and the average stress is 1.46 MPa as shown Figure 4.36 and Figure 4.37.

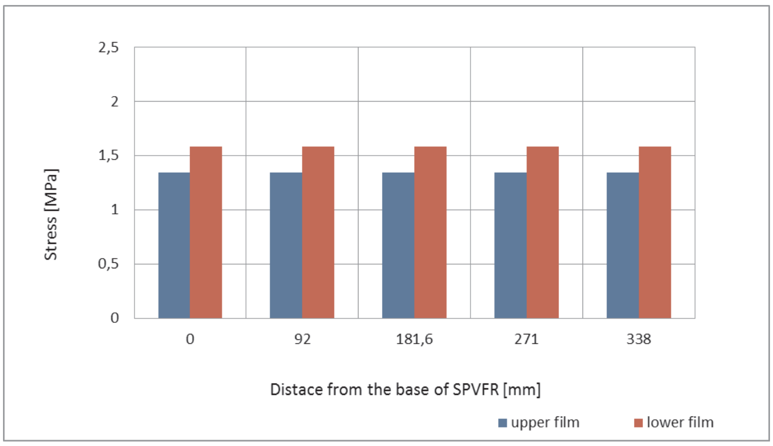

Figure 4.36. Stress Distributions Along SPVFR Due to Post-Tension Forces and Static Load at Top-Point.

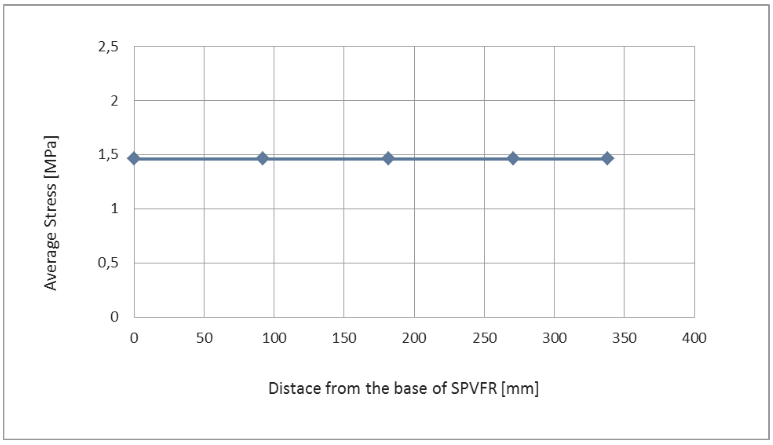

Figure 4.37. Average Stress Distributions Along SPVFR Due to Post-Tension Forces and Static Load at Top-Point.

4.8.3. Stress Distribution Due to Cyclic Load at Top-Point of the SPVFR

The results of stress distribution of the SPVFR subjected to lateral cyclic loading at top-point of the pile model are presented Figure 4.38. The stress distribution in the upper part of prescale film is 1.32 MPa and in the lower part is 1.46 MPa. Lateral forces of 200 N are recorded corresponding to maximum deflection of 4 mm at top-point of the pile model. According to the test results of the SPVFR subjected to lateral cyclic load at tip- point of the pile model, a range of compressive stress at prescale films are recorded; and the average stress of 1.394 MPa are calculated as shown in Figure 4.39.

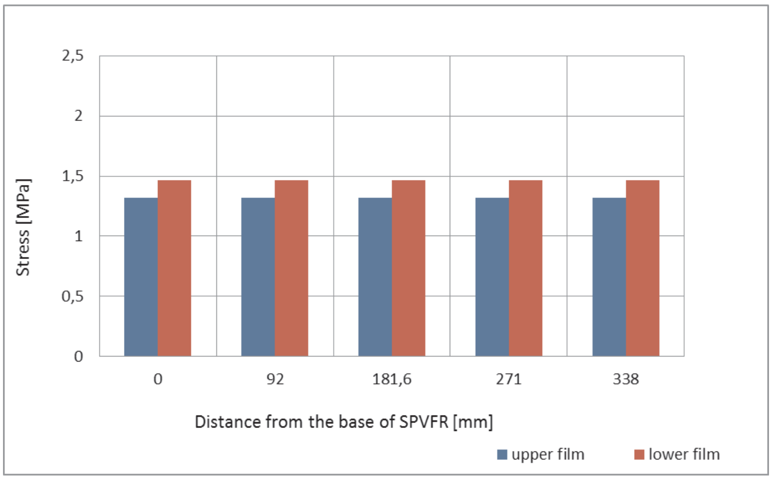

Figure 4.38. Stress Distributions Along SPVFR Due to Post-Tension Forces and Cyclic Load at Top-Point.

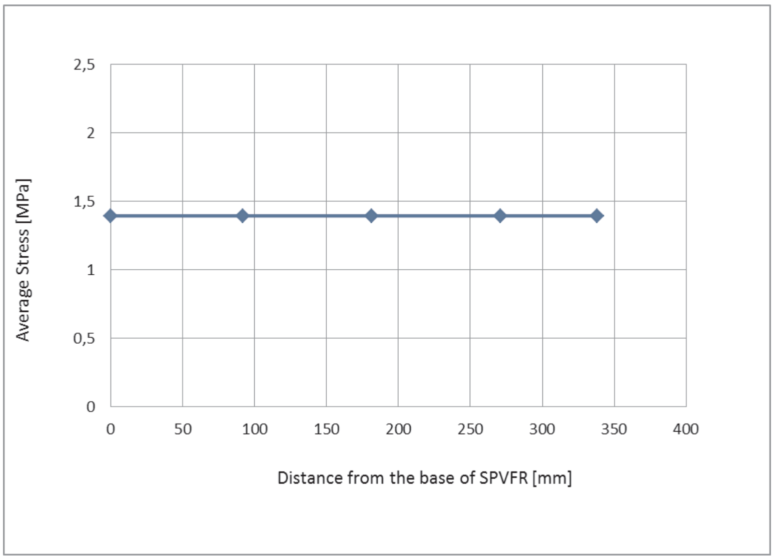

Figure 4.39. Averages Stress Distribution on SPVFR Due to Post-Tension Forces and Cyclic Load at Top-Point.

5. EVALUATION OF TEST RESULTS

5.1. Flexural Rigidity of the SPVFR

To calculate the flexural rigidity of the pile model from experimental data a three point bending test is conducted. In this test, stress-strain curve is constructed, and EI is calculated. Figure 5.1 illustrates the stress/strain relationship of the pile model and the mortar beam.

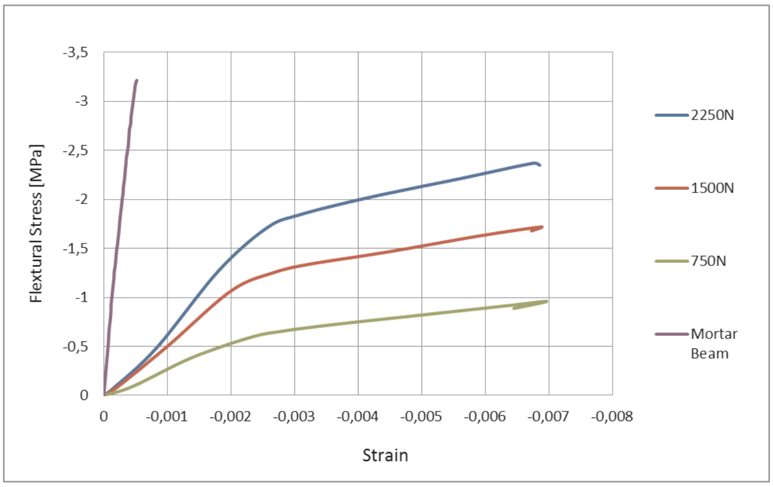

Figure 5.1. Shows Stress Strain Curves of the SPVFR.

The failure of segmental beam with post-tension force 750 N occurred at flexural stress of 0.6 MPa corresponding to 0.0025 strain. The value of flexural stress at failure of the pile model with post-tension forces of 750 N is increased 2 times, 3 times and 5.5 times when using segmental pile with post-tension force of 1500 N, segmental pile with post-tension force of 2250 N and Mortar beam respectively. The strain of the pile model with post-tension force of 750 N at failure is 0.0025, which 5 times more than the strains of mortar beam at failure. By increasing the post-tension force to 2250 N the strain value decreased up to 4 times the strain of beam mortar at failure. To calculate the flexural rigidity of segmental beam with post-tension force 2250 N, the general deflection equation of simple support beam subject to point load at the middle of the span is used:

$$\delta = \left[PL^3/48EI \right] \tag{5.1}$$

Table 5.1. Shows Numerical Values of Flexural Rigidity of the SPVFR.

[P]KN	[δ]Deflection [mm]	[L]Beam Length [mm]	EI [KN.m^2]	EIexp[KN.m^2]	The Error (Eexp)[%]
0.16	0.15	250	0.35		
0.35	0.228	250	0.499		
0.57	0.5	250	0.36		
EIaverage	0.406			0.39	4.1

5.2. The Shear Stress/Spring Stiffness Relationship of the SPVFR (1K/2K/3K) at Top-Point

The chart of static load with 3 spring Stiffnesses (1K/2K/3K) corresponding to 1 mm, 2 mm, 3 mm and 4 mm deflection are presented, in Figure 5.2 at 4 mm deflections the static load is more than cyclic load by 3%- 6% for the three different spring stiffnesses. On the other hand a significant change in the lateral load is considered by increasing the spring constant as shown in Figure 5.2 and Figure 5.3.

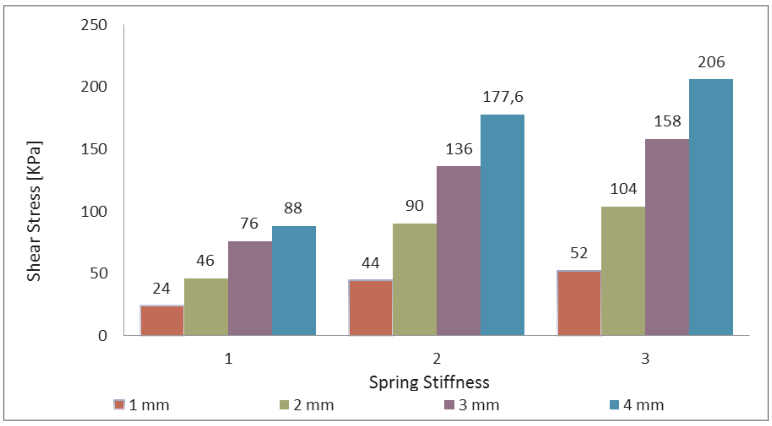

Figure 5.2. Static Load-Spring Stiffness Relationship (1:1K (4 N/mm), 2: 2K (8 N/mm) and 3:3 K (12 N/mm)) (Top-Point).

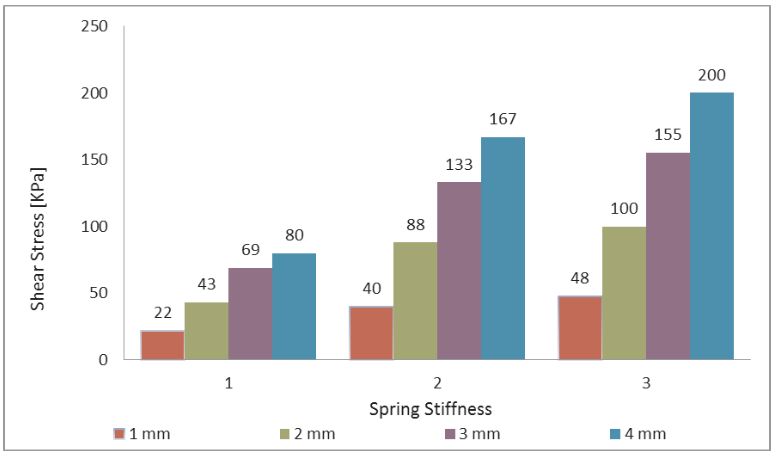

Figure 5.3. Cyclic Load-Spring Stiffness Relationship (1:1K (4 N/mm), 2: 2K (8 N/mm) and 3:3 K (12 N/mm)) (Top-Point).

5.3. P-y Curves of the SPVFR Based on Linear Springs (1K, 2K and 3K)

The p-y Curves of the SPVFR on linear springs 3K predict high value of stiffness compared to the p-y curves of the pile model 1K and 2K. For instance, the reaction force of the pile model 1K is 0.7075 N/mm, which increases two times when using the elastic spring 2K. However the reaction force of linear spring 3K is 3 times the reaction forces of elastic springs 1K Figure 5.4 shows the p-y curves of the pile model based on (1K, 2K and 3K) at 4mm deflection.

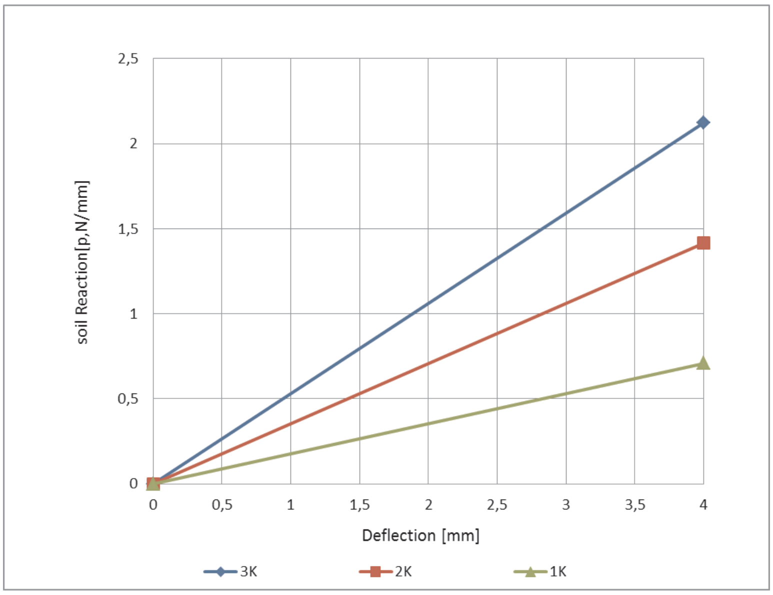

Figure 5.4. P-y Curves for SPVFR (1:1K (4 N/mm), 2: 2K (8 N/mm) and 3:3 K (12 N/mm)).

5.4. The Comparison of the Experimental Result of The SPVFR With Non-Dimensional and L-Pile Method

In this section, the value of the deflection, slope, bending moment, and shear force along the pile model calculated by using experimental data are compared with the results obtained form NDM and L-Pile Method as presented in the following Figures.

The results of the pile model placed on linear springs 1K and subjected to the static lateral load at top point up to 4 mm deflection are presented in Table 5.2. The experimental data shows that at 4 mm deflection, the maximum value of shear force is 88 N, whereas for the same condition using L-Pile the maximum value of deflection is 5.14mm corresponding to the same value of shear force 88N. The non-dimensional method gives low value of deflection 0.54 mm corresponding to 88 N at the top point. It implies that the predicted pile deflection shape value from the L-Pile analysis agrees well with that from experimental modeling, unlike the results that are obtained from NDM.

The following tables and figures illustrate that the NDM overestimated the value of the bending moment. On the other hand, the experimental model analysis and L-Pile agree well in term of deflection shape. Figure 5.5 to Figure 5.7 and Table 5.3 to Table 5.5 compared the relationship between experimental model analysis to L-Pile and NDM.

Table 5.2. Deflection, Slope, Bending Moment, Shear Force and Spring Reaction of SPVFR-1K/S.

Analysis Methods	Deflection (mm)	Position	Slope (Degree)	Position	Bending.M (KN.m)	Position	Shear Force (N)	Position
Exp	Min: 0 Max: 4	Tip Tip	Min: -0.059 Max: -0.2	Top Tip	Min:0 Max:0.01	Top Tip	Min: 0 Max: 88	Tip Top
L.Pile	Min: 0 Max: 5.13	Tip Top	Min: -.045 Max :.45	Top Tip	Min: 0 Max:0.061	Top and Tip 3D	Min:0 Max: 88	Tip Top
NDM	Min: 0 Max: 0.52	Tip Top	Min:0 Max:-0037	Top Tip	Min:0 Max:0.068	Top and Tip 3D	Min:0 Max: 88	Tip Top

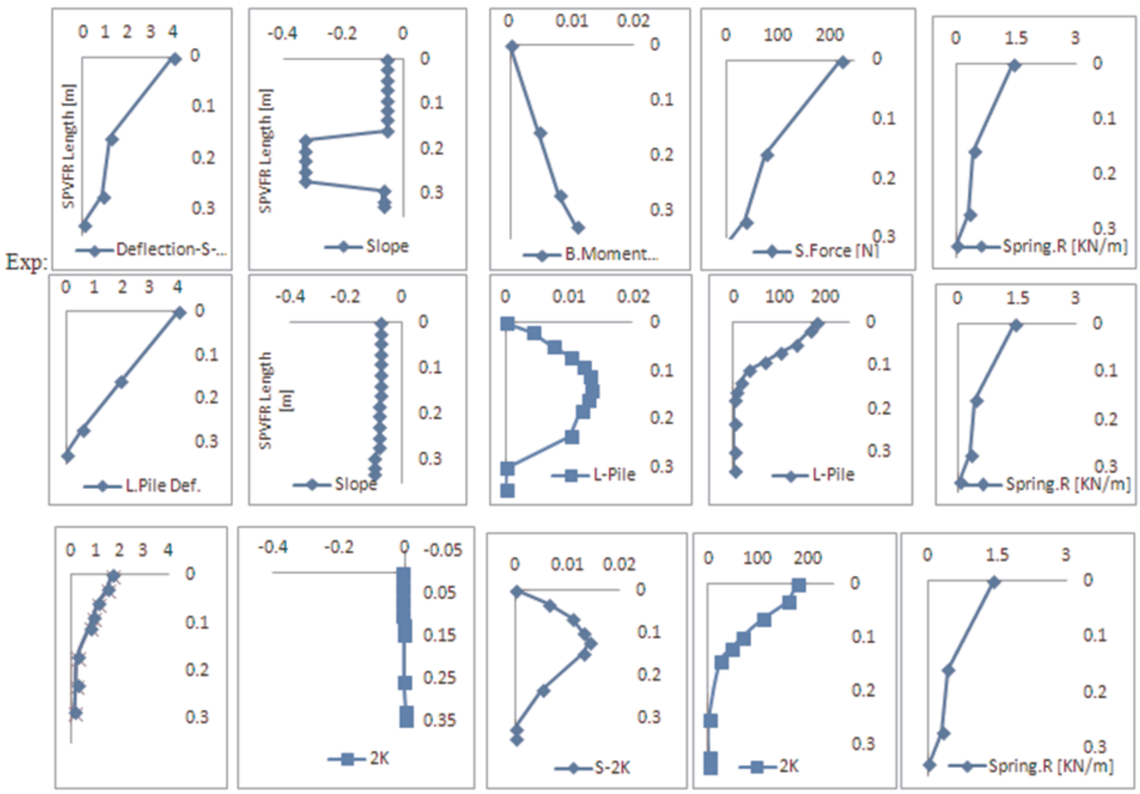

Figure 5.5. Deflection, Slope, Bending Moment, Shear Force and Spring Reaction of SPVFR-1K/S-(Exp-L.Pile-NDM).

Table 5.3. Deflection, Slope, Bending Moment, Shear Force and Spring Reaction of SPVFR-2K/S.

Analysis Methods	Deflection (mm)	Position	Slope (Degree)	Position	Bending.M (KN.m)	Position	Shear Force (N)	Position
Exp	Min: 0 Max: 4	Tip Tip	Min:-.057 Max:-0.33	Top Tip	Min:0 Max:0.01	Top Tip	Min:0 Max:177	Tip Top
L.Pile	Min: 0 Max:4	Tip Top	Min:-.045 Max:-0.45	Top Tip	Min: 0 Max:0.013	Top and Tip 3D	Min:0 Max:177	Tip Top
NDM	Min: 0 Max:1.66	Tip Top	Min:0 Max:-.006	Top Tip	Min:0 Max:0.014	Top and Tip 3D	Min:0 Max:177	Tip Top

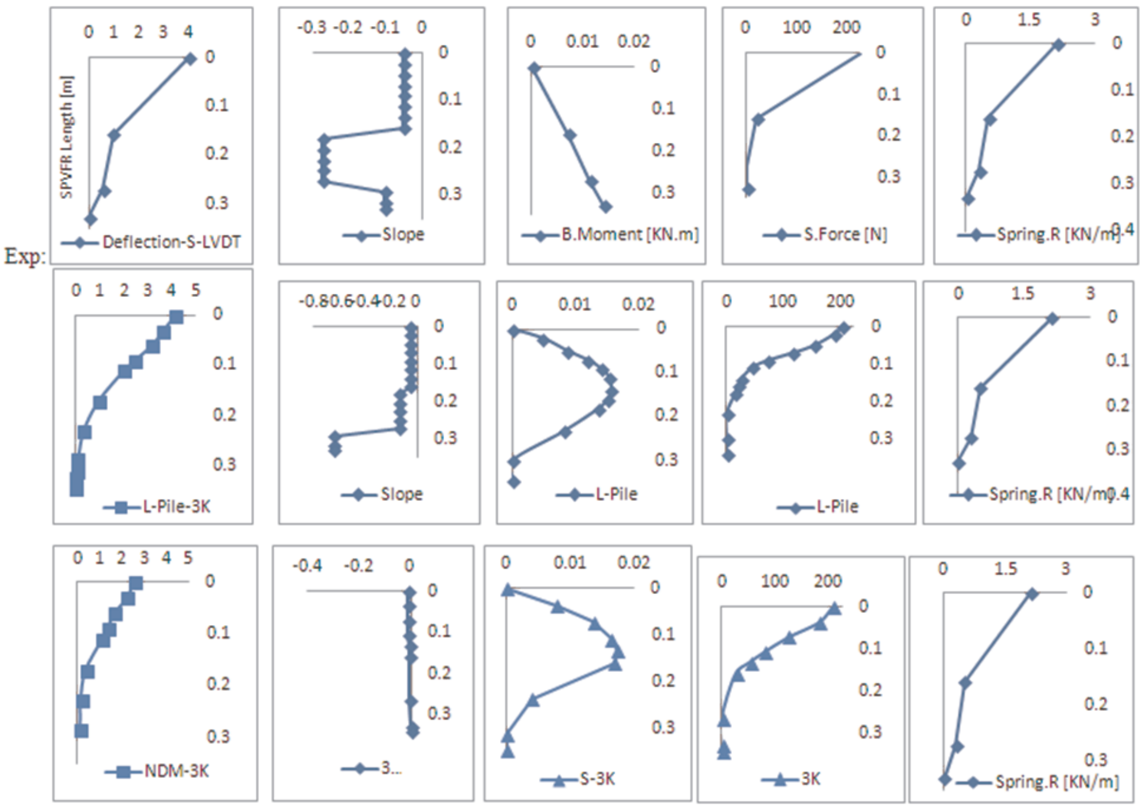

Figure 5.6. Deflection, Slope, Bending Moment, Shear Force and Spring Reaction of SPVFR-2K/S-(Exp-L.Pile-NDM).

Table 5.4. Shows the Deflection, Slope, Bending Moment, Shear Force and Spring Reaction of SPVFR-3K/S.

Analysis Methods	Deflection (mm)	Position	Slope (Degree)	Position	Bending.M (KN.m)	Position	Shear Force (N)	Position
Exp	Min: 0 Max: 4	Tip Tip	Min:-.052 Max:-0.27	Top Tip	Min:0 Max:0.01	Top Tip	Min:0 Max:206	Tip Top
P.F-Post Tension Top point Load	-	-	-	-	Min:0.0028 Max:0.018	Top Tip	-	-
L.Pile	Min: 0 Max:4	Tip Top	Min:-.049 Max:-0.63	Top Tip	Min: 0 Max:0.061	Top and Tip 3D	Min:0 Max:206	Tip Top
NDM	Min: 0 Max: 2.5	Tip Top	Min:0 Max:0.013	Top Tip	Min:0 Max:0.068	Top and Tip 3D	Min:0 Max:206	Tip Top

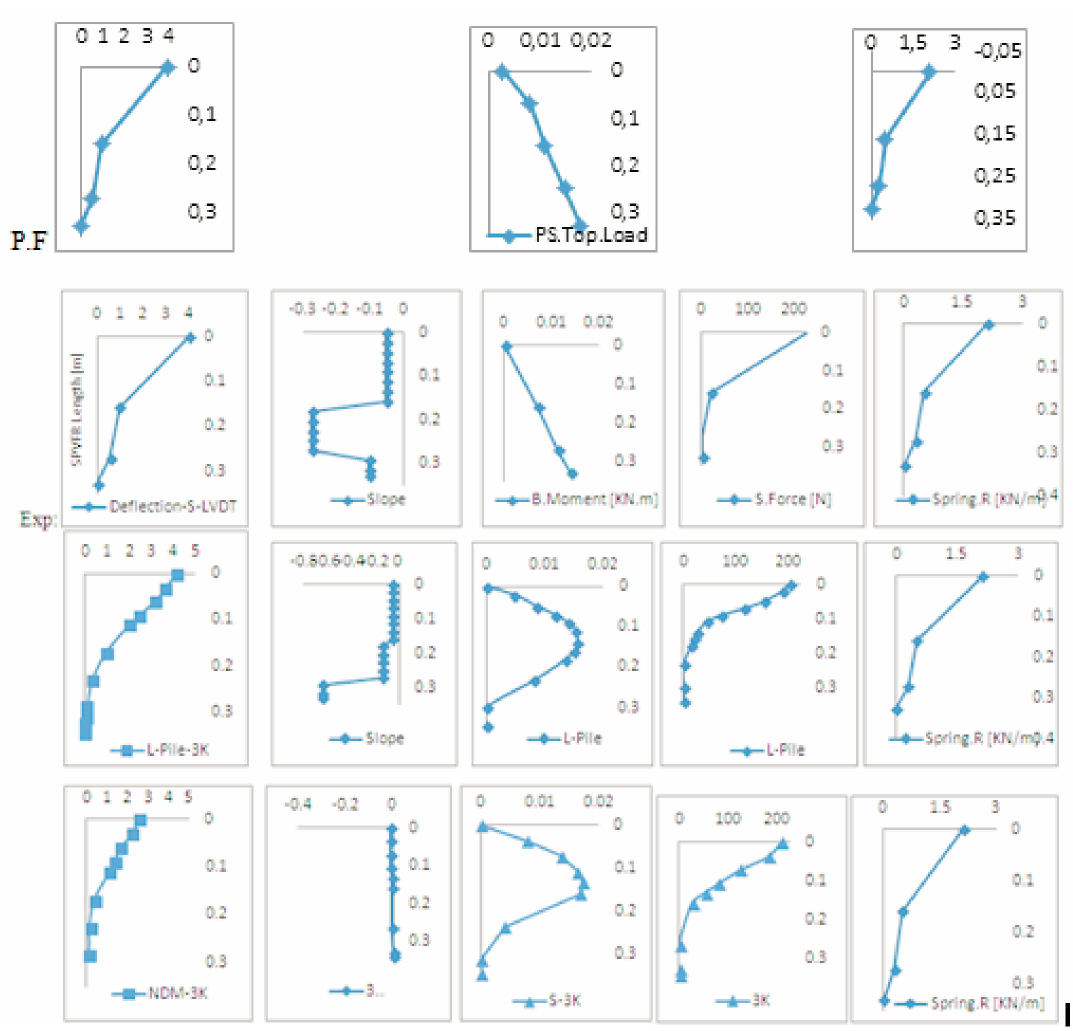

Figure 5.7. Deflection, Slope, Bending Moment, Shear Force and Spring Reaction of SPVFR-3K/S-(Exp-L.Pile-NDM), PF: prescale film.

Table 5.5. Shows the Deflection, Slope, Bending Moment, Shear Force and Spring Reaction of SPVFR-3K/Cyc.

Analysis Method	**Deflection (mm)**	**Position**	**Slope (Degree)**	**Position**	**Bending.M (KN.m)**	**Position**	**Shear Force (N)**	**Position**
Exp	Min: 0 Max: 4	Tip Top	Min:-.053 Max:-0.32	Top Tip	Min:0 Max:0.013	Top Tip	Min:0 Max:200	Tip Top
P.F-Post Top point Load	-	-	-	-	Min:0.0025 Max:0.02	Top Tip	-	-
L.Pile	Min: 0 Max: 4.15	Tip Top	Min:-.049 Max:-0.57	Tip Top	Min: 0 Max:0.0541	Top and Tip 3D	Min:0 Max:200	Tip Top
NDM	Min: 0 Max: 2.62	Tip Top	Min:0 Max:-.012	Tip Top	Min:0 Max:0.0168	Top and Tip 3D	Min:0 Max:200	Tip Top

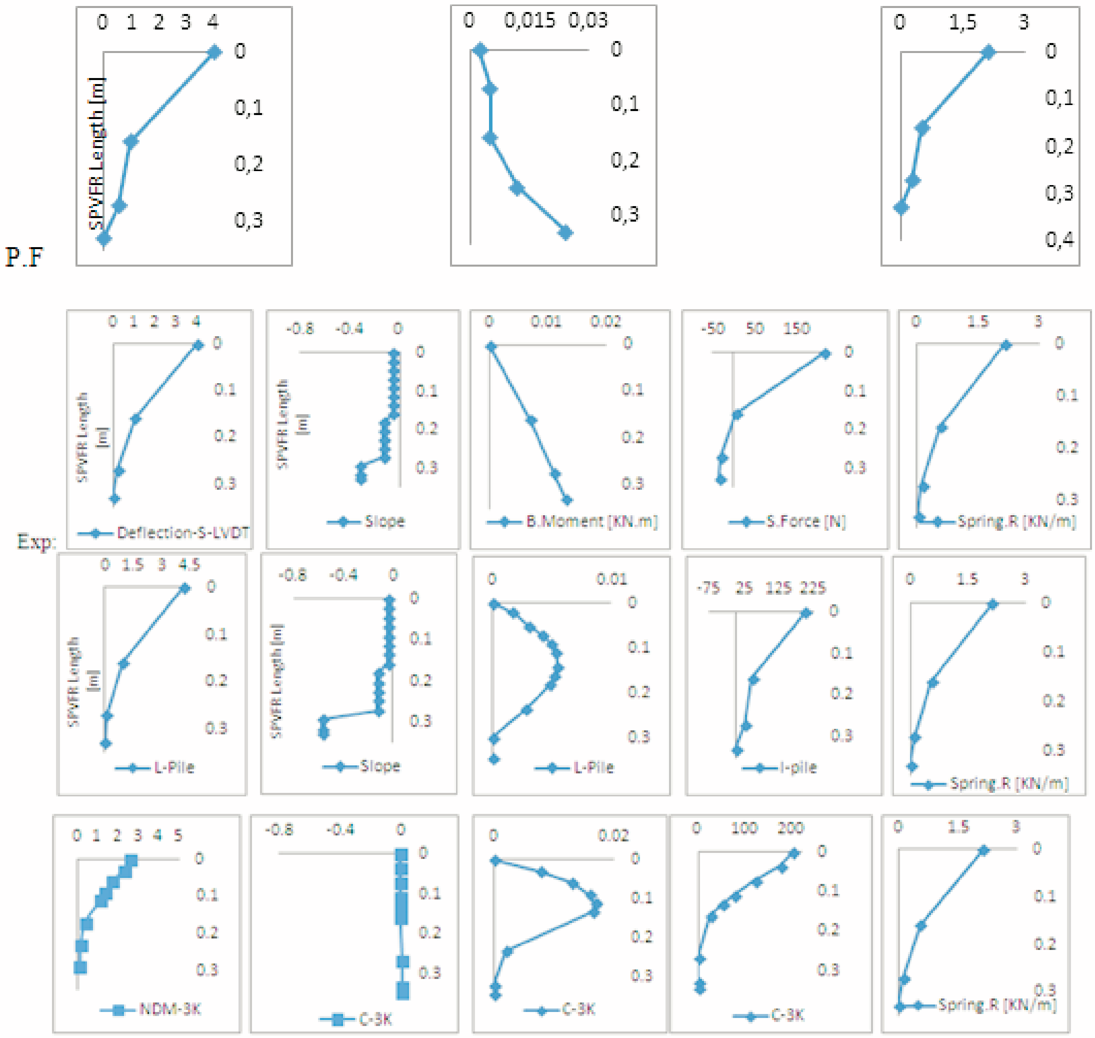

Figure 5.8. Deflection, Slope, Bending Moment, Shear Force and Spring Reaction of SPVFR-3K/C-(Exp-L.Pile-NDM), PF: prescale films.

5.5. Evaluation of Stress on SPVFR 3K Under Cyclic Load at The Top Pile Model

In this set of test, the lateral cyclic load is applied at top point of the pile model to produce maximum deflection of 4.00 mm at the top head of the pile model. The duration of cyclic tests is 200 seconds with 3 cycles/second. The prescale film at the top of the pile gives low values of stress because of the cyclic lateral load. The stresses of 0.9 MPa and 2.5 MPa are more concentrated than 0.5 MPa as shown in Figure 5.9.

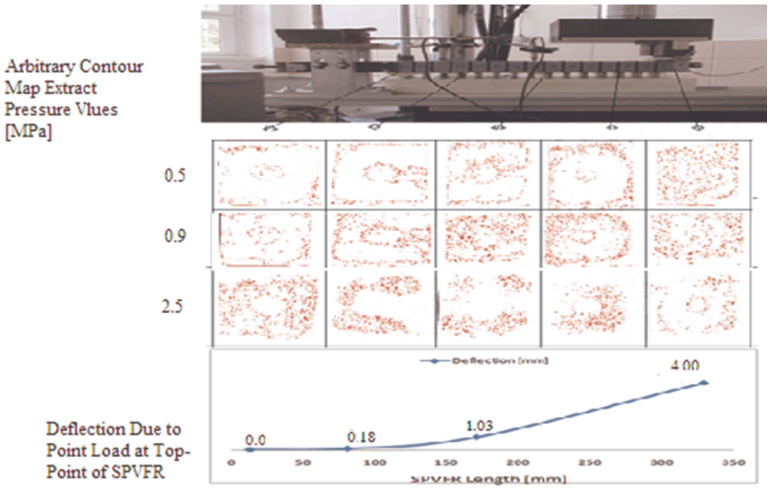

Figure 5.9. Values of Stress Distribution for Prescale Film Subjected to Prestress Forces and Lateral Cyclic Load at Top-Point of the SPVFR.

5.6. Stress Distribution on the Prescale Films along SPVFR Due to Post-Tension Force

The stress distributions are concentrated at prescale films number 1 and 2. The position of these prescale films is nearby the fixed part of the pile model as shown in Figure 5.10. It is also observed that after the prestress forces are applied to the pile model a concave shape is developed whereas the stress distribution of the lower part of the prescale films are 1.01 times more than the stress distribution of the upper part of the prescale films. The total average stress of all prescale films is 1.041 MPa. The stress distributions provided by scale details are shown in Figure 5.10.

5.7. Stress Distribution on the Prescale Films along SPVFR Due to Static Load/ Top Point

The stress distribution of prescale films number 11 and 12 are 1.66 MPa and 1.8 MPa respectively as shown in Figure 5.11. The position of these prescale films is adjacent to fixed part of the pile model. It is also observed that for each prescale film the stress is concentrated at the lower part. The stress value of a prescale film number 13 at mid-span of the pile model is 1.47 MPa. The prescale number 15 presented low level of stress 1.04 MPa. At 4 mm deflection, maximum moment of 0.012 KN.m is developed due to applied load at top point the pile model. This value of bending moment creates additional bending stress as shown in the following equation.

$$\sigma = \frac{P}{A} \pm \frac{M}{Z} \tag{5.2}$$

Where σ is the stress KN/m^2, P is the Normal force (KN), M is the moment (KNm), Z is the section modulus (m^3), A is the area (m^2)

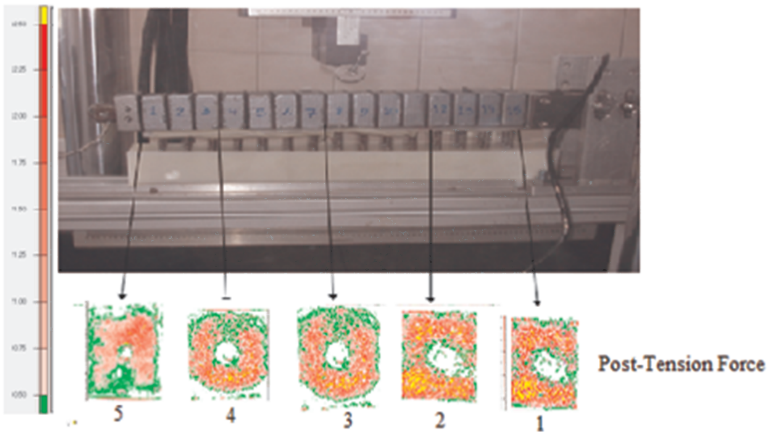

Figure 5.10. Stress Distribution of the Prescale Films Due to Post-Tension Forces.

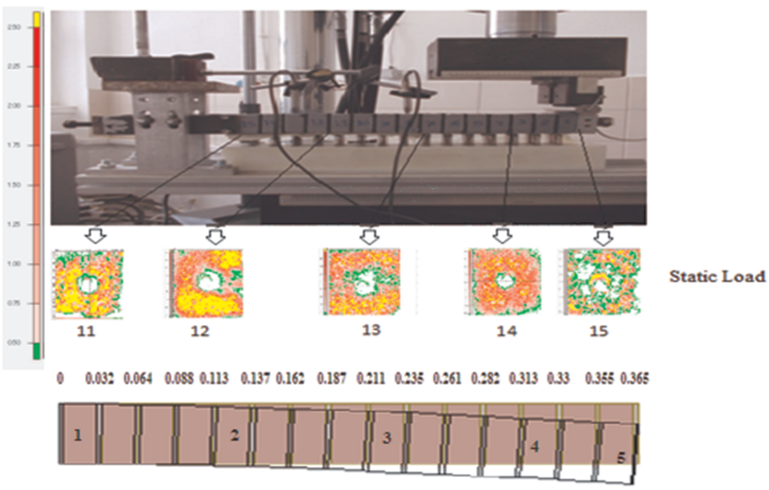

Figure 5.11. Stress Distribution of the Prescale Films Due to Post-Tension Forces and Lateral Load.

5.8. Stress Distribution on the Prescale Films along SPVFR Due to Cyclic load/ Top Point

The stress distribution of the prescale films number 16 and 17 are 2.07 MPa, and 1.49 MPa respectively. The position of prescale films number 16 and 17 are nearby the load cell, so high stress values are recorded comparing to other stress monitor films. According to the prescale film number 18, stress of 1.18 MPa is measured. The minimum value of stress distribution is considered at prescale film number 20, which is adjacent to the lateral load, is 1.05 MPa. To sum up, the high value of stress is concentrated adjacent to the load cell and decreases gradually by moving away from the fixed part to the point of lateral load. The pile model displacement play an important role on the stress distribution. The average stress distribution for all five prescale films is 1.39 MPa. The calculated bending moment developed a normal stress of 0.49 MPa by adding the normal stress due to bending moment and applied compression stress gives a total stress of 1.39 MPa. It is important to consider that, the prescale films have a significant effect on measuring the additional moment that resulted from the applied lateral load on the beam model. The value of bending moment is well agreed with L pile analysis.

6. CONCLUSIONS

The following conclusions are limited to the experimental setup used in this study. Although the three spring constants used to support the fixed beam/ pile have been selected to represent sand from loose to dense relative density, it is recognized that the real soil behavior will be different.

- It has been demonstrated that a segmental fixed beam/pile may be practically constructed in the laboratory by placing mortar blocks and rubber pads in an alternating order and connecting them with a cable passing through the center of these blocks. By applying tension to the cable, the beam is prestressed.
- It is possible to change the flexural rigidity almost four folds, by changing the value of the prestress forces from 750 N to 2250 N for the segmental beam/pile.
- With the limitations of spring support system used in this study, changing the spring constant from 2K to 3K (K=4 N/mm) causes a small increase in the load capacity of the pile at 4 mm displacement.
- Cyclic loading causes a slight decrease in the lateral load capacity of the segmental pile system. However this conclusion is limited to the linear behavior of the springs used and does not represent expected degradation under cyclic loading for real soil. The pile maintains its structural capacity under maximum displacement application even under 600 cycles applied for cyclic loading.
- From the measured deflections, corresponding spring reaction forces are determined. From the spring reaction forces, the boundary conditions are obtained and by integration shear forces are determined. The second integration gave the moment distribution. The stress maps obtained from prescale films are used to backcalculate the moment along the fixed beam/pile. The comparision of the moment distribution shows a similar trend with the experimental findings. The magnitude of the moment obtained from the backcalculation of prescale stress maps are upto two times of that obtained from the load-deflection measurements which is due to small number of deflection measurements which underestimated the beam curvature.

- The use of prescale films to map the stress distribution at the segment interfaces has proven to be consistent and repeatable. This technique provides a tool to evaluate the relative stress distribution on mortar block interface. The value of the contact stresses obtained by prescale films may be used to backcalculate the bending moment for the tested beam.
- For future research it is recommended that the beam displacements should be measured in more locations. The beam used in this study was fixed from one side. A ball joint type connection is recommended to have zero moment at the tip of the segmental beam.

APPENDIX A: Static/Cyclic Load at Mid-Point of the SPVFR 3K Force/Deflection Relationship

The load-displacement relationship of the pile model subjected to lateral static point load is presented in Figure A.1. The maximum load of 583 N is measured for 4 mm deflection. The load /deflection has a linear relationship as shown in the figure. In addition, the load-displacement relationship of the pile model subjected to lateral cyclic load is given in Figure A.2. The load that corresponds to 4 mm deflection is 440 N.

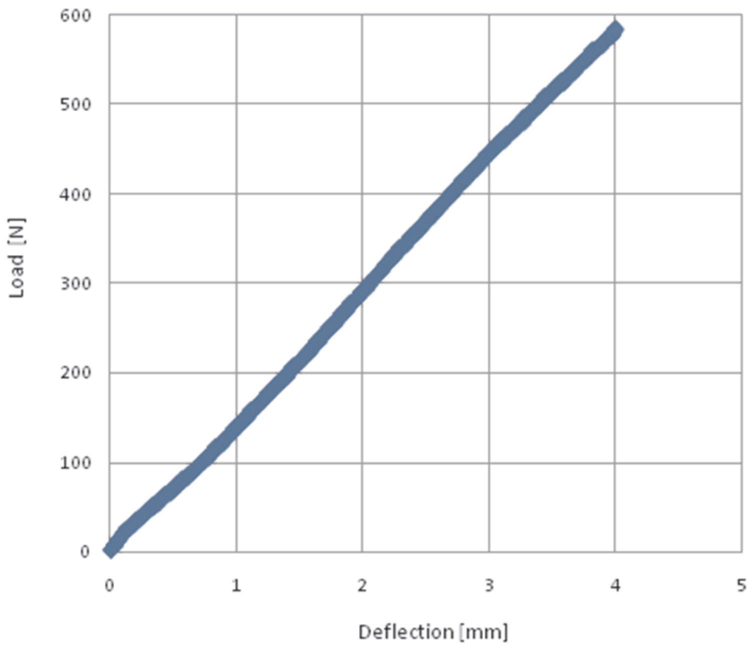

Figure A.1. Static Load at Mid-Point of the SPVFR -3K.

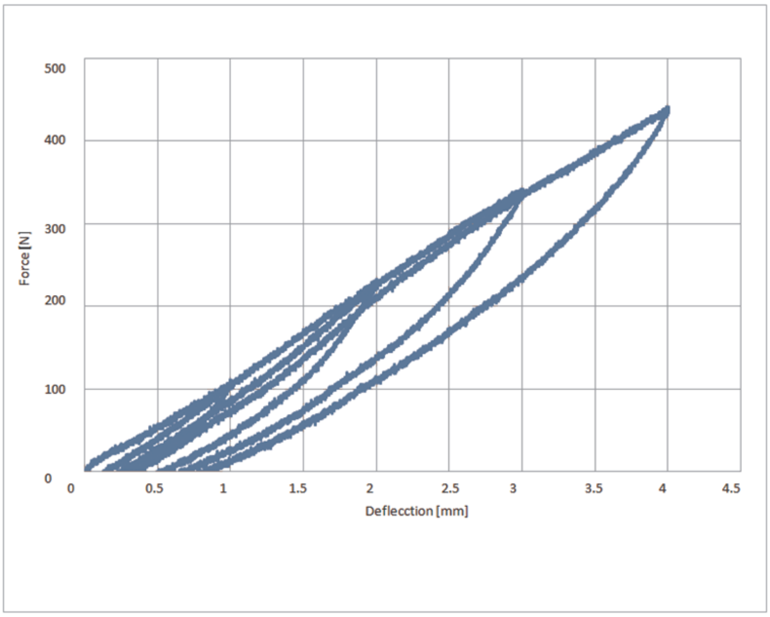

Figure A.2. Cyclic Load at Mid-Point of the SPVFR -3K.

A.1. Analysis of the SPVFR Using Non-Dimensional Method (NDM)

A.1.1. Slope of the SPVFR Placed on Elastic Springs (1K, 2K and 3K)

The slope of the pile model subjected to lateral static point load at top point and placed on linear springs 1K, 2K and 3K is presented in Figure A.3. It is observed that the slope of the SPVFR subjected to static lateral load decreased by increasing the stiffness of the springs. The slope of the pile model placed on 1K is - 3.95 x 10^{-3} degree, which decreased 2.4 times when the the pile model is placed on 2K. The slope of the pile model placed on 3K is less than the slope of 2K by 38%. It is observed that high values of slope develops by changing the spring stiffness from stiff to soft one. This implies that, the p-y curves of 3K are stiffer than the p-y curves of 2K and 1K, respectively.

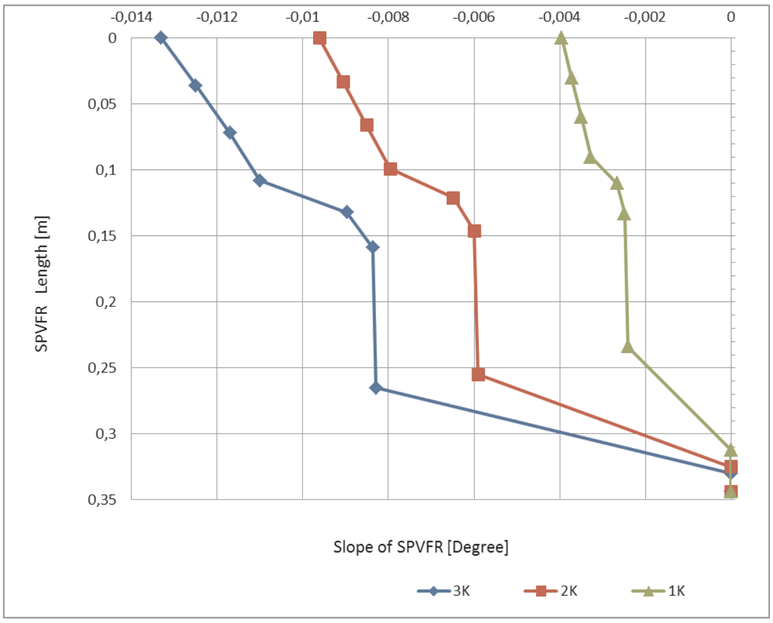

Figure A.3. Slope of the SPVFR Under Static Load at Pile Head (1K, 2K and 3K).

A.1.2. Bending Moment of the SPVFR Placed on Elastic Springs (1K, 2K and 3K)

The bending moment along the pile model length for different spring stiffness is presented in Figure A.4. According to the pile model placed on 1K, the peak bending moment is 6.12 x 10^{-3} KN.m, these values increased 2.3 times when the pile model is placed on 2K. In addition, the maximum bending moment of the pile model 3K is more than that of the pile model 2K by 23%. It can be stated that the stiffness of the springs has a significant part on increasing the moment capacity.

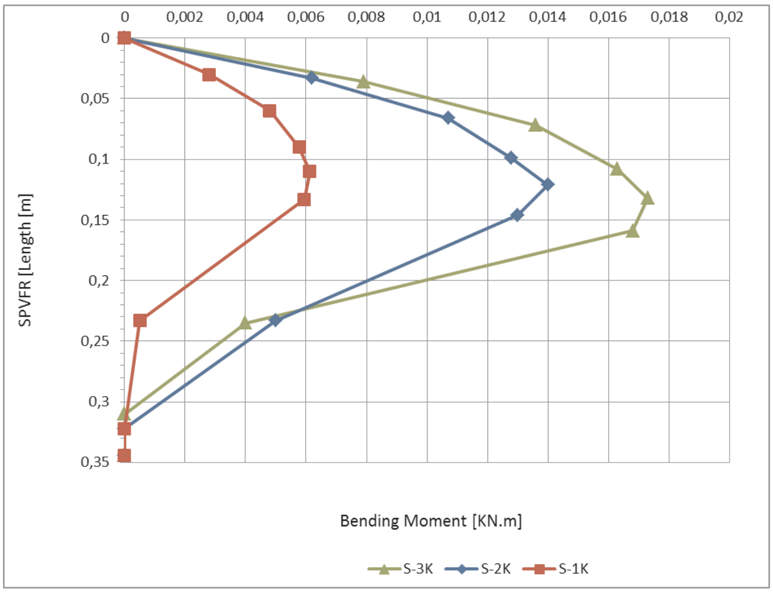

Figure A.4. Bending Moment Diagram Along SPVFR (1K, 2K and 3K).

A.1.3. Shear Force of the SPVFR Placed on Elastic Springs (1K, 2K and 3K)

Figure A.5 gives the distribution of shear forces along SPVFR for different spring stiffness (1K, 2K and 3K). The non-dimensional method of linear spring 1K and 2K predicts that at 4mm deflection the maximum shear force is 0.088 KN and 0.177 KN, respectively. By increasing the spring stiffness from 2K to 3K, the shear force raised up to 16% at the same level of deflection.

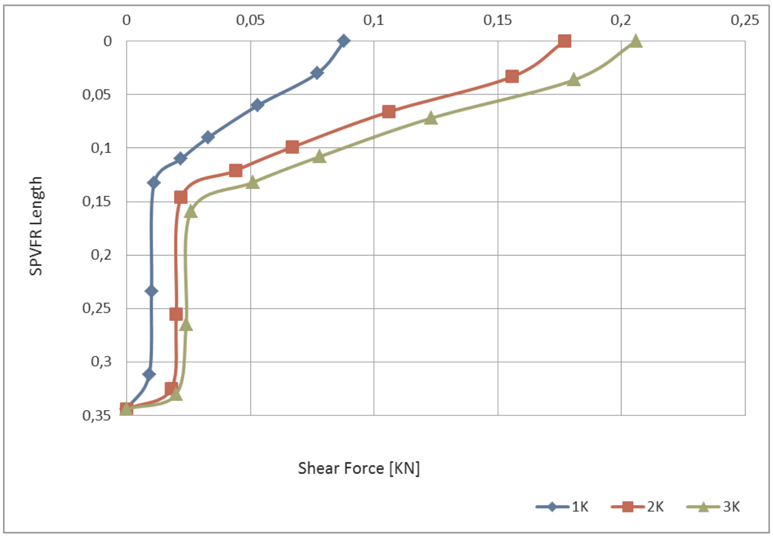

Figure A.5. Shear Force Diagram Along SPVFR (1K, 2K and 3K).

A.2. Bending Moment of the SPVFR Under Static and Cyclic Loading

The peak values of bending moment of the SPVFR placed on 1K under static load is 6.12 x 10^{-3} KN.m, which is 9% more than the maximum bending moment under cyclic loading. Figure A.6 illustrates the relationship of bending moment along the pile model length for static and cyclic loading. In addition, the maximum value of bending moment of the pile model placed on 2K under static loading is 0.014 KN.m , which is more than the peak value of bending moment under cyclic loading by 7%, as given in Figure A.7. For the pile model placed on 3K under static loading, the critical value of bending moment is 0.0168 KN.m , which is more than the peak value of bending moment under cyclic loading by 3% , Figure A.8 shows the bending moment diagram along the pile model under static and cyclic loading. It is obvious to state that high spring stiffness exhibits high value of bending moment resistance and the difference between peak values of bending moment under static and cyclic loading is lessened by changing the springs stiffness from 1K to 3K.

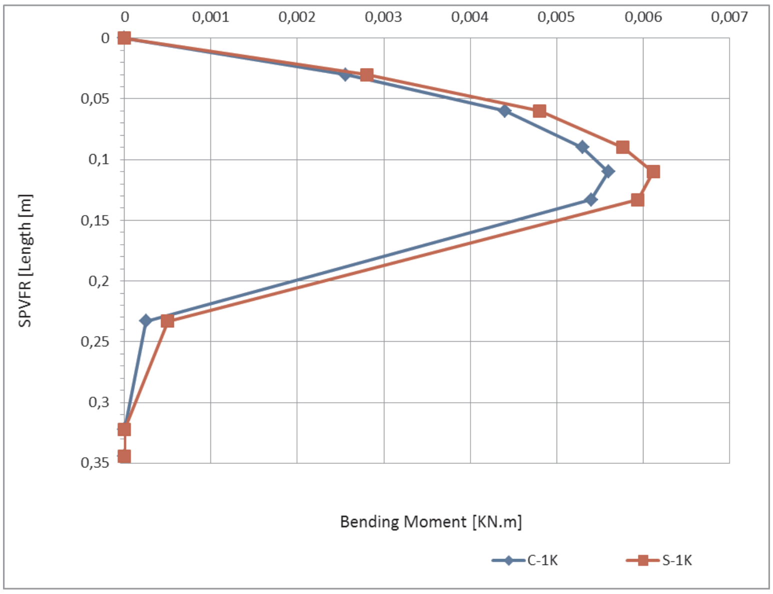

Figure A.6. The Bending Moment Diagram Along SPVFR Length Under Static / Cyclic Loading 1K.

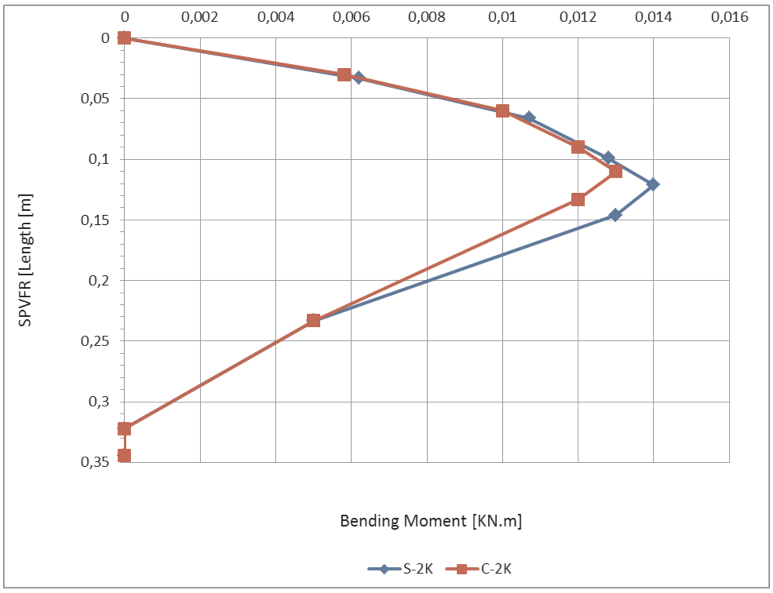

Figure A.7. The Bending Moment Diagram Along SPVFR Length Under Static / Cyclic Loading 2K.

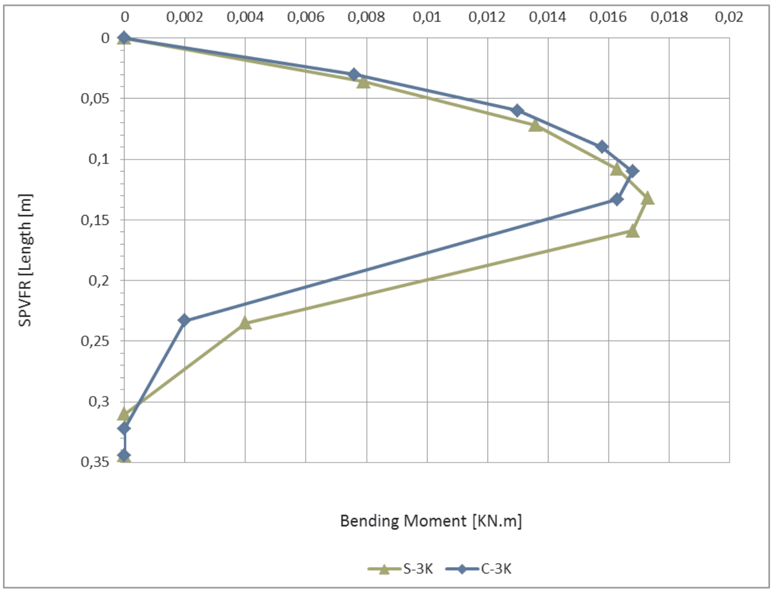

Figure A.8. The Bending Moment Diagram Along SPVFR Length Under Static / Cyclic Loading 3K.

A.3. Shear Force of the SPVFR under Static and Cyclic Loading

The peak value of shear force of the SPVFR placed on 1K under static load is 0.088 KN, which is greater than the maximum value of shear force of the pile model under cyclic loading by 10%, Figure A.9 illustrates the shear force diagram along the pile model length. The maximum shear force of the SPVFR placed on 2K under static load is more than the shear force of cyclic loading condition by 6%. Figure A.10 gives the shear force diagram along the pile model. For the pile model placed on 3K under static loading condition, the maximum value of shear force is 0.206 KN, which is 3% greater than the shear forces of the pile model under cyclic loading as shown in Figure A.11.

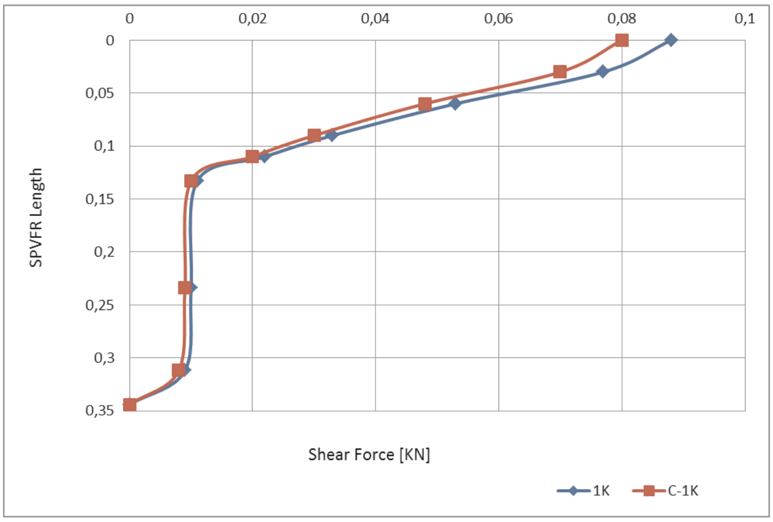

Figure A.9. The Shear Force Diagram Along SPVFR Length Under Static / Cyclic Loading 1K.

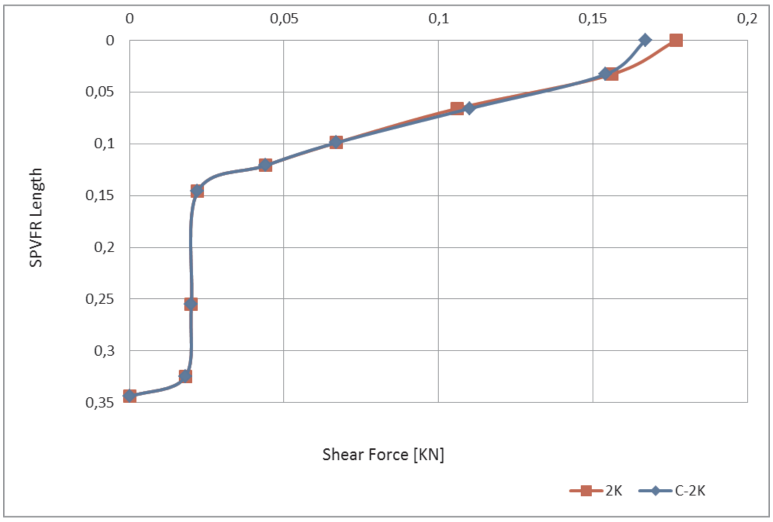

Figure A.10. The Shear Force Diagram Along SPVFR Length Under Static / Cyclic Loading 2K.

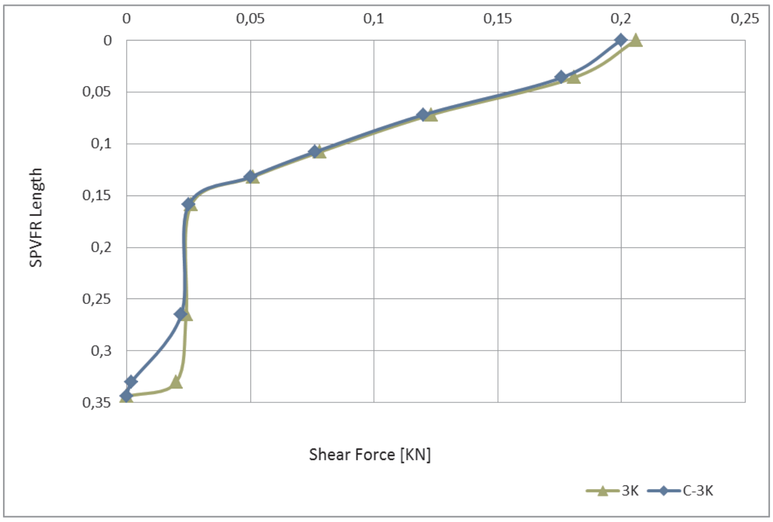

Figure A.11. The Shear Force Diagram Along SPVFR Length Under Static / Cyclic Loading 3K.

A.4. The Slope of the SPVFR Under Static and Cyclic Loading

For the SPVFR placed on springs 1K under static load, the peak value of the slope at the top of the pile, is -3.95 x 10^{-3} degree, and this value is greater than slope value of the pile model under cyclic loading by 11%. Figure A.12 shows the slope diagram along the pile model length for static and cyclic loading. The maximum slope values of the pile model placed on 2K under static load is 9.61 x 10^{-3} degree, which is greater than slope value for the same pile model under cyclic loading by 7% as shown in Figure A.13. For the pile model placed on 3K, the peak slope value in static loading condition is more than slope value in cyclic loading condition by 3% as given in Figure A.14.

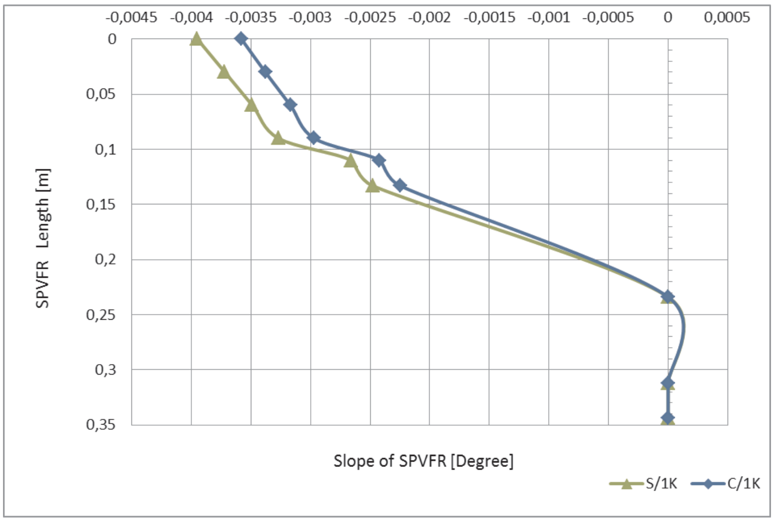

Figure A.12. The Slope Diagram Along SPVFR Length Under Static / Cyclic Loading 1K.

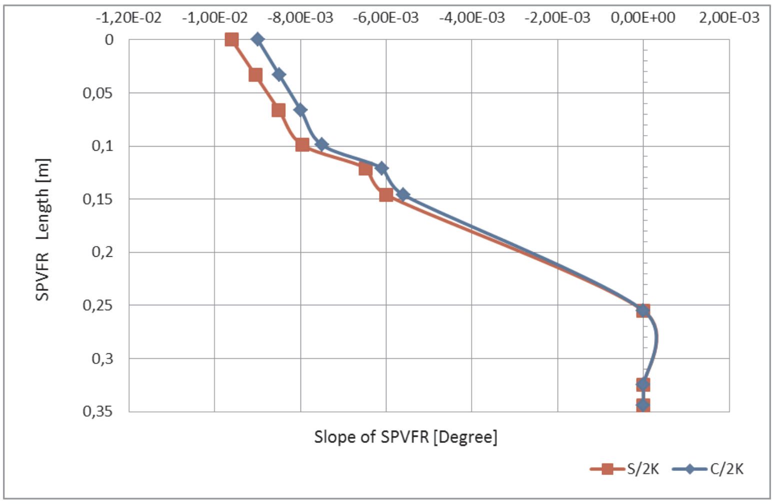

Figure A.13. The Slope Diagram Along SPVFR Length Under Static / Cyclic Loading 2K.

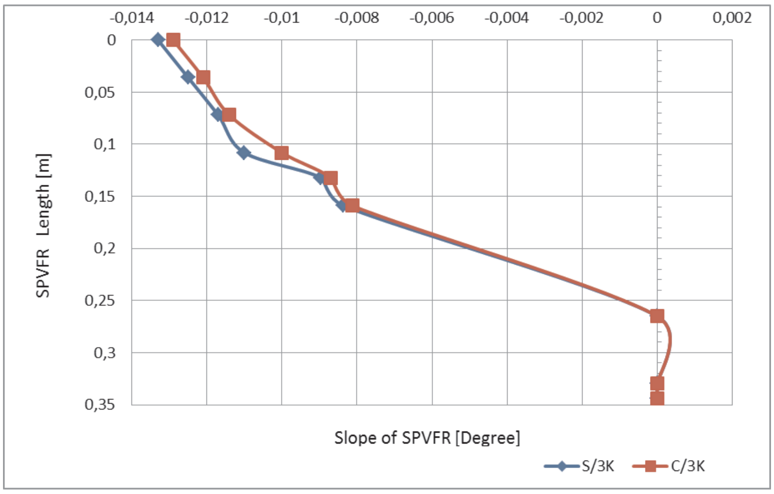

Figure A.14. The Slope Diagram Along SPVFR Length Under Static / Cyclic Loading 3K.

A.5. Analysis of the SPVFR (Mid-Point Loading) Winkler Analysis Method (WAM)

A.5.1. The Slope of the SPVFR (Static/Cyclic Loading)

The slope of the pile model under static load is 7.42x10^{-3} which is less than the slope of pile model under cyclic loading by 99.46% as shown in Figure A.15. The slight difference of slope is due to fact that the p-y curves of cyclic loading is slightly softer than the p-y curves static loading.

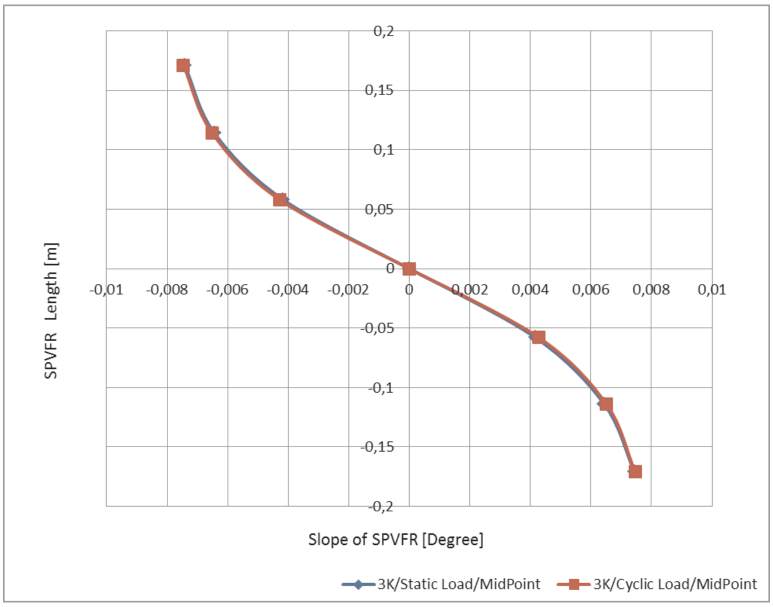

Figure A.15. Illustrates the Slope variation Along the Pile Length (Static/Cyclic).

A.5.2. The Bending Moment of the SPVFR (Static/Cyclic Loading)

The maximum value of bending moment diagram of the pile model of static loading condition is 0.0355 KN.m , which is greater than the bending moment under cyclic loading by 3% as presented in Figure A.16. It is evident that the prediction of the p-y curves under static and cyclic loading make slight changes in terms of stiffness. The stiffer value of p-y curves produce a high value of bending moment than the softer one.

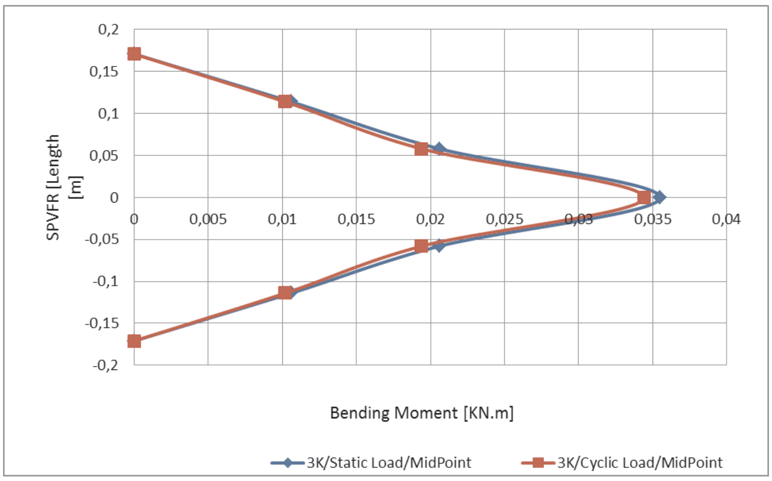

Figure A.16. Bending Moment Along the Pile Length (Static/Cyclic).

A.5.3. The Shear Force of the SPVFR (Static/Cyclic Loading)

The relationship of shear force of the pile model under static loading develops peak value of shear force 291.5 N at mid point, which is more than the shear force for the same model under cyclic loading by 2 N. Slight changes are observed between [∓0.058 m to ∓0.114 m] of the pile length. The reason for the slight changes in shear force is due to minor changes in p-y curves. The Figure A.17 shows the shear force distribution along the pile length.

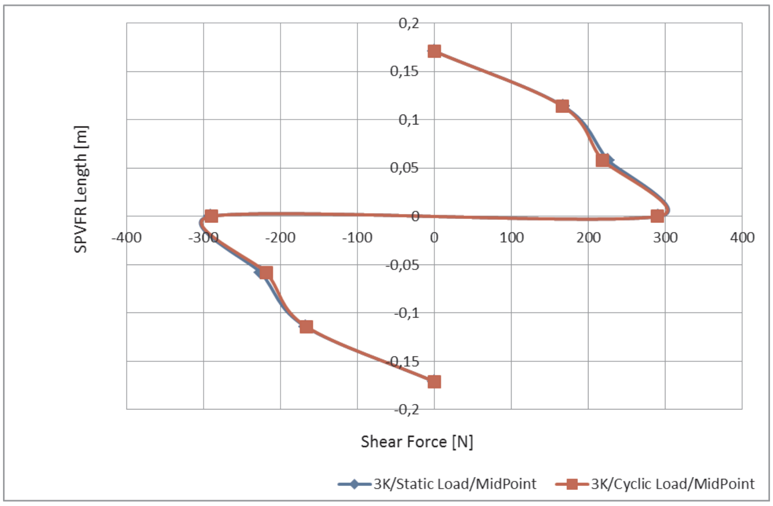

Figure A.17. Shear Force Along the Pile Length (Static/Cyclic).

A.5.4. The Slope of the SPVFR (1K-2K-3K)

The slope of the pile model subjected to lateral load at top point of the pile is presented in Figure A.18. The slope of the pile model placed on linear spring 1K and subjected to static load is calculated in three position at the top part of the pile (0-0.158 m) is (-0.0591) degree and at mid-length of the pile (0.18 m- 0.271 m) is (-0.2513) degree and at the lower part of the pile (0.294 m- 0.328 m) is (-0.1046) degree. For the cyclic loading condition, the calculated slope at the upper part of the pile is (-0.0591) degree and mid-part of the pile is (-0.4188) degree and lower part of the pile is (0.0548) degree.

The slope the pile model placed on linear springs (2K) and subjected to lateral static load is (-0.0565) degree at upper part, (-0.3326) degree at the mid- part and (-0.0685) degree at the lower part of the pile length as given in Figure A.18. For cyclic loading, the slope at the upper part is (-0.075) degree, mid-point is (-0.1216) degree and the lower part is (-0.0599) degree.

For the pile model placed on (3K) springs and subjected to static load, the slope at the upper part is (-.0521) degree, mid-part (-0.2758) degree and the lower part is (-0.104) degree. The slope at upper part of the pile under cyclic loading is (-0.0533) degree, at the mid-part is (-0.133) degree and the lower part is (-0.3196) degree.

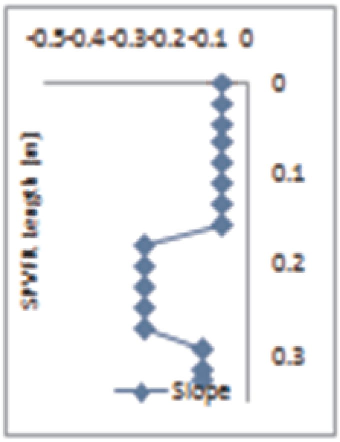

The Slope of SPVFR 1K-Static

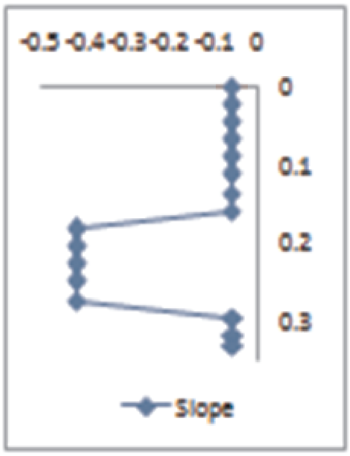

The Slope of SPVFR 1K-Cyclic

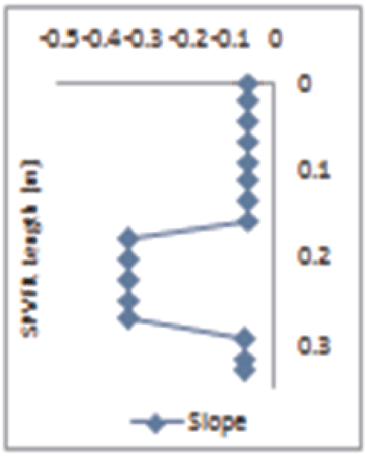

The Slope of SPVFR 2K-Static

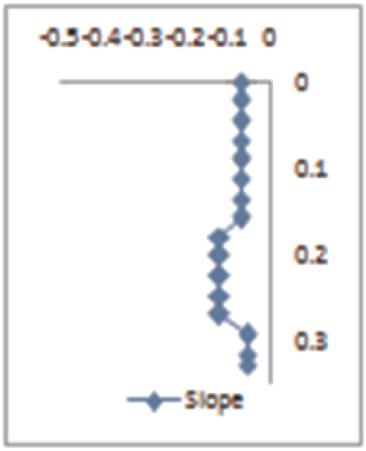

The Slope of SPVFR 2K-Cyclic

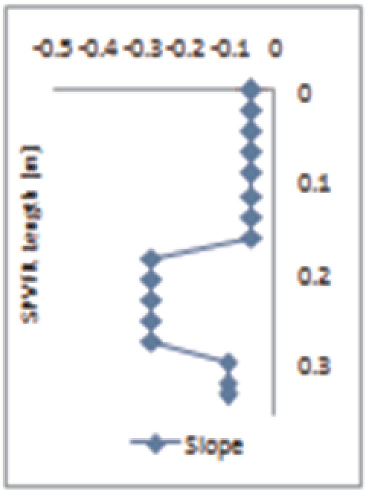

The Slope of SPVFR 3K-Static

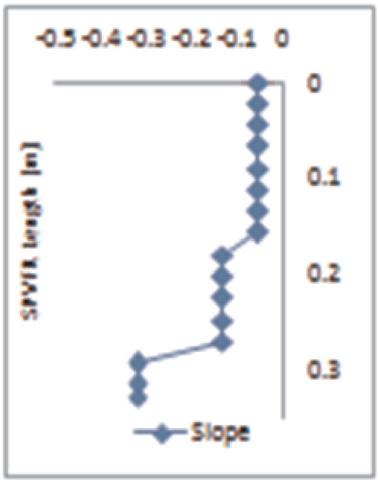

The Slope of SPVFR 3K-Cyclic

Figure A.18. The Slope Along the Pile Model Length.

A.5.5. The Bending Moment and shear force of the SPVFR (1K-2K-3K)

The bending moment along the pile model subjected static /cyclic load at top point is plotted and presented in Figure A.19. The maximum bending moment for the pile model placed on linear spring 1K and subjected to static load is 0.005 KN.m at the base of the pile, whereas for cyclic loading condition the maximum moment is 0.0045 KN.m at the pile tip. The high value of bending moment for the pile model placed on 2K under static loading is 0.0108 KN.m. For cyclic loading condition, the maximum moment is 0.0094 KN.m. For the pile model placed on linear springs 3K subjected to static loading, the maximum bending moment is 0.014 KN the pile base. For cyclic loading condition, the maximum bending moment is 0.013 KN.m. Figure A.20 shows the value of bending moment along the pile model for linear spring 2K and 3K.

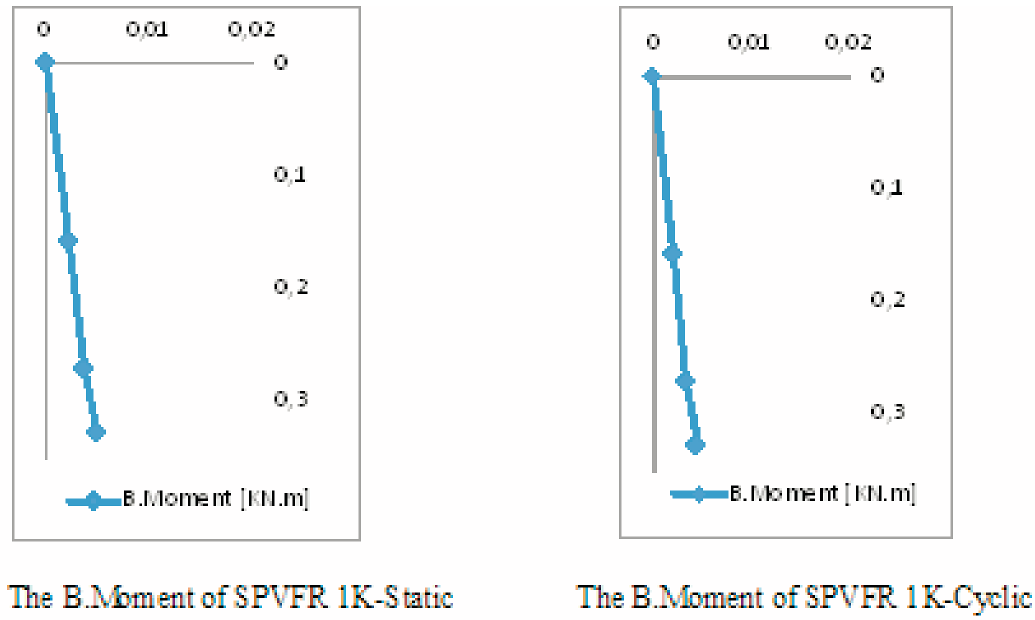

Figure A.19. The Bending Moment Diagram Along SPVFR-1K.

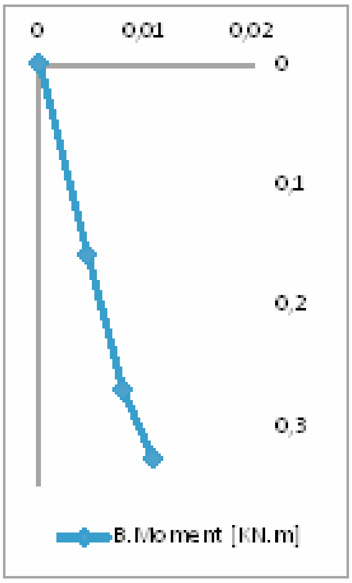

The B.Moment of SPVFR 2K-Static

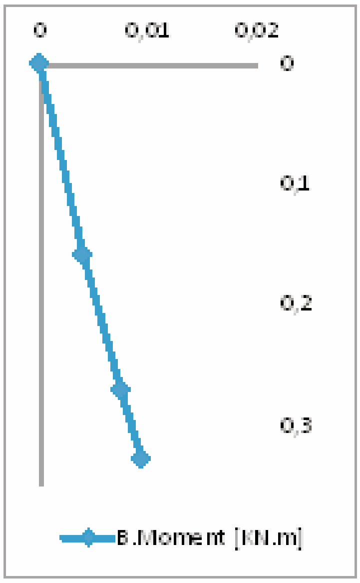

The B.Moment of SPVFR 2K-Cyclic

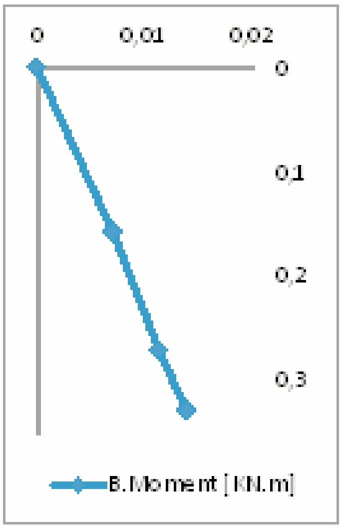

The B.Moment of SPVFR 3K-Static

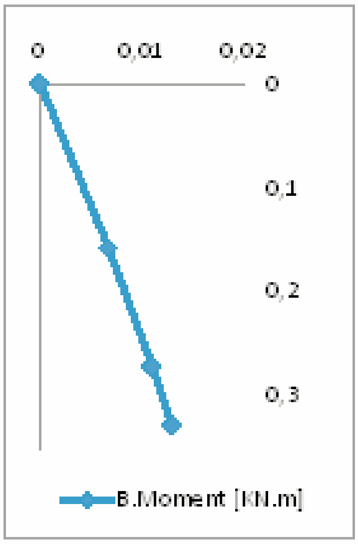

The B.Moment of SPVFR 3K-Cyclic

Figure A.20. The Bending Moment Diagram Along SPVFR-2/3K.

The shear forces and spring reaction along the pile model placed on three different linear springs and subjected to static and cyclic loading are presented in Figure A.21.

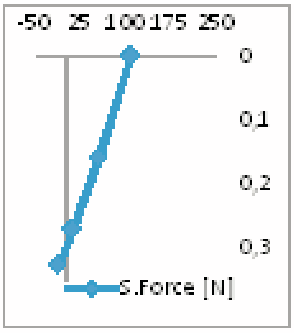

The Shear Force Along SPVFR/1K-Static

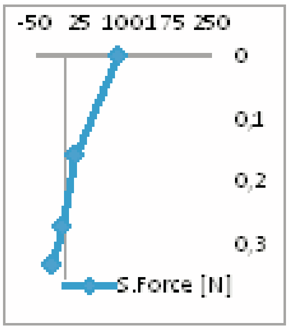

The Shear Force Along SPVFR/1K-Cyclic

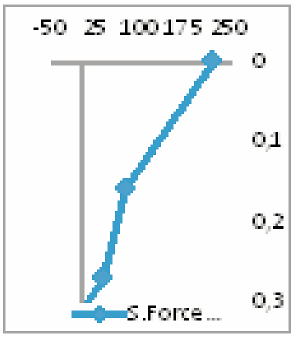

The Shear Force Along SPVFR/2K-Static

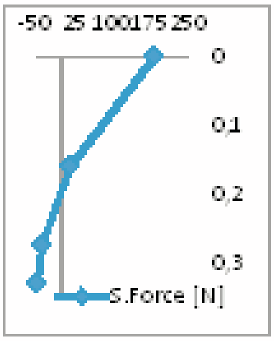

The Shear Force Along SPVFR/2K-Cyclic

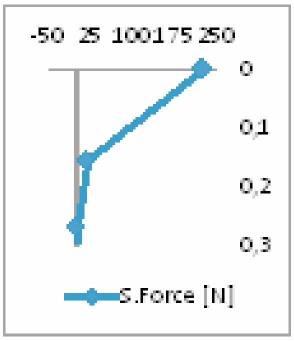

The Shear Force Along SPVFR/3K-Static

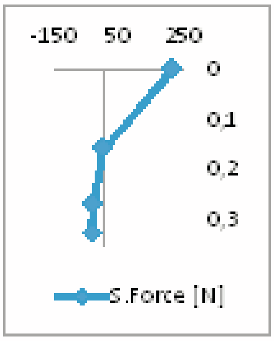

The Shear Force Along SPVFR/3K-Cyclic

Figure A.21. The Bending Moment Diagram Along SPVFR-2K.

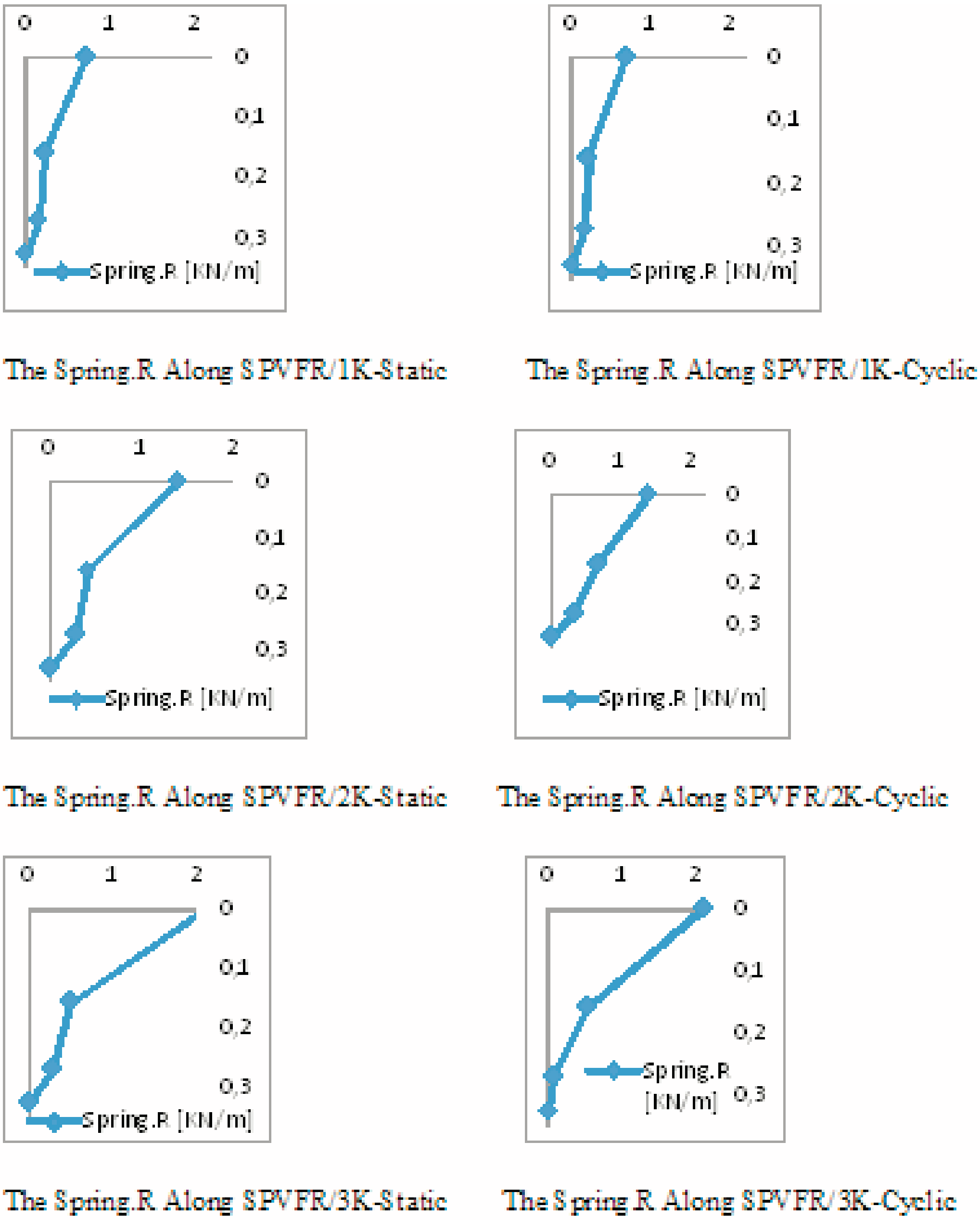

Figure A.22. The Bending Moment Diagram Along SPVFR-3K.

A.5.6. SPVFR on Winkler Foundation Test Results [Static/cyclic Load] at Tip-Point

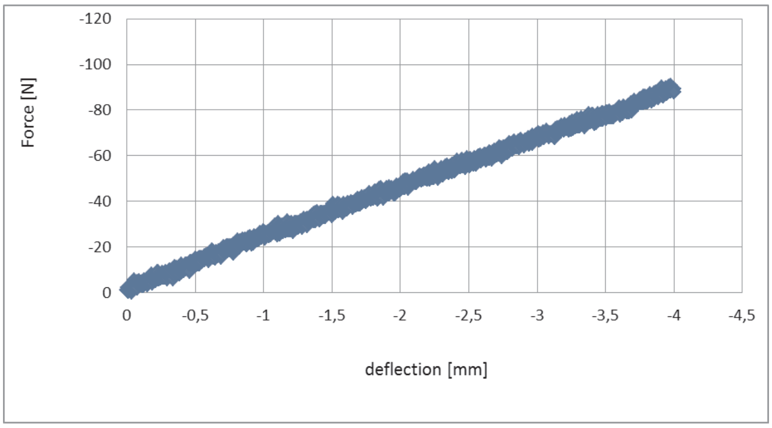

Figure A.23. Static Loads at Top-Point of the SPVFR 1K.

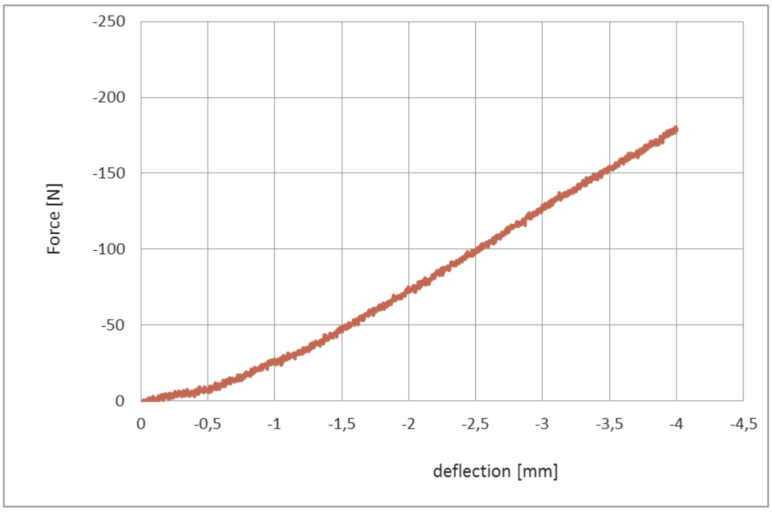

Figure A.24. Static Loads at Top-Point of the SPVFR 2K.

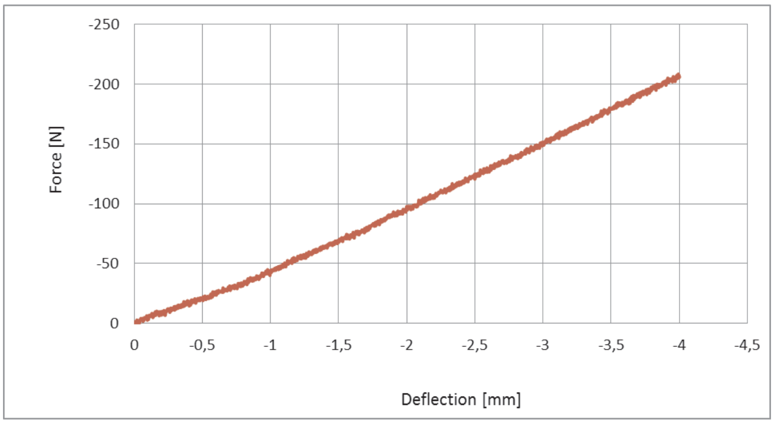

Figure A.25. Static Loads at Top-Point of the SPVFR 3K.

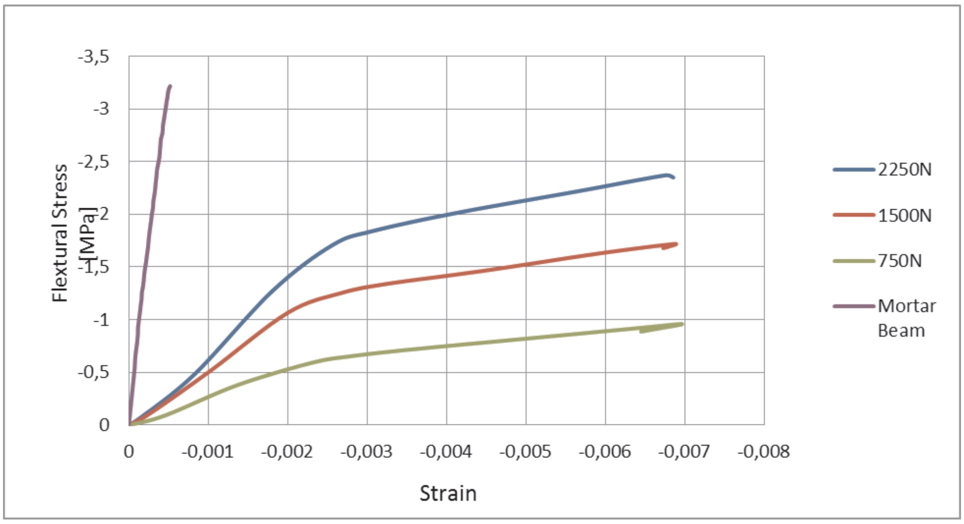

Figure A.26. Stress-Strain Relationship for SPTBM and Mortar Beam Model.

Cross-Section Properties

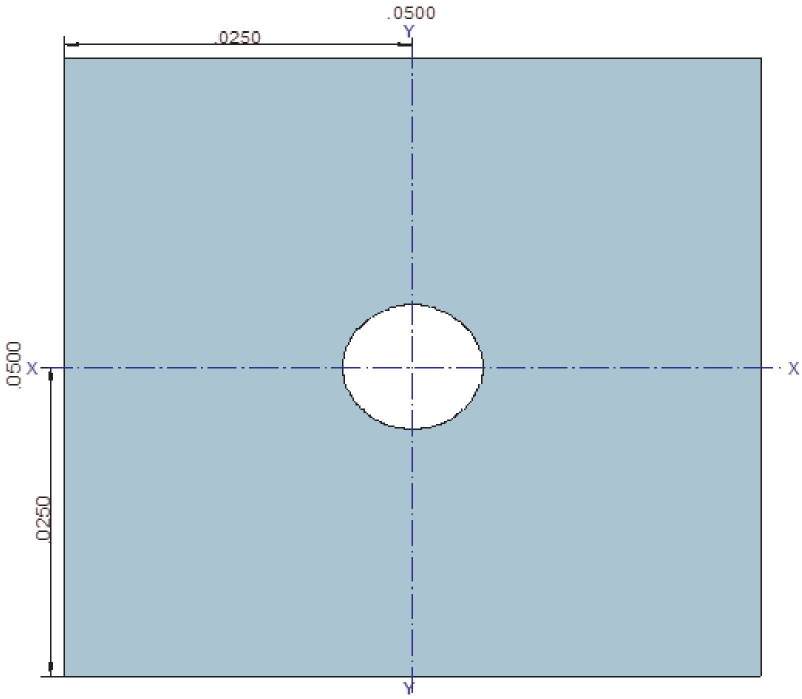

Figure A.27. Cross - Section of Mortar Block.

A= 2.4215 E-3

Ixx = 520.34E-9 Iyy = 520.34E-9

Ixy = 0.0000 Iuu = 520.34E-9

Ivv = 520.34E-9 Ir = 1.0407E-6

Ang = 0.0000° xx(T)= 20.814E-6

Zxx(B)= 20.814E-6 Zyy(L)= 20.814E-6

Zyy(R)= 20.814E-6 Zuu = 20.814E-6

Zvv = 20.814E-6 Zplx = 31.083E-6

Zply = 31.083E-6 Yc = 25.000E-3

Xc = 25.000E-3 rx = 14.659E-3

ry = 14.659E-3 ru = 14.659E-3

rv = 14.659E-3 Xpl = 25.000E-3

Ypl = 25.000E-3 Perim.= 200.00E-3

Stress Distribution on Prescale Film

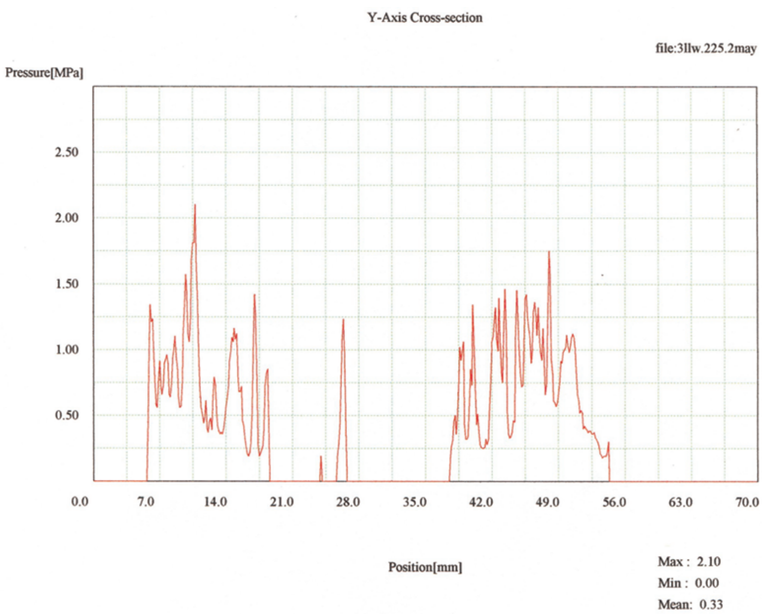

Figure A.28. Stress Distribution on Y-Axis Cross-Section of Prescale film No.3.

In Figure A.28, stress distribution in y-axis is presented, and it from 0 to 2.2 MPa. The stress distribution is recorded as zero at midpoint of prescale film, since there is an opening circle with diameter 1 cm. The stress distributions in the other part of prescale film no. 3 range between 0-2.1 MPa.

In the Figure A.29, the stress distribution in the x-axis ranges between 0-2.7 MPa. The zero stress level at midpoint of Prescale film is recorded; and the maximum stresses are due to high contact stress between mortar/rubber.

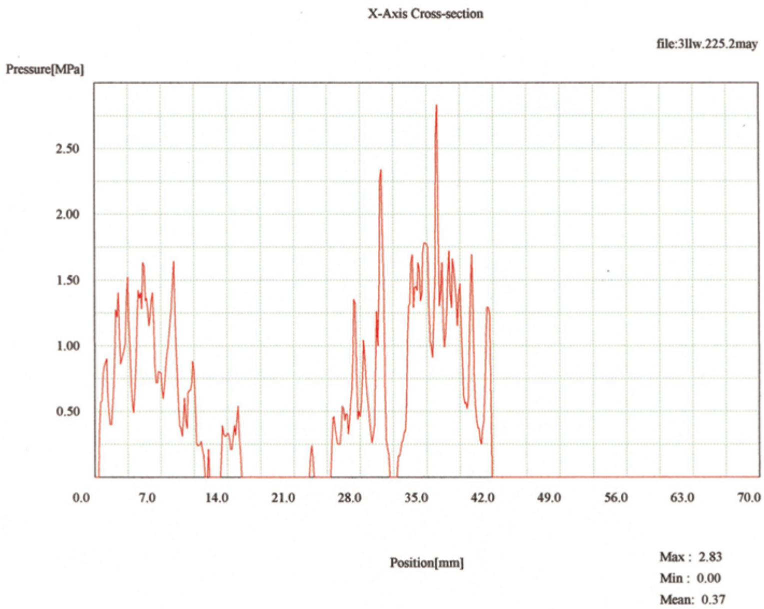

Figure A.29. Stress Distribution on X-Axis Cross-Section of Prescale Film No.3.

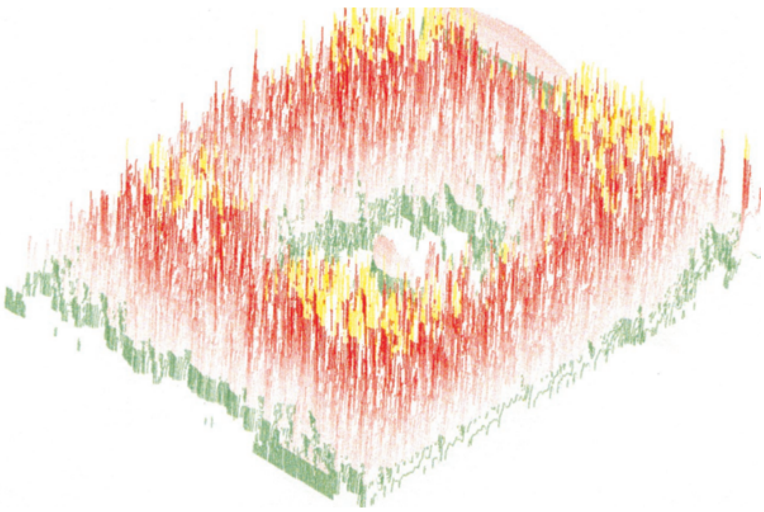

Figure A.30. 3-D Stress Distribution on the Upper Part of Prescale Film No.3.

In the Figure A.30, 3-D stress distribution on the upper part of prescale film no. 3 is given. According to the Figure A.30, the maximum stress is distributed in the four corners of prescale film. In the other part of prescale film, stresses distributions range between 0-2.5 MPa. The image of stress distribution as shown in Figure A.30 is due to presstress forces only.

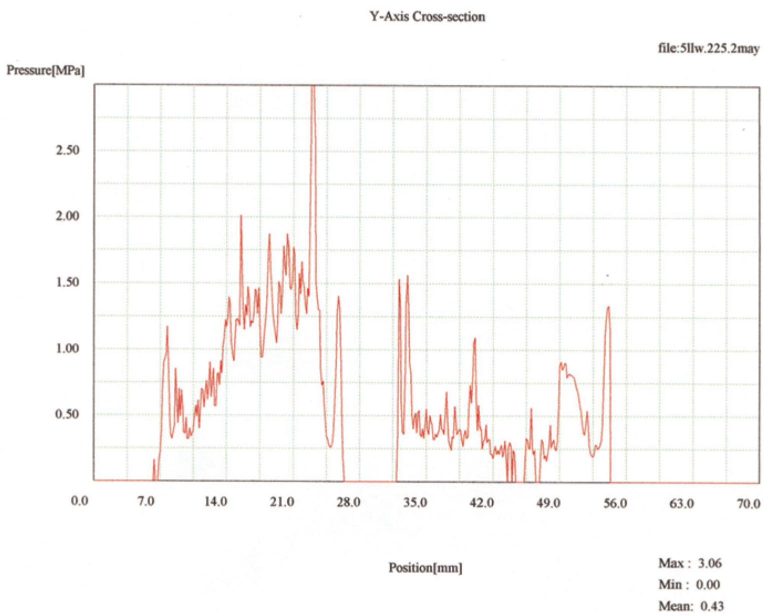

Figure A.31. Stress Distribution on Y-Axis Cross-Section of Prescale film No.5.

In Figure A.31, the stress distribution along y-axis is presented. High stress level is occurred at a point under the circle hole due to bearing contact between concrete/rubber. Zero stress level is recorded in the midpoint of prescale film. In the other parts of prescale film, the stress level occurs between 0-2 MPa.

In Figure A.32, the stress distribution along x-axis is obtained. The maximum stress level ranges between 0-1.75 MPa, and zero stress level at midpoint of prescale film is recorded. It is obvious that the stress values distribution in the y-axis are more than stress values distribution in the x-axis.

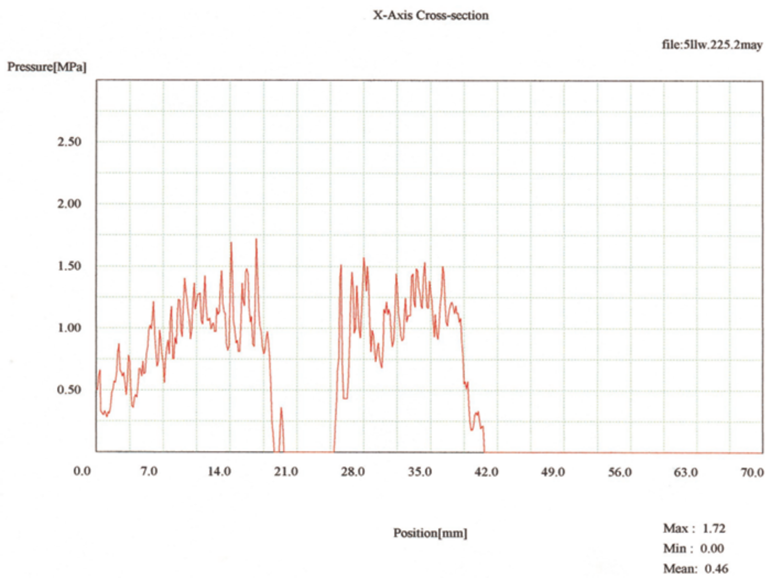

Figure A.32. Stress Distribution on X-Axis Cross-Section of Prescale Film No.5.

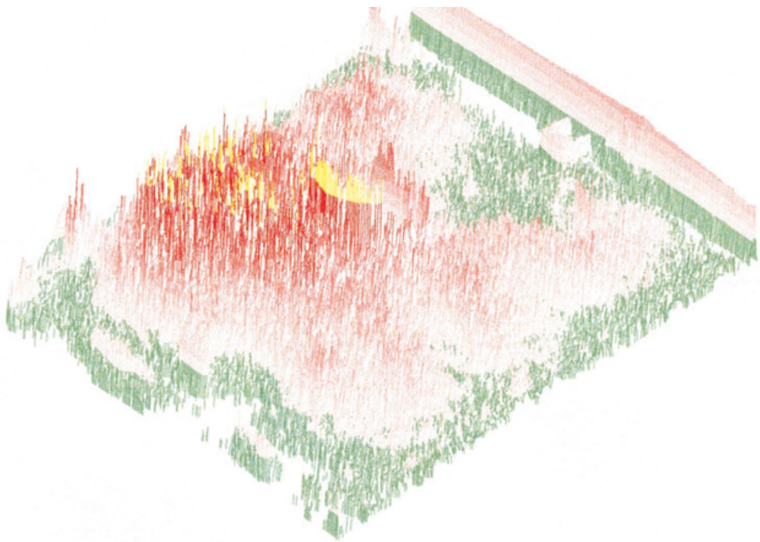

Figure A.33. 3-D Stress Distribution on the Upper Part of Prescale Film No.5.

In the Figure A.33, 3-D stress distribution on the upper part of prescale film no. 3 is presented. In the the Figure A.35, the maximum stress is distributed along the right edge of prescale film whereas minimum stresses are recorded in the other three edges. Stress distribution ranges between 0-2.5 MPa is recorded around the midpoint of prescale film.

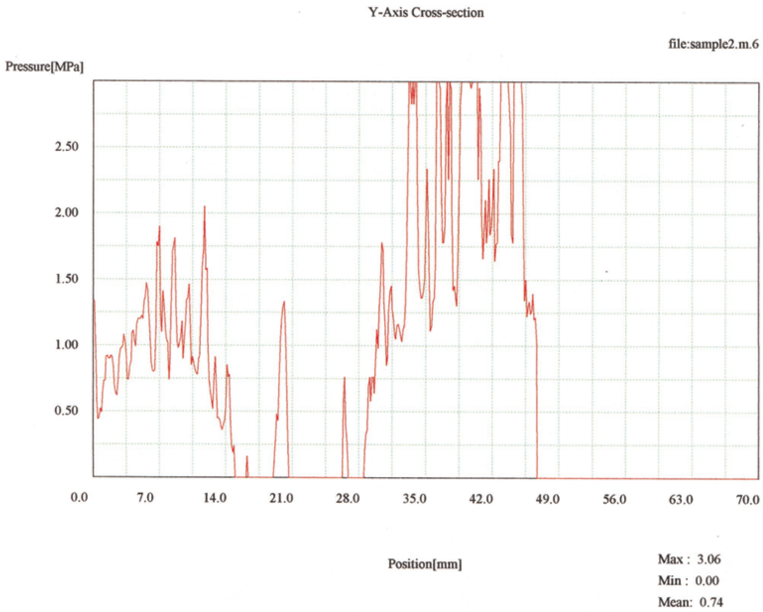

Figure A.34. 3-D Stress Distribution on the Upper Part of Prescale Film No.5.

A.6. Stress Distribution due to Prestress Force and Static Load at Midpoint of the SPVFR

In Figure A.34, the stress distribution in y-axis of prescale film no.6 is presented. The high pressure is recorded on the upper part of prescale film, which ranges between 0.75-3 MPa. In the lower part of prescale film low stress values are recorded, which range between 0.5-2 MPa. The imbalaca of stress distributions is due to the fact that SPVFR specimen is subjected to static load at midpoint and prestress forces.

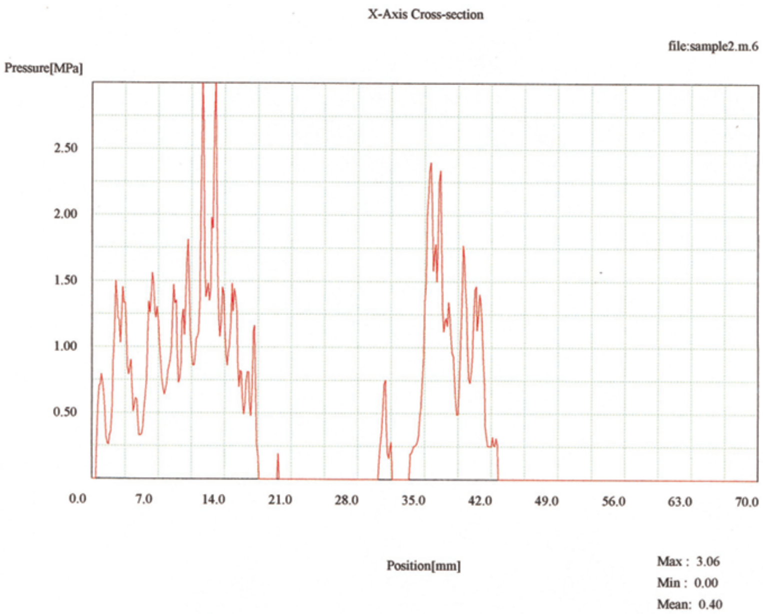

Figure A.35. Stress Distribution on X-Axis Cross-Section of Prescale Film No.6.

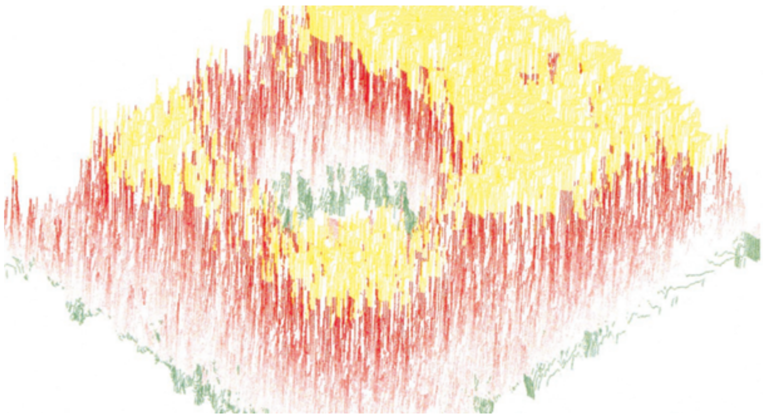

Figure A.36. 3-D Stress Distribution on the Upper Part of Prescale Film No.6.

In Figure A.35, the stress distribution in x-axis cross-section of prescale film no. 6 is given. In the opening area at midpoint of prescale film, zero stress values are recorded. Maximum values of stress are distributed on the left side of prescale film, which range between 0.4-3 MPa, whereas low values of stress are recorded on the right part of prescale film. In Figure A.36, 3-D stress distribution on the upper part of prescale film are recorded. High stress concentrations are observed in the upper part of prescale film, and the other two corners as shown in the stress image in the Figure A.36 [yellow color]. It is observed that stress distributions ranging between 0.5-2.5 are distributed in the other part of prescale film.

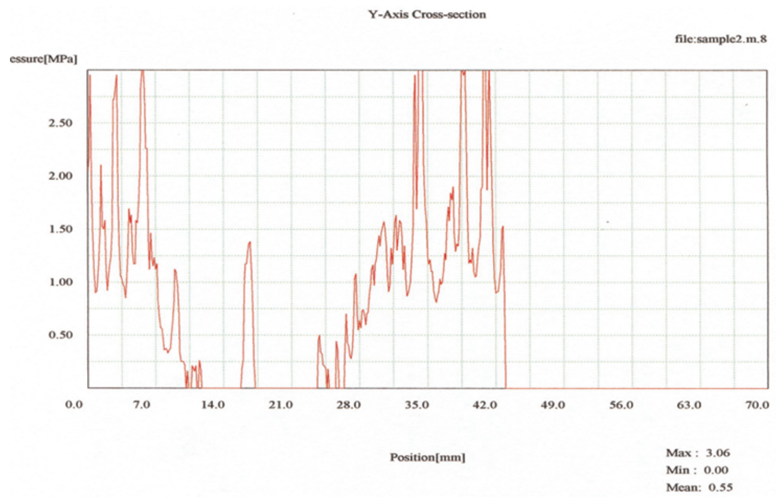

Figure A.37. Stress Distribution on Y-Axis Cross-Section of Prescale film No.8.

In the Figure A.37, stress distributions in y-axis of prescale film no.8 are obtained. The maximum stress values are recorded in the upper part of prescale sheet, which range between 0-3 MPa, whereas in the lower part, less stress distribution is presented. The mean stress values for all prescale film are 0.55 MPa as shown in Figure ??. In Figure A.38, the stress distribution in x-axis of prescale film is presented. The maximum stresses are found on the left side of prescale film, which range between 0-2.9 MPa. whereas less stresses are distributed on the right part and that is range between 0-2 MPa. The mean stresses are 0.36 MPa.

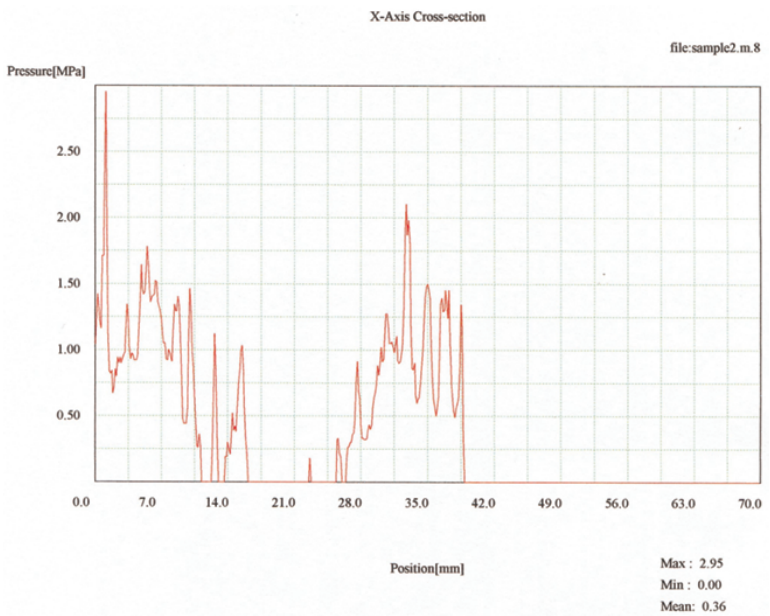

Figure A.38. Stress Distribution on X-Axis Cross-Section of Prescale Film No.8.

In the Figure A.39, 3-D stress distributions on the upper part of prescale film are presented. The maximum stress is recorded in the upper part of prescale film and other two edge of prescale film. Zero stress values are recorded in the midpoint. In the other part of prescale film, stress distribution ranging between 0-2.5 is presented.

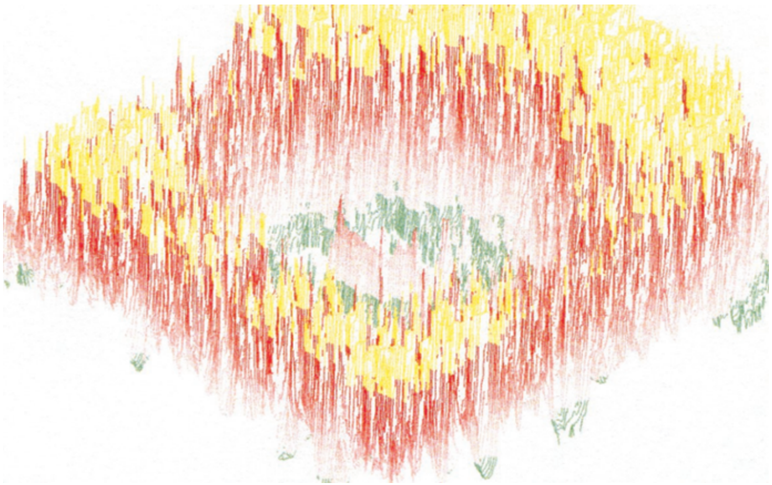

Figure A.39. 3-D Stress Distribution on the Upper Part of Prescale Film No.8.

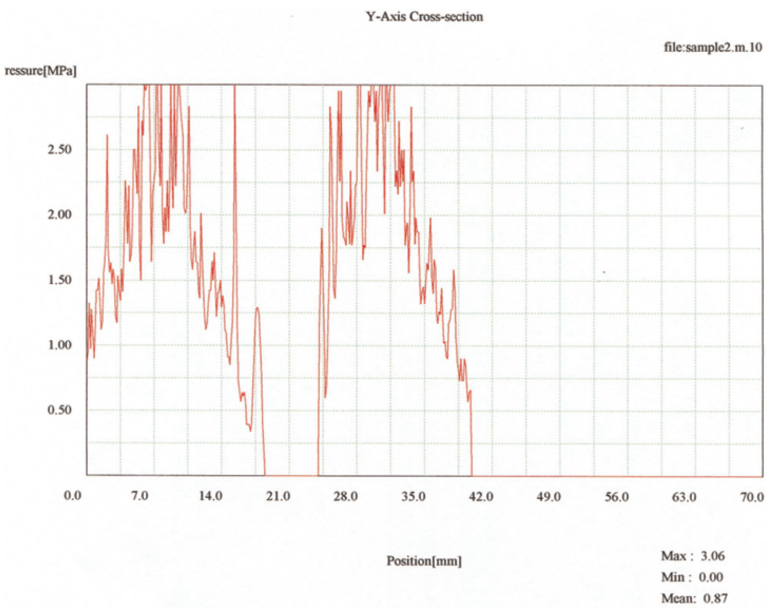

Figure A.40. Stress Distribution on Y-Axis Cross-Section of Prescale film No.10.

In the Figure A.40, stress distributions in the y-axis of prescale film no. 10 are presented. There are equal stress distributions in the upper and lower part of prescale film, which range between 0-3.06 MPa. The mean stress distributions are 0.87MPa.

In the midpoint of prescale film, the stresses are zero because of the position of the opening circle. In the Figure A.41, the stress distributions of prescale film in x-axis are obtained. In the opening position, zero stress level is presented, whereas stresses are equal on the left and right side of prescale film. The mean stresses are 0.7 MPa.

In Figure A.42, 3-D stress distributions of prescale film no. 10 are presented. High stress level, ranging between 2.5-3.06, are located in the lower right part of prescale film. In the other part of prescale film, the stress distribution values range between 0-2.5 MPA. The change in stress level is due to static point load at midpoint of the SPVFR.

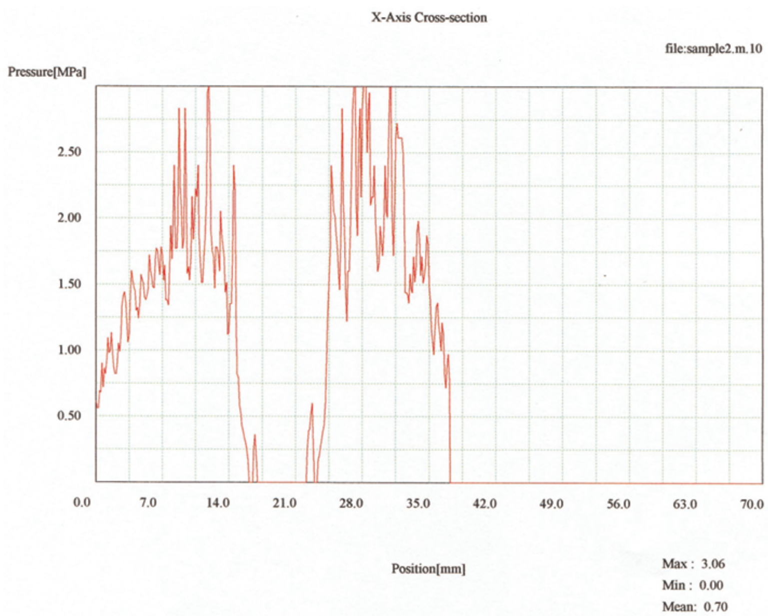

Figure A.41. Stress Distribution on X-Axis Cross-Section of Prescale Film No.10.

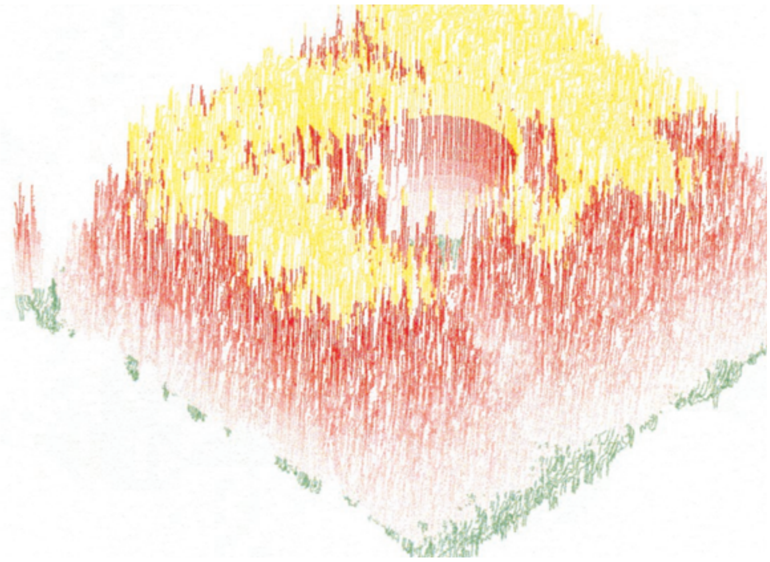

Figure A.42. 3-D Stress Distribution on the Upper Part of Prescale Film No.10.

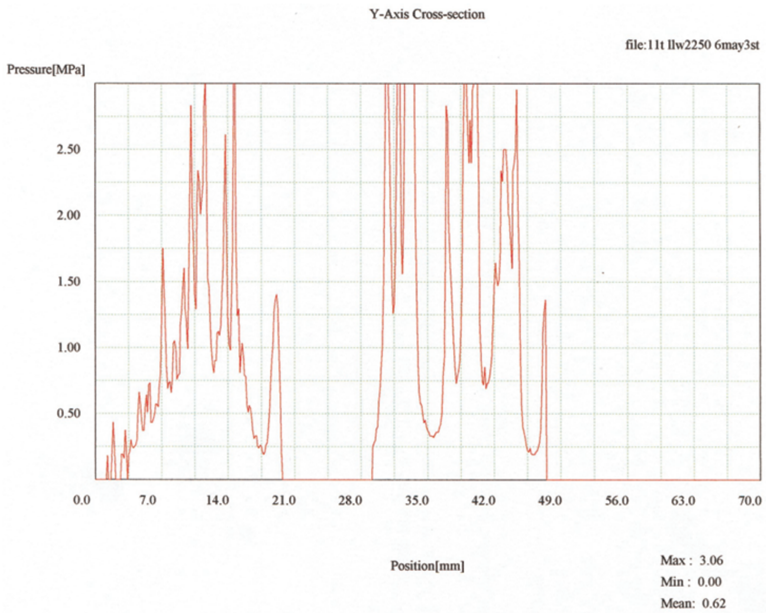

Figure A.43. Stress Distribution on Y-Axis Cross-Section of Prescale film No.11.

A.7. Stress Distribution due to Prestress Force and Static Load at Top-Point of the SPVFR

In the Figure A.43, the stress distributions in y -axis of prescale film are presented. In the upper part of prescale film, high stress values are presented comparing compared to the lower part. In the opening diameter, zero stress values are presented. The mean stresses are 0.62 MPa. In the Figure A.35, stress distributions along x-axis of prescale film no. 11 are obtained. The stresses, located on the left side of prescale film, are more than the right one. Zero stresses, which represent opening hole, are given. The mean stress values are 0.63 MPa, which are higher than mean stresses in the y-axis.

In the Figure A.49, the 3-D stress distributions of prescale film are presented. The maximum stresses are found in the lower part of prescale film. The zero stress values at midpoint of prescale film represented the opening circle of section.

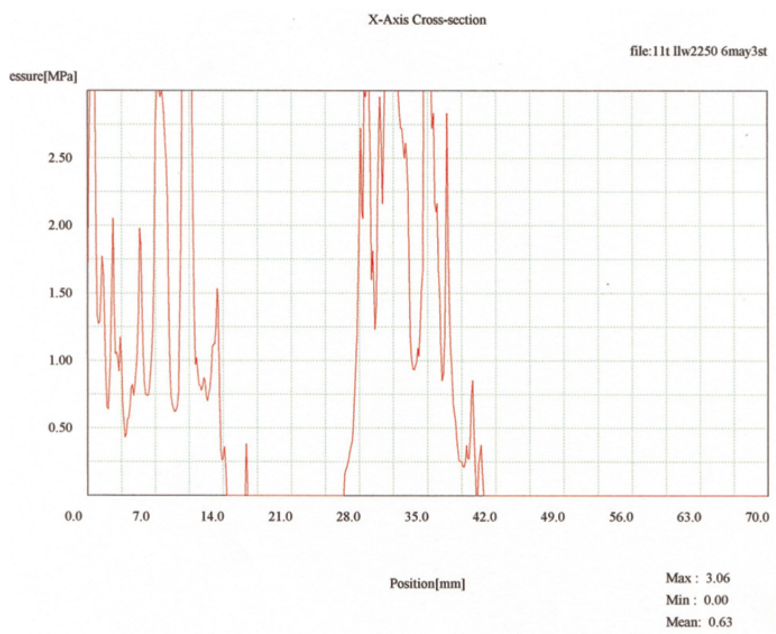

Figure A.44. Stress Distribution on X-Axis Cross-Section of Prescale Film No.11.

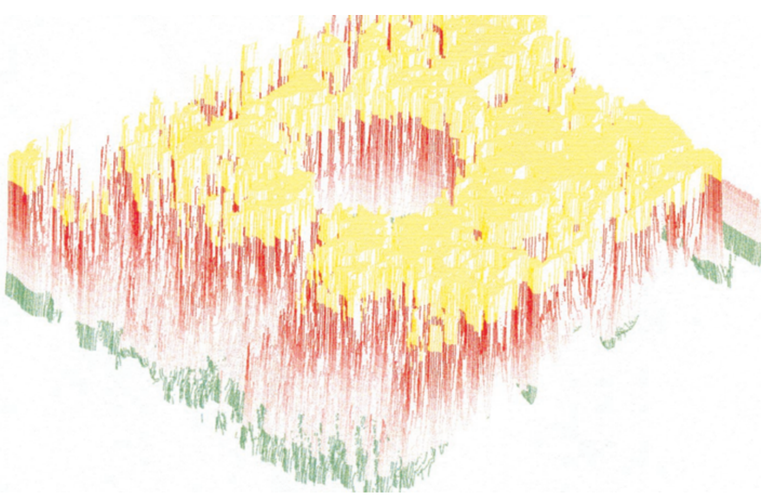

Figure A.45. 3-D Stress Distribution on the Upper Part of Prescale Film No.11.

In the Figure A.46, the stress distribution in y-axis of prescale film no 13 are presented. In the upper side of prescale film, stress values are presented, higher than the stress values in the lower part. The mean stresses are 0.61 MPa. In the opening diameter at midpoint of prescale film, zero stress values are presented. In the Figure A.47, the stress distribution in x-axis of prescale film no 13 are obtained. The stress distribution values on the left side of prescale film are higher than the right side, which ranged between 0-2.61MPa. The mean stress values are 0.36 MPa.

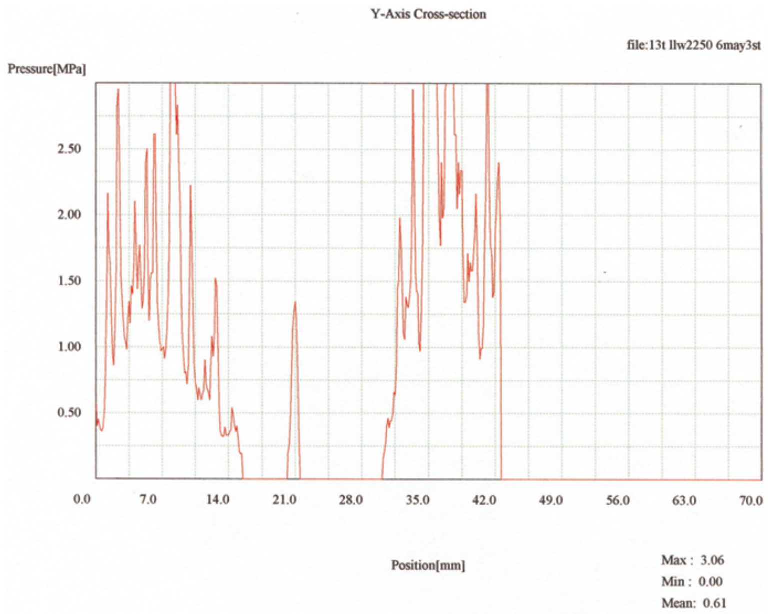

Figure A.46. Stress Distribution on Y-Axis Cross-Section of Prescale film No.13.

In the Figure A.48, 3-D stress distributions of prescale film are presented. The high values of stress are distributed in all areas of prescale film, which range between 0-3.06 MPa [yellow color]. The zero stress values represent for the opening part. In the middle area, the stresses distributions range between 0-2.5 [red color].

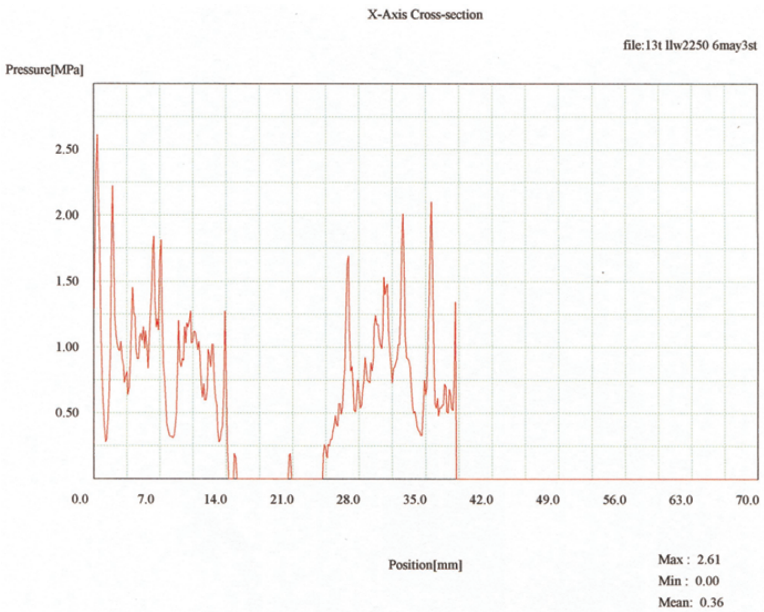

Figure A.47. Stress Distribution on X-Axis Cross-Section of Prescale Film No.13.

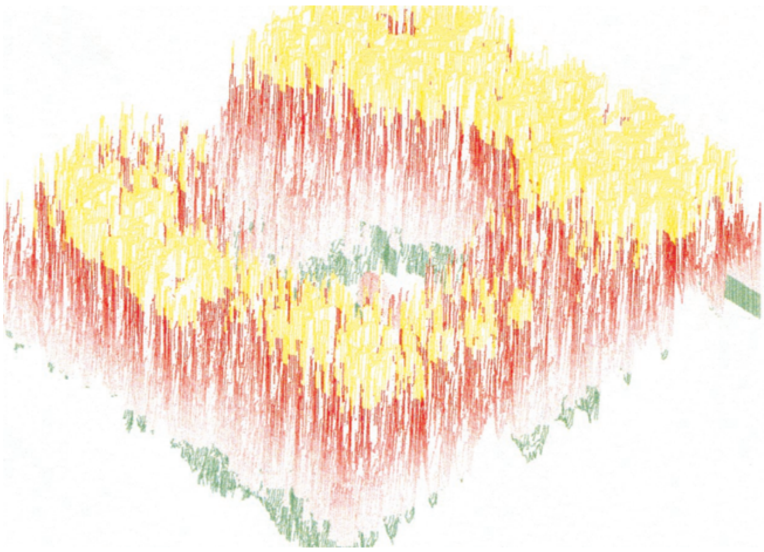

Figure A.48. 3-D Stress Distribution on the Upper Part of Prescale Film No.13.

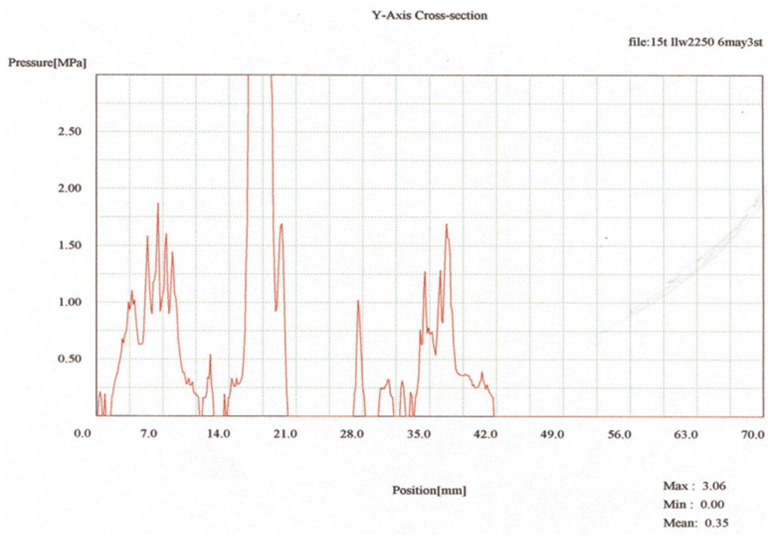

Figure A.49. Stress Distribution on Y-Axis Cross-Section of Prescale film No.15.

In the Figure A.49, the stress distributions in y-axis of prescale film no. 15 are presented. The stress values in the lower part of prescale film are higher than the upper part as shown in Figure A.49. The stress distributions range between 0-3.06 MPa; and the mean stress values are 0.35 MPa. In Figure A.50, the stress distributions in the x-axis of prescale film are obtained. The stress values on the right part of prescale film are higher than the left part. The mean stresses are 0.27 MPa, which is less than the mean stresses in y-axis.

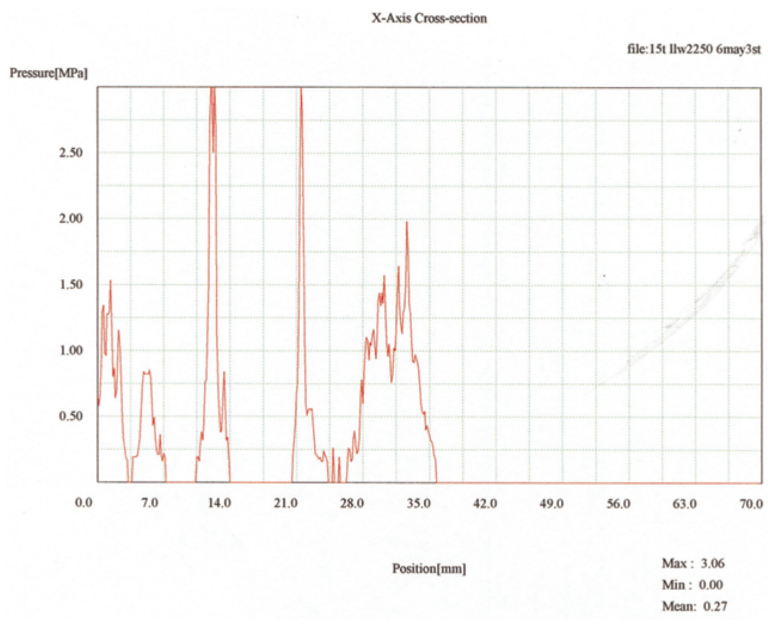

Figure A.50. Stress Distribution on X-Axis Cross-Section of Prescale Film No.15.

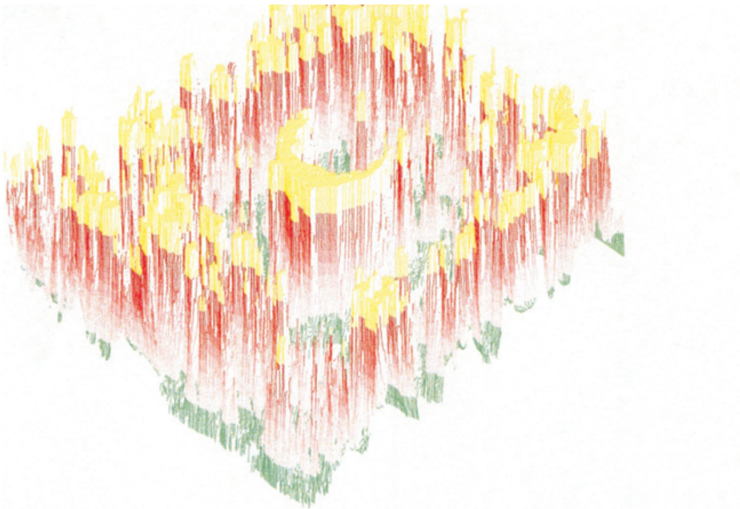

Figure A.51. 3-D Stress Distribution on the Upper Part of Prescale Film No.15.

In the Figure A.51, 3-D stress distributions on the upper part of prescale film no. 15 are obtained. The high stress levels are concentrated in the four edges of prescale film [yellow color]. In the other part of prescale film, the stress values range between 0-2.5 MPa.

In the Figure A.52, the stress distributions in y-axis of prescale film no.16 are presented. The stress distributions in the upper part of prescale film are higher than the lower part. The stress distributions are ranged between 0-3.06 MPa; and the mean stress values are 1 MPa. For the opening part at midpoint, zero stress values are recorded. In the Figure A.53, the stress distributions on x-axis of prescale film no.16 are obtained. In this part, equal stress distributions on the left and right parts of prescale film are observed, which range between 0-3.06 MPa; and zero stress values in the opening part are recorded. The mean stress values are 0.84 MPa.

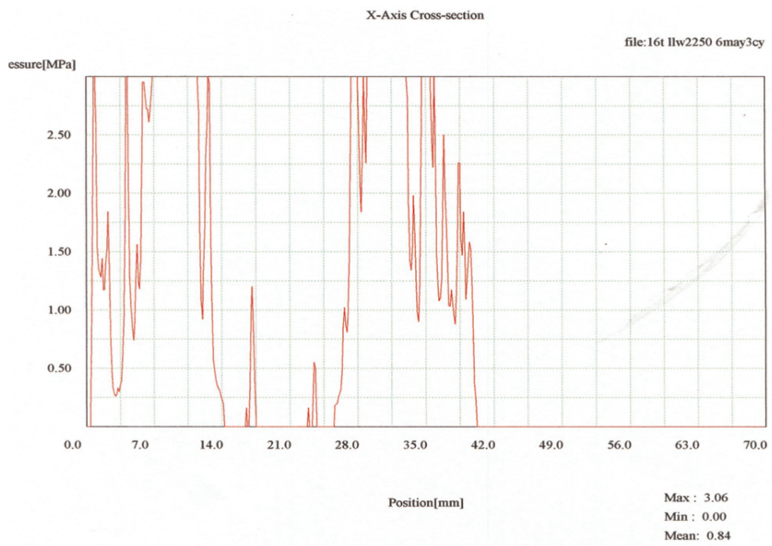

Figure A.52. Stress Distribution on Y-Axis Cross-Section of Prescale film No.16.

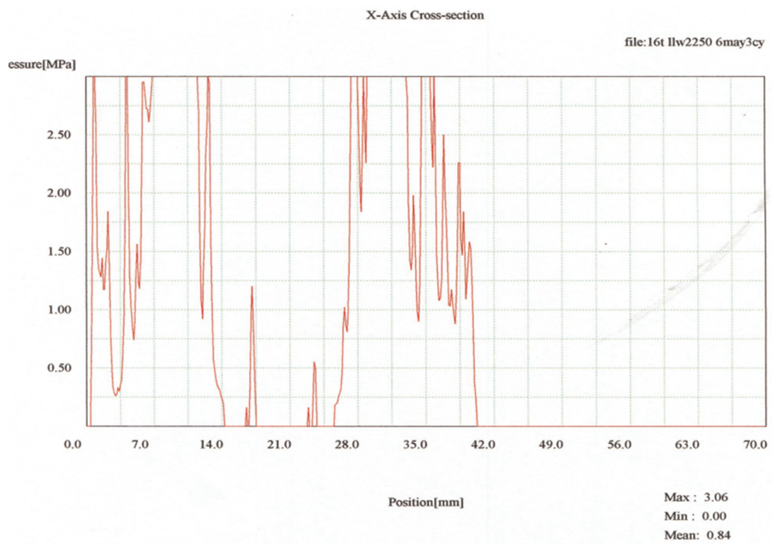

Figure A.53. Stress Distribution on X-Axis Cross-Section of Prescale Film No.16.

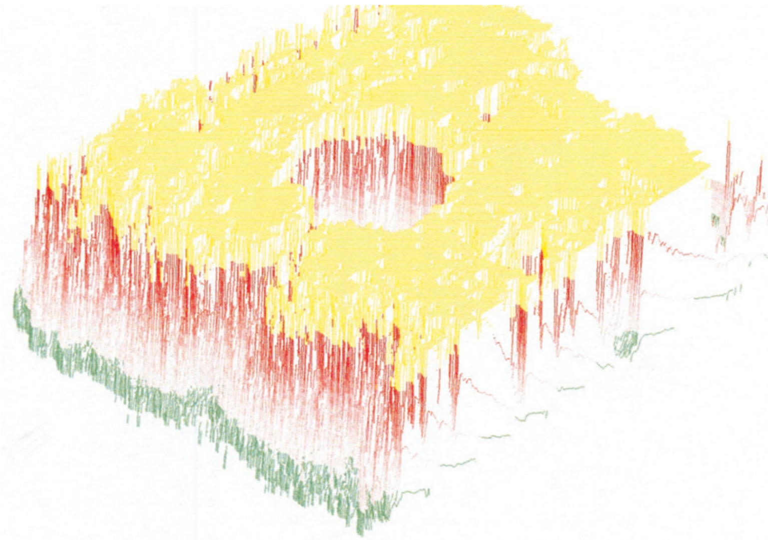

Figure A.54. 3-D Stress Distribution on the Upper Part of Prescale Film No.16.

In the Figure A.54, 3-D stress distributions of prescale film are presented. It is observed that the stress values are distributed equally in all parts of prescale film. In the position of the opening part diameter, zero stress values are recorded.

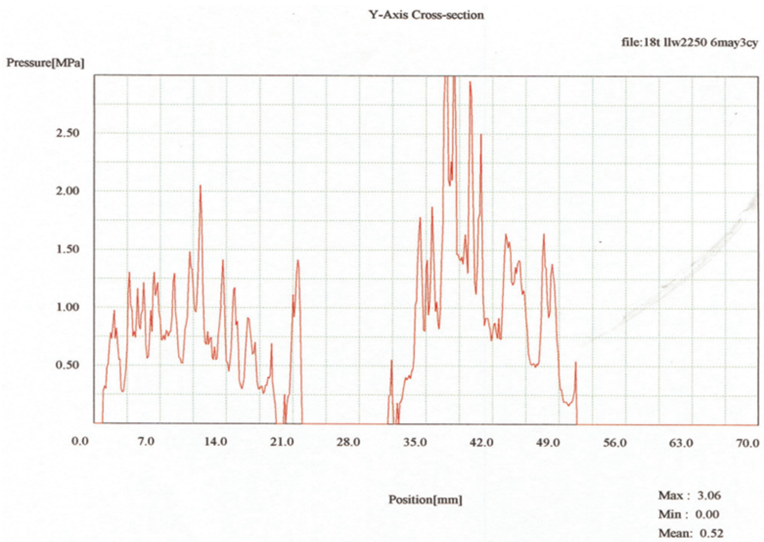

Figure A.55. Stress Distribution on Y-Axis Cross-Section of Prescale film No.18.

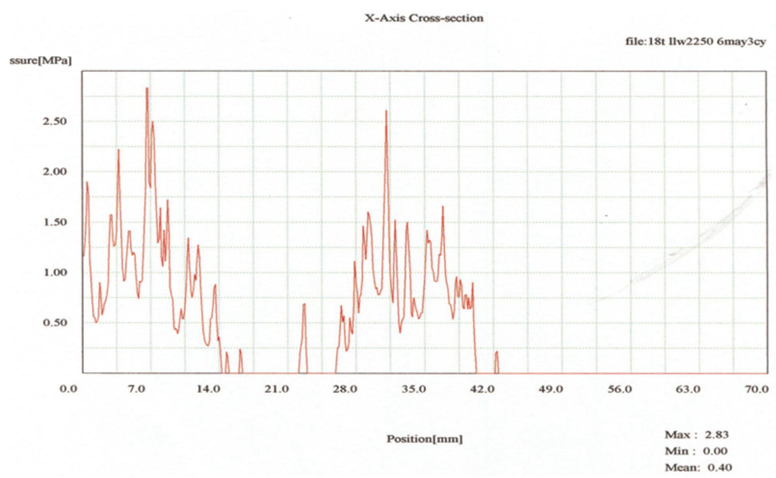

Figure A.56. Stress Distribution on X-Axis Cross-Section of Prescale Film No.18.

In the Figure A.55, stress distributions along y-axis of prescale film no. 18 are obtained. The upper part of prescale film is subjected to higher stress values than the lower part; and the stress values range between 0-3.06 MPa. The mean stress values are 0.52 MPa. In Figure A.56, stress distributions along x-axis of prescale film are presented. The stresses are distributed equally on the left and right parts of prescale film, which range between 0-2.83 MPa. The mean stress values are 0.4 MPa.

In Figure A.57, 3-D stress distributions of prescale film no.18 are presented. The high stress values are concentrated on the lower and right parts of prescale film. The other parts are subjected to the average stresses distribution ranged between 0-2.5 MPa. Zero stress values are recorded in the opening part of the prescale film.

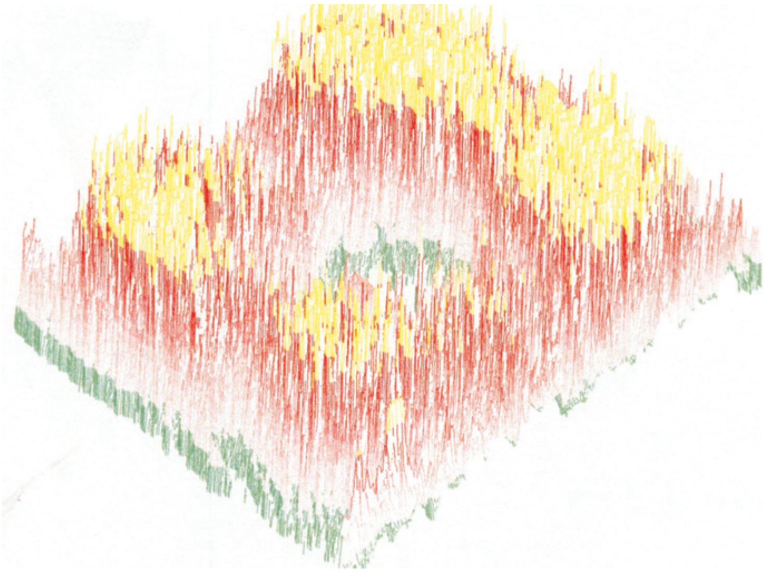

Figure A.57. 3-D Stress Distribution on the Upper Part of Prescale Film No.18.

In Figure A.58, stress distributions along y-axis of prescale film no. 20 are presented. The maximum stress distribution are located in the lower part more than the upper part of prescale film , which range between 0-3.06 MPa. In the opening part, zero stress values are recorded. The mean stress values are 0.38 MPa. In Figure A.59, stress distributions along x-axis of prescale film no.20 are presented. The stress distributions in the right part are higher than the left part as shown in Figure 3.11. The stress distributions are ranged between 0-3.06 MPa and the mean stress are 0.52 MPa.

In Figure A.60, 3-D stress distributions in the upper view of prescale film no. 20 are presented. From the figure high stress distribution are observed on the left side and the edges of prescale film (yellow color). On the other parts of prescale film, average stress values ranged between 0-2.5 MPa (red color) are distributed. In the opening part diameter, zero stress values are recorded.

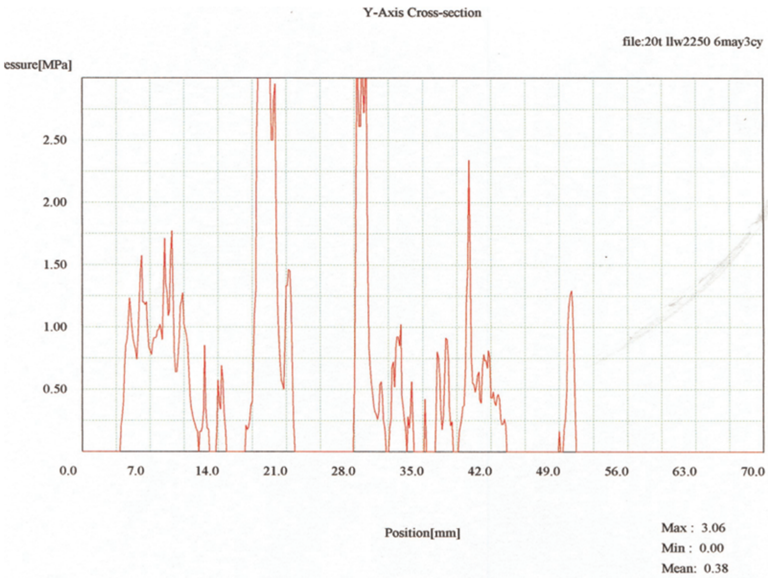

Figure A.58. Stress Distribution on Y-Axis Cross-Section of Prescale film No.20.

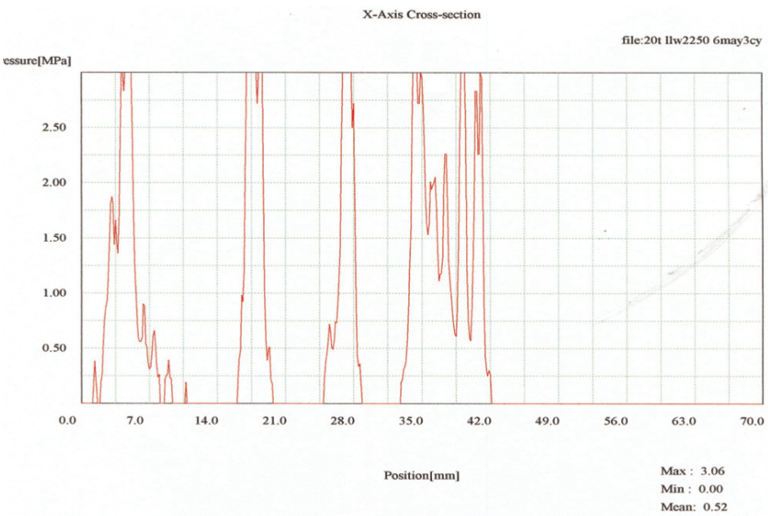

Figure A.59. Stress Distribution on X-Axis Cross-Section of Prescale Film No.20.

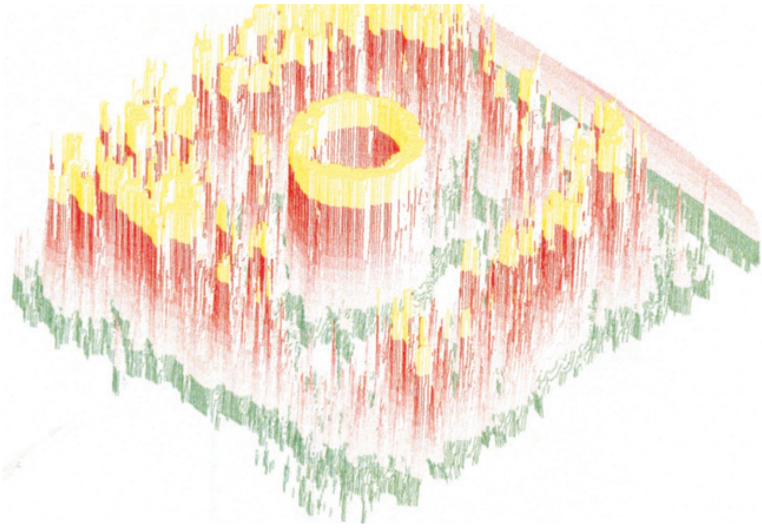

Figure A.60. 3-D Stress Distribution on the Upper Part of Prescale Film No.20.

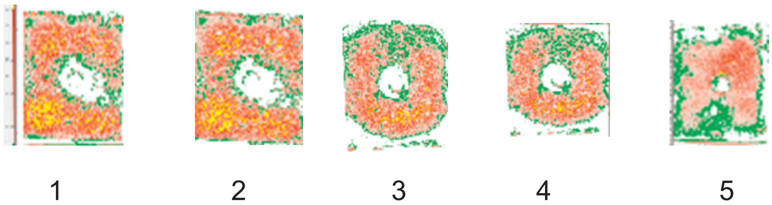

Figure A.61. Pure Post-Tension.

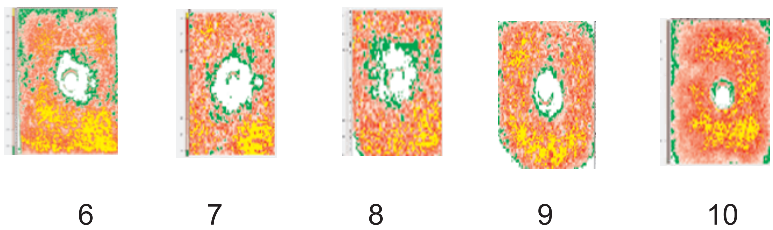

Figure A.62. Static Mid-Point.

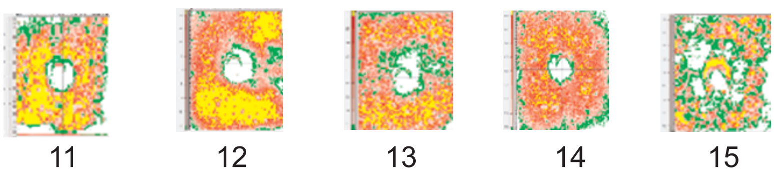

Figure A.63. Static Top-Point.

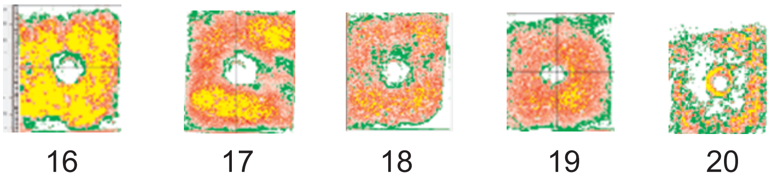

Figure A.64. Cyclic Top-Point.

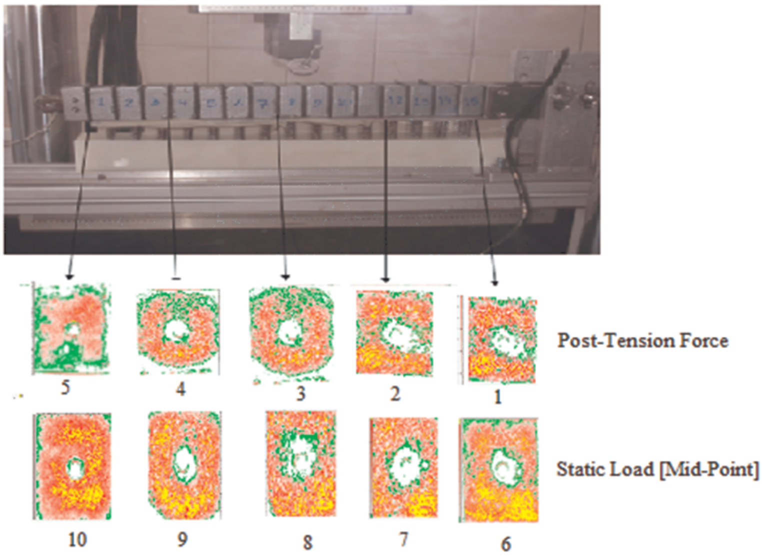

Figure A.65. Stress Distribution of the Prescal Film on SPVFR Subjected to Post-Tension Force and Static Load at Mid-Point.

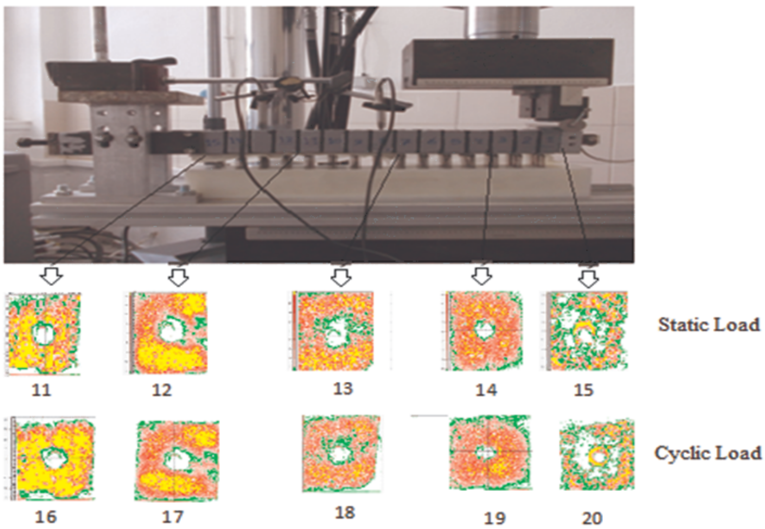

Figure A.66. Stress Distribution of the Prescal Film on SPVFR Subjected to Post-Tension Force and Static /Cyclic Load at Top-Point.

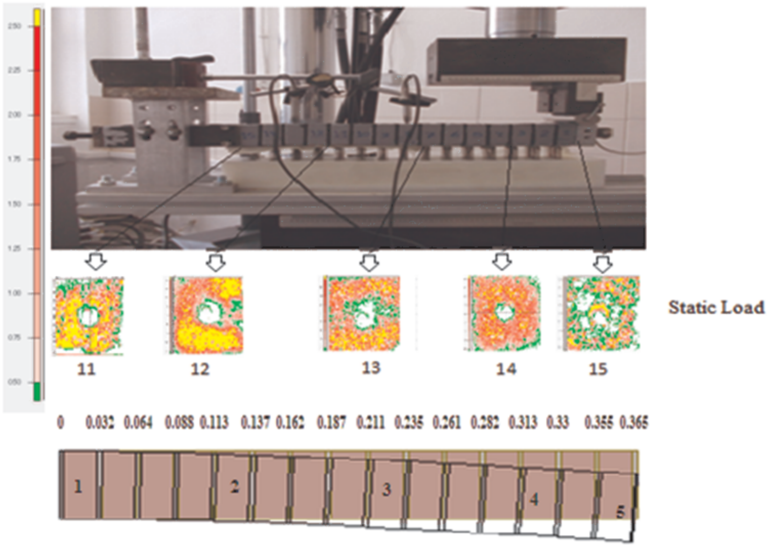

Figure A.67. Stress Distribution on the Prescale Films along SPVFR Due to Cyclic load at Top Point.

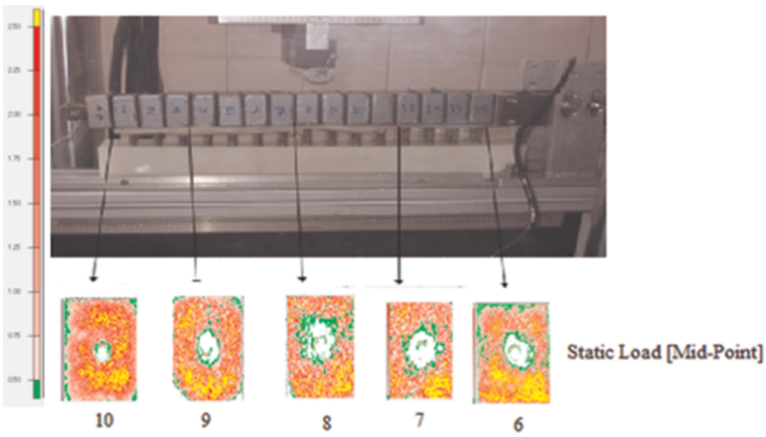

Figure A.68. Stress Distribution on the Prescale Films along SPVFR Due to Static load at Mid-Point.

Table A.1. Stress Distribution for SPVFR Subjected to Prestress Forces [Prescale Film No.5].

Sample Name	5llw 2250 2may01	Prescale Effective Rate(%)	67.4
Examination Date Time	2013.04.11 14:00	Pressed Area (mm2)	1743.0
Measurement Date Time	2013.05.07 10:10	Ave Pressure (MPa)	0.78
Prescale Type	LLW	Max Pressure (MPa)	3.06
Pressure Type	Continuous	Load(N)	1359
Resolution(mm)	0.125	Measured Area(mm2)	2371.0
Scan Count	1	-	-
Temperature(-C)	20	-	-
Humidity(%)	68	-	-
Pressure Range (MPa)	Pressed Area(mm2)	Ave Pressure(MPa)	Max Pressure(MPa)
p < 0.50	562.0	0.31	0.49
0.50 <= p<0.75	363.0	0.62	0.74
0.75 <=p<1.00	310.0	0.88	1.00
1.00<=p<1.25	227.0	1.12	1.25
1.25 <=p<1.50	152.0	1.36	1.49
1.50<=p<1.75	70.0	1.60	1.73
1.75<=p<2.00	34.0	1.84	1.98
2.00<=p< 2.25	13.0	2.10	2.22
2.25<=p<2.50	6.0	2.33	2.40
2.50<=p	6.0	2.75	3.06

Table A.2. Stress Distribution for SPVFR Subjected to Prestress Forces [Prescale Film No.6].

Sample Name	6L llw 2250 2may2st	Prescale Effective Rate(%)	67.9
Examination Date Time	2013.04.11 14:00	Pressed Area (mm2)	1816.0
Measurement Date Time	2013.05.02 18:11	Ave Pressure (MPa)	1.51
Prescale Type	LLW	Max Pressure (MPa)	3.06
Pressure Type	Continuous	Load(N)	2746
Resolution(mm)	0.125	Measured Area(mm2)	2004.0
Scan Count	1	-	-
Temperature(-C)	20	-	-
Humidity(%)	68	-	-
Pressure Range (MPa)	Pressed Area(mm2)	Ave Pressure(MPa)	Max Pressure(MPa)
p < 0.50	207.0	0.34	0.49
0.50 <= p<0.75	215.0	0.62	0.74
0.75 <=p<1.00	226.0	0.88	1.00
1.00<=p<1.25	209.0	1.13	1.25
1.25 <=p<1.50	198.0	1.37	1.49
1.50<=p<1.75	144.0	1.61	1.73
1.75<=p<2.00	114.0	1.85	1.98
2.00<=p< 2.25	75.0	2.10	2.22
2.25<=p<2.50	53.0	2.33	2.40
2.50<=p	375.0	2.95	3.06

Table A.3. Stress Distribution for SPVFR Subjected to Prestress Forces [Prescale Film No.8].

Sample Name	M.L llw 2250 2may02st	Prescale Effective Rate(%)	74.0
Examination Date Time	2013.04.11 14:00	Pressed Area (mm2)	1470.0
Measurement Date Time	2013.05.02 17:35	Ave Pressure (MPa)	1.34
Prescale Type	LLW	Max Pressure (MPa)	3.06
Pressure Type	Continuous	Load(N)	1975
Resolution(mm)	0.125	Measured Area(mm2)	1682.0
Scan Count	1	-	-
Temperature(-C)	20	-	-
Humidity(%)	68	-	-
Pressure Range (MPa)	Pressed Area(mm2)	Ave Pressure(MPa)	Max Pressure(MPa)
p < 0.50	203.0	0.32	0.49
0.50 <= p<0.75	174.0	0.62	0.74
0.75 <=p<1.00	188.0	0.88	1.00
1.00<=p<1.25	196.0	1.13	1.25
1.25 <=p<1.50	192.0	1.37	1.49
1.50<=p<1.75	137.0	1.60	1.73
1.75<=p<2.00	101.0	1.85	1.98
2.00<=p< 2.25	61.0	2.10	2.22
2.25<=p<2.50	39.0	2.33	2.40
2.50<=p	179.0	2.92	3.06

Table A.4. Stress Distribution for SPVFR Subjected to Prestress Forces [Prescale Film No.10].

Sample Name	10.L llw 2250 2may02st	Prescale Effective Rate(%)	80.5
Examination Date Time	2013.04.11 14:00	Pressed Area (mm2)	1446.0
Measurement Date Time	2013.05.02 18:03	Ave Pressure (MPa)	1.57
Prescale Type	LLW	Max Pressure (MPa)	3.06
Pressure Type	Continuous	Load(N)	2273
Resolution(mm)	0.125	Measured Area(mm2)	1490.0
Scan Count	1	-	-
Temperature(-C)	20	-	-
Humidity(%)	68	-	-
Pressure Range (MPa)	Pressed Area(mm2)	Ave Pressure(MPa)	Max Pressure(MPa)
p < 0.50	83.0	0.35	0.49
0.50 <= p<0.75	98.0	0.64	0.74
0.75 <=p<1.00	133.0	0.88	1.00
1.00<=p<1.25	177.0	1.13	1.25
1.25 <=p<1.50	232.0	1.37	1.49
1.50<=p<1.75	200.0	1.61	1.73
1.75<=p<2.00	160.0	1.85	1.98
2.00<=p< 2.25	101.0	2.10	2.22
2.25<=p<2.50	64.0	2.33	2.40
2.50<=p	198.0	2.87	3.06

Table A.5. Stress Distribution for SPVFR Subjected to Prestress Forces [Prescale Film No.11].

Sample Name	11t llw 2250 6may3st	Prescale Effective Rate(%)	51.8
Examination Date Time	2013.04.11 14:00	Pressed Area (mm2)	1651.0
Measurement Date Time	2013.05.06 17:20	Ave Pressure (MPa)	1.67
Prescale Type	LLW	Max Pressure (MPa)	3.06
Pressure Type	Continuous	Load(N)	2754
Resolution(mm)	0.125	Measured Area(mm2)	2072.0
Scan Count	1	-	-
Temperature(-C)	20	-	-
Humidity(%)	73	-	-
Pressure Range (MPa)	Pressed Area(mm2)	Ave Pressure(MPa)	Max Pressure(MPa)
p < 0.50	258.0	0.31	0.49
0.50 <= p<0.75	174.0	0.62	0.74
0.75 <=p<1.00	161.0	0.88	1.00
1.00<=p<1.25	140.0	1.13	1.25
1.25 <=p<1.50	133.0	1.37	1.49
1.50<=p<1.75	92.0	1.61	1.73
1.75<=p<2.00	69.0	1.85	1.98
2.00<=p< 2.25	49.0	2.11	2.22
2.25<=p<2.50	37.0	2.33	2.40
2.50<=p	538.0	3.00	3.06

Table A.6. Stress Distribution for SPVFR Subjected to Prestress Forces [Prescale Film No.13].

Sample Name	13t llw 2250 6may3st	Prescale Effective Rate(%)	69.6
Examination Date Time	2013.04.11 14:00	Pressed Area (mm2)	1485.0
Measurement Date Time	2013.05.06 17:27	Ave Pressure (MPa)	1.44
Prescale Type	LLW	Max Pressure (MPa)	3.06
Pressure Type	Continuous	Load(N)	2138
Resolution(mm)	0.125	Measured Area(mm2)	1635.0
Scan Count	1	-	-
Temperature(-C)	20	-	-
Humidity(%)	73	-	-
Pressure Range (MPa)	Pressed Area(mm2)	Ave Pressure(MPa)	Max Pressure(MPa)
p < 0.50	189.0	0.32	0.49
0.50 <= p<0.75	183.0	0.62	0.74
0.75 <=p<1.00	183.0	0.88	1.00
1.00<=p<1.25	178.0	1.13	1.25
1.25 <=p<1.50	170.0	1.37	1.49
1.50<=p<1.75	123.0	1.61	1.73
1.75<=p<2.00	93.0	1.85	1.98
2.00<=p< 2.25	60.0	2.10	2.22
2.25<=p<2.50	43.0	2.33	2.40
2.50<=p	262.0	2.94	3.06

Table A.7. Stress Distribution for SPVFR Subjected to Prestress Forces [Prescale Film No.15].

Sample Name	15t llw 2250 6may3st	Prescale Effective Rate(%)	54.3
Examination Date Time	2013.04.11 14:00	Pressed Area (mm2)	1485.0
Measurement Date Time	2013.05.06 17:32	Ave Pressure (MPa)	1.06
Prescale Type	LLW	Max Pressure (MPa)	3.06
Pressure Type	Continuous	Load(N)	1311
Resolution(mm)	0.125	Measured Area(mm2)	1621.0
Scan Count	1	-	-
Temperature(-C)	20	-	-
Humidity(%)	73	-	-
Pressure Range (MPa)	Pressed Area(mm2)	Ave Pressure(MPa)	Max Pressure(MPa)
p < 0.50	419.0	0.31	0.49
0.50 <= p<0.75	202.0	0.61	0.74
0.75 <=p<1.00	149.0	0.88	1.00
1.00<=p<1.25	104.0	1.12	1.25
1.25 <=p<1.50	83.0	1.37	1.49
1.50<=p<1.75	55.0	1.60	1.73
1.75<=p<2.00	38.0	1.85	1.98
2.00<=p< 2.25	26.0	2.11	2.22
2.25<=p<2.50	19.0	2.33	2.40
2.50<=p	148.0	2.96	3.06

Table A.8. Stress Distribution for SPVFR Subjected to Prestress Forces [Prescale Film No.16].

Sample Name	16t llw 2250 6may3cy	Prescale Effective Rate(%)	38.1
Examination Date Time	2013.04.11 14:00	Pressed Area (mm2)	1701.0
Measurement Date Time	2013.05.07 09:42	Ave Pressure (MPa)	2.08
Prescale Type	LLW	Max Pressure (MPa)	3.06
Pressure Type	Continuous	Load(N)	3531
Resolution(mm)	0.125	Measured Area(mm2)	2223.0
Scan Count	1	-	-
Temperature(-C)	20	-	-
Humidity(%)	73	-	-
Pressure Range (MPa)	Pressed Area(mm2)	Ave Pressure(MPa)	Max Pressure(MPa)
p < 0.50	194.0	0.30	0.49
0.50 <= p<0.75	97.0	0.62	0.74
0.75 <=p<1.00	94.0	0.88	1.00
1.00<=p<1.25	102.0	1.13	1.25
1.25 <=p<1.50	111.0	1.37	1.49
1.50<=p<1.75	83.0	1.61	1.73
1.75<=p<2.00	70.0	1.86	1.98
2.00<=p< 2.25	51.0	2.11	2.22
2.25<=p<2.50	38.0	2.33	2.40
2.50<=p	859.0	3.01	3.06

Table A.9. Stress Distribution for SPVFR Subjected to Prestress Forces [Prescale Film No.18].

Sample Name	18t llw 2250 6may3cy	Prescale Effective Rate(%)	76.3
Examination Date Time	2013.04.11 14:00	Pressed Area (mm2)	1816.0
Measurement Date Time	2013.05.07 09:53	Ave Pressure (MPa)	1.18
Prescale Type	LLW	Max Pressure (MPa)	3.06
Pressure Type	Continuous	Load(N)	2135
Resolution(mm)	0.125	Measured Area(mm2)	2199.0
Scan Count	1	-	-
Temperature(-C)	20	-	-
Humidity(%)	73	-	-
Pressure Range (MPa)	Pressed Area(mm2)	Ave Pressure(MPa)	Max Pressure(MPa)
p < 0.50	290.0	0.32	0.49
0.50 <= p<0.75	284.0	0.62	0.74
0.75 <=p<1.00	291.0	0.88	1.00
1.00<=p<1.25	262.0	1.13	1.25
1.25 <=p<1.50	225.0	1.37	1.49
1.50<=p<1.75	143.0	1.60	1.73
1.75<=p<2.00	94.0	1.85	1.98
2.00<=p< 2.25	52.0	2.10	2.22
2.25<=p<2.50	34.0	2.33	2.40
2.50<=p	141.0	2.90	3.06

REFERENCES

Alexiew, D., D., Brokemper and S., Lothspeich, 2005, "Geotextile Encased Columns (GEC): Load Capacity, Geotextile Selection and Pre-Design Graphs", *GSP 131 Contemporary Issues in Foundation Engineering*, Vol. 34, No. 1, pp. 1-14.

Aljorany, A.N., 2012, "Modelling and Analysis of the Pullout Behaviour of Granular Pile Anchor in Expansive Soils" *GSP 132 Contemporary Issues in Foundation Engineering*, Vol. 36, No. 3, pp. 15-34.

Alonso, J.A. and R., Jimenez, 2012, "Reliability-Based Design of Stone Columns for Ground Improvement Considering Settlement and Bulging as Failure Modes", N. Denies and N. Huybrechts (eds), *Proceedings of the International Symposium on Recent Research, Advances and Execution Aspects of Ground Improvement Works* - TC 211 IS-GI, Vol. III, ISSMGE Technical Committee TC 211 Ground Improvement, Belgian Building Research Institute, Brussels, pp. 319-328.

API (American Petroleum Institute), 2008, API RP2A: Recommended Practice for Planning, Designing and Constructing Fixed Offshore Platforms. Working Stress Design, 22nd edn. API, Washington, DC.

ASIRI, 2012, Amélioration Des Sols Par Inclusions Rigides, (with English translation on CD: Rigid Inclusions Ground Improvement) /Presses des Ponts/ISBN 978-2-85978-462-1.

Auvinet, G. and J.F., Rodriguez, 2006, Rigid Inclusions in Mexico City Soft Soils: History and Perspectives, Symposium Rigid Inclusions in Difficult Subsoil Conditions /ISSMGE TC36 /UNAM.

Baykal, G., 1982, *A Study on Numerical Analysis of Laterally Loaded Piles*, M.S. Thesis, Boğaziçi University.

Bernal, D. And E., Miranda, 1992, “Instability of Buildings Subjected to Earthquakes,” *Journal of Structural Engineering*, Vol. 118, No. 4, pp. 2239-2260.

Bowles, J.E., 1997, Foundation Analysis and Design, 6th ed., McGrow-Hill International press, London.

Briançon, L. and B., Simon, 2012, “Performance of a Pile-Supported Embankment Over Soft Soil”: *Full Scale Experiment, Accepted for Publication, Journal of Geotechnical and Geoenvironmental Engineering*/ASCE.

Brinch Hansen, J., 1961, The Ultimate Resistance of Rigid Piles Against Transversal forces. The Danish Geotechnical Institute, Bulletin , 12.

Broms, B. 1965, Design of Laterally Loaded Piles, Journal of the Soil Mechanics and Foundation Division, Vol. 91, No. 3, pp. 77-99.

Brown, D.A., C., Morrison, L.C., Reese, 1988, Lateral Load Behavior of Pile Group in Sand, *Journal of Geotechnical Engineering*, ASCE, Vol. 114 No. 11, pp. 1261-1276.

BS8006, 2010, *Code of Practice for Strengthened/Reinforced Soils and Other Fills, Section 8*, Design of Embankments with Reinforced Soil Foundations on Poor Ground.

Castro, J. and C., Sagaseta, 2012, “Consolidation Around Stone Columns Influence of Column Formation”, *International Journal for Numerical and Analytical Methods in Geomechanics*, Vol. 33, No. 8, pp. 851-877.

Chu J, S., Varaskin, U., Klotz and P., Menge, 2009, State of the Art Report: Construction Processes, *17th ISSMGE*, Alexandria, Egypt.

Chung, S.T. and C.H., Loh, 2002, Identification and Verification of Seismic Demand from Different Hysteretic Models, Journal of Earthquake Engineering, Vol. 6, No. 3, pp. 331-355.

Ciolko, A.T. and Tabatabai, H., 1999, “Nondestructive Methods for Condition Evaluation of Prestressing Steel Strands in Concrete Bridges” National Cooperative Highway Research Program, Transportation Research Board National Reaserch Council, NCHRP Project, pp.10-53.

Collins, M.P. and D., Mitchell, 1991, “Prestressed Concrete Structures”, *Prentice Hall*, Vol. 34, No. 2, pp. 766-786.

Cook, W.D. and D., Mitchell, 1988, “Studies of Disturbed Regions Near Discontinuities in Reinforced Concrete Members”, Structural Journal, American Concrete Institute, Vol. 85, No. 2, pp. 206- 216.

Corven, J., “Mid Bay Bridge Post-Tensioning Evaluation”, Final Report, Florida Department of Transportation, October, 2001 http://www11.myflorida.com/ structures /posttensioning .htm.

Corven, J. and A., Moreton, 2004, *Post-tensioning Tendon Installation and Grouting Material*, Corven Engineering, Tallahassee, FL. pp. 718-725.

Cox, W.R, L.C., Reese, and B.R., Grubbs, 1971, *Field Testing of Laterally Loaded Piles in Sand. Offshore Technicar*, Conference, Houston, Texas, pp. 459-472.

Davisson, M.T. and H.L., Gill, 1963, “Laterally Loaded Piles in a Layered Soil System,” *J. Soil Mech. Found. Diu.*, ASCE, Vol. 89, No. 2, pp. 63-94.

De Mello, L.G., M., Mondolfo, F., Montez, C.N., Tsukahara and W., Bilfinger, 2008, “First Use of Geosynthetic Encased Sand Columns in South America”, *Proceedings of 1st Pan-American Geosynthetics Conference*, Vol. 12, No. 2, pp. 1332-1341.

Durgunoğlu, H.T., 2004, “The Utilization of High Modulus Columns in Foundation Engineering”, in Turkish, Sixth Ord. Prof. Dr. Hamdi Peynircioglu Lecture Proceedings, of 10, Turkish National Conf. on SMFE.

Durgunoğlu, H.T., H.F., Kulaç, C,K., Oruç, C,R., Yıldız, J., Sıckling, I.E., Boys, T., Altuğu and C., Emrem, 2003, "A Case History of Ground Treatment with Jet Grouting Against Liquefaction for a Cigarette Factory in Turkey", *Grouting and Grout Treatment*, New Orleans, USA.

Durgunoğlu, H.T., O., Nur, O., Akbal, H.F., Kulaç, S., Ikiz, C.G., Olgun, 1995, "A Case Study on Determination of Soil Improvement Using CPT" *CPT'95 International Symposium on Cone Penetration Testing*, Vol. 2, No. 1, pp. 441-446.

Gniel, J., A., Bouazza, 2009, "Improvement of Soft Soils Using Geogrid Encased Stone Columns", *Geotextiles and Geomembranes*, Vol. 27, No. 6, pp. 167-175.

Gniel, J., and A., Bouazza, 2010, "Construction of Geogrid Encased Stone Columns: A New Proposal Placed on Laboratory Testing", *Geotextiles and Geomembranes*, Vol. 28, No.2, pp. 108-118.

Greenwood, D. A. 1970 "Mechanical Improvement of Soils Below Ground Surfaces", *Proc., Ground Engineering Conf., Institution of Civil Engineers*, London, Vol. 3, No. 2, pp. 11-22.

Hetényi M., 1964, *Beams on Elastic Foundation: Theory with Applications in the Fields of Civil and Mechanical Engineering*, Univ. of Michigan Press, Ann, Arbor, Michigan.

Hsiung, Y., and Y., Chen, 1997, Simplifirf Method for Analyzing Laterally Loaded Single Piles, J., Geotech and Geoenvir Eng, ASCE Vol. 123, No. 11, pp. 1018-29.

Kempfert, H.G., A., Jaup and M., Raithel, 1997, "Interactive Behaviour of a Flexible Reinforced Sand Column Foundation in Soft Soils", *12th International Conference on Soil Mechanics and Foundation Engineering, Hamburg*, Vol. 45, No. 32, pp. 1757-1760.

Khabbazian, M., V.N., Kaliakin and L.M., Christopher, 2008, "3D Numerical Analyses of Geosynthetic Encased Stone Columns", *International Foundation Congress and*

Equipment Expo., Vol. 12, No. 4, pp. 201-208.

Krawinkler, H. and E., Miranda, 2004, “Performance Based Earthquake Engineering” Chapter 9 of Earthquake Engineering: From Engineering Seismology to Performance Based Engineering, Edited by Y. Bzorgina and V. Bertero, CRC Press.

Lin, T.Y. and N., Burns, 1981, “Design of Prestressed Concrete Structures”, John Wiley and Sons, New York, pp . 646.

Magnan, J.P., N., Droniuc, Y., Canepa, A., Dhouib, 2005, “Reflexions Sur la Conception Des Colonnes Ballast´ees”. *In: Proceedings of 16th International Conference of Soils Mechanics and Foundation Engineering*, Osaka, Vol. 3, No. 1, pp. 1377-1380.

Mahin, S.A., and V.V. Bertero, 1976, “Problems in Establishing and Predicting Ductility in Aseismic Design”, *Proceedings, International Symposium on Earthquake Structural Engineering*, St. Luis, Missouri, August, pp. 613-628.

Matlock, C.H. and Reese, 1970, “Correlations for Design of Laterally Loaded Piles”, *Proceeding of the II Annual Offshore technology.*

McClelland, B. and J., Focht, 1958, *Soil Modulus for Laterally Loaded Piles*, Transactions, ASCE, Vol. 123, No. 2954, pp. 1049-1086.

McKenna, J.M., W.A., Eyre and D.R., Wolstenholme, 1975, “Performance of an Embankment Supported by Stone Columns in Soft Ground”, *Geotechnique*, Vol. 25, No. 1, pp. 51-59.

Mitchell, J.K. and Wentz, J.R., 1991, Performance of improved Ground During Loma Prieta Earthquake, Report No UCB/EERC-91-12, Earthquake Engineering Research Center, University of California, Berkeley.

Murugesan, S., and K., Rajagopal, 2006, “Geosynthetic-Encased Stone Columns: Numerical Evaluation”, *Geotextiles and Geomembranes*, Vol. 24, No. 1, pp. 349-358.

Murugesan, S., and K., Rajagopal, 2007, "Model Tests on Geosynthetic-Encased Stone Columns", *Geosynthetics International*, Vol. 14, No. 6, 346-354.

Nilson, A.H., 1978, "Design of Prestressed Concrete", John Wiley and Sons, New York, pp. 526.

Özkeskin, Ç., O., Erol, Z., Çekinmez, 2012, Settlement Reduction and Stress Concentration Factors in Rammed Aggregate Piers Determined From Full- Scale Group Load Tests.

Pecker, A., 2004, Design and Construction of the Rion Antirion Bridge. Proc. ASCE Geo-Trans 2004 on Geotechnical Aspects of Transportation Engineering.

Priebe, H.J., 1995, The Design of Vibro Replacement, *Ground Engineering* Dec., pp. 31-37.

Raithel, M., A., Kirchner, C., Schade and E., Leusink, 2005, "Foundation of Constructions on Very Soft Soils with Geotextile Encased Columns-State of the Art", *Geotechnical Special Publication*, No. 130-142, Geo-Frontiers 2005, pp. 1867-1877.

Rao S., S., Gandhi and P., Ambily, 2007, "Behavior of Stone Columns Based on Experimental and FEM Analysis", J., Geotech, Geoenviron. Eng., Vol. 133, No. 4, pp. 405-415.

Rathmeyer, H., 1975, Piled Embankment Supported by Single Pile Caps, ISSMFE Conference, Istanbul, Vol. 1, pp. 283-290.

Reese, A., 1977, "Cyclic Lateral Loading of a Large Scale Pile Group," *J. Geotech. Eng. Diu ASCE*, Vol. 113, No. 11, pp. 1326-1343.

Reese A., and Y., Welch, 1975, "Lateral Load Behavior of Pile Groups in Sand", *J. Geotch. Eng. Diu.*, ASCE, Vol. 114, No. 11, pp. 1261-1276.

Reese, L.C. and Matlock, H., 1956, *Non-Dimensional Solutions for Laterally Loaded*

Piles with Soil Modulus Assumed Proportional to Depth., Proceedings of the 8th Texas Conference on Soil Mechanics and Foundation Engineering, Austin, pp, 1-41.

Reese, L.C. and W.F., Van Impe, 2001, *Single Piles and Pile Group under Lateral Loading.*, A.A., Balkema, Rotterdam, pp. 463.

Reese, L.C., W.R., Cox and F.D., Kooper, 1974, "Analysis of Laterally-Loaded Piles in Sands", *Proc. 6th. Annual Offshore Technology Conference*, Huston, Texas, OTC 2080.

Reese, L.C., C., Lymon, 1977, "Laterally Loaded Piles: Program Docwnentation," Journal of the Geotechnical Engineering Division, American Society of Civil Engineers, Vol. 103, No. GT4, Proc. Paper 12862, pp. 287-305.

Reissner E.W, 1967, Note on *The Formulation of the Problem of the Plate on an Elastic Foundation, Acta Mechanica*, Vol. 4, No.1, pp. 88-91.

Schweiger, H.F., 2008, *Overview of Design Concepts of Ground Improvement Techniques in TC17*, Website: www.bbri.be/go/tc17.

Simon, B. and F., Schlosser, 2006, *Soil Reinforcement by Vertical Stiff Inclusions in France. Symposium Rigid Inclusions in Difficult Subsoil Conditions*/ISSMGE TC36/UNAM.

Simon, B. and F., Schlosser, 2006, Soil Reinforcement by Vertical Stiff Inclusions in France, Symposium Rigid Inclusions in Difficult Subsoil Conditions /ISSMGE TC36/UNAM.

Slocombe, B.C. and M.P., Moseley, 1991, "The Testing and Instrumentation of Stone Columns", ASTM STP 1089.

Slocombe, B.C., A.L., Bell, J.I., Baez, 2000, "The Densification of Granular Soils Using Vibration Methods", *Geotechnique*, Vol. 50, No. 6, pp. 715-725.

Sondermann W. and J., Wehr, 2004, Deep Vibro Techniques in Ground Improvement, 2nd edition /Edit. Mosley M. P. and Kirsch K /Spon Press- pp. 57-92.

Terzaghi, K. and R.B., Peck, 1955, Soil Mechanics in Engineering Practice, 2nd Edition, John Wiley and Sons, New York.

Van Impe, W. and P., Silence, 1986, "Improving of the Bearing Capacity of Weak Hydraulic Fills by Means of Geotextiles", *Proceedings of the 3rd International Conference on Geotextiles*, Vol. 12. No. 4, pp. 1411-1416.

Veletsos, A.S. and N.M., Newmark, 1960, "Effect of Inelastic Behavior on the Response of Simple Systems to Earthquake Motions", *Proc., 2nd World Conf. on Earthquake Engrg.*, Vol. 2, pp. 895-912.

Warner, R.F., and K.A., Faulkes, 1979, "Prestressed Concrete", Pitman, Melbourne, pp. 336.

Wu, C., Y.S., Hong and H.C., Lin, 2009, "Axial Stress-Strain Relation of Encapsulated Granular Column", *Computers and Geotechnics*, Vol. 36, No. 1, pp. 226-240.